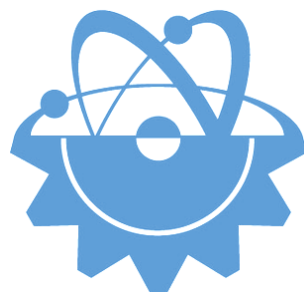


ISSN-Printed: 2536-5010  
ISSN-Online: 2536-5134

Volume 9, N 2, 2019

# EJT

EUROPEAN JOURNAL OF TECHNIQUE



Copyright © 2017 International Engineering, Science & Education Group

Email (for orders and customer services enquiries): [info@ineseg.org](mailto:info@ineseg.org), [ejt@ineseg.org](mailto:ejt@ineseg.org), [ejtineseg@gmail.com](mailto:ejtineseg@gmail.com)

Visit our home page on [www.ineseg.org](http://www.ineseg.org) or <https://dergipark.org.tr/ejt>

All Rights Reserved. No part of this publication may be reproduced, stored in a retrieval system or transmitted in any form or by any means, electronic, mechanical, photocopying, recording, scanning or otherwise, except under the terms of the Copyright, under the terms of a license issued by the Copyright International Engineering, Science & Education Group (INESEG), without the permission in writing of the Publisher. Requests to the Publisher should be addressed to the Permissions Department, International Engineering, Science & Education Group (INESEG), or emailed to [info@ineseg.org](mailto:info@ineseg.org)

Designations used by companies to distinguish their products are often claimed as trademarks. All brand names and product names used in this journal are trade names, service marks, trademarks or registered trademarks of their respective owners. The Publisher is not associated with any product or vendor mentioned in this journal.

This publication is designed to provide accurate and authoritative information in regard to the subject matter covered. It is sold on the understanding that the Publisher is not engaged in rendering professional services. If professional advice or other expert assistance is required, the services of a competent professional should be sought.

## **EUROPEAN JOURNAL OF TECHNIQUE (EJT)**

**ISSN-Printed: 2536-5010**

**ISSN-Online: 2536-5134**

**Scope:** European Journal of Technique (EJT) established in 2010. It is a peer –reviewed international journal to be of interest and use to all those concerned with research in various fields of, or closely related to, Engineering disciplines. European Journal of Technique (EJT) aims to provide a highly readable and valuable addition to the literature which will serve as an indispensable reference tool for years to come. The coverage of the journal includes all new theoretical and experimental findings in the fields of Engineering or any closely related fields. The journal also encourages the submission of critical review articles covering advances in recent research of such fields as well as technical notes.

### ***The scopes include:***

- Mechanical Engineering
- Textile Engineering
- Electrical-Electronics Engineering
- Computer and Informatics Engineering
- Civil and Architecture Engineering
- Mining Engineering
- Chemical Engineering
- Metallurgical and Materials Engineering
- Environmental Engineering
- Food Engineering
- Geological Engineering
- Industrial Engineering
- Renewable Energy

### ***Editor-in-Chief***

- Musa YILMAZ

### ***Publisher Of Journal***

- Heybet KILIÇ

## ETHICS and POLICIES

European Journal of Technique (EJT) is committed to following the Code of Conduct and Best Practice Guidelines of COPE (Committee on Publication Ethics). It is a duty of our editors to follow Cope Guidance for Editors and our peer-reviewers must follow COPE Ethical Guidelines for Peer Reviewers. We expect all prospective authors to read and understand our Ethics Policy before submitting any manuscripts to our journals.

Please note that submitted manuscripts may be subject to checks using the iThenticate service, in conjunction with CrossCheck, in order to detect instances of overlapping and similar text.

The [iThenticate](#) software checks submissions against millions of published research papers, documents on the web, and other relevant sources. If plagiarism or misconduct is found, consequences are detailed in the policy.

The chief goal of our policy is threefold: to provide advice for our authors, to maintain the scholarly integrity of our journals and their content, and to detail the ethical responsibilities of EJT, our editors and authors.

We expect all authors to read and understand our ethics policy before submitting to any of our journals. This is in accordance with our commitment to the prevention of ethical misconduct, which we recognise to be a growing problem in academic and professional publications. It is important to note that most incidents of plagiarism, redundant publication, copyright infringement or similar occur because of a lack of understanding, and not through fraudulent intent. Our policy is one of prevention and not persecution.

If you have any questions, please contact the relevant editorial office, or European Journal of Technique (EJT)' ethics representative: [ejtineseg@gmail.com](mailto:ejtineseg@gmail.com)

Download a PDF version of the Ethics and Policies [PDF,392KB].

### Authors' Responsibilities

#### Authors should:

- Ensure that all researched work submitted is original, fully referenced and that all authors are represented accurately. The submission must be exclusive and not under consideration elsewhere.
- Provide accurate contact details for a designated corresponding author, who shall be deemed by the publisher and editor as fully responsible for the authorship of the paper and all communications concerning the ethical status and originality of the paper. This includes any queries or investigations that may arise, pre- or post publication.
- Openly disclose the source of all data and third party material, including previously unpublished work by the authors themselves. Anything that could compromise the originality of the submission should be expressly avoided and/or discussed with the editorial office in the first instance.
- Identify any third party material that they intend to include in their article, and obtain written permission for re-use in each instance from the relevant copyright holders. Such permissions should be submitted once the manuscript is accepted, or requires small changes to be accepted. For further guidance on seeking permission to use 3rd party material please see the Rights and Permissions section.
- Openly disclose any conflict of interest - for example, if publication were to benefit a company or services in which the author(s) has a vested interest.

- Expect to formally agree publication terms which defines the author and the publishers rights for the work. Visit our website for further information.
- Expect the editor to scan submissions using plagiarism detection software at [iThenticate](#) to check a paper's originality before sending out for review.
- Fully correspond and comply with the editor and publisher in any requests for source data, proof of authorship or originality in a timely manner, providing reasonable explanation for discrepancies or failures to disclose vital information.
- Fully co-operate with any consequent investigations if the editor and/or publisher are dissatisfied with the evidence available or the explanations provided.
- Expect transparency, efficiency and respect from the publisher and the editor during the submissions process.
- Remain in good communication with both the publisher and the editor.
- When necessary, submit corrigenda in a timely and responsible fashion.
- Co-operate fully with the publication of errata and with the retraction of articles found to be unethical, misleading or damaging.
- Remain in good communication with the editor(s), the publisher and any co-authors.

## Editors' Responsibilities

### Editors should:

- Read and understand COPE guidelines as well as EJT's ethics policy, and follow them during all editorial processes.
- Protect the reputation of their journal(s) and published work by only publishing content of the highest quality and relevance in a timely and responsible manner.
- Carry out thorough, objective and confidential peer review for original article submissions that pass the initial quality check and editorial assessment, in adherence with COPE guidelines and EJT' ethics policy.
- Detail and justify any article types which will not be peer reviewed (e.g. editorials, opinion pieces etc.).
- Provide a transparent review and publication process as far as is possible, with full respect and care paid to the author(s).
- Provide advice and give reasonable explanation and updates to authors during the submissions process and once a decision has been made.
- Allow authors the right to appeal any editorial decision.
- Only accept papers based on the original merit, quality and relevance of their content.
- Support authors in queries concerning the originality of their submissions and request the support of EJT if necessary.
- Advise the publisher of any third party material which has been included for which they do not believe sufficient permission has been cleared.

- Be ready and prepared to publish corrections, corrigenda, errata when necessary, as well as retract articles that (the editor and EJT) deem unethical, misleading or damaging.
- Remain in good communication with both the publisher and the author(s).

## Reviewers' Responsibilities

### Reviewers should:

- Adhere to EJT's policy of confidential peer review of their journals. This includes, but is not restricted to, keeping their identity hidden from authors and not externally distributing any work that is passed to them for their eyes only.
- Only accept invitations to review work that is relevant to their own expertise and speciality.
- Review submitted work in a responsible, impartial and timely manner.
- Report any suspected ethical misconduct as part of a thorough and honest review of the work.
- Avoid the use of unnecessarily inflammatory or offensive language in their appraisal of the work.
- Accept the commitment to review future versions of the work and provide 'follow up' advice to the editor(s), if requested.
- Seek advice from the editor if anything is unclear at the time of invitation.
- Remain in good communication with both the publisher and the editor.

## EJT's Responsibilities

### EJT will:

- Protect the reputation of our journals and published work by only publishing content of the highest quality and relevance in a timely and responsible manner.
- Provide detailed information concerning both our understanding of publication ethics and our implementation of the same. Emphasise a desire for prevention, not eventual detection, of ethical misconduct.
- Uphold our COPE membership (or of such similar organisations) and keep our editorial offices, publishing staff and society partners up-to-date with their guidelines and policies, adapting our own where appropriate (and publicising any update).
- When necessary, request proof of originality/accuracy from the corresponding author of any work submitted to any of our journals.
- Use plagiarism detection software when necessary for any submission to any journal at any stage of the submissions and publication process.
- Provide a transparent submissions and publication process, with full respect and care paid to the author. This includes detailed and dedicated instructions to authors for each journal, outlining referencing style, accepted article types and submission processes.

- Investigate thoroughly any suggestion of ethical misconduct detected during any stage of the submissions process. This can include, but is not restricted to, the following: plagiarism, redundant publication, fabrication or misuse of data and authorial disputes.
- When necessary, retract articles that we deem to be unethical, misleading or damaging.
- When necessary, publish errata, corrigenda and retractions in a timely and responsible fashion, detailing the decision online in an open access format and publishing in print as soon as possible.
- Remain in good communication with editors, authors, reviewers and society partners (where applicable).

## Further reading

- Authorship of the paper: Authorship should be limited to those who have made a significant contribution to the conception, design, execution, or interpretation of the reported study.
- Originality and plagiarism: The authors should ensure that they have written entirely original works, and if the authors have used the work and/or words of others that this has been appropriately cited or quoted.
- Data access and retention: Authors may be asked to provide the raw data in connection with a paper for editorial review, and should be prepared to provide public access to such data.
- Multiple, redundant or concurrent publication: An author should not in general publish manuscripts describing essentially the same research in more than one journal or primary publication. EJT do not view the following uses of a work as prior publication: publication in the form of an abstract; publication as an academic thesis; publication as an electronic preprint. Information on prior publication is included within each EJT and its journal Guideline for Authors.
- Acknowledgement of sources: Proper acknowledgment.
- Disclosure and conflicts of interest: All submissions must include disclosure of all relationships that could be viewed as presenting a potential conflict of interest.
- Fundamental errors in published works: When an author discovers a significant error or inaccuracy in his/her own published work, it is the author's obligation to promptly notify the journal editor or publisher and cooperate with the editor to retract or correct the paper.
- Reporting standards: Authors of reports of original research should present an accurate account of the work performed as well as an objective discussion of its significance.
- Hazards and human or animal subjects: Statements of compliance are required if the work involves chemicals, procedures or equipment that have any unusual hazards inherent in their use, or if it involves the use of animal or human subjects.
- Use of patient images or case details: Studies on patients or volunteers require ethics committee approval and informed consent, which should be documented in the paper.

EJT has also accessed and learned from the existing policies of other publishers and leading experts as well as open access articles that detail and define ethical misconduct.

- 'Plagiarism and the law', Joss Saunders, Learned Publishing, 23:279-202: <http://www.ingentaconnect.com/content/alpsp/lp/2010/00000023/00000004/art00002>
- iThenticate Plagiarism Resources: <http://www.ithenticate.com/resources/6-consequences-of-plagiarism>

## **Editor-in-Chief**

Musa Yilmaz, Batman University, Turkey

## **International Editorial Board**

Aayush Shrivastava	University of Petroleum and Energy Studies, Dehradun, India
Adelino Pereira	Engineering Institute of Coimbra, Portugal
Ahmad Fakharian	Islamic Azad University, Qazvin, Iran
Ahmed Saber	Cairo University, Egypt
Arvind Kumar Jain	Rustam Ji Institute of Technology, India
Aydogan Ozdemir	Istanbul Technical University, Turkey
Baseem Khan	Hawassa University, Hawassa, Ethiopia
Behnam Khakhi	University of California Los Angeles, US
Behnam Mohammadi-ivatloo	University of Tabriz, Tabriz, Iran
Bharti Dwivedi	Institute of Engineering & Technology, Lucknow, UP, India
Carlos A. Castro	University of Campinas – UNICAMP, Brasil
Deepak Kumar	University of Petroleum & Energy Studies (UPES), India
Ernesto Vazquez	University of Nuevo Leon, Mexico
Faisal Khan	COMSATS Institute of Information Technology, Pakistan
Farhad Shahnia	Murdoch University, Perth, Australia
Farrokh Aminifar	University of Tehran, Iran
Fatih Kocycigit	Dicle University, Turkey
Fiaz Ahmad	National University of Computer and Emerging Sciences, Pakistan
Furkan Emre Sahin	Maxim Integrated, San Jose, CA, US
Gouthamkumar Nadakuditi	V R Siddhartha Engineering College, India
Hafiz Ahmed	School of Mechanical, Coventry University, UK
Hamed Pourgharibshahi	Lamar University, US
Hassan Bevrani	University of Kurdistan, Iran
Hemant Kumar Gianey	Thapar University, Patiala, Punjab, India
Hessam Golmohamadi	Semnan University, Semnan, Iran
Hilmy Awad	Helwan University, Cairo, Egypt
Idris Candan	Kocaeli University, Turkey
Jamshed Ahmed Ansari	Sukkur IBA University, Pakistan
José A. Domínguez-Navarro	University of Zaragoza, Spain
Kalpana Chauhan	Galgotias College of Engineering and Technology, India
Khaled Ellithy	Qatar University, Doha, Qatar
Kim-Doang Nguyen	South Dakota State University, US
Kundan Kumar	KIIT University, India
Lalit Kumar	GBPIET Pauri, India
Leila Mokhnache	University of Batna 2, Algeria
Linquan Bai	ABB Inc., US
Md Shafiullah	King Fahd University of Petroleum & Minerals, Saudi Arabia
Mohamed Shaaban	Universiti Malaysia Sarawak, Malaysia
Mohammed Albadi	Sultan Qaboos University, Oman

Mohd Tariq	Aligarh Muslim University, India
Mousa Marzband	Northumbria University, Newcastle upon Tyne, United Kingdom
Neeraj Kanwar	Manipal University Jaipur, India
Nishant Kumar	Indian Institute of Technology Delhi, India
Nitin Kumar Saxena	Wolaita Sodo University, Ethiopia
Nouar Tabet	University of Sharjah, UAE
Omar Hafez	Umm Al-Qura University, Makkah, Saudi Arabia
Omveer Singh	Gautam Buddha University, India
Payam Teimourzadeh Baboli	University of Mazandaran (UMZ), Iran
Payman Dehghanian	George Washington University, US
Ragab A. El Sehiemy	Faculty of Engineering, Kafrelsheikh Univrsity, Egypt
Rajeev Kumar Chauhan	Galgotias College of Engineering and Technology, India
Rajiv Singh	G.B. Pant University of Agriculture & Technology, India
Reza Sharifi	Amir Kabir university Tehran, Iran
Rudranarayan Senapati	Kalinga Institute of Industrial Technology, India
Saleh Y. Abujarad	Universiti Teknologi Malaysia, Malaysia
Sanjay Dambhare	College of Engineering, Pune, India
Saptarshi Roy	NIT Warangal, India
Shailendra Kumar	Indian Institute of Technology Delhi, India
Shariq Riaz	The University of Sydney, Australia
Shengen Chen	University of Maine, US
Syafaruddin	Universitas Hasanuddin, Indonesia
T. Sudhakar Babu	VIT University, Vellore, India
Thamer Alquthami	King Abdulaziz University, Saudi Arabia
Theofilos Papadopoulos	Democritus University of Thrace, Greece
Uday P. Mhaskar	CSA Group, US
Vedat Veli Cay	Dicle University, Turkey
Yogesh Rohilla	K Lakshmiapat University, Jaipur, India
Yunfeng Wen	School of Electrical Engineering, Chongqing University, China
Zbigniew M. Leonowicz	Wroclaw University of Science and Technology, Poland

## ***Publisher of Journal***

Heybet Kilic

## CONTENTS

IMITATION OF FUZZY LOGIC CONTROLLER BASED ARTIFICIAL NEURAL NETWORK, AND APPLICATION OF INVERTED PENDULUM SYSTEM CONTROL	121-136
IMPEDANCE IMAGE RECONSTRUCTION WITH ARTIFICIAL NEURAL NETWORK IN ELECTRICAL IMPEDANCE TOMOGRAPHY	137-144
A COMPARISON STUDY FOR IMAGE DENOISING	145-150
AN OVERVIEW TO ANTENNA TERMINOLOGY AND DESIGN A COMPACT DUAL BAND ANTENNA BY USING HFSS PROGRAM FOR C AND X BANDS APPLICATIONS	151-158
ENERGY PREDICTION BASED ON MODELLING AND SIMULATION ANALYSIS OF AN ACTUAL GRID-CONNECTED PHOTOVOLTAIC POWER PLANT IN TURKEY	159-174
ENVIRONMENTAL NOISE TRACKING SYSTEM BASED ON WEB OF THINGS	175-185
INTEGRATION OF WIND POWER PLANTS TO THE GRID AND REACTIVE POWER SUPPORT	186-196
NUMERICAL ANALYSES OF A STRAIGHT BLADED VERTICAL AXIS DARRIEUS WIND TURBINE: VERIFICATION OF DMS ALGORITHM AND QBLADE CODE	195-208
INVESTIGATION OF MECHANICAL AND THERMAL BEHAVIOR OF BASALT CUTTING WASTE (BCW) ADDED CLAY BRICK	209-218
PANTOGRAPHY APPLICATION WITH REAL-TIME PLC BASED ON IMAGE PROCESSING IN GANTRY ROBOT SYSTEM	219-229
PRODUCTION OF AA7075/B4C COMPOSITE MATERIALS BY SEMI-SOLID STIRRING METHOD	230-240
INVESTIGATING THE UTILIZATION OF WASTE GLASS POWDER, COLEMANITE ORE WASTE AND SUGAR FACTORY FILTER CAKE IN GYPSUM-LIME BASED MORTARS	241-252
CONDENSATION ANALYSIS OF THE INSULATION OF WALLS ACCORDING TO DIFFERENT LOCATIONS IN MARDIN PROVINCE	253-262
DETERMINING EFFECTS OF HEAT TRANSFER FINS ON THE SOLIDIFICATION PROCESS OF PCM AND NANO-PCM WITH A RECTANGULAR COOLER	263-274
EFFECT OF FORMING HISTORY ON CRASHWORTHINESS OF A SPOT-WELDED AND DOUBLE-HAT ELLIPTICAL THIN-WALLED TUBE	275-285
DYNAMIC ANALYSIS OF UNIFORM AND NON-UNIFORM CROSS-SECTION CANTILEVER SANDWICH BEAMS	286-297
EVALUATION OF RENEWABLE ENERGY SOURCE ALGAE AS BIODIESEL FEEDSTOCK	298-311
INVESTIGATION OF MICROSTRUCTURE AND MICROHARDNESS PROPERTIES OF CO AND CR REINFORCED NIAL INTERMETALLIC COMPOUND PRODUCED BY SHS METHOD	312-319
EVENT DATA VISUALIZATION THROUGH PROCESS MINING: A CASE FOR EMERGENCY MEDICAL SERVICE SYSTEM IN ADANA	320-329
USE OF NANO HEXAGONAL BOR NITRIDE (HBN) ADDED CUTTING FLUID IN MILLING OF HARD TO CUT MATERIALS	330-337
THE EXPERIMENTAL INVESTIGATION OF ANNEALING PARAMETERS EFFECTS ON AL2024-T3 MATERIALS' FORMABILITY AND MECHANICAL PROPERTIES	338-346

## IMITATION OF FUZZY LOGIC CONTROLLER BASED ARTIFICIAL NEURAL NETWORK, AND APPLICATION OF INVERTED PENDULUM SYSTEM CONTROL

Murat SAM<sup>1\*</sup>, M. Serhat CAN<sup>2</sup>

*Fuzzy Logic Controllers (FLCs) are effective solutions for nonlinear and parameter variability systems, but it contains multiple mathematical operations causing the controller to react slowly. This study aims to obtain a controller that can imitate the effective control performance of the FLC, which is easy to design both in software and hardware, and has a short response time. Artificial neural networks (ANNs) provide effective solutions in system modeling. Modeling of FLC has been realized by using of ANN's learning and parallel processing capability. The design process of the FLC and the training processes of the ANN were studied in Matlab SIMULINK environment. In the study, FLC was modelled at high similarity ratio with small ANN structure. ANN results were obtained very faster than the FLC control performance. The control performances of two controllers were observed to be very close to each other. As a result, ANN model has smaller structure than FLC, which makes it possible to implement the controller easily in terms of hardware and software.*

*Key words: Fuzzy logic controller, artificial neural network, fuzzy logic controller modelling.*

### 1. Introduction

Today, with the development of technology, some demands in our daily activities such as speed, safety and comfort are increasing. For example, while people aim to only travel between two cities in the early ages, they are now looking for solutions to how they can perform faster, safer and more comfortably travelling. To ensure a faster, safer and more comfortable travelling, advanced and often complex control systems are required.

There is a relationship between an input signal applied to a controlled system and the system's response to this input signal. This relationship, sometimes linear or nonlinear, is known as the transfer function of the system and can be formulated with a mathematical expression.

$$y = m * x + n \quad (1)$$

The Eq. (1) is an example for linear systems. Here m and n represent constant coefficients, x represents the input, and y represents the output response of the system to the input signal. It is also

---

<sup>1</sup> Department of Electrical and Electronics Engineering, Gaziosmanpasa University, Tokat, Turkey, (murat.sam0218@gop.edu.tr)

<sup>2</sup> Department of Electrical and Electronics Engineering, Gaziosmanpasa University, Tokat, Turkey, (mehmetserhat.can@gop.edu.tr)  
 <https://orcid.org/0000-0003-2356-9921>

easy to control because the mathematical models of linear control systems are simple and easy to obtain. The condition that a system to be controlled is linear is that changes in the input signal always affect the output at the same rate. The change in the x input shown in Eq. (1) will affect the y output response of the system at the same rate.

According to Newton, the universe functions systematically in a linear way like clockwork. Small changes cause small effects, and large changes cause large effects. Linearity, which is one of Newton's main concepts, contradicts the theory of complexity. Because this theory rejects linearity and predictability, it argues that predictability of complex systems is very difficult [1]. Complex systems are generally nonlinear systems and are very difficult to control. They don't have a specific equation, and some complex systems can have great effects on the output even at the slightest changes in the input [2].

Easy to design controllers such as Proportional-Integral-Derivative (PID) are sufficient for the Linear Time-Invariant (LTI) systems, while the control of non-LTI systems, whose parameters may change over time, requires more advanced control methods and algorithms. FLCs and ANNs are used for non-LTI systems. FLCs are designed using rules specific to the system-specific expert experience. ANN has inference and learning skills between system inputs and outputs. These two methods provide effective control solutions in non-LTI systems.

Fuzzy logic, which forms the basis of FLC, was proposed by Zadeh in 1965 as an extension of classical set theory. Later, the subject was dusted, thanks to the articles published by Zadeh in 1975, the first implementation studies related to FLC were carried out by Mamdani and Assilian. In 1987, Hitachi's FLC system was used and its commercial advantages were proved. Fuzzy logic uses fuzzy sets. Fuzzy sets are slightly different sets inspired by crisp sets. The difference is due to membership values. Unlike crisp sets, instead of the membership values 1 and 0 in crisp sets, it uses this range completely, which uses infinite values in real numbers. Actually, fuzzy logic is inspired from the sentences we use randomly in daily life. FLCs fulfill the task of control using an algorithm encoded with terms that do not express certainty when making decisions. In this way, the machine is able to think more humane and tries to provide a more realistic control [3].

The first theories on ANN, another of these methods, were put forward by Mc Culloch and Pitts in 1943. Later, in 1949, Hebb conducted a study to explain how the neurons of the human brain were self-learning. In 1958, Rosenblatt proposed the Perceptron ANN model based on the model proposed by McCulloch and Pitts. In the 1960s, Widrow and Hoff successfully carried out both theoretical and practical applications of ANN. Later in 1970s, even though the pace of development decreased due to practical difficulties in solving many real-world problems, the single-layer constraint was eliminated by Paul Werbos in 1974 and many restricted processes were calculated [4-6]. Although the ANN method, which also has problems, has been interrupted occasionally, in the light of the Hopfield article in 1982, many limitations have been eliminated. Even though new problems arise from these dates, new solutions have been produced. ANN is still popular today.

With the ANN structure and generalization feature, it can generate appropriate responses for untold input data and thus solve complex problems. Since ANN consists of a combination of many cells, it is important in solving complex nonlinear problems [7].

ANN architecture can contain multiple layers. The multilayer ANN architecture makes it easy to solve nonlinear problems. Multilayer structures consist of at least three layers. An input layer, an output layer must be present, and least one hidden layer between them. Connections exist only between cells on different layers. [8]. These cells also update their weights and connections according

to the error rate of the returned data and form the most suitable structure. Once this structure is established, the system can properly check for new incoming data. This method is used in many different areas.

## 2. Related works

ANN provides effective solutions in system modeling [9]. Although FLCs are effective in many applications, both of the software and hardware design of a FLC's presents a number of difficulties. In addition, the controller contains multiple mathematical operations causing the controller to react slowly. In the literature, there are only few studies regarded with modeling of FLCs by ANN in control applications.

Diaz and Soriano [10] reported that DC-DC converters are high-efficiency tools used to power different systems, have a nonlinear behavior and may affect the stability of differences in the main parameters. In this study, different control strategies, linear and nonlinear controllers applied to a Buck converter are examined and compared. There are three main control strategies discussed in the study. First, an optimal control-based design was used using Quadratic Performance Index, the second was a knowledge-based fuzzy control, and thirdly an ANN was proposed as a dynamic emulator of fuzzy control. Some comparisons have been made on the variation of several factory parameters about the systems created by the plant and the controller. In addition, the calculation time in the simulation was compared between the two intelligent controllers.

In another study, fractional order PID ( $PI^{\lambda}D^{\mu}$ ) control was considered. This is a challenge for real-time applications, since the implementation of fractional-order operators is achieved with integer-grade transfer functions. In the present article, mathematical difficulties are mentioned in the design stage of the  $PI^{\lambda}D^{\mu}$  controller and ANN design issues that will give the same performance as the  $PI^{\lambda}D^{\mu}$  controller are examined [11, 12]. Önder et al., used ANN for predict of nonlinear system dynamics [13].

This study aims to imitation of the FLC by using ANN to be easy to design both in software and hardware, and has a short response time. For the imitation process ANN is used. The reason for using ANN is that it has parallel operation feature. Parallel processing enables the processing speed to be increased. This improves the control performance of the controller and allows for easy design. The design process of the FLC and the training processes of the ANN were studied in Matlab SIMULINK environment. The performance of the designed controllers has been tested on the inverted pendulum system. In the study, FLC was modelled at high similarity ratio with small ANN structure. ANN results were obtained very faster than the FLC control performance. The control performances of two controllers were observed to be very close to each other. As a result, ANN model has smaller structure than FLC, which makes it possible to implement the controller easily in terms of hardware and software.

## 3. Mathematical background

### 3.1. Fuzzy logic controller

In the classical set theory, the degree of membership of an element is as crisp as 0 and 1. On the other hand, in fuzzy set theory, a different kind of set definition has been made. In fuzzy sets, membership values can be considered as infinitely real number equivalents in the closed range [0 1] instead of crisp sets. Fuzzy logic control system is actually a structure created by using the sentences

we use in our daily life, such as increase the temperature, a little slow down the cart speed. FLCs also fulfills the task of control using an algorithm encoded with terms that do not express such certainty when deciding on a case. The main goal here is to think more humane and to provide a more realistic control [3]. A FLC architecture is shown in Fig. 1.

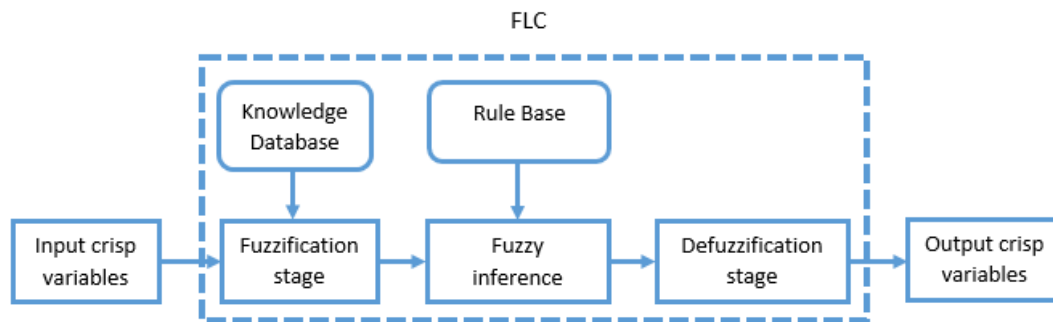


**Figure 1. FLC controller structure.**

In fuzzy set theory, the degree of belonging of an element to a set is realized by the membership functions. Real-life crisp quantities are passed through membership functions and fuzzy membership degrees are calculated, and these calculated membership degrees and input quantity are included in fuzzy subsets. In fuzzy sets, the degree of membership of an element is indicated by  $\mu$ . The selection of membership functions on the FLC greatly affects the control performance.

Fuzzification is the process of converting crisp real-life values into fuzzy values. In any fuzzification process, quantities such as speed and temperature are called antecedent variables. These antecedent values applied to some membership functions, and so obtained fuzzy values in the closed  $[0, 1]$  range. FLC designs use a varying number of membership functions for each antecedent variable. Usually an odd number such as 3, 5 and 7 membership functions are preferred. It is possible to use the same or different membership functions for input and output variables in applications. The fuzzy values from the membership functions are subjected to a number of fuzzy operations in the FLC. These are the rules for the operation of the FLC. The number of these rules is proportional to the number of membership functions. Therefore, as membership functions increase, more rules are needed. The search for the number of rules provides better control results in most cases. As a disadvantage, the increase in the number of rules increases the number of fuzzy processes and therefore makes it difficult to implement FLC both of software and hardware.

In the fuzzy inference stage, the input variable obtained by fuzzification process is applied to the fuzzy operator such as min, max by fuzzy rules. Fuzzy rules are fuzzy instructions prepared with expert experience. These instructions indicate where the fuzzified input variable is directed at the output according to the values it receives in different fuzzy subsets. The realization of a fuzzy rule is the process of subjecting it to operators in fuzzy set theory. The fuzzy result values obtained after the fuzzification and fuzzy inference processes should be converted to the actual control signal applicable to the controlled system. The process of converting fuzzy values into crisp values is called defuzzification process. There are different methods used for defuzzification. Due to the difference in the way these methods work, differences in results may occur depending on the type of study. Expert experience in FLC design may still be required here. Nowadays, the method suitable for the needs of the system in need of control can be tested by simulation and trial studies.

### 3.2. Artificial neural networks

ANN is a very complex nonlinear calculation tool that can model extremely complex functions. It is preferred where it is impossible or very difficult to find any given functional relationship between the sequence of inputs and the corresponding sequence of outputs. ANNs can be represented by means of an appropriately selected architecture and a successful learning result created by ANN [14]. The basic element of ANN is the cells. Cells, the main processing element of ANN, are nonlinear. In this way, it has become one of the most important tools for the solution of complex nonlinear problems and their architecture usually has parallel distributed cells. This parallel structure allows easy learning. Thanks to its generalization feature, it can produce appropriate responses for entrances not encountered. Thus, it can solve even complex problems of unknown function [7].

ANNs are composed of cells. These cells are used in groups in layers. An ANN input layer consists of at least three layers, the hidden layer and the output layer. There are no cells in the input layer. Input signals from the input layer are transmitted to the cells in the hidden layer by weights. The number of hidden layers may be multiple according to the application. The connections between the cells between the hidden layers and the cells in the output layer are carried out by means of weights. The cells in the hidden layer and the output layer are the basic information processing units within the ANN. There are three basic elements in the cell model. These are synapses, collector and activation functions. The synapses between the cells consist of directed connections, and these connections have weights. The collector is used to collect the inputs. The activation function is used to process a neuron output in a way that is necessary to update weights [15].

There are several network architectures for ANN. Structuring the neurons of a neural network is closely related to the learning algorithm used to train the network. In general, network architectures can basically define three different classes of network architecture [16].

One of these is a single layer network structure, in the simplest form it connects directly to a neuron output layer. It is the second class of a feedforward neural network. The compute nodes comprise one or more inter layers, called hidden layers, that contain inter layer cells. The function of the cells in the hidden layers is to interfere in some way between the input and the output. Adding one or more hidden layers can help generate higher-level statistics from the input of the network. A recurrent neural network separates itself from a forward neural network because it has at least one feedback loop. For example, a recurrent network may consist of a single layer of neurons that feeds the output signal of each cell to the inputs of all other neurons. There are no self-feedback loops in the network [16]. In the Fig. 2, single-layer and multilayer ANN examples are shown.

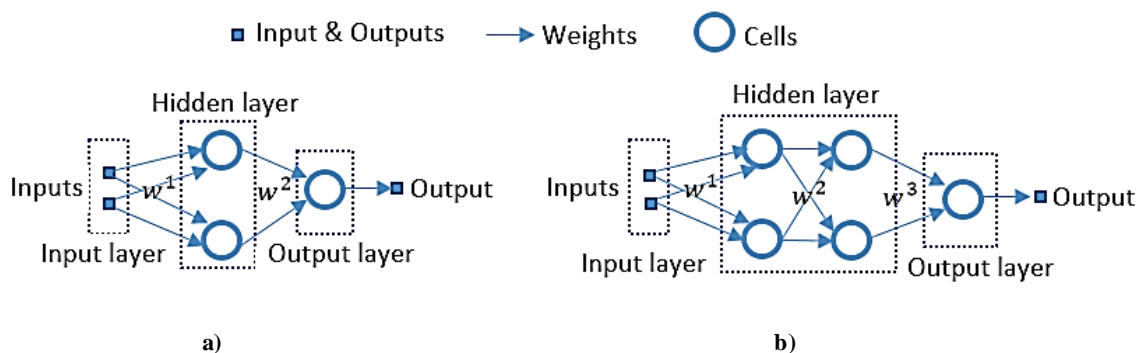


Figure 2. a) Single-layer ANN b) Multilayer ANN

### 3.3. Cart and inverted pendulum system

The inverted pendulum is a classical control problem which has been the subject of many articles in order to test the control performance of the designed a controller. As shown in Fig. 3, it consists of a cart that can move linearly along the  $x$ -axis and a rod that can move angularly in the  $x$ - $y$  axis with a hinge. This system can be likened to a rod held upright in the palm. The inverted pendulum has a nonlinear transfer function and can therefore easily become unstable. A general representation of a cart-inverted pendulum free body diagram is shown in the Fig. 3.

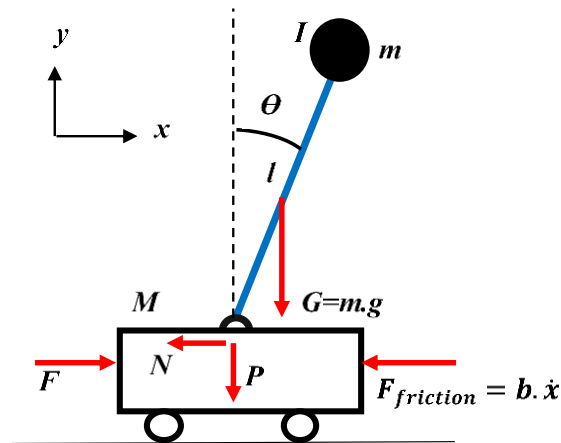


Figure 3. Cart-inverted pendulum free body diagram.

The symbols used in the Fig. 3 and in the following equations, and their values used in the simulation studies in this article are presented in Tab. 1 below.

Table 1. Symbols, their explanations and values used in the study.

Symbols	Explanations	Values	Units
$M$	Mass of cart	0.455	$kg$
$m$	Mass of pendulum	0.21	$kg$
$l$	Length of pendulum	0.61	$m$
$g$	Acceleration of gravity	9.8	$m/s^2$
$\theta$	Angle of pendulum	Variable	$rad$
$G$	Weight of pendulum	2.0580	$N$
$F$	Force	Variable	$N$
$F_{friction}$	Friction force	Neglected	$N$
$b$	Friction coefficient	Neglected	$N*s/m$
$x$	Distance on $x$ axis	Variable	$m$
$N$	weight component on $x$ axis	Variable	$N$
$P$	weight component on $y$ axis	Variable	$N$

According to free body diagram shown in Fig. 3, and Newton's second law;

$$\ddot{x} = \frac{1}{M} \sum_{cart} F_x = \frac{1}{M} (F - N - b\dot{x}) \quad (2)$$

$$\ddot{\theta} = \frac{1}{I} \sum_{pendulum} \tau = \frac{1}{I(-Nl \cos \theta - Pl \sin \theta)} \quad (3)$$

The dynamic equations in the  $x$  and  $y$  directions of the pendulum are as follows.

$$N = \sum_{pendulum} F_x = m\ddot{x}_p \quad (4)$$

$$P = mg + \sum_{pendulum} F_y = m(\ddot{y}_p + g) \quad (5)$$

However, the  $x$  and  $y$  position coordinates of pendulum can be represented with equations as following.

$$x_p = x + l \sin \theta \quad (6)$$

$$\ddot{x}_p = \ddot{x} - l\dot{\theta}^2 \sin \theta + l\ddot{\theta} \cos \theta \quad (7)$$

$$y_p = -l \cos \theta \quad (8)$$

$$\ddot{y}_p = l\dot{\theta}^2 \cos \theta + l\ddot{\theta} \sin \theta \quad (9)$$

The  $\ddot{x}_p$  and  $\ddot{y}_p$  values in Eq. (7) and Eq. (9) can be substituted in Eq. (4) and Eq. (5). So the following equations are obtained.

$$N = m\ddot{x} + ml\ddot{\theta} \cos \theta - ml\dot{\theta}^2 \sin \theta \quad (10)$$

$$P = m(l\dot{\theta}^2 \cos \theta + l\ddot{\theta} \sin \theta + g) \quad (11)$$

The  $N$  and  $P$  values in Eq. (10) and Eq. (11) can be substituted in Eq. (2) and Eq. (3). So the following equations are obtained.

$$(M + m)\ddot{x} + b\dot{x} + ml\ddot{\theta} \cos \theta - ml\dot{\theta}^2 \sin \theta = F \quad (12)$$

$$P \sin \theta + N \cos \theta - mg \sin \theta = ml\ddot{\theta} + m\ddot{x} \cos \theta \quad (13)$$

$$-Pl \sin \theta - Nl \cos \theta = I\ddot{\theta} \quad (14)$$

$$(I + ml^2)\ddot{\theta} + mg l \sin \theta = -ml\ddot{x} \cos \theta \quad (15)$$

In order to get rid of the nonlinearities caused by  $\sin$  and  $\cos$  functions in the above equations, the following approaches are made by accepting that the pendulum changes in a little  $\phi$  range.

$$\cos \theta = \cos(\pi + \phi) \approx -1 \quad (16)$$

$$\sin \theta = \sin(\pi + \phi) \approx -\phi \quad (17)$$

$$\dot{\theta}^2 = \dot{\phi}^2 \approx 0 \quad (18)$$

These approaches are in Eq. (16), Eq. (17) and Eq. (18) can be substituted in Eq. (12) and Eq. (15). And also  $U$  is used instead of  $F$ . So the following equations are obtained.

$$(I + ml^2)\ddot{\phi} - mgl\phi = ml\ddot{x} \quad (19)$$

$$(M + m)\ddot{x} + b\dot{x} - ml\ddot{\phi} = u \quad (20)$$

Laplace transform of the Eq. (19) and Eq. (20) at zero initial conditions are shown below.

$$(I + ml^2)\Phi(s)s^2 - mgl\Phi(s) = mlX(s)s^2 \quad (21)$$

$$(M + m)X(s)s^2 + bX(s)s - ml\Phi(s)s^2 = U(s) \quad (22)$$

The transfer functions of the pendulum and the cart from Eq. (21) and Eq. (22) are obtained as shown below.

$$P_{pend}(s) = \frac{\Phi(s)}{U(s)} = \frac{\frac{ml}{q}s}{s^3 + \frac{b(I + ml^2)}{q}s^2 - \frac{(M + m)mgl}{q}s - \frac{bmgl}{q}} \quad \left[ \frac{rad}{N} \right] \quad (23)$$

$$P_{cart}(s) = \frac{X(s)}{U(s)} = \frac{\frac{(I + ml^2)s^2 - gml}{q}}{s^4 + \frac{b(I + ml^2)}{q}s^3 - \frac{(M + m)mgl}{q}s^2 - \frac{bmgl}{q}s} \quad \left[ \frac{m}{N} \right] \quad (24)$$

Where  $q$  value;

$$q = [(M + m)(I + ml^2) - (ml)^2] \quad (25)$$

#### 4. Simulation studies and results

To perform simulation works, the cart-inverted pendulum model was created using Eq. (23) and Eq. (24) in Simulink. The design of the FLCs was made with Fuzzy Toolbox. The ANN design for the modelling of the FLC was made using Matlab's Neural Network Toolbox.

##### 4.1. FLC design

In both FLCs used to control the cart-inverted pendulum, the error ( $e$ ) and the change of the error ( $ce$ ) were used as input variables. However, the same input membership functions and the same output membership functions were used in both FLCs. The only difference is the universal set range of variables. The universal set of input and output variables is shown in Tab. 2.

**Table 2. Fuzzy subset ranges of variables on the universal set.**

Cart	NB	NS	Z	PS	PB
$e$	[-6.5 -3.25]	[1.3 -3.25]	[1.3 0]	[1.3 3.25]	[3.25 6.5]
$ce$	[-3 -1.5]	[0.6 -1.5]	[0.6 0]	[0.6 1.5]	[1.5 3]
$u$	[-63 -31.5]	[12.6 -31.5]	[12.6 0]	[12.6 31.5]	[31.5 63]
Pendulum	NB	NS	Z	PS	PB
$e$	[-0.5 -0.25]	[0.1 -0.25]	[0.1 0]	[0.1 0.25]	[0.25 0.5]
$ce$	[-2 -1]	[0.4 -1]	[0.4 0]	[0.4 1]	[1 2]
$u$	[-100 -50]	[20 -50]	[20 0]	[20 50]	[50 100]

The membership functions used are shown in Fig. 4 and Tab. 2, a total of 5 gauss membership functions are used: Negative Big (NB), Negative Small (NS), Zero (Z), Positive Small (PS), and Positive Big (PB).

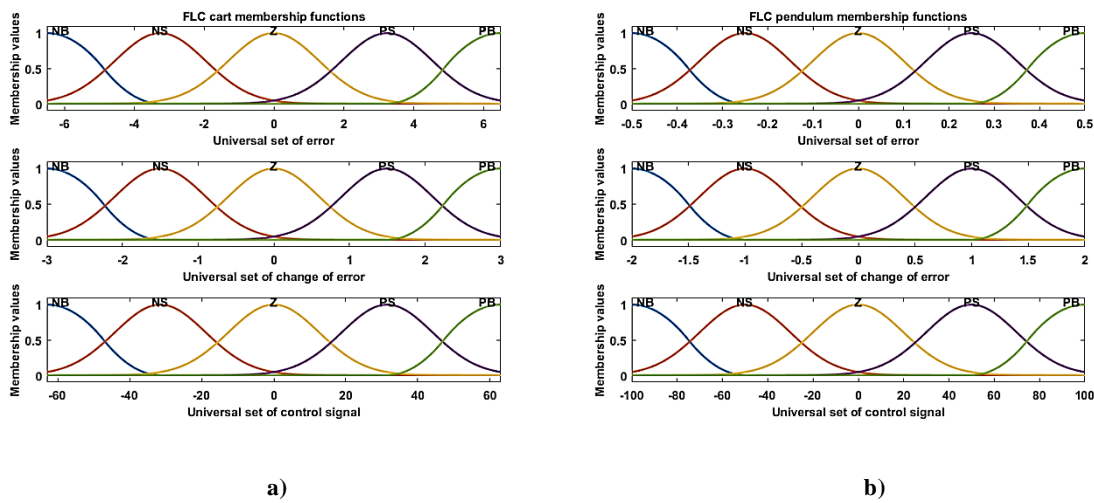


Figure 4. a) Membership functions of cart. b) Membership functions of pendulum.

The rules established according to the membership functions in Fig. 4 are shown in Tab. 3. As can be seen from Tab. 3, there are a total of 25 rules in FLCs.

Table 3. Rule table of FLCs

		<i>e</i>				
		NB	NS	Z	PS	PB
<i>ce</i>	NB	PB	PB	PS	PS	Z
	NS	PB	PS	PS	Z	NS
	Z	PS	PS	Z	NS	NS
	PS	PS	Z	NS	NS	NB
	PB	Z	NS	NS	NB	NB

The relationship between the input variables and the output variables according to the rules in Tab. 3 is shown in Fig. 5.

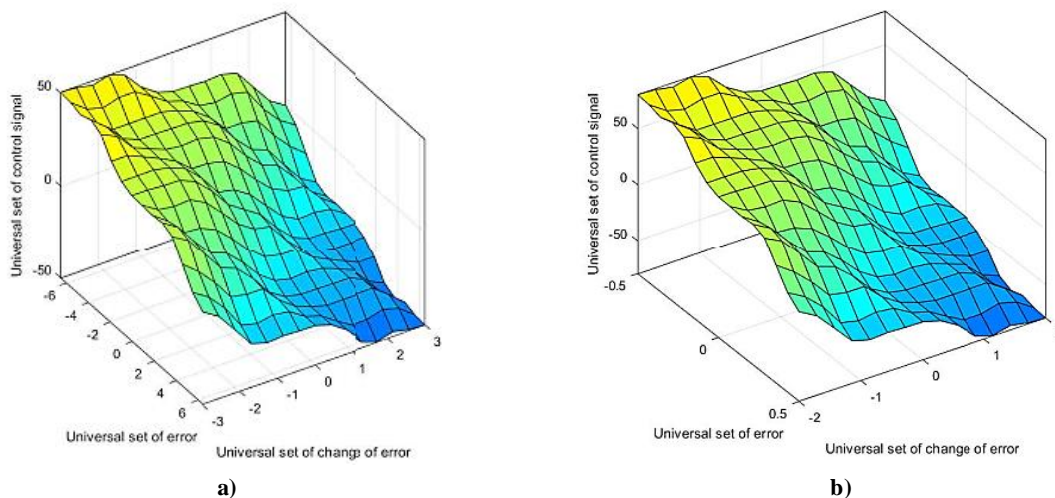


Figure 5. Representation of FLC's relationships between input and output variables a) Cart b) Pendulum.

The exact design used for FLC training is shown in Fig. 6. As shown in Fig. 6, the position controls of the cart and inverted pendulum are realized as closed loop control structure with two separate FLC units. For FLC\_cart, the error of the cart position error and the change of the error of the cart position are used as the input signal, while the change of the error of the pendulum angle and the error of the pendulum angle is used as the input signal for FLC\_pend. The outputs of these two FLCs were summed, and this final check mark was intended to move the cart to the desired position and to keep the pendulum upright without falling.

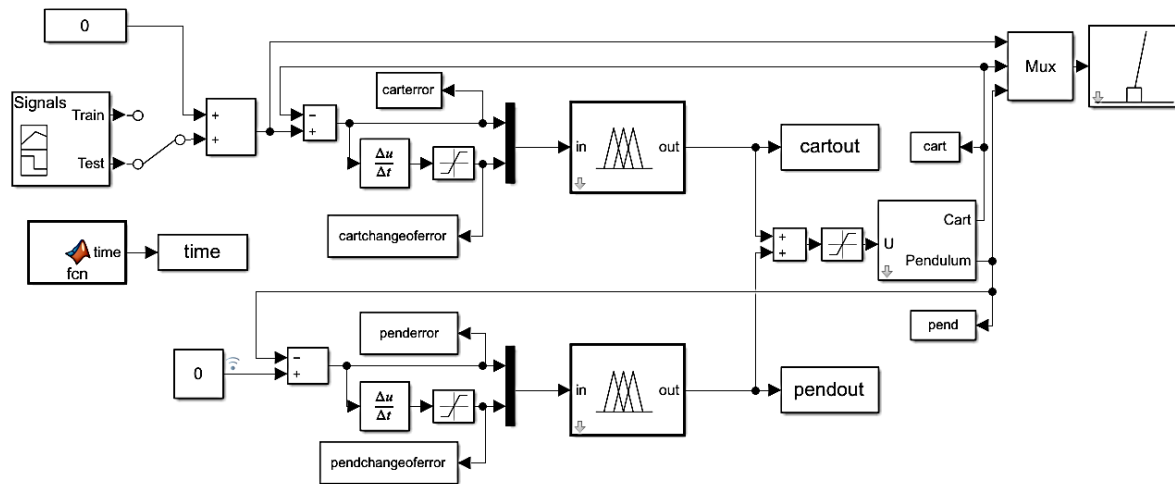


Figure 6. The exact design used for FLC training.

#### 4.2. Training of ANN

On the FLC design made on Matlab Simulink, different reference values were given for cart and control was performed. During the control process, input variables ( $e$  and  $ce$ ) and output variables ( $u$ ) of FLC\_cart and FLC\_pendulum were transferred from Simulink to the Matlab workspace with the "to workspace" block. Thus, ANN's training set was created.  $e$  and  $ce$  values are taken as the input variables of the training set and  $u$  is taken as the output variable of the training set. The same architecture was used for both FLC\_cart and FLC\_pend ANNs. Feed forward network structure was used including each ANN, 2 variable input layer, two 5-cell hidden layers and one variable output layer. "tansig" function was used as the activation function in the hidden layers and "purelin" function was used as the activation function in the output layer.

The success rate of the training was measured according to the MSE performance. The training was done with the Levenberg-Marquardt algorithm called "trainlm" in the Matlab. The Levenberg-Marquardt algorithm update derived from steepest descent and Newton algorithms was given in Eq. (26). [17]

$$\Delta w = (J^T J + \mu I)^{-1} J^T e \quad (26)$$

Where  $w$  is the weight vector,  $I$  is the unit matrix,  $\mu$  is the combination coefficient,  $J$  represents the Jacobian matrix in dimension  $(PxM) \times N$ ,  $e$  represents the error vector in dimension  $(PxM) \times 1$ . And  $P$  is the number of training samples,  $M$  is the number of outputs,  $N$  is the number of weights.  $\mu$  is an

adjustable variable. If this parameter is too big, the method behaves like a steepest descent method, if it is too small the method behaves like a Newton method. An adaptive structure for this parameter was given in Eq. (27). [17]

$$\mu(n) = \begin{cases} \mu(n-1)k & E(n) > E(n-1) \\ \mu(n-1)/k & E(n) \leq E(n-1) \end{cases} \quad (27)$$

In Eq. (27),  $k$  is a constant number.  $E$  shows the fitness value.

The contents of the ANN block, which ANN block placed instead of the FLC block, were shown in the Fig. 7. These contents were created by Matlab during the ANN's training and then turned into Simulink block with "gensim" function. The Feed-forward network was used as ANN structure. The ANN contains ten cells, two inputs, an output, four layers, three activation functions, collectors, and many weights. The first layer is the input and the last layer is the output. Each layer has biases and also weights coming from the previous layer.

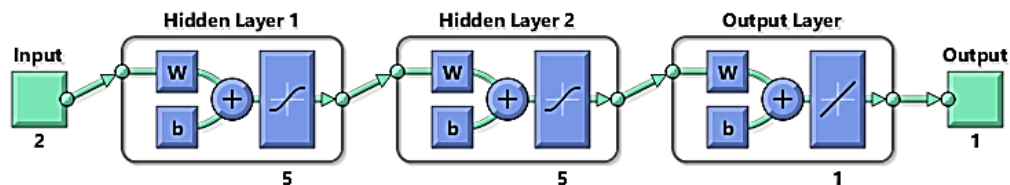


Figure 7. Ann structure and contents

The ANN training process is as follows.

Fig. 8 shows the graph obtained during ANN training. 500 iterations were made for the training. The mean square error (MSE) rate during training of cart decreased to 0.3669 at 359 iterations. MSE rate during training of pendulum decreased to 0.0078433 at 500 iterations.

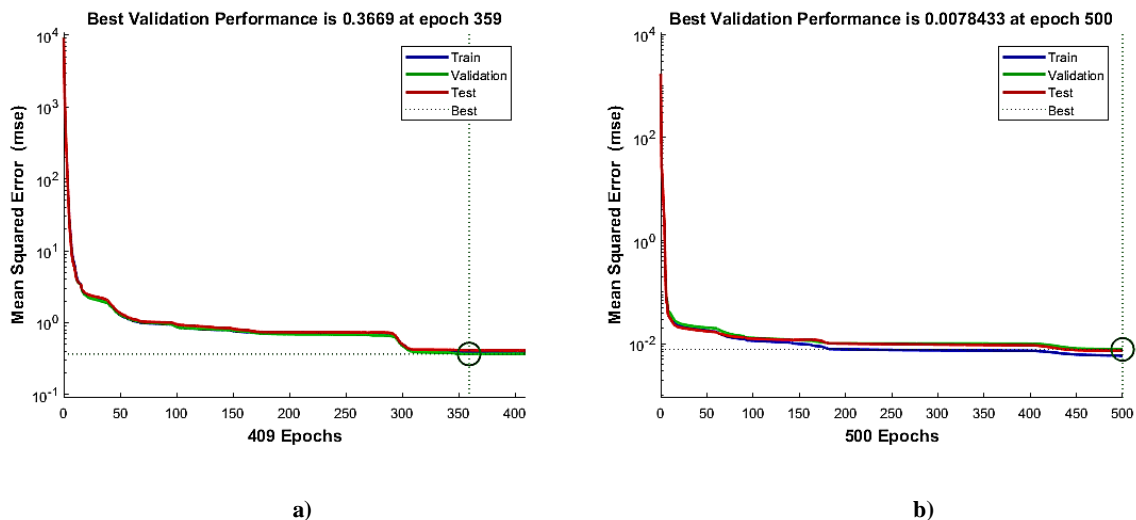


Figure 8. ANN's training performance graph. a) cart b) pendulum

The regression graph plotted during ANN training is shown in Fig. 9. Here, the collection of data on the regression curve is an indicator of a good training.

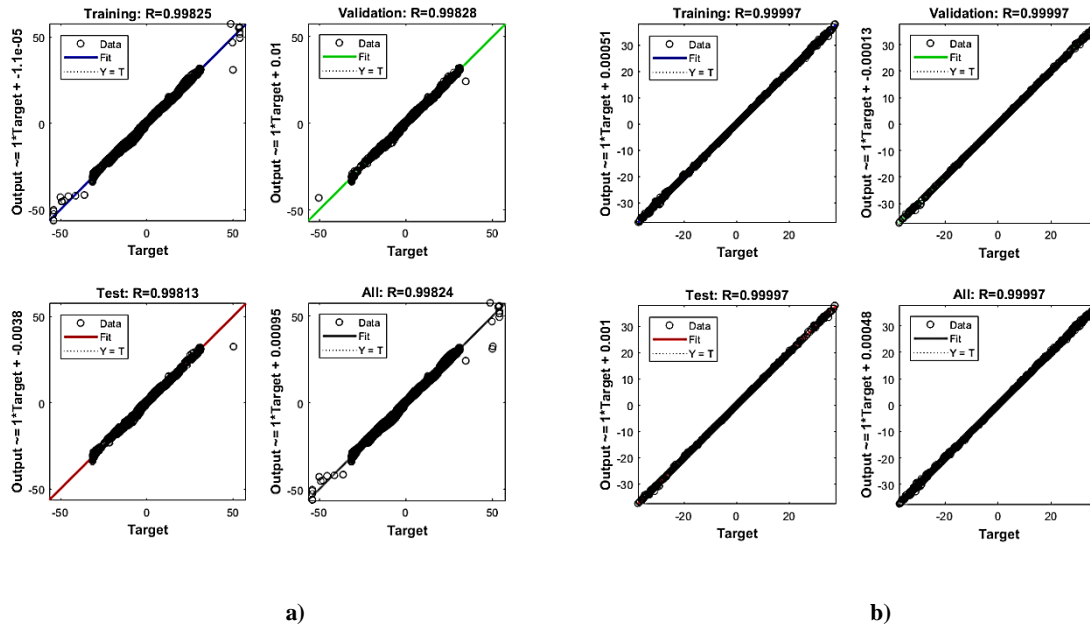


Figure 9. ANNs training regression graphs. a) cart b) pendulum

Fig. 10 shows a block diagram of the cart-pendulum system. Here, the FLCs were removed and replaced with ANNs.

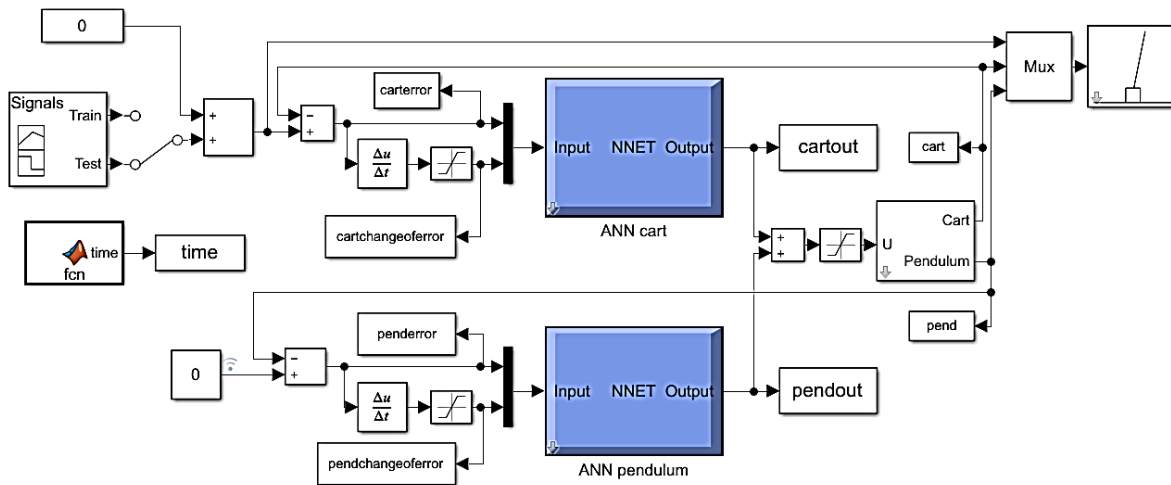


Figure 10. Control block diagram created with ANNs instead of FLCs.

The Simulink Diagram was run with the test set, which completely different from training set. The FLC and the ANN controllers were run separately and tested. And the results obtained are as follows.

Fig. 11 is a position graph of the cart and it shows the comparison between the control results of the two controllers. Here, the MSE value calculated based on the difference between the cart position controlled by the FLC and the reference position is 10.1312. Similarly, the MSE value calculated based on the difference between the cart position controlled by the ANN and the reference position is 10.1177. As can be seen, the MSE values of both controllers are very close to each other. This shows us that ANN is able to imitate FLC highly rate. Furthermore, the calculated MSE value which based

on the difference between cart position control performances of these two controllers is 0.000806, which is very small.

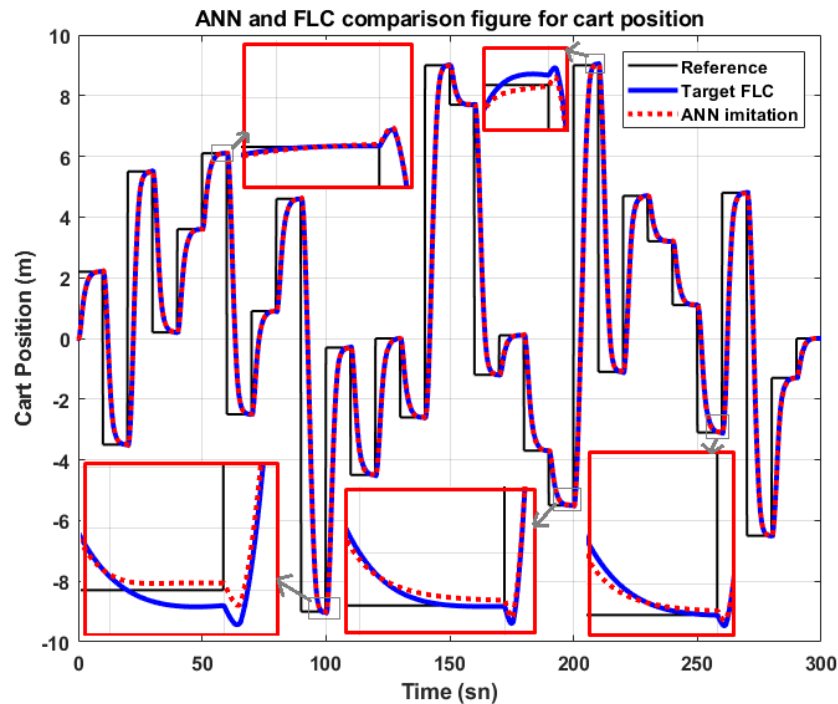


Figure 11. Position graph of the cart position controlled by ANN and FLC.

Fig. 11 is the position graph of the cart, and it shows the comparison between the control results of two controllers. In order to make this difference more clarity, the position difference graph of Fig. 12 is obtained by subtracting the position of the cart controlled by the ANN from the position of the cart controlled by the FLC. When Fig. 12 is examined, it is seen that the biggest difference between the control results of two controllers is 15 cm and this difference closes in a short time.

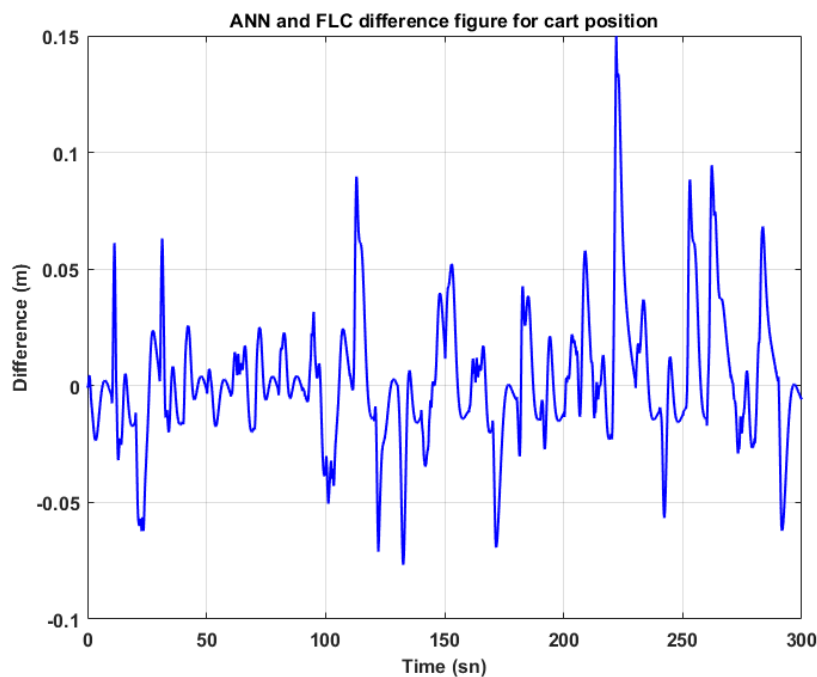


Figure 12. Difference graph of cart position control results between FLC and ANN.

Fig. 13 is an angle graph of the pendulum and it shows the comparison between the control results of FLC and ANN controllers. Here, the MSE value calculated based on the difference between the pendulum angle controlled by the FLC and the reference angle (0 radian) is 0.0032098. Similarly, the MSE value calculated based on the difference between the pendulum angle controlled by the ANN and the reference angle is 0.0031916. As can be seen, the MSE values of both controllers are very close to each other as cart position. This shows us that ANN is able to imitate FLC highly rate. Furthermore, the calculated MSE value which based on the difference between pendulum angle control performances of these two controllers is  $1.595 \cdot 10^{-5}$ , which is very small.

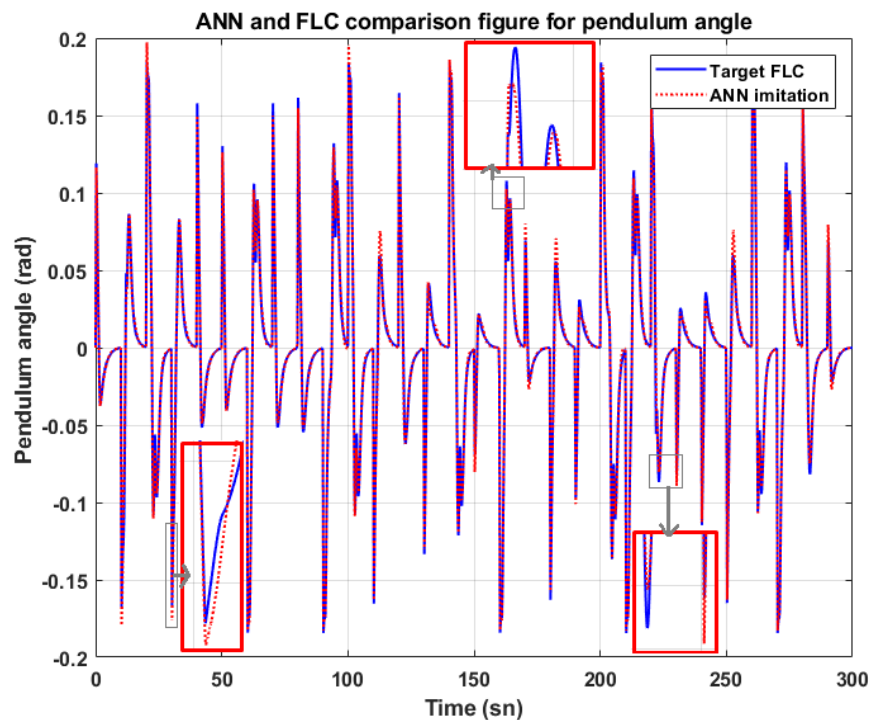


Figure 13. Position graph of the pendulum angle controlled by ANN and FLC.

Fig. 13 is the angle graph of the pendulum, and it shows the comparison between the control results of two controllers. In order to make this difference more clarity, the angle difference graph of Fig. 14 is obtained by subtracting the angle of the pendulum controlled by the ANN from the angle of the pendulum controlled by the FLC. When Fig. 14 is examined, it is seen that the biggest difference between the control results of two controllers is 0.038 radian and this difference closes in a short time.

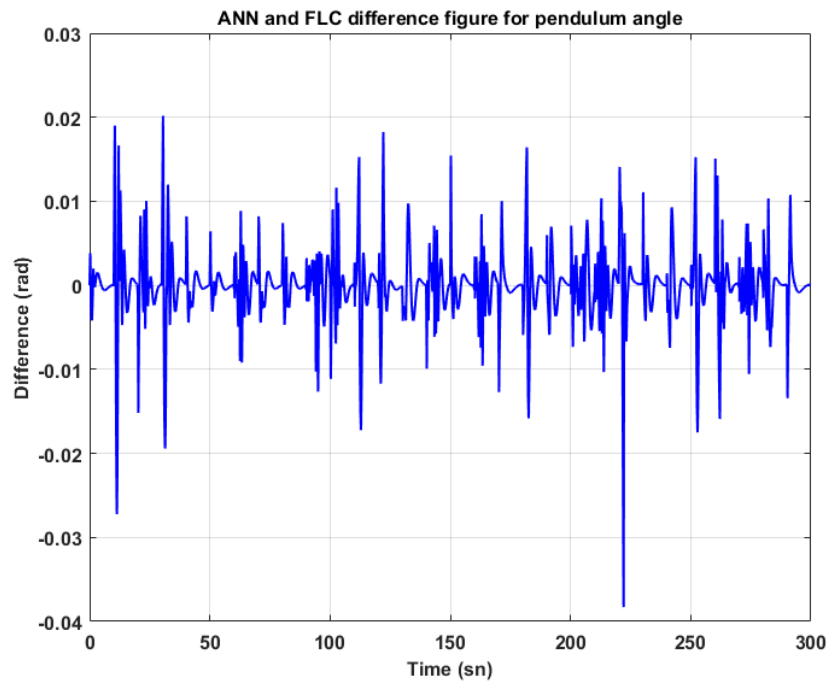


Figure 14. Difference graph of pendulum angle control results between FLC and ANN.

## 5. Conclusion

The ANN can be used for the imitation process of many systems, the FLC is one of them. The ANN has a parallel operation feature and so it runs very faster than the FLC. Further, the ANN design both in software and hardware is easier than the FLC design.

With the using of the data of the FLC's input and output, the trained ANN successfully imitated the FLC and managed to perform the control process under different reference values. According to the position values of the car, the MSE value of the difference between the FLC and the ANN controllers is 0.000806. For the angle values of the pendulum, the MSE value of the difference between the FLC and the ANN controllers was obtained as  $1.595 \cdot 10^{-5}$ .

Since the operations used by ANN are easier than those used by the FLC, while a 300-second simulation was performing with 178.799 real seconds with FLC, the same simulation was performed with ANN in 2.059 real seconds. The system designed with ANN will be easier to use and design in various control applications as it is containing less complex mathematical operations. This study can be improved by using more training data, more cell numbers, more iteration or different training algorithms in the ANN training process.

## References

- [1] Sayğan, S. (2014). Örgüt Biliminde Karmaşıklık Teorisi. *Ege Academic Review*, 14(3).
- [2] Ramezani, M. R., Kamyad, A. V. (2010). Approximation of general nonlinear control systems with linear time varying systems. In 2010 18th Iranian Conference on Electrical Engineering (pp. 680–685). Presented at the 2010 18th Iranian Conference on Electrical Engineering, Isfahan, Iran. <https://doi.org/10.1109/IRANIANCEE.2010.5506987>
- [3] Altaş, İ. H. (1999). Bulanık Mantık: Bulanıklılık Kavramı. *Enerji, Elektrik, Elektromekanik-3e*, 62, 80–85.

- [4] Pamuk, Z., Yurtay, Y., Yavuzylmaz, O. (2015). Establishing the Potential Clients Using Artificial Neural Networks. *Balkan Journal of Electrical and Computer Engineering*, 3, 219–224.
- [5] Yegnanarayana, B. (2009). *Artificial Neural Networks*. PHI Learning Pvt. Ltd.
- [6] Tolon, M., Tosunoğlu, N. G. (2008). Tüketici Tatmini Verilerinin Analizi: Yapay Sinir Ağları Ve Regresyon Analizi Karşılaştırması. *Gazi Üniversitesi İktisadi ve İdari Bilimler Fakültesi Dergisi*, 10(2), 247–259.
- [7] Ergezer, H., Dikmen, M., Özdemir, E. (2003). Yapay sinir ağları ve tanıma sistemleri. *PiVOLKA*, 2(6), 14–17.
- [8] Kilic, E., Ozbalci, U., Ozcalik, H. R. (2012). Lineer Olmayan Dinamik Sistemlerin Yapay Sinir Ağları ile Modellenmesinde MLP ve RBF Yapılarının Karşılaştırılması. *ELECO2012 Elektrik-Elektronik ve Bilgisayar Mühendisliği Sempozyumu*, (29.11. 2012-01.12. 2012).
- [9] Tasdemir, S. (2018). Artificial Neural Network Model for Prediction of Tool Tip Temperature and Analysis. *International Journal of Intelligent Systems and Applications in Engineering*, 6(1), 92–96. <https://doi.org/10.18201/ijisae.2018637937>
- [10] Diaz, N. L., Soriano, J. J. (2007). Study of Two Control Strategies Based in Fuzzy Logic and Artificial Neural Network Compared with an Optimal Control Strategy Applied to a Buck Converter. In *NAFIPS 2007 - 2007 Annual Meeting of the North American Fuzzy Information Processing Society* (pp. 313–318). Presented at the NAFIPS 2007 - 2007 Annual Meeting of the North American Fuzzy Information Processing Society. <https://doi.org/10.1109/NAFIPS.2007.383857>
- [11] Efe, M. Ö. (2011). Neural Network-Assisted  $PI^2D^\mu$  Control. *Fractional Dynamics and Control* pp 19-31  
doi: 10.1007/978-1-4614-0457-6\_2
- [12] Efe, M. Ö. (2011). Neural Network Assisted Computationally Simple  $PI^2D^\mu$  Control of a Quadrotor UAV. *IEEE Transactions On Industrial Informatics*, vol. 7, no. 2
- [13] Efe, M. Ö., Kaynak, O., Abadoglu, E. (1999). Neural Network Assisted Nonlinear Controller For A Bioreactor, *International Journal of Robust and Nonlinear Control* 9(11),799-815  
doi: 10.1002/(SICI)1099-1239(199909)9:11<799::AID-RNC441>3.0.CO;2-U
- [14] Marini, F., Bucci, R., Magri, A. L., Magri, A. D. (2008). Artificial neural networks in chemometrics: History, examples and perspectives. *Microchemical Journal*, 88(2), 178–185. <https://doi.org/10.1016/j.microc.2007.11.008>
- [15] Sreelakshmi, K., Ramakanthkumar, P. (2008). Neural networks for short term wind speed prediction. *World Academy of Science, Engineering and Technology*, 42, 721–725.
- [16] Haykin, S. S. (2009). *Neural networks and learning machines*/Simon Haykin. New York: Prentice Hall,.
- [17] Çavuşlu, M. A., Becerikli, Y., Karakuzu, C. (2016). Levenberg-Marquardt Algoritması ile YSA Eğitiminin Donanımsal Gerçeklenmesi. *Türkiye Bilişim Vakfı Bilgisayar Bilimleri ve Mühendisliği Dergisi*, 5(1).

## IMPEDANCE IMAGE RECONSTRUCTION WITH ARTIFICIAL NEURAL NETWORK IN ELECTRICAL IMPEDANCE TOMOGRAPHY

*Beyhan KILIC*<sup>1\*</sup>

*Electrical impedance tomography views the electrical properties of the objects by injecting current with surface electrodes and measuring voltages. Then using a reconstructing algorithm, from the measured voltage-current values, conductivity distribution of the object calculated. Finding internal conductivity from surface voltage-current measurements is a reverse and ill-posed problem.*

*Therefore, high error sensitivity, and making approximations in conceiving complex computations cause to limited spatial resolution. The classic iterative image reconstruction algorithms have reconstruction errors. Accordingly, Electrical impedance tomography images suffer low accuracy. It is necessary to evaluate the collected data from the object surface with a new approach. In this paper, the forward problem solved with the finite element method to reconstruct the conductivity distribution inside the object, the reverse problem solved by the neural network approach. Image reconstruction speed, conceptual simplicity, and ease of implementation maintained by this approach.*

*Key words: electrical impedance tomography, finite element methods, biomedical image reconstruction, neural network*

### 1. Introduction

Electrical impedance tomography (EIT) creates the object's internal electrical conductivity or resistivity by injecting current with electrodes on the surface, and the corresponding voltages are measured with electrodes using the neighboring method. The measured current and voltages values are used to reconstruct the object's internal conductivity distributions [1].

The image of conductivity distribution is constructed with the iterative process by measured current and voltages. The first step is to find voltage and current distributions to create an impedance profile. This procedure is defined as "the forward problem." to reconstruct the electrical conductivity distributions inside the object from the knowledge of the measured electrode voltages and applied current is an inverse problem [2]. Imaging the internal impedance distribution by processing voltage-current data, which is measured from objects surface, is a nonlinear and ill-posed inverse problem. The none-linearity of the problem requires a regularization, but the linearization approximation is incapable of reconstructing the objects that have complex geometries or to a large extent, contrasts. Therefore an Iterative solution is inevitable.

---

<sup>1</sup> Faculty of Electrical and Electronics, Department of Electrical Engineering, Yildiz Technical University, Istanbul, Turkey, (beykilic@yildiz.edu.tr)  <https://orcid.org/0000-0002-8438-8369>

The most common non-linear method is Newton–Raphson. This technique works by searching the conductivity distribution that reduces the difference between applied potentials and the calculated potential from the forward problem by the finite element method. The drawback of this algorithm is that it is computationally complex, requires numerous orders of magnitude and computational time is high as compared to the linear methods [3].

EIT is entirely non-invasive and radiation-free. EIT has an advantage over other imaging techniques, such as its portability, low-cost, and faster imaging capabilities [4]. EIT is suitable for medical imaging of the body and pathological situations [5-6]. Though advantages, EIT technology suffers lower spatial resolution in comparison to other imaging systems like magnetic resonance imaging (MRI) and computed tomography (CT). For Improving spatial resolution, electrode numbers can be increased, but implementing a lot of electrodes can not be possible in most real situations [7].

## 2. EIT Fundamentals

Impedance or resistivity is defined as the current and voltage ratio [8]. The human cell is resistive, piecewise homogeneous, and linear volume conductor. Different tissue has different resistivity value. Tissue resistivity values are shown in Tab. 1. The blood resistivity depends strongly on hematocrit (Hct) [9]. The EIT converts the different electrical properties of biological tissues to critical information for pathological diagnosis situations.

**Table1. different biological tissue resistivity values**

Tissue	Resistivity Values
Blood	1.6 $\Omega\text{m}$
Heart	2.5 $\Omega\text{m}$
Lungs	20 $\Omega\text{m}$
Bone	177 $\Omega\text{m}$
Fat	25 $\Omega\text{m}$

The first step is to determine voltage-current distributions from the object surface for imaging impedance. This problem is defined as "the forward problem" for a given impedance profile voltage-current values. The results of the forward problem and the measured values used to impedance values. Finally, impedance images are reconstructed. The second step is to reconstruct impedance images and named inverse problem. Impedance image reconstruction process is shown in Fig. 1.

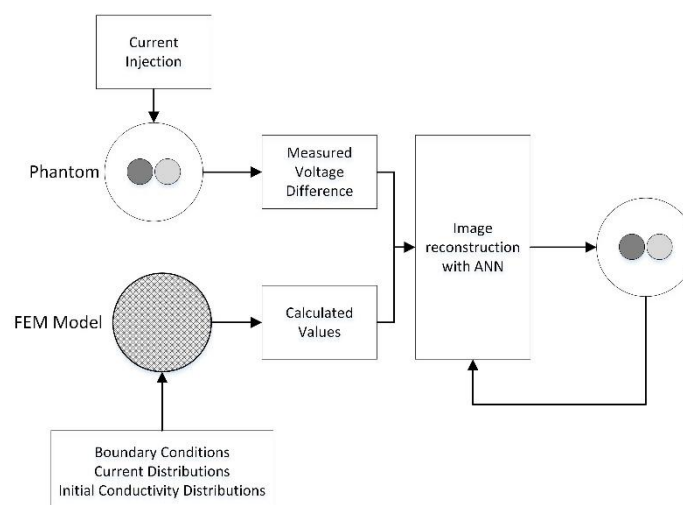


**Figure 1. Block diagram for the image reconstruction process in EIT**

Electrodes used in medical imaging are generally found as the surface electrodes in most of the cases. In other fields, the electrodes can be soldered or penetrated to the object. The injected current amplitude and frequency are required to be chosen very carefully for the medical EIT, whereas the magnitude could be increased more for the non-biological sample imaging with EIT. Contact impedance is found a crucial issue in EIT in most of the applications, and hence the four-electrode method is preferred.

### 3. The Solution of The Forward Problem

Measuring the voltages from the object's or phantom surface is defined as the forward problem. Solving the forward problem is to collect data from the subject's surface or phantom. The current or voltage is applied to the object, and the resulting current or voltage is calculated. Typically, the current is applied from an alternating current (AC) source to a few electrodes, and the measuring voltages are calculated to form the remaining electrodes. Voltage measured from the other electrode pair by the principle of the neighboring method [9]. The current is injected into pairs of electrodes numbers one and second. Subsequently, the voltage is measured between the electrode pairs three and four and so on [10].

#### 3.1. Additional instructions (Word Style TS Heading 2)

The forward problem can be solved analytically for simple objects but in the case of the complex objects. The domain is discretized into small elements called mesh or finite elements. The problem is defined for a continuous domain; therefore, area equations are valid for all finite elements. The resistivity of each finite element is assumed homogenous. While the size of the finite element goes to zero, the solution approaches to the real solution. The mathematical expressions of the FEM are well-defined in literature [11-12-13]. The continuous domain is found by attaching the finite elements. Each element has two node numbers: local and global. The finite elements are unified by common nodes.

$K_n$  element matrix and  $Q_n$  vector are unified as a master matrix.  $K_n$  element matrix is given in Eq. 1. The problem is converted to a linear problem form differential equation by modeling discrete finite element a continuous domain.

$$K\phi = Q \quad (1)$$

Where;

$K_{n \times n}$  : master matrice  
 n : node number in mesh  
 $\phi$  : node voltage vector  
 Q : node current vector

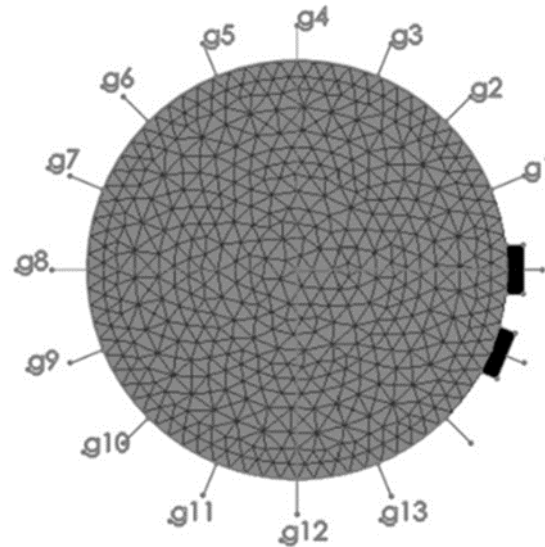


**Figure 2. Finite element model**

In this study, the domain is separated into 1016 finite triangle elements and 541 nodes. Figure 2 shows the domain. The master matrix is solved with the frontal solution. The method was developed by Irons B.M [14], and Ider at al. modified it [15-16]. The master matrix is solved during the matrix generation stage before the matrix is completed. The frontal length of the matrix depends on mesh structure and the numbering technique of nodes. In a well-defined mesh, the frontal size of the mesh shouldn't change extremely. The test mesh consisting of 541 nodes and 1016 finite elements is shown in Fig. 2. The potential variations of the studied domain are known approximately. The system contains sixteen electrodes. Two of them are current injection electrodes, remaining are voltage measurement electrodes, and the conductivity is assumed to be 0.002 S/cm. For sixteen different boundary conditions, for  $I=5$  mA, the problem is solved synchronically. The measured voltage values which are used to test the accuracy of the calculated solution are given in Tab. 2.

**Tablo 2. The calculated and the measured voltage differences of the test set**

Difference voltage	Measured value (mV)	Calculated value (mV)
V1	47.8695	47.901628
V2	20.84387	20.906145
V3	12.53245	12.588936
V4	8.947047	8.99501696
V5	7.202337	7.244238
V6	6.382648	6.421197
V7	6.155331	6.192814
V8	7.229110	6.448648
V9	8.967458	7.270297
V10	12.534843	9.013852
V11	12.605730	12.588936
V12	20.906145	20.923509
V13	47.734701	47.704444

### 3.2. The Inverse Problem

The reconstruction of the image of the objects inside by using data measured from the object surface is an ill-posed problem. As a result of this ill-condition, the image reconstruction system is highly sensitive to measurement errors, and spatial resolution is low, especially in the center of the object. Besides, to simplify the calculation complexity, some assumptions must be made.

Each assumption is accurate for special conditions. These assumptions limit the accuracy of the solution. Therefore, the image reconstruction problem comes across poor accuracy and limited spatial resolution. In the electrical impedance image reconstruction process, it is necessary for a new approach to evaluate the data measured from the surface of the object. The Artificial Neural Network ANN method is suitable for this process because ANN consists of neurons with weighted value. There is a structural correlation between ANN and FEM. The neurons are matched with finite elements. The conductivity distribution is modeled by finite elements as given in Eq. 2.

$$C(n) = \sum_{i=1}^1 b(n, i) * u(i) \quad (2)$$

Where;

$C(n)$ ,  $n = 1, 2, \dots, N$ , different conductivity numbers

$u(i)$ ,  $i = 1, 2, \dots, 256$ , for different projections, 16 voltage differences measured from the surface.

$b(n, i)$ , element weightiness matrix.

The weight matrix shows the best approach in terms of least squares from voltage measurements to conductivity changes. The weight matrix is calculated iteratively during the training of the ANN. The error backpropagation algorithm is used this process.

In this study, the ANN used to provide the recognition of conductivity changes from  $16 \times 16 = 256$  voltage differences taken from the circular disc surface with a radius of 15 cm is shown in Fig. 1.

The voltages differences taken from the surface applied to the ANN input, the conductivity patterns are recognized by the multi-layer ANN. During the network training process, inputs and desired outputs are used for training. The learning process is realized through changing of the elements of the weight. Here, the backpropagation algorithm of the error is used. The difference between the instantaneous output values and the target output, the error is backpropagated across the network, changing the link weights. This calculation is iterated until the desired error value is reached.

### 3.3. Simulation of Conductivity Patterns

To solve the inverse problem, an ANN used to form the analogy from voltages difference to conductivity changes. For this purpose, the 1016-finite elements network used in the forward solution is divided into 16-element groups and turned into a coarse network [17]. The voltage difference calculated by the finite element method in the forward solution is normalized in the range (0-1) and applied to the mesh input layer. The network was trained, 64 different conductivity values were matched with the model given in Fig. 2. Since there is no need to make a mathematical definition between the input layer and the output layer in ANN, the problem is both conceptually simplified, and the solution is reached faster. A trained network can recognize different conductivity patterns in seconds. The ANN was trained on the circular finite element geometry with 64 finite elements. The Ankara Standard Data, 16 sets of voltages, were used to test the performance of the net [10]. The test object is a 2D circular disk. The number of the input layer is selected as 104 and the output layer 64. The number of a hidden

layer of the network is two. In the stage forward problem solution. At the end of 81340 iterations, 0.259% error rate was achieved.

In Figure 3a and Fig. 3b, the conductivity distribution graph obtained with ANN for the case where the object with conductance value of 0.002 S/cm is in the center of the phantom is shown. The reconstructed conductivity images for two objects with a conductivity of 0.02 S/cm between the center and the surface are given in Fig. 4a and in Fig. 4b. The conductivity image obtained by ANN with two objects having a conductivity of 0.02 S/cm was obtained with 0.05% error. The conductivity distribution of the object having a conductance of 0.02 S/cm between the phantom center and the surface is given in two dimensions in Fig. 5a and in three dimensions in Fig. 5b. The conductivity image was obtained with 0.03% error.

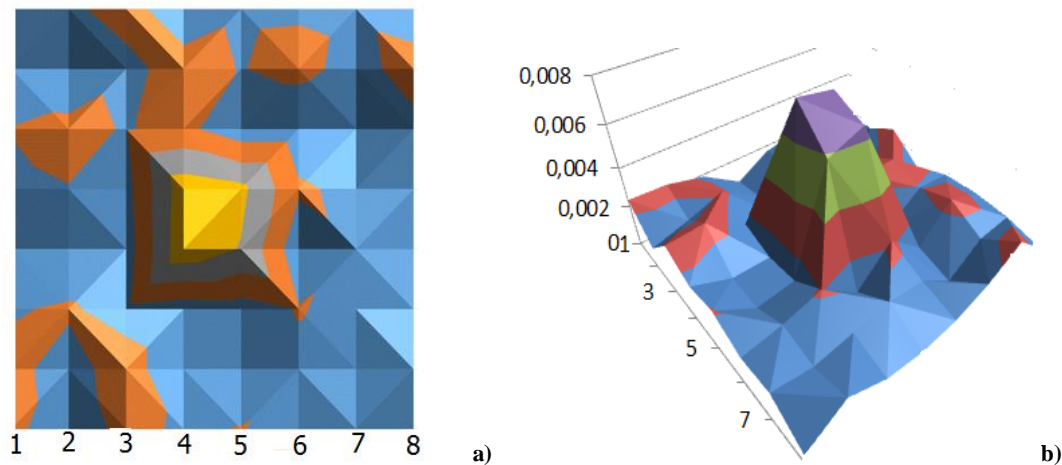


**Figure 3. a) Two dimensional reconstructed conductivity image, error % 0,02 b) Two dimensional reconstructed conductivity image, error % 0,02**

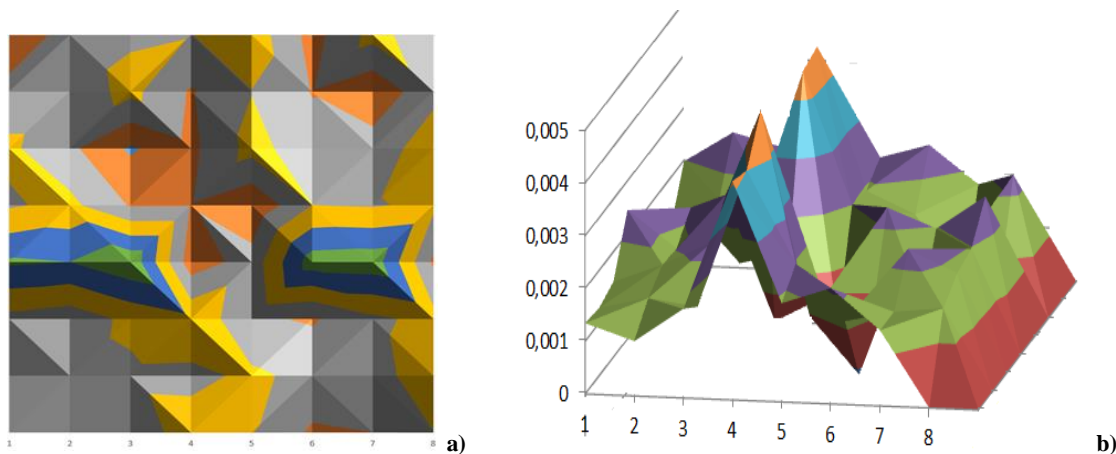


**Figure 4. a) Two-dimensional reconstructed conductivity image of two objects, error % 0,05 b) Three dimensional reconstructed conductivity image of two objects, error % 0,05**

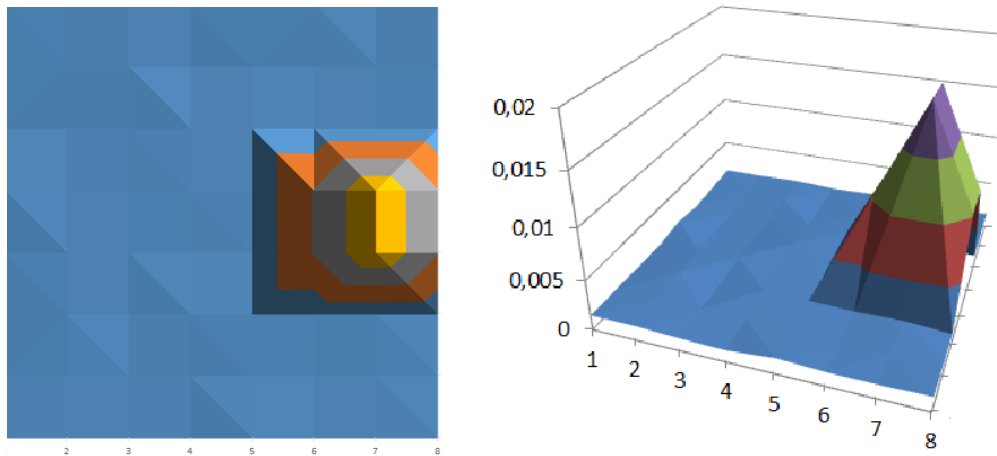


Figure 5. a) Two dimensional reconstructed conductivity image, error % 0,03 b) Two dimensional reconstructed conductivity image, error % 0,3

#### 4. Conclusion

EIT is a non-invasive, and with no potential hazard imaging tool for monitoring medical application. It is widely used in numerous medical imaging. In this paper, steps to solve the EIT problem are briefly discussed. FEM in the forward solution and the artificial neural network (ANN) in inverse solution.

In this paper, ANN has been proposed to generate images of conductivity changes from the phantom surface area measurements on electrical impedance imaging. The forward problem was solved with FEM so that the problem was solved directly using ANN. Since FEM and ANN have structural matching, in reverse problem solving, there is no need to make new assumptions, therefore error rate decreases. The conductivity contrast was found to be approximately equal to one. The resolution will be reduced in a multi-conductivity environment where there are significant variations in the conductivity. EIT can be preferred for monitoring patients. After the completion of training in artificial neural networks, it is possible to perform automatic data analysis with ANN, since results are obtained in a short time.

#### References

- [1] Adler, A., Guardo, R., (1994). A Neural Network Image Reconstruction Technique for Electrical Impedance Tomography. *IEEE Transactions on Medical Imaging*, 13(4).
- [2] Martin, S., Choi, C.T.M., *Electrical Impedance Tomography: A Reconstruction Method Based on Neural Networks and Particle Swarm Optimization*, Springer, Cham, Switzerland, 2015.
- [3] Khan, T.A., Ling, S.H., (2019). Review On Electrical Impedance Tomography. *Artificial Intelligence Methods and its Applications Algorithms*, 12(5), 88, 1-18.
- [4] Webster, J. G., *Electrical Impedance Tomography*, Adam Hilger Series of Biomedical Engineering, Adam Hilger, New York, USA, 1990.
- [5] Hikmah, A. (2019). Two-Dimensional Electrical Impedance Tomography (EIT) For Characterization of Body Tissue Using a Gauss-Newton Algorithm, OP Conf. Series: *Journal of Physics: Conf. Series*, 1248

- [6] Miller, A., Blott, S., *et al.* (1992). Review of Neural Network Applications in Medical Imaging and Signal Processing. *Medical and Biological Engineering and Comp.*, 30(5), 449–464
- [7] Malmivuo, J., Plonsey, R., *Bioelectromagnetism Principles and Applications of Bioelectric and Biomagnetic Fields*, Oxford Scholarship, 1995.
- [8] Uzunmwangho, R., Ibo, A.O., *Introduction To Electrical Engineering*, Odus Press, 2017
- [9] Graham, B.M., Enhancements in Electrical Impedance Tomography (EIT) Image Reconstruction for Three-Dimensional Lung Imaging, Ph.D. thesis, University of Ottawa, 2007
- [10] Ankara Standard Data Set, European Community Concerned Action in Impedance Imaging, Image Reconstruction Meeting, Oxford, UK, 14-17, 1994
- [11] Pursiainen, S., Hakula, H., (2006). A High-order Finite Element Method for Electrical Impedance Tomography, *Progress In Electromagnetics Research Symposium*, Cambridge, 57-62.
- [12] Garnadi, A.D., (1997). Electrical Impedance Tomography Based on Mixed Finite Element Model, *Proceedings CMSE'97*, Bandung, 4, 6-7.
- [13] Woo, E.J., Hua, P., *et al.* (1994). Finite-Element Method in Electrical Impedance Tomography, *Medical and Biological Engineering and Computing*, 32(5), 530-536.
- [14] Irons, B.M., (1970) A Frontal Solution Program for Finite Element Analysis, *International Journal for Numerical Methods in Engineering*, 2, 25-32.
- [15] Ider, Y.Z., Gencer, N., *et al.* (1990). Electrical Impedance Tomography of translationally uniform cylindrical objects with general cross-sectional boundaries, *IEEE Medical Imaging*, 9(1), 49-59.
- [16] Ider, Y.Z., Nakiboğlu, B., *et al.* (1992). Determination of The Boundary of an Object Inserted Into a Water-filled Cylinder, *Clinical Physics and Physiological Measurement* 13(A), 151-154
- [17] Kılıç, B., Elektrik Empedans Tomografisinde Sonlu Eleman Yöntemi ile Modelleme ve Görüntü Oluşturma Algoritmaları, Doktora Tezi (Ph.D. thesis), Yıldız Teknik Üniversitesi, 1998.

## A COMPARISON STUDY FOR IMAGE DENOISING

*Muhammet Fatih ASLAN<sup>1\*</sup>, Akif DURDU<sup>2</sup>, Kadir SABANCI<sup>3</sup>*

*Image denoising is the detection and removal of outliers in a image. A measured analog signal is affected by both the device from which the measurement is performed and the noise from the environment. Various types of noise are available. With the developed noise reduction methods, it is tried to eliminate the existing noise. In this study, Bandelet Transform and Bilateral Filter denoising methods are compared. Both methods have been used to eliminate noise of different types and different rates added to the benchmark and retina images. Bandelet transform is performed for both hard and soft threshold. Peak Signal-to-Noise Ratio, Mean Squared Error, Mean Structural Similarity and Feature Similarity Index are used as a comparison method.*

Key words: *Bandelet transform, Bilateral filter, Image denoising*

### 1. Introduction

Today digital images are used in many areas such as intelligent traffic surveillance, medicine, astronomy, satellite television systems, etc. With the increasing need for digital images, denoising has gained importance. Noises cause distortion of spatial resolution in an image and reduce its contrast. Therefore, it negatively affects the edge properties of the image. Processes on noisy images can cause erroneous results. For example, the noise makes difficult to detect tumors and lesions. Thus, denoising must be applied before image analysis.

The images taken with sensors or cameras are usually exposure to noise. No matter how good the cameras are, there is always a need for image enhancement to improve their performance. Noises can result from the device, a data collection process, transmission, compression, environment conditions, etc. [1, 2].

The types of noise occurring in the image are varied. Gaussian Noise, Random Noise, Salt and Pepper Noise, Poisson Noise, Speckle Noise, etc. are general noise types [3]. Different types of noise occur in different imaging applications. For example, in the stages of image acquisition or transmission, quantum noise in X-rays and nuclear imaging, speckle noise in ultrasound imaging, and Rician noise in magnetic resonance imaging occur [4]. The structure of the noises is completely different from each other. Therefore, denoising methods can give good results in some filters and bad results in others. In this study, two denoising methods are compared by using three different noise types.

---

<sup>1</sup>Department of Electrical&Electronics Engineering, Karamanoglu Mehmetbey University, Karaman, Turkey, (mfatihhaslan@kmu.edu.tr)  <http://orcid.org/0000-0001-7549-0137>

<sup>2</sup>Department of Electrical&Electronics Engineering, Konya Technical University, Konya, Turkey, (adurdu@ktun.edu.tr)  <http://orcid.org/0000-0002-5611-2322>

<sup>3</sup>Department of Electrical&Electronics Engineering, Karamanoglu Mehmetbey University, Karaman, Turkey, (kadirsabanci@kmu.edu.tr)  <http://orcid.org/0000-0003-0238-9606>

Although there are many studies [4-11] that have been developed to denoising, most algorithms are not yet at the desired level [12]. Wavelet-based methods have good results in image denoising due to their sparseness and multiple resolution structure. Therefore, many wavelet based algorithms have been developed [13].

Image denoising is the common problem in image processing. Therefore, so much work has been done for image denoising. Zhang, et al. [14] investigated how a high-quality image can be reconstructed from a high-resolution and high-noise astronomical image. For this purpose 2G-bandelet denoising compressed sensing is proposed. As a result, a fast algorithm that preserves more image details and textures is created. Wang and Gao [15] used the second-generation Bandelet Transform (BT) and non-subsampled contourlet transform as a hybrid. The new denoising method performed better performance than the other two transform. Hazavei and Shahdoosti [16] proposed new multiresolution image denoising method using Bilateral Filter (BF) and complex wavelet thresholding. The advantages of both filters are combined. Experiments on real images showed the effectiveness. He, et al. [17] presented a new retinal image denoising approach that could preserve the details of the retinal vessels while removing image noise. The filter technique used combines the advantages of both BF and matched filter which employs the Gaussian-shape of the cross-section of the vessel. The results showed that this hybrid method was very successful. Finally, in another study by Ceylan and Ozturk [18] a similar performance comparison study was carried out using different denoising methods such as ridgelet, tetrolet, wavelet and curvelet. Denoising methods were evaluated according to the comparison results.

In this study, denoising was applied to the retina and five benchmark images. BT, which is one of the multiple resolution methods, was used with hard and soft thresholding methods which are the most popular threshold methods. Besides this transform, a BF was used to protect the edges and perform a non-linear transformation. The performances of the two methods were compared on three different types of noise

## 2. Methodology

### 2.1. Bandelet Transform

BT proposed by Pennec and Mallat [19] is a transformation adapted to the geometric content of the image. In wavelet-based methods, the same texture values in the image have different directions. To solve this problem, geometric regularity is achieved by using Bandeletization.

BT uses the anisotropic regularity of natural images by creating orthogonal vectors with the direction in which the function has the maximum regularity. BT is a self-adapting multidimensional geometry analysis method that takes advantage of the recognized geometric information of images compared to non-adaptive algorithms such as curvelet and contourlet transformations. The geometric redundancy of an image is removed by bandeletization. In this way, the wavelet transform coefficients are adapted to the image geometry to capture the singularities of the image edges. [20, 21].

### 2.2. Bilateral Filter

BF, an alternative to wavelet-based denoising methods, was proposed by Tomasi and Manduchi [22]. Unlike other conventional filters, in BF, both spatial and density information between a point and adjacent points are considered. BF takes the weighted totals of local neighborhood pixels. Each pixel is replaced by the weighted average of its neighbors. The weights are determined to depend on both the

spatial distance and the intensity distance. Thus, the edges are protected during noise cancellation [23, 24].

### 3. Application and Results

In this study, five benchmark images and 40 fundus images taken from the DRIVE dataset [25] were used. The used benchmark images and some fundus images are shown in Figure 1. First, Random, Gaussian and Rician noises were added to these images respectively (sigma = 5, 10, 15 for Random noise; signal-to-ratio (SNR) = 3, 5, 10 for Gaussian and Rician noise). Then, these noises were removed by BT and BF.

A thresholding process was applied to the detail coefficients obtained by BT. In this study, hard and soft thresholding methods were used. After the threshold value was applied, reconstruction was performed. The threshold  $T$  is calculated as follows:

$$T = \sigma \sqrt{2 \log(M)} \quad (1)$$

**Table 1. Denoising performance results of fundus images**

Type of Noise	Noise Ratio	Evaluation Criteria	Bandelet-Hard	Bandelet-Soft	Bilateral Filter
Random	Sigma=5	PSNR	38,9224	34,4843	35,7433
		MSE	8,3338	23,1562	17,5101
		MSSIM	0,6696	0,4798	0,3567
		FSIM	0,9883	0,9248	0,9148
	Sigma=10	PSNR	32,9028	28,2764	32,5224
		MSE	33,3276	96,7056	36,4667
		MSSIM	0,4799	0,2752	0,3615
		FSIM	0,9549	0,7915	0,9166
	Sigma=15	PSNR	29,3756	24,6809	29,8126
		MSE	75,0805	221,3092	67,9410
		MSSIM	0,3630	0,1839	0,3696
		FSIM	0,9085	0,6764	0,9198
Gaussian	Snr=3	PSNR	17,3931	15,2594	19,6052
		MSE	1247,3080	2038,7836	769,5456
		MSSIM	0,0400	0,0301	0,0481
		FSIM	0,3919	0,3262	0,4860
	Snr=5	PSNR	19,3243	17,1597	22,5609
		MSE	800,4200	1316,5242	394,6266
		MSSIM	0,0532	0,0393	0,0709
		FSIM	0,4526	0,3799	0,5932
	Snr=10	PSNR	24,2172	21,9646	30,9685
		MSE	259,5216	434,9683	57,1614
		MSSIM	0,1006	0,0775	0,1816
		FSIM	0,6157	0,5327	0,8604
Rician	Snr=3	PSNR	38,6165	26,6154	37,6522
		MSE	8,9420	147,1538	11,4536
		MSSIM	0,4774	0,1643	0,3648
		FSIM	0,9562	0,6947	0,9177
	Snr=5	PSNR	34,2520	25,8929	37,0590
		MSE	24,4282	172,4614	13,0325
		MSSIM	0,3288	0,1405	0,3723
		FSIM	0,9018	0,6703	0,9233
	Snr=10	PSNR	28,0683	23,9843	33,3060
		MSE	101,4507	263,6581	30,4246
		MSSIM	0,1743	0,1022	0,3263
		FSIM	0,7629	0,6080	0,9362

Performance was compared with both methods after the noise was removed. Peak Signal-to-Noise Ratio (PSNR), Mean Squared Error (MSE), Mean Structural Similarity (MSSIM) and Feature Similarity

Index (FSIM) metrics were used as comparison criteria. The results of Retina and Benchmark images are shown in Table 1 and Table 2.

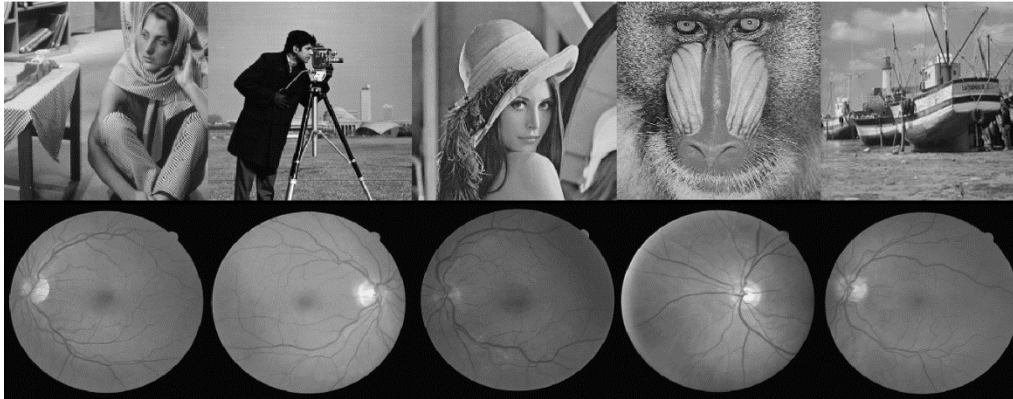


Figure 1. The images used in the application

Table 2. Denoising performance results of benchmark images

Type of Noise	Noise Ratio	Evaluation Criteria	Bandelet-Hard	Bandelet-Soft	Bilateral Filter
Random	Sigma=5	PSNR	38,9197	34,8545	31,4374
		MSE	8,3390	21,2700	48,1022
		MSSIM	0,9394	0,8588	0,7156
		FSIM	0,9960	0,9778	0,9073
	Sigma=10	PSNR	32,9062	28,6082	29,8290
		MSE	33,3014	89,6368	68,7643
		MSSIM	0,8593	0,7227	0,7119
		FSIM	0,9851	0,9248	0,9067
	Sigma=15	PSNR	29,3811	24,9829	28,0706
		MSE	74,9854	206,5270	102,2293
		MSSIM	0,7935	0,6233	0,7105
		FSIM	0,9694	0,8696	0,9076
Gaussian	Snr=3	PSNR	17,3997	14,8921	19,4050
		MSE	1228,4930	2173,6538	784,7663
		MSSIM	0,2675	0,1881	0,3044
		FSIM	0,6415	0,5648	0,7055
	Snr=5	PSNR	19,2674	16,7403	21,9790
		MSE	800,9177	1423,5575	432,6751
		MSSIM	0,3257	0,2480	0,3767
		FSIM	0,6943	0,6192	0,7744
	Snr=10	PSNR	24,1006	21,5181	27,9438
		MSE	263,5003	475,8568	105,6665
		MSSIM	0,4874	0,4105	0,5881
		FSIM	0,8121	0,7496	0,8987
Rician	Snr=3	PSNR	38,5874	25,7080	31,9966
		MSE	9,0021	178,5469	42,5126
		MSSIM	0,8617	0,5664	0,7191
		FSIM	0,9844	0,8435	0,9086
	Snr=5	PSNR	34,1621	25,1344	31,6675
		MSE	24,9396	203,2743	45,8304
		MSSIM	0,7735	0,5310	0,7194
		FSIM	0,9623	0,8323	0,9091
	Snr=10	PSNR	28,1726	23,4804	30,3140
		MSE	99,0426	295,1275	62,1657
		MSSIM	0,6165	0,4734	0,6862
		FSIM	0,8964	0,7988	0,9136

#### 4. Conclusion

In this study, an image denoising application was performed comparing the performance of BT and BF. As shown in Table 1 and Table 2, the performance of denoising methods varies at different noise types and different images. In terms of image difference, BF showed better results in fundus images. In the denoising application performed with BT, similar results were obtained in both image types. When examined in terms of noise type, BF was better in both image types in Gaussian noise. BT was generally better in case of random and rician noise. However, as the noise ratio increases, the BF has performed better image denoising.

#### References

- [1] Buades, A., Coll, B., and Morel, J. M. (2004). On image denoising methods. *Technical Note, CMLA (Centre de Mathematiques et de Leurs Applications)*, 5, pp. 1-40.
- [2] Motwani, M. C., Gadiya, M. C., Motwani, R. C., and Harris, F. C. Survey of image denoising techniques." *Proc., Proceedings of GSPX*, pp. 27-30.
- [3] Boyat, A., and Joshi, B. K. Image denoising using wavelet transform and median filtering. *Proc., Engineering (NUICONe), 2013 Nirma University International Conference on, IEEE*, pp. 1-6.
- [4] Buades, A., Coll, B., and Morel, J.-M. A non-local algorithm for image denoising. *Proc., Computer Vision and Pattern Recognition, 2005. CVPR 2005. IEEE Computer Society Conference on, IEEE*, pp. 60-65.
- [5] Portilla, J., Strela, V., Wainwright, M. J., and Simoncelli, E. P. (2003). Image denoising using scale mixtures of Gaussians in the wavelet domain. *IEEE Transactions on Image processing*, 12(11), pp. 1338-1351.
- [6] Luisier, F., Blu, T., and Unser, M. (2007). A new SURE approach to image denoising: Interscale orthonormal wavelet thresholding. *IEEE Transactions on image processing*, 16(3), pp. 593-606.
- [7] Elad, M., and Aharon, M. (2006). Image denoising via sparse and redundant representations over learned dictionaries. *IEEE Transactions on Image processing*, 15(12), pp. 3736-3745.
- [8] Dabov, K., Foi, A., Katkovnik, V., and Egiazarian, K. (2007). Image denoising by sparse 3-D transform-domain collaborative filtering. *IEEE Transactions on image processing*, 16(8), pp. 2080-2095.
- [9] Pu, Y.-F., Zhang, N., Zhang, Y., and Zhou, J.-L. (2016). A texture image denoising approach based on fractional developmental mathematics. *Pattern Analysis and Applications*, 19(2), pp. 427-445.
- [10] Aggarwal, H. K., and Majumdar, A. (2016). Hyperspectral image denoising using spatio-spectral total variation. *IEEE Geoscience and Remote Sensing Letters*, 13(3), pp. 442-446.
- [11] Lahmiri, S., and Boukadoum, M. (2015). A weighted bio-signal denoising approach using empirical mode decomposition. *Biomedical Engineering Letters*, 5(2), pp. 131-139.
- [12] Buades, A., Coll, B., and Morel, J.-M. (2010). Image denoising methods. A new nonlocal principle. *SIAM review*, 52(1), pp. 113-147.
- [13] Kaur, S., and Singh, N. (2014). Image Denoising Techniques: A Review. *International Journal of Innovative Research in Computer and Communication Engineering*, 2(6).
- [14] Zhang, J., Zhang, H., Shi, X., and Geng, S. (2019). High Noise Astronomical Image Denoising via 2G-Bandelet Denoising Compressed Sensing. *Optik*.
- [15] Wang, X., and Gao, J. Image Denoising Method Based on Nonsampled Contourlet Transform and Bandelet Transform. *Proc., 2009 First International Conference on Information Science and Engineering*, pp. 1278-1281.
- [16] Hazavei, S. M., and Shahdoosti, H. R. (2017). Using Complex Wavelet Transform and Bilateral Filtering for Image Denoising. *arXiv preprint arXiv:1702.01276*.
- [17] He, Y., Zheng, Y., Zhao, Y., Ren, Y., Lian, J., and Gee, J. (2017). Retinal Image denoising via bilateral filter with a spatial kernel of optimally oriented line spread function. *Computational and mathematical methods in medicine*, 2017.
- [18] Ceylan, M., and Canbilin, A. E. (2017). Performance Comparison of Tetrolet Transform and Wavelet-Based Transforms for Medical Image Denoising. *International Journal of Intelligent Systems and Applications in Engineering*, 5(4), pp. 222-231.

- [19] Le Pennec, E., and Mallat, S. (2005). Sparse geometric image representations with bandelets. *IEEE transactions on image processing*, 14(4), pp. 423-438.
- [20] Villegas, O. O. V., Domínguez, H. d. J. O., and Sánchez, V. G. C. A comparison of the bandelet, wavelet and contourlet transforms for image denoising. *Proc., Artificial Intelligence, 2008. MICAI'08. Seventh Mexican International Conference on*, IEEE, pp. 207-212.
- [21] Ashraf, R., Bashir, K., Irtaza, A., and Mahmood, M. T. (2015). Content based image retrieval using embedded neural networks with bandletized regions. *Entropy*, 17(6), pp. 3552-3580.
- [22] Tomasi, C., and Manduchi, R. Bilateral filtering for gray and color images. *Proc., Computer Vision, 1998. Sixth International Conference on*, IEEE, pp. 839-846.
- [23] Ahmed, S. S., Messali, Z., Ouahabi, A., Trépout, S., Messaoudi, C., and Marco, S. (2014). Bilateral Filtering and Wavelets based Image Denoising: Application to Electron Microscopy Images with Low Electron Dose. *International Journal on Recent Trends in Engineering & Technology*, 11(2), pp. 153-164.
- [24] Kumar, B. S. (2013). Image denoising based on non-local means filter and its method noise thresholding. *Signal, image and video processing*, 7(6), pp. 1211-1227.
- [25] Staal, J., Abràmoff, M. D., Niemeijer, M., Viergever, M. A., and Van Ginneken, B. (2004). Ridge-based vessel segmentation in color images of the retina. *IEEE transactions on medical imaging*, 23(4), pp. 501-509.

## AN OVERVIEW TO ANTENNA TERMINOLOGY AND DESIGN A COMPACT DUAL BAND ANTENNA BY USING HFSS PROGRAM FOR C AND X BANDS APPLICATIONS

*Ali Recai ÇELİK<sup>1\*</sup>, Muhammed Bahaddin KURT<sup>2</sup>*

*Antennas are used to transform the traveling signals into the electromagnetic waves in the free space. There are many types of the antennas using in the various areas. Microstrip patch antennas have been used for many applications such as mobile communications, radar applications, microwave imaging, satellite systems, remote sensing, radio frequency identifications, wireless systems, synthetic aperture radar, telemetry, aerospace, weather mapping and detecting etc. These applications operate at L, S, C, X and K microwave bands or combinations of these bands. In this study, a comprehensive study of the antenna terminology is presented and a compact dual-band antenna operating at the C-band and X-band is developed and analyzed. Defected Ground Structure techniques are used on the ground side and some other modification techniques are used on the patch side in order to obtain the resonant frequencies in these two bands. The FR4-epoxy material is chosen as a substrate for the designed patch antenna with dielectric constant of 4.5, and height of 1.6 mm. The antenna structure is optimized and simulated using High Frequency Structured Simulator program which uses the Finite Element Methods solver technique. A large number of the antenna parameters are obtained and explained at the result part of the study.*

*Key words: C band, X band, HFSS, Microstrip patch antenna*

### 1. Introduction

Developments in the various areas of the radio frequencies and microwave technologies have been observed significantly over the last decades. Most of the applications of these areas operate at S, C and X bands that cover 2-4 GHz, 4-8 GHz and 8-12 GHz, respectively [1]. Antennas have critical roles for many applications such as mobile communications, radar applications, microwave imaging, satellite systems, remote sensing, radio frequency identifications, wireless systems etc. An antenna needs to be optimized in order to be used in these specific applications. For this aim, several properties like bandwidth, size, gain, directivity, etc. must be adjusted to get the desired results. Among the various types of the antennas, microstrip patch antennas (MPAs) are suitable for using in many applications due to their compact size and low-profile structures. However, MPAs have the greatest disadvantage of their narrow bandwidth [2].

<sup>1</sup>Department of Electrical and Electronics Engineering, University of Dicle, Diyarbakir, Turkey, (eeecalik@gmail.com)  
 <https://orcid.org/0000-0002-6917-5170>

<sup>2</sup>Department of Electrical and Electronics Engineering, University of Dicle, Diyarbakir, Turkey, (bkurt@dicle.edu.tr)  
 <https://orcid.org/0000-0001-6983-2081>

Received: Received: 10 August 2019; Accepted: 19 December 2019

Doi: <https://doi.org/10.36222/ejt.604953>

In this paper, firstly the basic terminology of an antenna is explained. Then, information about the High Frequency Structural Simulator (HFSS) program which is widely utilized in the analysis of the electromagnetic structures [3] is given. Finally, a dual band antenna which operates at C-band and X-band is designed by using defected ground structure (DGS) techniques on the ground side and some other modification techniques on the patch side. The modified MPA have slots on the ground and parasitic elements on the patch in order to obtain broad bandwidth in contrast to conventional MPAs. Design and analysis of the antenna is achieved by HFSS software.

## 2. Important Antenna Parameters and HFSS Program

In the development process of an antenna, it is necessary to keep various parameters in the specific values [4]. Some of the basic antenna parameters can be summarized as return loss ( $RL$ ), reflection coefficient ( $\Gamma$ ), antenna impedance ( $Z_A$ ), voltage standing wave ratio ( $VSWR$ ), bandwidth ( $BW$ ), gain ( $G$ ), directivity ( $D$ ), efficiency ( $e$ ) and half power beamwidth ( $HPBW$ ). In this section, these important antenna parameters are introduced and the relationships between them are explained with some equations.

### 2.1. $RL$ , $\Gamma$ , $Z_0$ , $VSWR$ , $BW$ , $G$ , $D$ , $e$ , Radiation Pattern and $HPBW$

Both the antenna and the transmission cable which connecting the antenna to signal source should have same impedance values for transferring electromagnetic energy efficiently [5]. Transceivers and their transmission lines are generally have  $50\Omega$  impedance. If the antenna has  $Z_A$  that is different from  $50\Omega$ , then there is a mismatch and an impedance matching is required. The  $RL$  is the other expression of the mismatch. It is a logarithmic ratio measured in decibel (dB) that compares the power reflected by the antenna to the power that is fed into the antenna from the transmission line. There are significant relationships between the parameters of  $RL$ ,  $\Gamma$ ,  $Z_0$ , and  $VSWR$  as given below [2]:

$$\Gamma = \frac{V_{REFL}}{V_{INC}} = \frac{Z_A - Z_0}{Z_A + Z_0} \quad (1)$$

$$RL = -20 \log \Gamma \quad (2)$$

$$VSWR = \frac{1 + |\Gamma|}{1 - |\Gamma|} \quad (3)$$

where  $V_{INC}$  and  $V_{REFL}$  are incident and reflection voltage for the antenna feed point, respectively.  $Z_0$  is the input impedance and generally equal to  $50\Omega$ . According to the Equations (1-3), as the  $RL$  falls below -10 dB or  $\Gamma$  falls below 1 or  $VSWR$  falls below 2, the impedance matching of the antenna will increased and the performance of the antenna will be good. Hence, one of the important purposes for an antenna designer is obtaining the mentioned values for  $RL$ ,  $\Gamma$  and  $VSWR$ .

Another basic antenna parameter is  $BW$  which means the interval of the frequencies where the antenna can operate efficiently. In other words,  $BW$  is the number of frequencies for  $RL < -10$  dB and  $1 < VSWR < 2$ . It can be formulated according to Eq. 4 [2].

$$BW = 2 \frac{f_{max} + f_{min}}{f_{max} - f_{min}} \% \quad (4)$$

where  $f_{max}$  and  $f_{min}$  mean the maximum and minimum values of the frequency range, respectively.

Directivity is the ability of an antenna to focus in a particular direction when transmitting or receiving energy. Another important parameter that expresses the performance of the antenna is Gain. There are significant relationships between the parameters of  $G$ ,  $D$  and  $e$  as given in Eq. 5 [6]:

$$G = e \times D \quad (5)$$

The relative strength of the radiated field at the different directions from the antenna is indicated by 'Radiation Pattern' which can be both two-dimensional and three-dimensional. The angular width, in which the power across the maximum radiation direction is halved, is defined as *HPBW* and is a measure of the directionality. In decibels, half of the power is expressed as 3dB, for this reason the *HPBW* is generally referred to 3 dB beamwidth. Two-dimensional and three-dimensional radiation patterns are given in Fig. 1 as an example [7]. The expression of the HPBW is also shown on this figure.

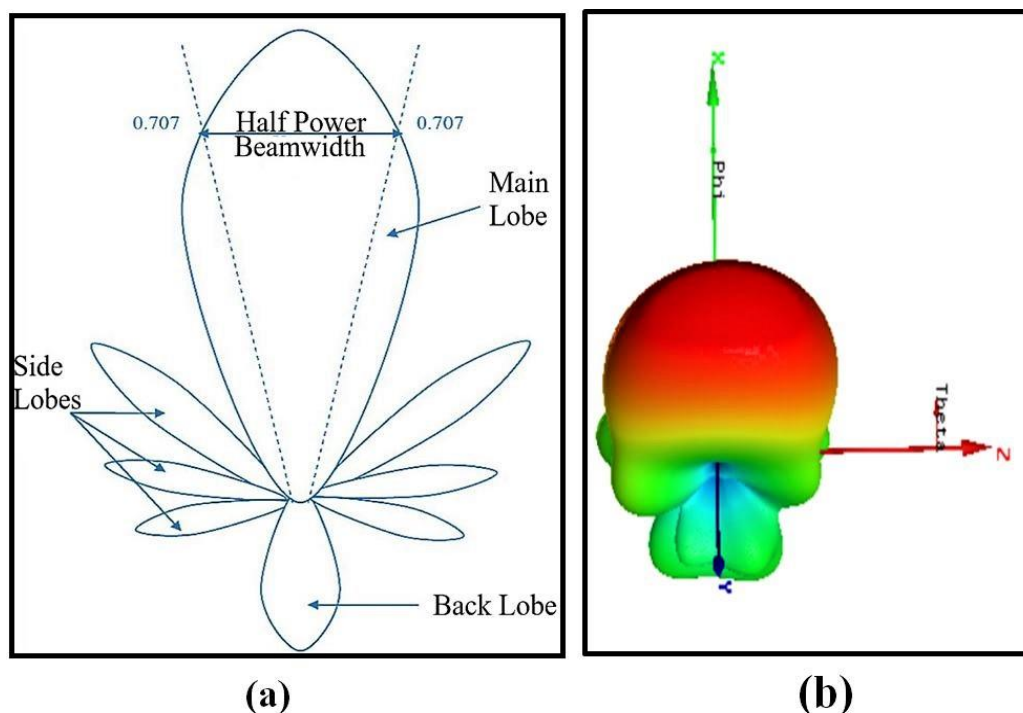


Figure 1. Radiation patterns: a) Two-dimensional, b) Three-dimensional.

## 2.2. HFSS Program

There are several antenna simulator programs to achieve the aims of designing parameters, modelling antennas and analysing the behaviours of them. These are generally classified into two numerical methods, namely Finite Difference Time Domain (FDTD) and Finite Element Method (FEM). The most known programs such as FEKO, Antenna Magus and HFSS use the FEM method that is a technique for finding approximate solutions to boundary value problems for differential equations [8]. Another important program Computer Simulation Technology (CST) Microwave Studio is based on the FDTD method [9].

In this study, the HFSS program is preferred to develop a compact dual-band antenna. HFSS is high performance electromagnetic field simulation software. Electromagnetic problems can be solved quickly and clearly by using it. Near and far electromagnetic fields can be drawn, parasitic parameters (S, Y, Z) can be calculated and the antenna performance can be optimized by using this program.

### 3. Design and Analysis of Dual-Band MPA

MPAs consist of a radiating patch, a ground plane and a dielectric substrate. They are generally fed by a microstrip line or a coaxial line. In this study, the microstrip feedline method which is easy to design and fabricate is used. An inset fed MPA is preferred to design due to certain planar shortages of the microstrip line feeding [10]. Firstly, design parameters of the antenna are calculated based on the transmission line model for obtaining desired resonant frequencies approximately. In the second stage of the development process, some modification such as using slots and parasitic elements are implemented to improve the performance of the antenna. Therefore, certain parameters are determined and the process is completed successfully. The transmission line model is given in Eq. 5 to 11 [6].

$$W = \frac{c}{2f_0 \left[ \frac{(\epsilon_r + 1)}{2} \right]^{1/2}} \quad (5)$$

$$\epsilon_{r_{eff}} = \frac{\epsilon_r + 1}{2} + \frac{\epsilon_r - 1}{2} \left( 1 + \frac{12h}{W} \right)^{-1/2} \quad (6)$$

$$L_{eff} = \left[ \frac{c}{2f_0 (\epsilon_{r_{eff}})^{1/2}} \right] \quad (7)$$

$$\Delta L = 0.412h \frac{(\epsilon_{r_{eff}} + 3) \left( \frac{W}{h} + 0.264 \right)}{(\epsilon_{r_{eff}} - 0.258) \left( \frac{W}{h} + 0.8 \right)} \quad (8)$$

$$L = L_{eff} - \Delta L \quad (9)$$

$$x_0 = \frac{c}{(2\epsilon_{r_{eff}})^{1/2}} \left( \frac{4.65 \times 10^{-12}}{f_0} \right) \quad (10)$$

$$y_0 = \frac{L}{\pi} \cos^{-1} \left( \frac{R_{in}}{R_{in0}} \right)^{1/2} \quad (11)$$

where  $W$  and  $L$  mean width and length of the rectangular patch,  $x_0$  and  $y_0$  mean gap and distance of the inset fed, respectively.

As mentioned before, for the developed antenna the dielectric substrate is selected as “FR4-Epoxy” material which has the dielectric constant ( $\epsilon_r$ ) of 4.5 and height ( $h$ ) of 1.6 mm [11]. Firstly, the resonance frequency of the antenna is desired to be around 7 GHz (for C band). Hence, the transmission line model is used these values to calculate the antenna parameters. Input parameters and obtained output parameters are given in Table I. The top view and design parameters of the antenna are shown in Fig. 2.

**Table 1. Obtained output parameters according to the inputs.**

Inputs	Outputs
Dielectric Thickness = 1.6 mm	Patch Width = 15 mm
Conductor Thickness = 0.035 mm	Patch Length = 13 mm
Relative Permittivity = 4.5	Inset Gap = 2 mm
Solution Frequency = 7 GHz	Inset Distance = 5 mm
Input Impedance = 50 Ohm	Substrate Size = 42 x 35 mm <sup>2</sup>

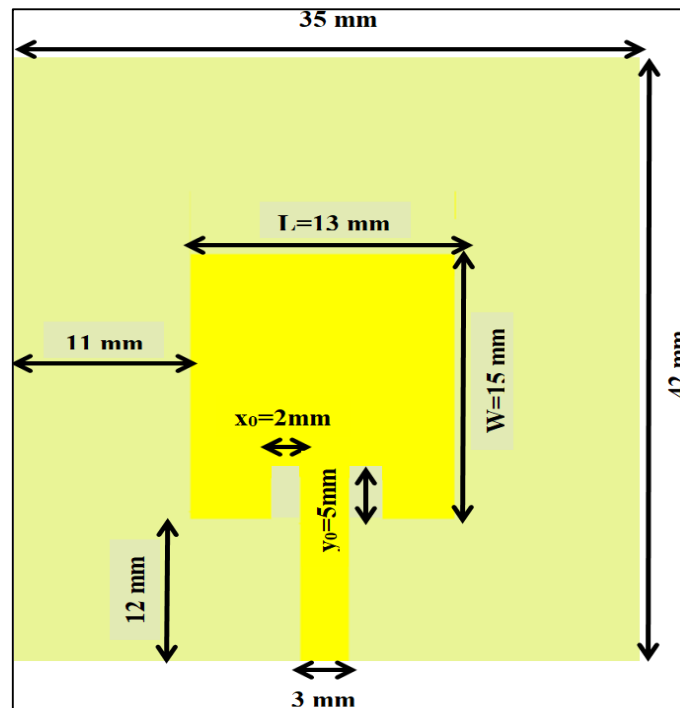


Figure 2. Designed inset-fed antenna to obtain 7 GHz resonance frequency.

### 3.1. Development Process and Modification Techniques

The RL result of the designed antenna is given in Fig. 3. According to this plot, it is seen that the first step of the development process has been completed successfully. Between the 5.8 GHz and 8.2 GHz, the RL values are under the -10 dB level meaning the antenna is working efficiently. So, transmission line model has provided obtaining the 7 GHz resonance frequency which is approximately in the C-band of the microwave spectrum. After this stage, the main purpose is obtaining new resonance frequency around the 10 GHz for working in the X-band applications.

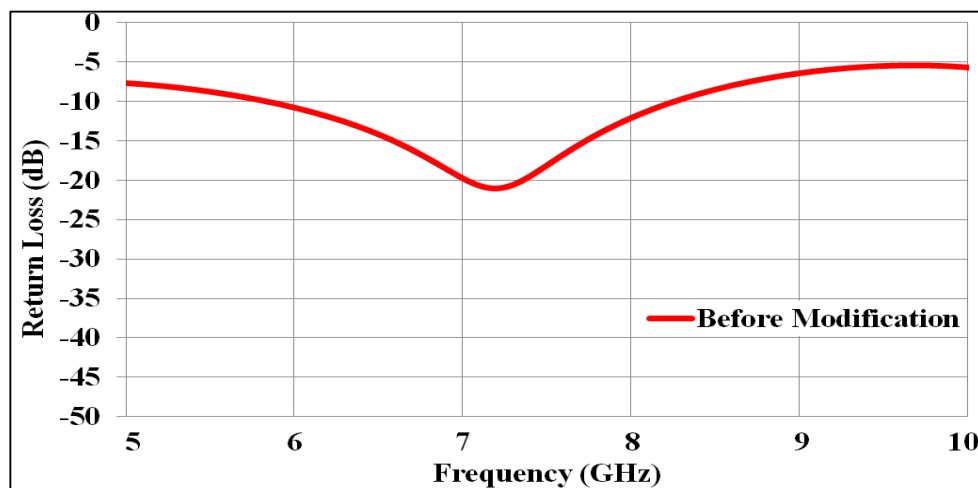


Figure 3. Return loss of the inset-fed antenna before implementing any modification techniques.

The new resonance frequencies can be occurred and BW of the antenna can be enhanced by using DGS approach [12,13]. The methods of etching slot(s) on the ground plane and adding parasitic element(s) on the patch side are the most used methods in order to improve the bandwidth of a compact MPA [14, 15].

In this study, a new resonance frequency is obtained by using L-shaped and inverted L-shaped slots. The sizes and the positions of these slots are determined empirically in order to set the new frequency around the 10 GHz. Moreover, two parasitic elements having rectangular shape are added to reduce the RL values to lower levels.

The proposed antenna after making some modifications is shown in Fig. 4. After the modifications, the new RL result is obtained as seen in Fig. 5. According to this plot, the second resonance is occurred between the 9.6 GHz and 11.2 GHz that is in the X-band of the microwave spectrum. Furthermore, the RL level approaches -50 dB values that provides one of the purposes of this work. Even if the first resonance frequency shifted to left, it has still stayed at the desired range for C-band. Also, the 3-D plot of the gain values is shown in Fig. 6. It is clearly seen from the figure that the proposed antenna has omnidirectional radiation pattern meaning the antenna emits uniform wave power in all directions in a plane.

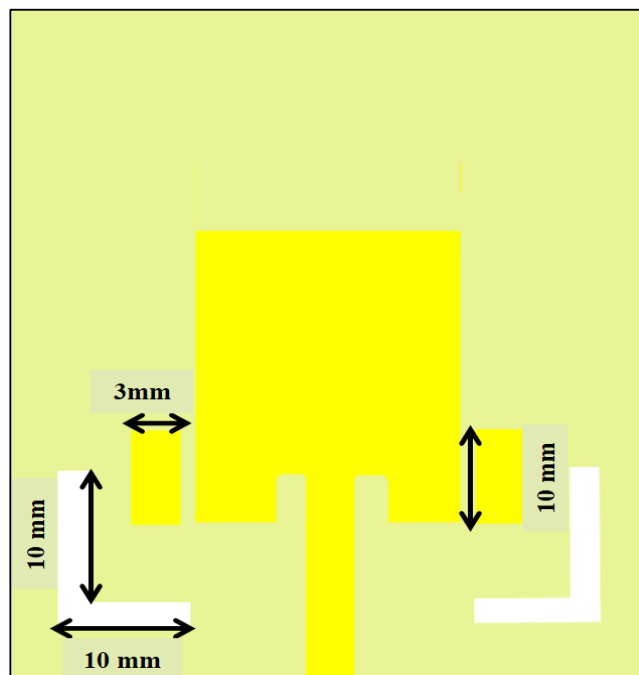


Figure 4. Proposed antenna after making some modifications.

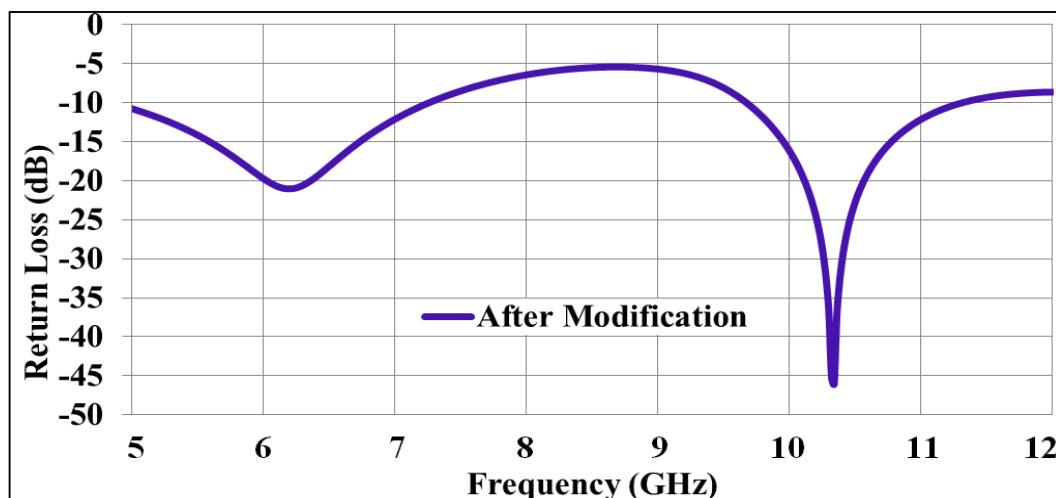


Figure 5. Return loss of the antenna after implementing some modification techniques.

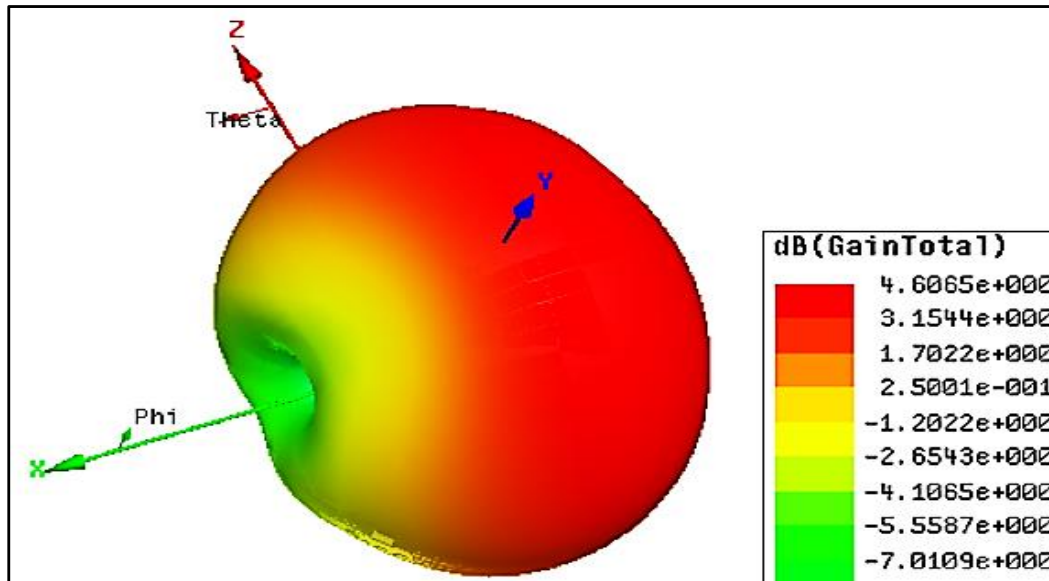


Figure 6. 3-D polar plot of the gain.

#### 4. Conclusions

The various types of the antennas with different properties are used in several applications. The performance of an antenna is related to impedance matching, bandwidth, gain, efficiency, beamwidth and size of the antenna. Optimization of these parameters is continued by researchers so as to obtain better analysis results. For this purpose, the simulation programs and their tools play a critical role in the development process of the antenna. In this paper, a comprehensive study of the antenna terminology is presented and HFSS simulation program is introduced. In the simulation study, a compact ( $42 \times 35 \times 1.6 \text{ mm}^3$ ) microstrip dual-band antenna operating at the two broad frequency bands that make it suitable for C and X-bands applications is proposed. This antenna has FR-4 Epoxy substrate and inset-fed rectangular patch. DGS and trial-error optimization technique are used to improve the return loss performance of the antenna. Two slots are etched on the ground plane and two parasitic elements are added to the patch side of the antenna. After the parametric analysis, the bandwidths of 34% (5.8-8.2 GHz) and 15% (9.6-11.2 GHz) are obtained in the C-band frequency range (4-8 GHz) and X-band frequency range (8-12 GHz), respectively. The proposed antenna is applicable for various systems working in the C-band such as satellite communication, weather radar systems, Wi-Fi and ISM Band applications, and for various systems working in the X-band such as radar applications and space communications. Some other modification techniques can be implemented to obtain whole frequency range of C and X bands. It is considered that, the proposed antenna will be ready to fabrication process after some improvements.

#### Acknowledgment

This paper is the extended version of a conference paper which was presented orally in the International Engineering and Natural Sciences Conference (IENSC'18). The research is supported by the Researching Projects Committee of the University of Dicle (DUBAPK) with the project number of 14-MF-71. We are grateful to DUBAPK for financial assistance.

## References

- [1] Islam, M. F., et al., Dual band microstrip patch antenna for SAR applications. *Australian Journal of Basic and Applied Sciences*, 4(2010), 4585-4591.
- [2] Balanis, C. A., *Antenna Theory: Analysis and Design*, John Wiley and Sons Inc., New Jersey, USA, 2015.
- [3] Ansys Hfss (ver. 15), Ansys Corporation. Canonsburg, PA, USA. Retrieved from <http://www.ansys.com/Products/Electronics/ANSYS-HFSS>, 2014.
- [4] Celik A.R., Kurt, M.B., Development of a novel ultra-wideband, stable and high directive monopole disc antenna for radar-based microwave imaging of breast cancer, *Journal of Microwave Power and Electromagnetic Energy*, 52(2), 75-93.
- [5] Kraus, J.D., *Antennas*, McGraw Hill, New York, USA, 1988.
- [6] Ulaby, F., 2006. *Fundamentals of Applied Electromagnetics*, 5th edition, Prentice Hall, Washington DC. USA, 2006.
- [7] Celik, A.R., *Research & Reviews in Engineering*, Gece Kitapligi, Ankara, Turkey, 2019.
- [8] Bardi, I., Cendes, Z., New directions in HFSS for designing microwave devices, *Microwave Journal*, 41(8), 22-36.
- [9] Computer Simulation Technology, <http://www.cst.com>
- [10] Garg, R., et al., *Microstrip Antenna Design Handbook*, Artech House Antennas and Propagation Library, 2001
- [11] FR4 Epoxy Properties, Available: <https://www.microwaves101.com/encyclopedias/fr-4>
- [12] Guha, D., et al., Microstrip patch antenna with defected ground structure for cross polarization suppression, *IEEE Antennas and Wireless Propagation Letters*, 4(2005), 455-458.
- [13] Dong, J., et al., Compact planar ultrawideband antennas with 3.5/5.2/5.8 GHz triple band-notched characteristics for internet of things applications, *Sensors*, 17(2017).
- [14] Bah, J., et al., Ground slotted monopole antenna design for microwave breast cancer detection based on time reversal MUSIC, *Progress In Electromagnetics Research C*, 59(2015), 117-126.
- [15] Wani, Z., Kumar, D., Dual-band-notched antenna for UWB MIMO applications, *International Journal of Microwave and Wireless Technologies*, 35(2015), 1-6.

## ENERGY PREDICTION BASED ON MODELLING AND SIMULATION ANALYSIS OF AN ACTUAL GRID-CONNECTED PHOTOVOLTAIC POWER PLANT IN TURKEY

*Osman CICEK<sup>1\*</sup>, Mohamed Alageli M. MILLAD<sup>2</sup>, Faruk ERKEN<sup>3</sup>*

*Turkey has invested in generating solar power industry to meet the energy demand as well as saving the national energy resources. The government has also substituted some of the energy consumption with clean energy sources, especially on-grid PV power plants. In recent years, a number of incentives are provided to persuade investors to invest in solar energy sector in Turkey. In this context, KRMN-SNAPS 1.6 MW PV power plant is installed in Konya Province in the Central Anatolia region of Turkey. The most important information that have to be known in advance are the cost and duration of the investment. Therefore, pre-investment production analysis of the PV power plant is very essential. The performance of the power plant depends on some parameters for instance temperature, irradiance and sunshine duration. In this study, solar PV arrays are modelled by using MATLAB/Simulink and the power plant is simulated based on the above mentioned meteorological parameters. The simulation results of the PV power plant were compared with the actual production data. In the simulation, long-term average data on production of the location were used and it is observed that the simulation results and the one year's actual production data are compatible with each other.*

*Key words: Renewable energy, PV systems, on-grid PV power plants, energy prediction, energy policy.*

### 1. Introduction

In the last few decades, Turkey is one of the greatest growing economical countries in the world for the most industrial fields [1]. This development has increased not only the consumption of the resources of both local and imported energy (oil, natural gas and coal) to supply all the operating needs, but also has risen the anxiety of energy resources shortage in the country [2]. Furthermore, in the developing countries, the rapid growth in population and industrialization have led to increasing the energy demands with an increase in power consumption.

Energy, as a civilization factor, is considered as one of the main indicators that can be used to recognize the economic and social development strength level of any country. This has brought out the

<sup>1</sup> Department of Electrical and Electronic Engineering, Faculty of Engineering and Architecture, Kastamonu University, Kastamonu, Turkey, (ocicek@kastamonu.edu.tr)  <https://orcid.org/0000-0002-2765-4165>

<sup>2</sup> Kastamonu University, Faculty of Engineering and Architecture, Department of Materials Science and Nanotechnology Engineering, 37000 KASTAMONU, TURKEY, (mohamedmillad@yahoo.com)

<sup>3</sup> Department of Electrical and Electronic Engineering, Faculty of Engineering and Architecture, Kastamonu University, Kastamonu, Turkey, (ferken@kastamonu.edu.tr)  <https://orcid.org/0000-0003-2048-1203>

existence of a direct proportional relationship between energy consumption and social development. Therefore, energy consumption increases with economic development and welfare [3, 4].

There is no doubt that the increased demand of energy in all over the world has raised the level of CO<sub>2</sub> emissions into the ozone layer as a result of burning petroleum products which pollute the atmosphere and cause global warming [5, 6]. Therefore, a major benefit of using Renewable Energy Sources (RESs) for instance hydroelectric, geothermal, wind, biomass, solar energy etc., is the reduction of pollutant emission in the air [7]. In addition to the benefits of RESs, the energy safety concerns have increased the importance of RESs all around the world [8-12].

RESs are also called alternative energy [13]. One of the most important alternative energy sources is solar energy, because of its ubiquity, abundance, and sustainability. [14-16]. In addition, the demands for solar applications have enhanced by 20% to 25% over the last two decades and this market is growing worldwide [17]. Turkey has approximately imported 60% of its energy sources. Turkey has an appropriate geographical location to take advantage of using sun light as a source of energy in order to meet some of the electrical demand, providing better ecological life and reducing the power cost. [18].

A number of incentives has been implemented to enhance the ratio of RESs in power generation in Turkey. As a result of these charming regulations, many solar power plant has been installed in Turkey. One of these plants is KRMN-SNAPS 1.6 MW PV power plant installed in Konya Province in the Central Anatolia region of Turkey. The efficiency and profitability of these power plants are important for investors. The energy produced from the power plant depends on many production factors for instance temperature, humidity, wind, irradiance and sunshine duration. It is important to predict the power values of the power plant based on these factors.

PV systems are used to generate electricity from solar energy, and they are classified into three main types such as on-grid connected, off-grid connected and hybrid PV system. On-grid solar systems are by far the most common and widely used in houses and power generating stations. These systems are connected to the public electricity grid and do not require a battery storage system. Grid system consists of solar panels, inverters, a power conditioning unit and grid connection equipment [19].

The most basic component of a PV system is the PV module. It is made up of several photovoltaic solar cells, which generate different amounts of direct current depending on the manufacturing substance such as mono crystalline, poly-crystalline and thin film technologies [20]. PV module is rated on the bases of the power delivered under Standard Testing Conditions (STC) i.e. a cell temperature of 25 degrees Celsius (°C) and an irradiance of 1 kW/m<sup>2</sup> with an air mass 1.5 (AM1.5).

In this study, all the components of the power plant are simulated in MATLAB/Simulink using the actual parameters. Due to the long-term data, the power and the energy values of the power plant were estimated and compared with the actual values of 2018.

## 2. Electrical Characteristics of Solar Cell

The operating principle of PV cells is that the electron-hole pairs, which absorbs photons having energy exceeding the band-gaps of the material and so generates current when sun light sheds on PV cells depending on the irradiance [21]. Fig. 1 indicates the simplified electrical equivalent circuit of PV cell and explains its principle of operating under the illumination.

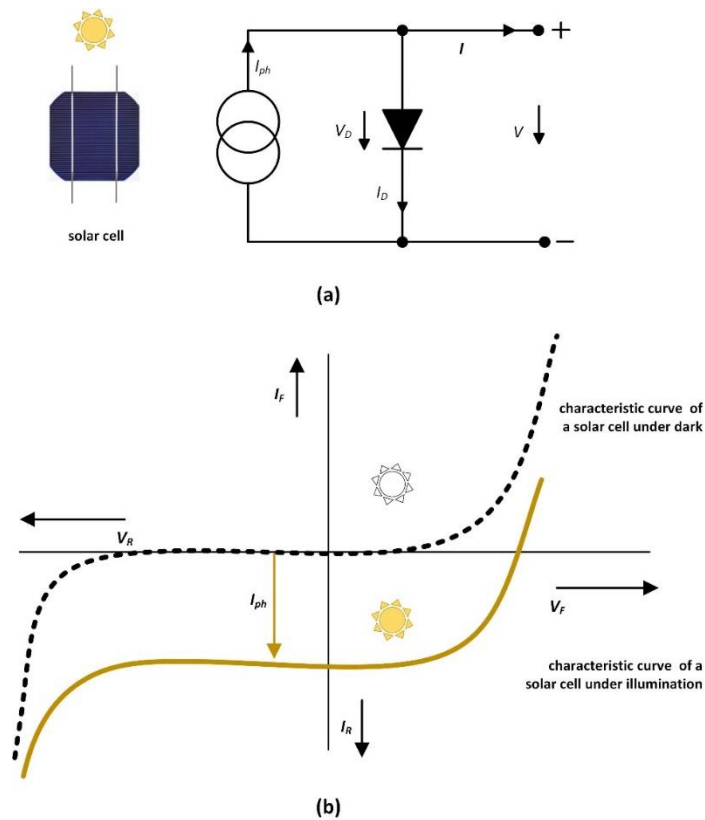


Figure 1. The ideal electrical circuit (a) and characteristic curve (b) of PV cell under the illumination [22].

The current expressions can be written according to the electrical circuit in Fig. 1 as following:

$$I_{pv} = I_{ph} - I_D \tag{1}$$

$$I_{pv} = I_{ph} - I_o \left[ e^{\frac{qV}{nkT}} - 1 \right] \tag{2}$$

According to the numbers of diodes, there are two types of a solar cell equivalent circuit, the single-diode and two-diode model as shown in Fig. 2. A few milliohms of series resistance  $R_s$  is occurred owing to the movement of current through the  $p-n$  junctions and the contact resistance between the metal contact and the silicon in the PV cell. Moreover, the power losses and leakage currents occur as a parallel resistance  $R_p$  in the equivalent circuit [22].

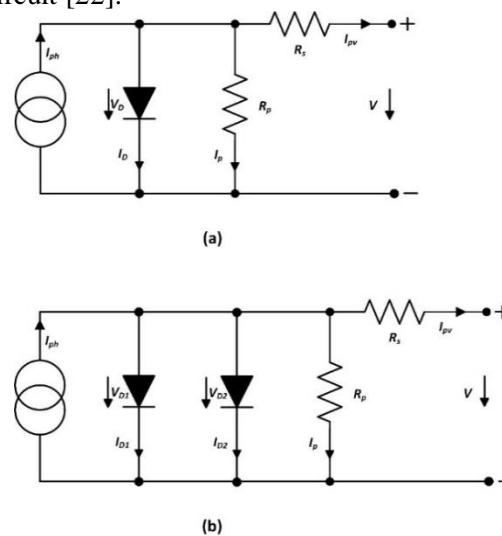


Figure 2. The single diode (a) and the two diodes (b) electrical equivalent circuit of PV cell.

The single-diode equivalent circuit of PV cell is shown in Fig 2a. [23]. Here,  $I_{ph}$  and  $I_d$  are photocurrent generated by solar radiation and the current of diode, respectively.  $R_p$  is the parallel resistance,  $I_p$  is the current of parallel resistance,  $R_s$  is the series resistance,  $I_{pv}$  is the current of PV module and  $V$  is the PV module voltage.

The basic equations of PV cell can be derived from semiconductor theory and electrical circuits analysis methods as it given below [24]:

$$I_{pv} = I_{ph} - I_D - I_p \quad (3)$$

The diode current can be written using shockley diode equation:

$$I_D = I_o \left[ e^{\frac{q(V+I_{pv}R_s)}{nkT}} - 1 \right] \quad (4)$$

Here;  $q$  is the electron charge ( $1.602 \times 10^{-19}C$ ),  $n$  is the ideality factor (1.6),  $I_o$  is the reverse saturation current of the diode,  $K$  is Boltzmann constant ( $1.38 \times 10^{-23}J/K$ ) and  $T$  is the temperature in Kelvin. If the values of  $I_p$  and  $I_D$  are written into Eq.1:

$$I_{pv} = I_{ph} - I_o \left[ e^{\frac{q(V+I_{pv}R_s)}{nkT}} - 1 \right] - \frac{(V+I_{pv}R_s)}{R_p} \quad (5)$$

The two diode equivalent circuit is consisted of a current source, two diodes are connected in parallel, the  $R_s$  and the  $R_p$  (Fig 2b). According to Kirchhoff's Law:

$$I_{pv} = I_{ph} - I_{D1} - I_{D2} - I_p \quad (6)$$

The currents of the two diodes can be derived from Eq.4 as:

$$I_{D1} = I_{o1} \left[ e^{\frac{q(V+I_sR_s)}{nkT}} - 1 \right] \quad (7)$$

$$I_{D2} = I_{o2} \left[ e^{\frac{q(V+I_sR_s)}{nkT}} - 1 \right] \quad (8)$$

The equation of PV current is obtained by substituting Eq.7 and Eq.8 into Eq.6:

$$I_{pv} = I_{ph} - I_{o1} \left[ e^{\frac{q(V+I_{pv}R_s)}{nkT}} - 1 \right] - I_{o2} \left[ e^{\frac{q(V+I_{pv}R_s)}{nkT}} - 1 \right] - \frac{(V+I_{pv}R_s)}{R_p} \quad (9)$$

The  $I_{pv}$  can be calculated from the above equation.

### 3. Electrical Characteristics of PV Module

PV module is constructed by connecting PV cells in series to obtain an adequate output voltage. While PV systems are commonly operated as multiples of 12 volts, PV module is typically designed for optimal operation conditions in these systems. The main target of this design is connecting of appropriate number of PV cells in series to sustain the voltage of the module ( $V_m$ ) within a comfortable range of the battery system voltage under conditions of average irradiance. Consequently, the output power of the module can be maintained close to the maximum.  $V_m$  is normally about 80% of the open circuit voltage of the module  $V_{oc}$ . Silicon single cell open-circuit voltages is typically in the range of 0.5– 0.6 volts, with a generating capacity of 2~3 watts per individual cell. PV module is made up of a parallel-series configuration of PV cells as it is shown in Fig. 3. Here, Fig. 3a and b illustrate the symbol and the equivalent circuit of PV module, respectively.

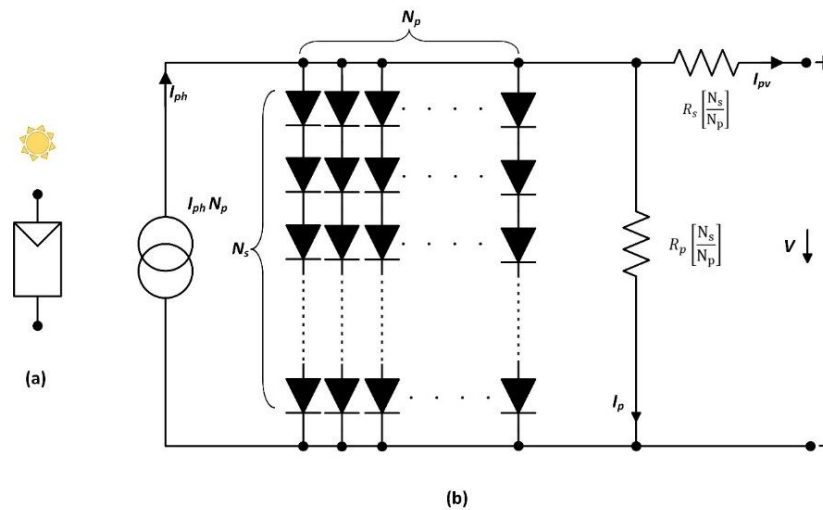


Figure 3. Symbol (a) and the equivalent electrical circuit (b) of PV module.

The PV module can be modelled mathematically as given in the next equations. PV module photo-current is [25]:

$$I_{ph} = [I_{sc} + K_i(T - 298)] \frac{G}{1000} \quad (10)$$

PV module reverse saturation current,  $I_{rs}$  and saturation current,  $I_o$  are given as:

$$I_{rs} = I_{sc} / \left[ e^{\left( \frac{qV_{oc}}{N_s nkT} \right)} - 1 \right] \quad (11)$$

$$I_o = I_{rs} \left[ \frac{T}{T_r} \right]^3 e^{\left( \frac{qE_{g0}}{nk} \left( \frac{1}{T} - \frac{1}{T_r} \right) \right)} \quad (12)$$

The output current of PV module is:

$$I_{pv} = N_p I_{ph} - N_p I_o \left[ e^{\left( \frac{q(V + I_{pv} R_s)}{N_s nkT} \right)} - 1 \right] - \frac{(V + I_{pv} R_s)}{R_p} \quad (13)$$

Here,  $N_s$  is the number of PV cells connected in series;  $N_p$  is the number of the parallel connections of cells;  $I_{ph} N_p$  is the summation of the  $I_{ph}$  produced in each PV cell.  $R_s$  and  $R_p$  are the equivalent series and parallel resistances of the array, respectively.  $I_{sc}$  is short circuit current supplied by PV module under short-circuits condition.  $K_i$  is the short-circuit current coefficient of cell which equals to 0.0017A at STC.  $T$  is the operating temperature (K) for PV module.  $G$  is the solar radiation ( $W/m^2$ ).  $V_{oc}$  is open circuit voltage (V) which means lack of current;  $n$  is the ideality factor of the diode which equals to 1.6.  $T_r$  is the nominal temperature (298.15 K).  $E_{g0}$  is the band gap energy of the semiconductor (1.12 eV).

#### 4. Grid-Connected PV System Sizing

According to the amount of energy to be produced or needed; on-line PV systems are based on the principle of consuming or transferring the generated energy to the network rather than storage in the batteries. The location selection criteria of the solar power plants directly affects the processes from the installation stage to the operation phase and the electricity production costs. Site selection is determined according to efficiency, legal regulations and environmental impact assessment criteria.

#### 4.1. Geographical coordinates

Project's name is KRMN-SNAPS 1.6 MW PV power plant is investigated. It is located within the boundaries of Çumra, which is a town and district of Konya Province in the Central Anatolia region of Turkey, at a longitude of 32.83°E, latitude of 37.55°N and at an altitude of 1012m. The project site is approximately 1.8 km from Okçu neighbourhood and 5.5 km from Çumra center.

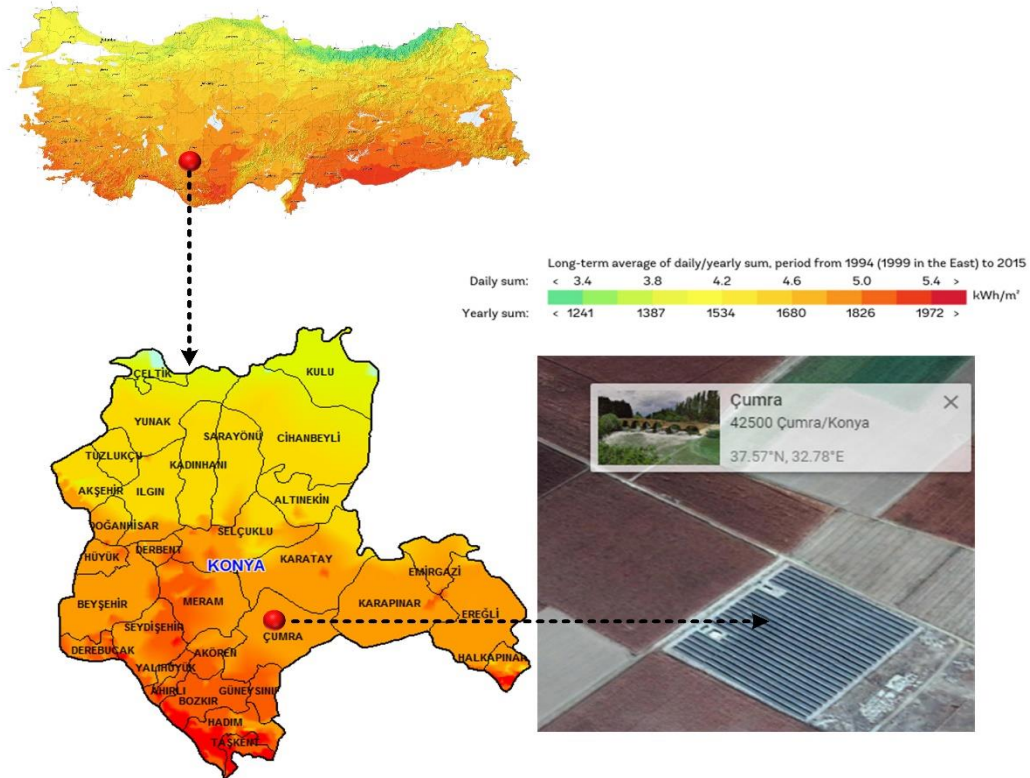


Figure 4. Long-term average of daily/yearly sum. period from 1994 to 2015 of Geographical map at a longitude 32.83°E of, latitude 37.55°N and at an altitude of 1012m.

#### 4.2. Solar radiation in the project site

The annual average of sunshine duration in Turkey is 2640 hours. In this case, the daily average of sunshine hours is 7.2h. Furthermore, the country has an annual average of radiation intensity of 1311 kWh/m<sup>2</sup>, which equals 3.6 kWh/m<sup>2</sup> per day.

The total annual sunshine duration of KRMN-SNAPS 1.6MW in Çumra is 2985.64 hours. At the same time, the daily average of sunshine hours is 8.18 h. Moreover, the project site has an annual average radiation intensity of 1646.55 kWh / m<sup>2</sup>, which equals 4.51 kWh/m<sup>2</sup> per day. The total sunshine-hours and the total radiation intensity are 13.5% and 25.5% of Turkey, respectively. Global solar irradiation per m<sup>2</sup>-day and average sunshine-hours of project location during the year are shown in Fig. 5.

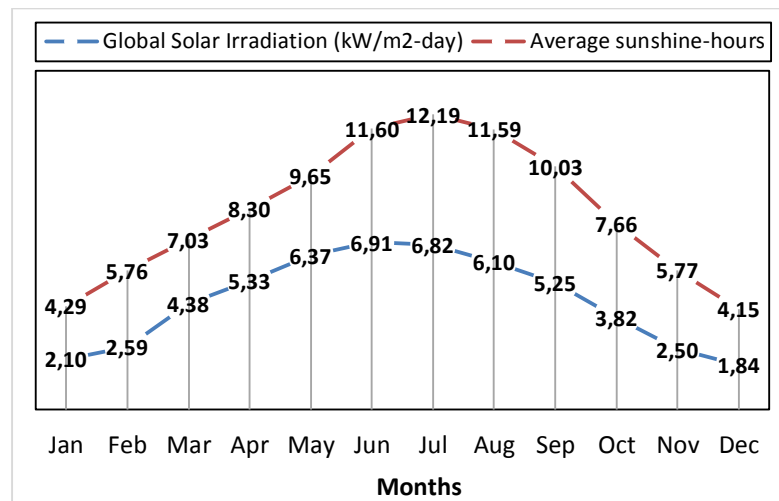


Figure 5. Global solar irradiation per m<sup>2</sup>-day and average sunshine-hours during the year in Çumra/Turkey.

Photovoltaic Geographical Information System (PVGIS) is an online free solar radiation database of the selected location in Europe, Africa, America and Asia for stand-alone or grid-connected systems or plants. Furthermore, the solar radiations data as MONTHLY, DAILY and HOURLY DATA can be supplied. Therefore, for this location, PVGIS Estimates of long-term monthly averages irradiation are given in Table 1.

Table 1. Monthly Solar Irradiation: PVGIS Estimates of long-term monthly averages for KRMN-SNAPS 1.6MW at a longitude 32.83°E of, latitude 37.55°N and at an altitude of 1012m [29].

Month	$H_h$	$H_{opt}$	$H(90)$	$I_{opt}$	$T_{24h}$	$N_{DD}$
Jan	2080	3160	3110	60	2.8	496
Feb	3020	4130	3610	52	3.9	393
Mar	4580	5470	3900	39	7.4	303
Apr	5460	5800	3170	24	12.0	138
May	6730	6500	2650	10	17.1	24
Jun	7880	7250	2320	4	21.2	3
Jul	8110	7650	2520	8	25.2	2
Aug	7410	7680	3430	20	24.9	6
Sep	5940	7060	4500	36	21.0	41
Oct	4070	5520	4590	50	13.9	195
Nov	2760	4300	4240	60	8.3	352
Dec	1910	2990	3060	62	3.6	447
Year	5010	5630	3420	31	13.4	2400

$H_h$  : Irradiation on horizontal plane (Wh/m<sup>2</sup>/day)

$H(90)$ : Irradiation on plane at angle: 90deg. (Wh/m<sup>2</sup>/day)

$H_{opt}$  : Irradiation on optimally inclined plane (Wh/m<sup>2</sup>/day)

$I_{opt}$  : Optimal inclination (deg.)

$T_{24h}$  : 24 hour average of temperature (°C)

$N_{DD}$  : Number of heating degree-days (-)

### 4.3. PV Power plant

Some incentives are regulated to increase the RESs capacity in Turkey. KRMN-SNAPS 1.6 MW project aims to generate energy in the facility located within the boundaries of Çumra. The project was established on approximately 21924 m<sup>2</sup>. This project has a total power of 1791.04 kWp / 1600 kW. Since solar panels with mono crystal technology are more suitable for the location, a total number of 6180, Solar-world brand 290W mono crystal solar panels, were used.

#### 4.4. Utility grid

PV arrays are connected directly to the utility grid via special equipment to modulate the output of the inverter to be similar to the grid parameters. The power produced from these systems is effectively utilized, as there are no costs due to no energy storage system included. In this way, Energy is directly supplied to feed the electrical network via PV power plants. However, in standalone systems, energy must be instantly consumed through connecting electrical loads or has to be stored in batteries.

#### 4.5. The Characteristic of PV module

Experimentally, the PV module is the most important component of the system for its long service life and reliability. Most of the manufacturers give a twenty to twenty-five years guarantee for each modules [19]. The PV modules used in KRMN-SNAPS 1.6 MW PV power plant are of 290Wp rating, made up of monocrystalline. They have an efficiency of 17.03% under STC and fixed characteristic. It is produced with its linear performance warranty covering a period of 25 years. The values of  $V_{oc}$  and  $I_{sc}$  are 39.9V and 9.97A under STC, respectively. Voltage and current values at maximum power point are 31.4V and 9.33A, respectively. In addition, maximum system voltage and reverse current are 1000V and 25A, respectively, while operating range of PV module is from  $-40^{\circ}\text{C}$  to  $85^{\circ}\text{C}$ . The solar panels installed in such a way are structure to structure and leg centre-to-centre distance is at 4 m. The distance between modules (Panel to panel) and grounds to lower edge of the module are 25 mm and 400 mm, respectively. To have a better yield, the modules are cleaned twice in a month.

#### 4.6. Power conditioning unit/grid tie inverter

Inverters convert the electricity produced in solar panels from DC to AC used by network. In the KRMN-SNAPS 1.6MW GES project, 72 ABB brand inverters were used. The values of rated DC input power and rated DC input voltage are 28600W and 750V, respectively. The output of the inverter is synchronized automatically with same voltage and frequency as that of grid.

#### 4.7. Power Evacuation

The transformer used to transfer the generated energy to the grid has a rated power of 1600kVA. The voltage equals to 380 V at primary side of the transformer and 33kV at secondary side that directly connected to grid. The transformer has an efficiency of about 98,83%.

#### 4.8. The layout of the solar power plant

KRMN-SNAPS 1.6 MW PV power plant project aims to generate energy in the facility located within the boundaries of Okçu neighbourhood. The entire capacity of the plant is 1.6 MW that built over approximately 21924 square meters of land. The area of this project contained of two block. Each one block is producing a maximum power of about 800 kW, so a summation of 72 circuits are needed to generate a peak of 1.6 MW power. The total number of PV modules is 6180. A total number of 20 PV modules are connected in series to form one string and a total 72 strings combined to one inverter, 51 of which consist of 4 parallel panels and 21 of which 5 parallel panels. Converted AC power feeds the 380V/33kV transformer. The secondary side of the transformer as it mentioned before is directly plugged to the 33 kV high voltage network. The PV power plant is designed in such a way that it has less cost, high reliability, and generating as much energy as possible. During nights, when the solar

irradiance needed to generate energy is not available, the energy required for operating internal equipment of the solar plant such as lighting, initial starting of the batteries and control room appliances can be supplied from the power of grid.

#### **4.9. Tilt angle**

The maximum solar irradiance facing on PV array can be obtained by adjusting a suitable slope that is related to the latitude of its location and it known as the tilt angle [26]. The PV power plant implements latest technology for tracking the appropriate angle of solar modules. In addition, a technology that can be controlled manually to adjust the seasonal tilt of PV array is used to absorb as much irradiance as possible and generating maximum power. In order to obtain more power output by absorbing more solar radiation, the tilt angle of the PV array should be adjusted manually regarding to the different seasons of the year. In order to produce the highest energy depending on the season, the tilt angle can be set to  $47.82^\circ$  in winter and  $17.82^\circ$  in summer [29]. However, due to the high labour cost, the tilt angle is set to  $25^\circ$ , which is the optimum value for all the year.

#### **4.10. Simulation using PVSYST**

The selection of location and system equipment and the modeling of the optional system is very important for the on-grid or off-grid PV power plant to be installed. The PVSYST package program is used for this purpose. 3D simulation of the planned PV power plant can be performed, the performance of the system is obtained, and the shadows falling on the PV modules in the sunrise and sunset can be analysed in real time.

Thus, the performance of the power plant can be evaluated before installation. In this context, the PVSYST analysis was performed for the installed PV system, and the project was conducted jointly for two projects with an analysis power of 800 kWe. Analysis revealed that the total annual power generation is 3027 MWh. This value is the total electricity production value of the two projects. One of the program outcomes of the simulation results is Fig. 6.

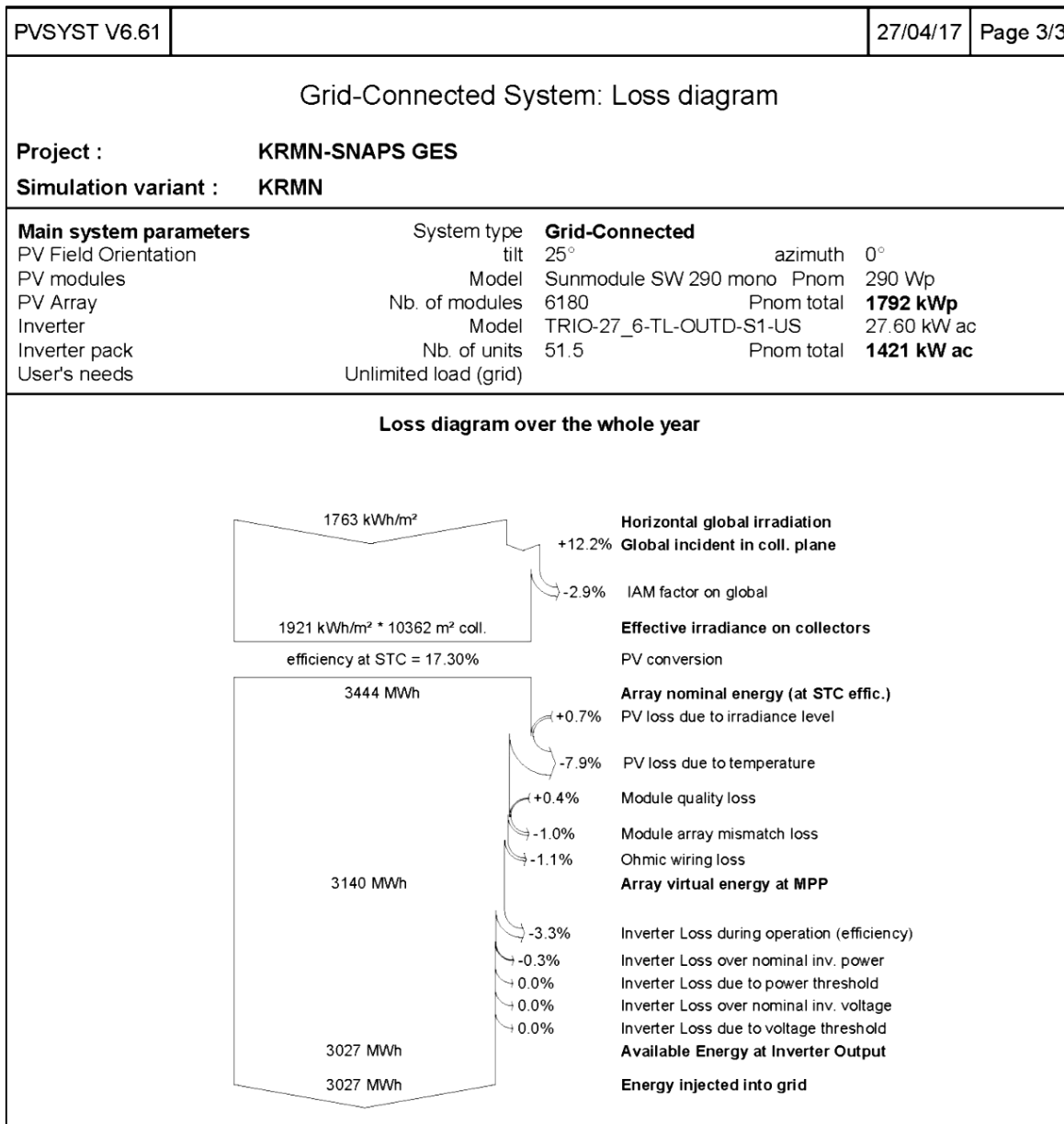


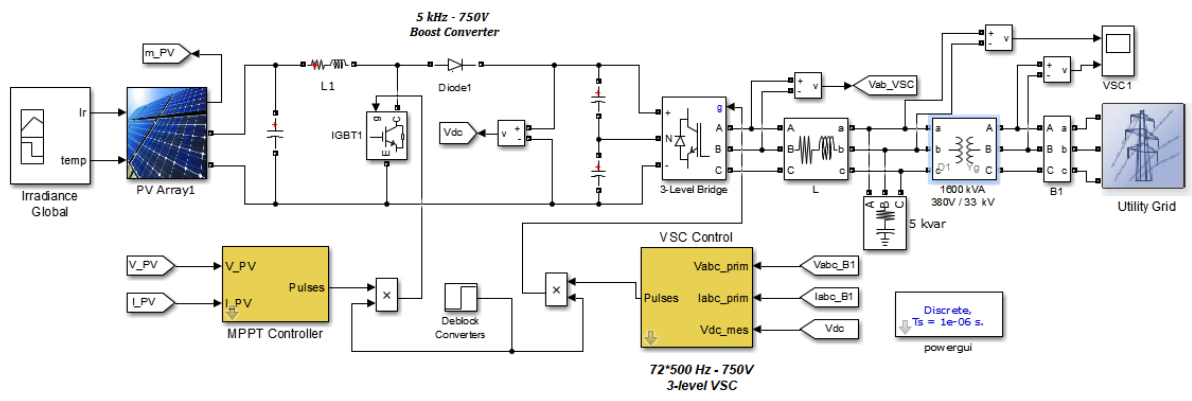
Figure 6. Grid-connected system: Loss diagram for the KRMN-SNAPS 1.6 MW PV power plant.

### 5. Modelling and simulation of the solar power plant

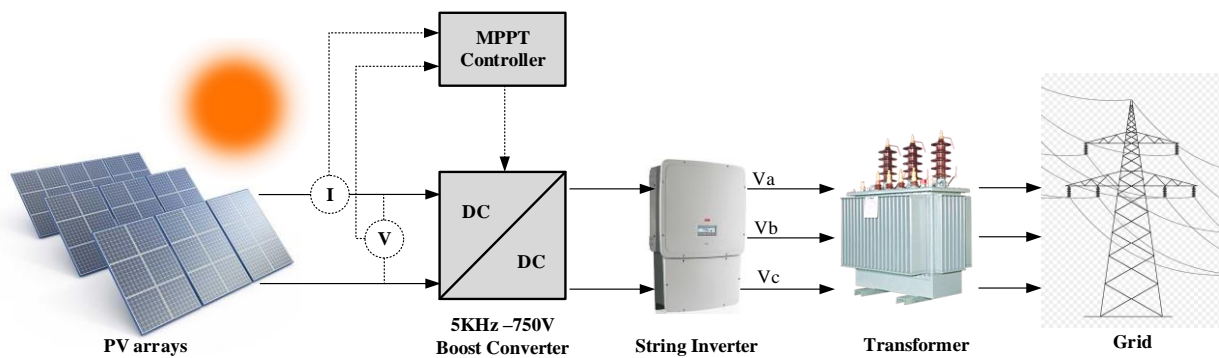
In the study, a 1600-kW PV array connected to a 33 kV grid via a DC-DC boost converter and a three-phase three-level Voltage Source Converter (VSC) is simulated in MATLAB/Simulink. The screen image of the Matlab/Simulink and schematic diagram for the modeled power plant are given in Fig. 7.

Incremental Conductance and Integral Regulator techniques are implemented in the boost converter as Maximum Power Point Tracking (MPPT) [27]. 5-kHz DC-DC boost converter is used to increase the voltage from PV system output voltage to 750 V DC. The MPPT system automatically varies the duty cycle to generate the optimum voltage and to produce maximum power.

The VSC converts the 750 V DC link voltage to 380 V AC and maintains unity power factor. A 5 kVar capacitor bank is used to filter harmonics produced by VSC. 1600-kVA 380V/33kV three-phase coupling transformer is utilized for connecting the PV system to the grid. As a utility grid 33 kV, 8 km distribution feeder is used.



(a)



(b)

Figure 7. The modeled power plant: (a) The screen image of the Matlab/Simulink, (b) the schematic diagram.

Located in the sunbelt Turkey, although it differs geographically, it is known that there is no big difference in solar radiation values. In the study, Çumra/Konya region is selected, which is eligible in terms of sunshine duration and solar radiation values. Average daily solar radiation values per month required for analysing the performance of the PV power plant are obtained from PVGIS. One-day global irradiance distribution for one month of each season is shown in Fig. 8 for the sampling of global irradiance ( $W/m^2$  per day) data.

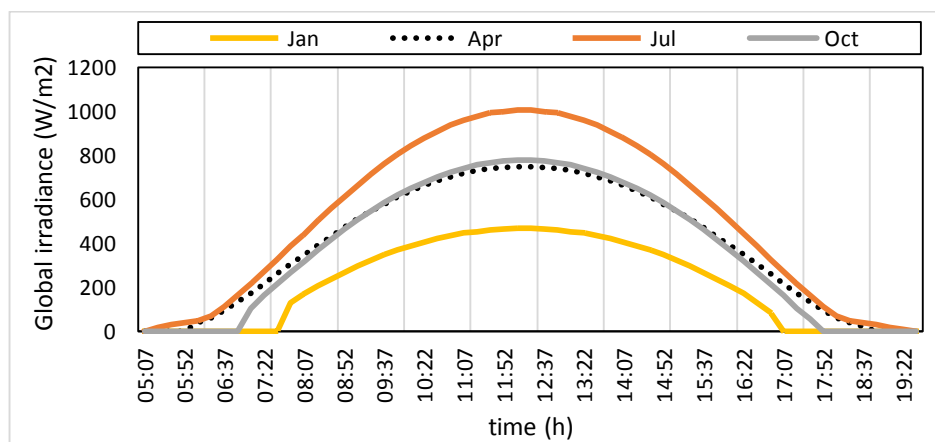


Figure 8. A daily global irradiance ( $W/m^2$  per day) distribution of the location of the PV.

The power produced by the PV power plant is influenced not only by the global irradiance  $G_{cell}^{eq}$  ( $W/m^2$ ), but by many environmental factors such as the temperature of the PV module  $T$  ( $^{\circ}C$ ), ambient temperature  $T_a$  ( $^{\circ}C$ ), wind speed  $V_{wind}$  ( $m/s$ ) and direction, and relative humidity. Besides, the global irradiance and temperature on individual solar cells are not the same as in the case of partial shading. [28]. A simplified model is used to estimate the temperature of solar cell.

$$T = 0.943T_a + 0.028G_{cell}^{eq} - 1.528v_{wind} + 4.3, \quad (14)$$

Although this model was originally developed to estimate the temperature of the PV module, it can also be used to estimate cell temperature under partial shading conditions [28]. Environmental factors that directly affect the power produced by the PV module are obtained from Turkish State Meteorological Service and the average daytime temperature of the PV module is calculated for each month. The global irradiance  $G_{cell}^{eq}$  ( $W/m^2$ ), ambient temperature  $T_a$  ( $^{\circ}C$ ), wind speed  $V_{wind}$  ( $m/s$ ) and the calculated average temperature of the PV module  $T$  ( $^{\circ}C$ ) are given in Table 2.

**Table 2. The calculated average daytime temperature of the PV module on KRMN-SNAPS 1.6MW at a longitude 32.83 $^{\circ}$ E, a latitude 37.55 $^{\circ}$ N and at an altitude of 1012m.**

	$T_a$	$G_{cell}^{eq}$	$v_{wind}$	$T$
<b>Jan</b>	4,9	326,1	3,4	12,8
<b>Feb</b>	6,8	385,6	3,1	16,9
<b>Mar</b>	10,8	438,4	3,5	21,4
<b>Apr</b>	16,0	436,9	3,8	25,9
<b>May</b>	21,4	443,4	3,2	32,0
<b>Jun</b>	25,6	481,5	3,5	36,6
<b>Jul</b>	30,0	518,4	4,7	39,9
<b>Aug</b>	29,5	566,3	4,5	41,1
<b>Sep</b>	25,3	565,4	3,9	37,9
<b>Oct</b>	17,2	497,9	2,9	30,1
<b>Nov</b>	11,2	430,3	2,8	22,5
<b>Dec</b>	5,9	310,2	3,2	13,7

The grid power and the grid current curves obtained from the simulation for a day of July are shown in Fig. 9. In the simulation, a one second scale was used instead of an hour as the time axis. These simulations were repeated for hourly global irradiance values shown for four months in Fig. 9 for all months of the year.

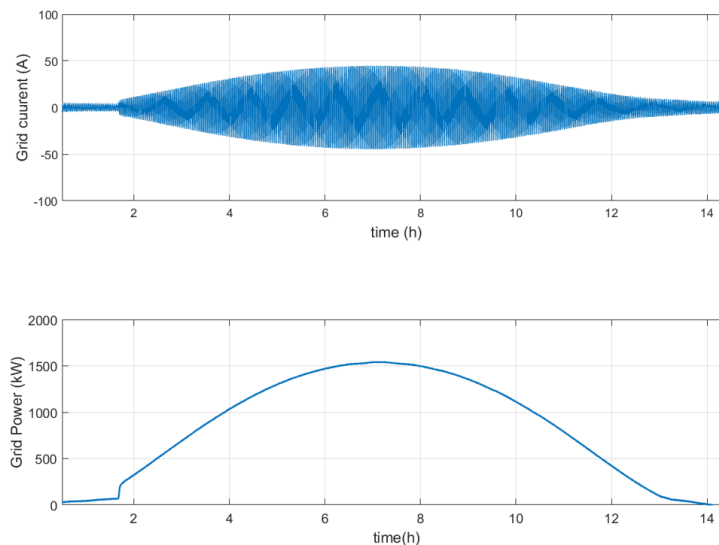


**Figure 9. The grid power and grid current curves of the PV power plant obtained from model.**

The power generation values of the power plant were obtained using monthly total global irradiance data obtained from the power curves. Monthly energy generation data obtained from the simulation and monthly generation data of the power plant in 2018 are given in Table 3. While the actual total energy production of the power plant was 3,122,015.50 KWh, it was obtained from the PVYST and our simulation as 3,027,000.00 KWh and 3,008,281.40 KWh, respectively. The same production data are also shown in Fig. 10.

**Table 3. The actual and estimated monthly energy generation.**

<i>Month</i>	<i>Actual (KWh)</i>	<i>Estimated (KWh)</i>	<i>Error (KWh)</i>
<b>Jan</b>	133,864.6	143,451.6	-9587.0
<b>Feb</b>	202,639.2	179,107.5	23531.7
<b>Mar</b>	256,521.3	233,724.8	22796.5
<b>Apr</b>	314,250.0	280,145.8	34104.2
<b>May</b>	303,687.5	289,438.9	14248.6
<b>Jun</b>	327,629.9	327,663.0	-33.1
<b>Jul</b>	345,619.6	332,743.2	12876.4
<b>Aug</b>	350,145.1	355,974.6	-5829.5
<b>Sep</b>	293,946.2	282,858.7	11087.5
<b>Oct</b>	255,618.1	267,434.4	-11816.3
<b>Nov</b>	178,000.0	181,756.0	-3756.0
<b>Dec</b>	160,094.0	133,982.9	26111.1
<b>Total</b>	<b>3,122,015.50</b>	<b>3,008,281.40</b>	<b>113.734,10</b>

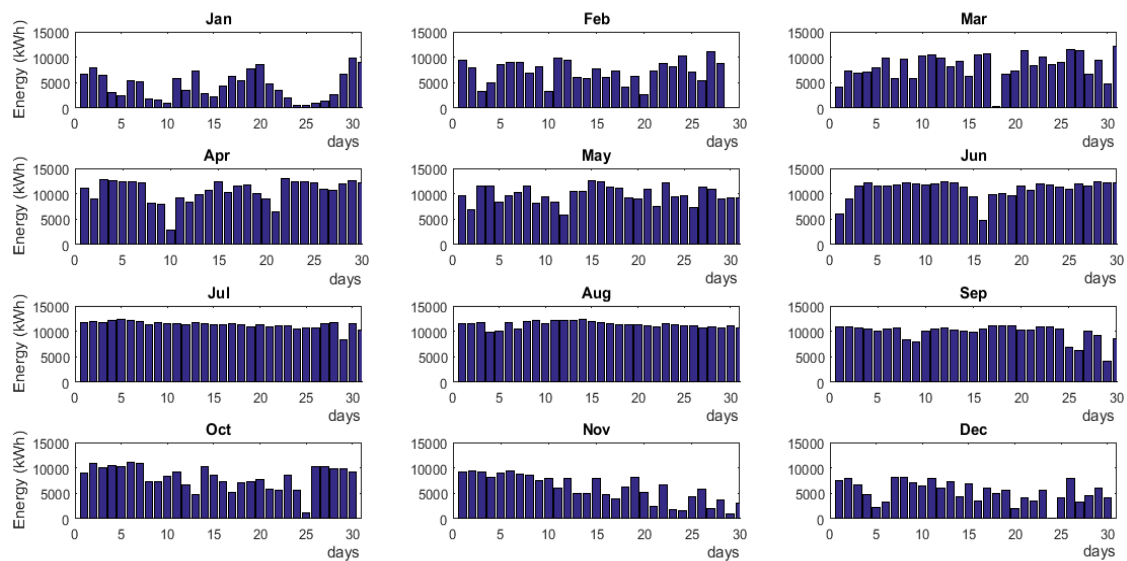


**Figure 10. Actual daily energy production of the power plant by months in 2018.**

As can be seen, there is no big difference between actual values and simulation values. The energy production of a PV power plant varies depending on many meteorological factors except irradiance. These factors are not the same for all the years. Fig. 10 shows the actual variation in the daily energy production of the power plant by months. There are no major changes in the continental climate in the summer months. However, in the spring, the autumn and especially the winter months, there may be changes in the climate for the different years. Besides, as can be seen in Fig. 11a, in the months of summer, the estimation values were closer to the actual values, but in the months of the other seasons, the error was greater. Considering the meteorological differences that may occur over the years, it is thought that the power plant average production value of many years will overlap with the estimation values.

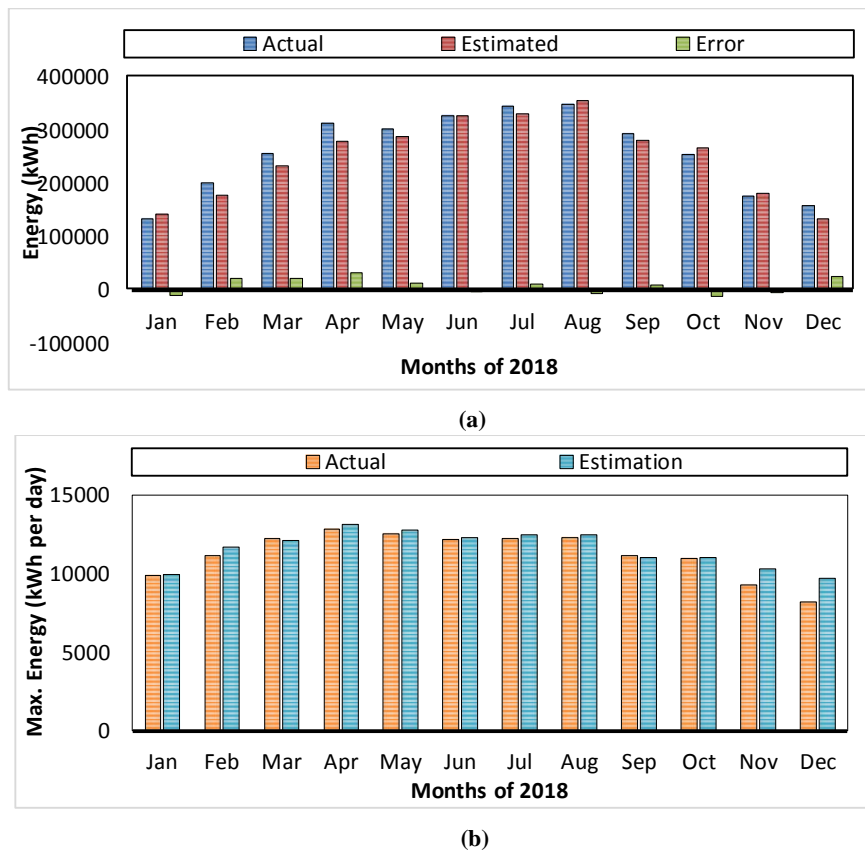


Figure 11. The actual and estimation energy production values of the PV power plant according to months.

The power plant's daily production data for 2018 are available. In the simulation, daily production estimates for each month were also obtained by using the values of global clear-sky irradiance on a fixed plane,  $G_c$  ( $W/m^2$ ). These values are compared with the maximum energy produced by the power plant for each month per day. The actual and estimated values of these data are given in the Fig. 11b. Since the values predicted by the simulation represent the maximum energy that can be generated, the estimation values in all months were higher than the actual values. However, in the warmer months when the meteorological changes were less in years, the values were closer to each other.

## 6. Conclusion

The performance of a PV power plant primarily depends on weather conditions. However, when the long-term data are used, actual production performance of the power plant over the years can be achieved. In the study, 1.6 MW PV power plant installed in Konya Province in the Central Anatolia region of Turkey was evaluated through production performance. The PV power plant is modelled on the bases of parameters that significantly affect performance, such as temperature, radiation, wind, and sunshine duration. The monthly energy production data of the power plant were compared with the actual values. While the actual total energy production of the power plant in 2018 was 3,122,015.50 KWh, it was obtained from the PVYST and the resulted simulation as 3,027,000.00 KWh and 3,008,281.40 KWh, respectively. Compared to monthly values, it is observed that especially in the warmest months when climatic changes are low, the estimation values overlap with actual values. The maximum energy that the power plant can produce in a day for each month were also estimated by using clear sky radiation values. The performance and production values of the power plant can be estimated over the years by modelling the PV power plant.

## Acknowledge

The authors would like to thank KRMN-SNAPS Solar Energy Company for its supports and contributions during this study.

## References

- [1] Erdal, G., Erdal H. and Esengün K. (2008). The causality between energy consumption and economic growth in Turkey. *Energy Policy*, 36(10), 3838-3842.
- [2] Neetu and Surender (2017). A Review Paper on Residential Grid Connected Solar Photovoltaic System Using Matlab Simulink. *International Journal of Advance Research, Ideas and Innovations in Technology*, 3(5), 92-96.
- [3] Koç, E., Şenel, M.C. (2013). Dünyada ve Türkiye’de Enerji Durumu -The State of Energy in World and Turkey - General Evaluation. *Mühendis ve Makina*, 54(639), 32-44.
- [4] Ministry of Energy and Natural Resources (MENR) (2017). Electricity generation-distribution statistics according to types of energy resources, Republic of Turkey: Prime Ministry, Ankara, 2017.
- [5] Marchal, V., Dellink, van Vuuren, D., Clapp, C., Château, J., Lanzi, E., Magné, B. van Jasper, V. OECD ENVIRONMENTAL OUTLOOK TO 2050, OECD, 2011.
- [6] IEA, CO<sub>2</sub> Emissions from Fuel Combustion, IEA, 2017, INTERNATIONAL ENERGY AGENCY, 2017. Available: <https://www.iea.org/publications/freepublications/publication/CO2-emissions-from-fuel-combustion---2017-edition---overview.html>. [Accessed 24 1 2017].
- [7] Nguyen K.Q. (2007). Alternatives to grid extension for rural electrification: Decentralized renewable energy technologies in Vietnam. *Energy Policy*, 35(4), 2579–2589.
- [8] Özçelik, M . (2017). A Micro Hybrid Wind-Pv Based on Grid Energy System With Enhanced Efficiency. *European Journal of Technique (EJT)*, 7 (2), 109-118.
- [9] Kabalci, Y., Kabalci E. (2017). Modeling and analysis of a smart grid monitoring system for renewable energy sources. *Solar Energy*, 153, 262-275.
- [10] Kozlova, M., Collan, M. (2016). Modeling the effects of the new Russian capacity mechanism on renewable energy investments, *Energy Policy*, 95, 350-360.
- [11] Akpınar, E . (2018). Statistical analysis of wind speed distribution based on weibull and rayleigh methods of iskenderun-turkey. *European Journal of Technique (EJT)*, 8 (1), 17-34.
- [12] Oguz, E , Çimen, H , Oğuz, Y . (2017). Simulation and Power Flow Control Using Switching’s Method of Isolated Wind-Solar Hybrid Power Generation System with Battery Storage. *Balkan Journal of Electrical and Computer Engineering*, 5 (2), 40-49.
- [13] Rathore, N. Panwar, N. Renewable energy sources for sustainable development. New Delhi: New India Publishing Agency, 2007.
- [14] Hosenuzzaman, M., Rahim, N., Selvaraj, J., Hasanuzzaman, M., Malek, A., Nahar, A. (2015). Global prospects, progress, policies, and environmental impact of solar photovoltaic power generation. *Renewable and Sustainable Energy Reviews*, 41, 284-297.

- [15] Solangi, K., Islam, M., Saidur, R., Rahim, N., Fayaz, H. (2011). A review on global solar energy policy. *Ren Sustain Energy Rev*, 15(4), 2149–2163.
- [16] Ahmed F., Al Amin, A., Hasanuzzaman, M. Saidur, R. (2013). Alternative energy resources in Bangladesh and future prospect. *Renew Sustain Energy Rev*, 25, 698–707.
- [17] Selvara, J. Rahim, N.A. (2009). Multilevel Inverter For Grid-Connected PV System Employing Digital PI Controller. *IEEE Transactions On Industrial Electronics*, 56(1), 149-158.
- [18] Kaya, D. (2006). Renewable energy policies in Turkey. *Renewable and Sustainable Energy Reviews*, 10, 152–163.
- [19] Goetzberger, A. Hoffmann, V. Photovoltaic Solar Energy Generation, Germany: Springer-Verlag Berlin Heidelberg, 2005.
- [20] Sudeepika, P., Gayaz Khan, G. (2014). Analysis Of Mathematical Model Of PV Cell Module in Matlab/Simulink Environment. *International Journal of Advanced Research in Electrical, Electronics and Instrumentation Engineering*, 3(3), 7823-7829.
- [21] Luque, A. Hegedus, S. Handbook of Photovoltaic Science and Engineering, England: John Wiley & Sons Ltd, 2003.
- [22] Sonnenenergie D. G. F. Planning and Installing Photovoltaic Systems: A guide for installers, architects and engineers, Berlin: Earthscan, 2008.
- [23] Tsai, H.-L., Tu, C.-S., Su Y.-J. (2008). Development of Generalized Photovoltaic Model Using MATLAB/SIMULINK, in Proceedings of the World Congress on Engineering and Computer Science WCECS, San Francisco, USA.
- [24] Villalva, M., Gazoli, J., Filho, E. (2009). Comprehensive approach to modeling and simulation of photovoltaic arrays. *IEEE Trans Power Electron*, 24, 1198–1208.
- [25] Reddy, N.A., Raju, K.D. (2017). Mathematical Modeling of Soft Switched Single Stage Multistring Inverter with Multi-Rated ETT Photovoltaic Modules. *Inter. J. Advance Research, Ideas and Inovations in Tech.*, 3(1), 489-499.
- [26] Labeled, S., Lorenzo, E. (2004). The impact of solar radiation variability and data discrepancies on the design of PV systems. *Renewable Energy*, 29(7), 1007-1022.
- [27] de Brito, M., Sampaio, L., Jr., L., e Melo, G., Canesin, C. (2011). Comparative Analysis of MPPT Techniques for PV Applications, in *IEEE, 2011 International Conference on Clean Electrical Power (ICCEP)*, Ischia, Italy.
- [28] Gao, Y., Dong, J., Isabella, O., Santbergen, R., Tan, H., Zeman, M., Guoqi, Z. (2019). Modeling and analyses of energy performances of photovoltaic greenhouses with sun-tracking functionality, *Applied Energy*, 233–234, 424–442.
- [29] PVGIS. Photovoltaic Geographical Information System - Interactive Maps. European Commission, Joint Research Centre, Institute for Environment and Sustainability Renewable Energies Unit, [Online]. Available: <http://re.jrc.ec.europa.eu/pvgis/apps4/pvest.php>. [Accessed 12 March 2019].

## ENVIRONMENTAL NOISE TRACKING SYSTEM BASED ON WEB OF THINGS

Müsemma ALTINDAŞ<sup>1</sup>, Levent GÖKREM<sup>2\*</sup>

*Environmental noise is a collection of unwanted, disturbing or health-threatening sounds. As in the whole world, noise pollution is one of the common types of pollution that affect public health and comfort in different forms in our country. The level of noise in an environment affects human health negatively in terms of physical, psychological, physiological and performance. In this system, based on the environment we work on, web objects based environmental noise monitoring system is aimed to be made. In this study, an environmental noise monitoring network has been established which enables monitoring of indoor areas throughout the day by using sound sensor so that this system can be accessed from any environment where internet is available. As a result, remote environmental noise monitoring is provided in real time. In this study, the objective of the noise monitoring network as a sub-based web object is a project which is intended to control the problems arising from the public health, labor force, industrialization and the development of modern life. As a result of the researches and observations, it is recommended to present them to the field in order to provide awareness and sensitivity to environmental noise pollution. The measuring accuracy of the system was tested with the HT-80A noise meter.*

Key words: Noise, Internet of Things, Web of Things, Tracking System

### 1. Introduction

Noise has been recognized as an environmental problem arising from industrialization and the development of modern life, negatively affecting people's hearing and perception, which can disrupt psychological, physical and physiological balance and reduce their ability to work. Noise measurement is done with the sonometer, it is a stringed instrument that measures the intensity of sound. The sonometer gives the intensity of the sound in a decibel type. The decibel (dB) is the unit of sound intensity and is a logarithmic unit used to measure the volume and express the ratio of the physical two values. The decibel value varies logarithmically according to sound intensity. The decibel is associated with the 10-based logarithm. "1" bel is "10" decibels. 20 dB is "10" times more severe than 10dB, 30dB is "100" times more severe than 10dB because of the calculation of the decibel at the base of the log10. "0" decibels is measured as the operating starting level of the human ear and 140dB as the sound produced by the jet engine (Table 1).

<sup>1</sup> Department of Mechatronics Engineering, University of Tokat Gaziosmanpaşa, Tokat, TR, (musemmaaltindas@gmail.com)  
 <https://orcid.org/0000-0001-7536-1079>

<sup>2</sup> Department of Mechatronics Engineering, University of Tokat Gaziosmanpaşa, Tokat, TR, (levent.gokrem@gop.edu.tr)  
 <https://orcid.org/0000-0003-2101-5378>

**Table1. dB Ratings and subjective evaluations of some types of noise [1]**

Noise Level (dB)	Examples	Subjective Assessment
140	Close to the Jet engine	Damaging
130	Onset of pain	
105	Powerful rock music	
100	Car klaxon sound 3m away	Sky-High
90	City street noise	
82	Factory noise	
80	School without acoustic insulation, canteen noise	High
62	Open traffic road	
62	The noise of a secondary road	Middle
50	Clerical noise	
40	Music played at a low level in the residence	Low
20	Whisper	Very Low
8	Human breathing	
0	Beginning of hearing	

The effect of noise pollution on human health also varies according to sound intensity and length of noise duration. For example, the human ear can withstand 85 dB of noise without damage for 8 hours, but this violence over 94 dB of noise, this time is reduced to 1 hour. 55-65 dB noise causing psychological disturbance, 65-90 dB noise disturbing the peace, 90 and above are described as noise causing physiological disorder [1]. A classification of the effects of noise has been made in Table 2.

**Table 2. A classification of the effects of noise**

I. Noise in Degrees 55-65 dB	Slight, Feeling bored, Anger, Concentration, Sleep disorder
II. Noise in Degrees 65-90 dB	Physiological noise, Heartbeat change, Respiratory acceleration, Decreased brain pressure
III. Noise in Degrees 90-120 dB	Physiological noise, Headache
IV. Noise in Degrees 120-140 dB	Disorder of the inner ear
V. Noise in Degrees 140 > dB	The eardrum burst

Noise is a factor affecting life. It is known that those exposed to noise above 140 dB have hearing problems and go up to the eruption of the eardrum. Therefore, noise measurements are extremely important. Purpose of noise measurements are made with the aim of assessing complaints, checking compliance with the law, determining the number of exposures, calibration accuracy, Environmental Impact Assessment (EIA) noise mapping. External factors and related factors affecting noise measurement should be considered during the measurement. The first study before noise measurement

is that a planning should be made on how often, when and for what purpose the noise should be evaluated [2]. An accurate planning will ensure that the correct noise measurement results are received. Noise measurement should be carried out in accordance with the 'Environmental Noise Assessment and Management Regulation' [3]. Measurements of the sound pressure are performed with noise measuring devices and are used for continuous monitoring of the noise level. With portable noise measuring devices, it can quickly and easily control noise intensity and perform regular measurements with these devices. But today systems face ease of remote access due to the frequent use of internet protocol therefore, remote data operation has started to be preferred. With remote access, it can be controlled with any device from anywhere with internet access and can be instantly informed of the environment measured by the scenarios created [4]. These systems are called web-based systems. Today, industrial automation systems, greenhouse automation, smart (home) automation and smart devices over the internet tracking systems have been developed. It is possible to examine and follow audit systems at cheap costs using improved software. This can be accomplished with micro-controller and communication modules at a cheap cost.

In this study, a web-based decibel tracking system was developed. With this work developed, a device with internet connection can be accessed from any place at any time via web interface. We can monitor and record the ADC (Analog to Digital Converter) values and decibel values obtained from the sensor we use in our developed noise measurement device under control by providing remote access and these application are made according to the noise values determined by the Ministry of Environment and Urbanization.

## 2. Materyal

Internet of Things (IoT) is the communication network that allows us to control the physical events in our environment and to analyze with monitoring them, which is covering with software, access services and devices [5]. IoT was first used in a presentation prepared for a company by Kevin Ashton in 1999. Nowadays, the number of systems that provide remote access and control over the internet is increasing. This is accomplished by the concept of IoT. The control systems developed with micro controller and communication modules provide the opportunity to examine and follow systems at low costs using the developed software [6].

Web-based systems are IoT-supported systems. Communication modules are used to connect the microcontroller to the internet network. With the microcontroller, it can enter the web interface like a web browser, save data and keep the resulting values under control [7-10].

In the developed web-based system, all operations are performed on the designed server hardware. In the hardware part, the sound sensor is used. Instant decibel tracking is done with sound sensor and control cards. While the decibel tracking system is made, sensor values can be monitored by connecting to the web interface programmed into the flash memory of communication module and micro controller hardware from the desired location with a device with internet connection.

Firsly the circuit to be make up the connection between the sound sensor and the microcontroller must be established and make sure that ADC values are taken from the sensor correctly. In the example circuit, Arduino as microcontroller and a Grove sound sensor as sound sensors are used. ADC values taken from the sound sensor should be converted to decibels according to the noise level of the environment. This method is described in obtaining noise data in 3. The resulting decibel values should be algorithmically programmed in accordance with the noise degrees specified in Table 2 and the data sharing should be adjusted as a result of these degrees. The resulting decibel values are connected to the

modem via the WiFi module that is connected to the microcontroller. Here the wifi module transmits the decibel values obtained by the microcontroller to the modem. As Wifi module, the Arduino-compatible ESP8266 module is used. This module transmits data to the modem to which it is connected. However, data sent to the modem will not be immediately available for sharing. One of the ports determined by the IP address of the modem is opened to the access of external connections by performing Port forwarding. So, data is transferred to the purchased web server site on the opened port and made available to clients in the web interface. The following diagram of the system and the technical features of the circuit elements and brief information about the working structures are given.

### 2.1. Microcontroller (Arduino)

Arduino is an I/O card, a versatile Developer Hardware card that includes Processing / Wiring language applications. It has one Atmel AVR microcontroller and side equipment for other circuit elements. It has a 5V regulated integrated circuit and a 16 MHz crystal oscillator. In addition, the circuit elements in the Arduino's model according to their varies. For example, the Arduino Uno card has ATmega328 microcontroller, 14 digital I/O pins, 6 PWM outputs, 6 ADC inputs and 32 KB flash memory [11].

### 2.2. Sound Sensor

The Grove sound sensor was made to detect the intensity of the surrounding noise (Fig. 1). LM2904 amplifier integration and it has a microphone. It filters the high-frequency signal from the microphone with amps, enabling Arduino's signal reception. There is also a manual potentiometer on it which provides output gain. Wide voltage range, internal signal filtering, item Min. typical Max. The unit has features such as voltage 3.5 5.0 10 VDC, operating frequency 50 - 20,000 Hz, sensitivity -48 - 66 dB, signal-to-noise ratio > 58 dB, output signal range digital signal (0-1023) [12].



Figure 1. Grove sound sensor and cable connection table

### 2.3. WiFi Module (ESP8266)

Fig. 2 shows Esp8266 Wi-fi module and cable connection. This module can both connect to wireless networks and create a wireless network access point. In this project, it should be used to connect to the wireless network as needed. It is quite economical and useful. Supports TCP / IP protocol. Technical features; 802.11 b/g/n support, Wi-Fi direct (P2P) support internal TCP/IP protocol stack,

+19,5 dBm output power (802.11 b mode) leakage current < 10uA, low power consumption with internal 32-bit processor, STUDIO 1.1/2.0, SPI and UART support STBC, 1x1 MIMO, MIMO 2x1, waking up and receiving the data packet the time of < 2ms, stand-by power consumption: < 1mW [13].

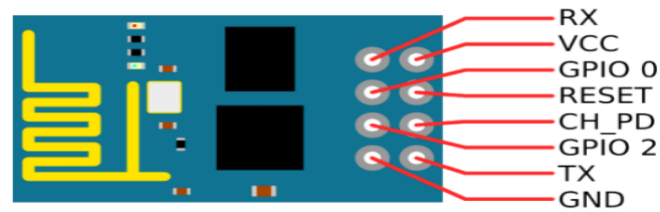


Figure 2. Esp8266 Wi-fi module and cable connection

The noise is measured by the sound sensor and transmitted to the microcontroller. The microcontroller then converts the ADC values from the sound sensor to decibels and transmits them to the modem via the Wi-fi module. The data is transferred to the web server site through the port routing process performed on the modem. This process is summarized in the following diagram (Fig. 3).

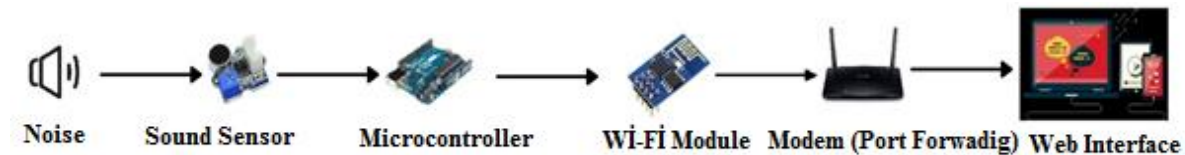


Figure 3. Circuit elements process order

### 3. Method

Noise values are measured in analog with improved software and sound sensor. ADC (Analog to digital converter) values obtained by the sound sensor must be converted to Decibel values by the formula in the logarithmic base. For this reason, the ADC values obtained with the sound sensor must be calculated using the formula with the actual decibel values and reduce the error share by keeping the error sampling number high. As a result, the decibel value corresponding to each ADC value will be created in a healthy way.

In order to move in this logic, a logarithmic function and graph are created based on the noise data and decibel values are obtained. Therefore, regression analysis is performed to create the noise function. Regression analysis is a statistical analysis used to quantify the relationship between a criterion variable and one or more prediction variables. It mainly aims to determine the property of the relationship between variables and is used to predict results using data that has a cause-and-effect relationship between them. However, the noise function is certain and due to keeping the sampling number high it is able to minimize the share of error and obtain decibel values.

$$L_F = \ln\left(\frac{F}{F_0}\right) N_p = 10 \log_{10}\left(\frac{F^2}{F_0^2}\right) dB = 20 \log_{10}\left(\frac{F}{F_0}\right) dB \quad (1)$$

$$G_{dB} = 20 \log \left( \frac{V}{V_0} \right) dB \quad (2)$$

In the Formula (1) given above,  $L_F$  represents the area decibel ratio,  $F$  represents the measured area and  $F_0$  represents the reference area. In Formula (2),  $G$  is the power gain of decibels in electrical circuits.  $V$  measured voltage,  $V_0$  is also the reference voltage. But since our  $V/V_0$  is set by the sensor and given to us as ADC output, the value is between 0-1023. These values are in the range of positive values, so our chart is as in the following image [14,16].

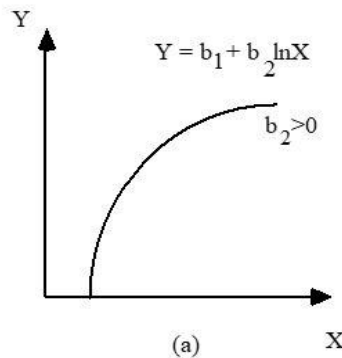


**Figure 4. Logarithmic function graph of applied regression method**

Fig. 4 shows logarithmic function graph of applied regression method. In this regression method;

$$Y = b_1 + b_2 \ln X + u \quad (3)$$

It is a model that includes dependent and independent variable in the form. Here;  $Y$  is the dependent (result) variable and is considered to have a certain error.  $X$  is independent (reason) variable and is thought to be measured without error. ' $b_1$ ' is constant and is the value where  $Y$  is equal when  $X=0$ . ' $b_2$ ' is the regression coefficient and shows the amount of change in its own unit in  $Y$  with 1 unit change in its own unit within  $X$ . ' $u$ ' is the random error value and the average is zero. The variance is thought to show normal distribution. This assumption is necessary for checks of coefficients [14-15].

An important point to be mentioned above is that the ADC value varies from 0 to 1023. That is, because 0 dB equals 0 ADC,  $b_1$  will not have any effect on the function at first. As a result of these calculations and applications, the noise function used in the micro controller software was obtained by calculating the decibel values corresponding to the sampled ADC values under the heading of regression calculation in Microsoft Office Excel.

#### 4. System Architecture

While the system designed for this study measures decibel values, an interface is needed that can obtain historical data of momentarily seen and measured values. Some basic components are required for this. These components are web interface, server and modem.

#### 4.1 Design of The Web Interface

Web design is an important factor that reveals the visual status of the interface to be designed. There are many design programs that can work in accordance with NET-based software systems. By designing the desired template, the desired logo through such programs, it can produce the objects according to their type and put them together on the index cursor. Css, image, script, theme, style files created with design programs such as index.it must be merged into a web file with an html extension. It is possible to modify the contents of the integrated index file with various pad++ extension programs. Fig. 5 shows Web interface design home page.

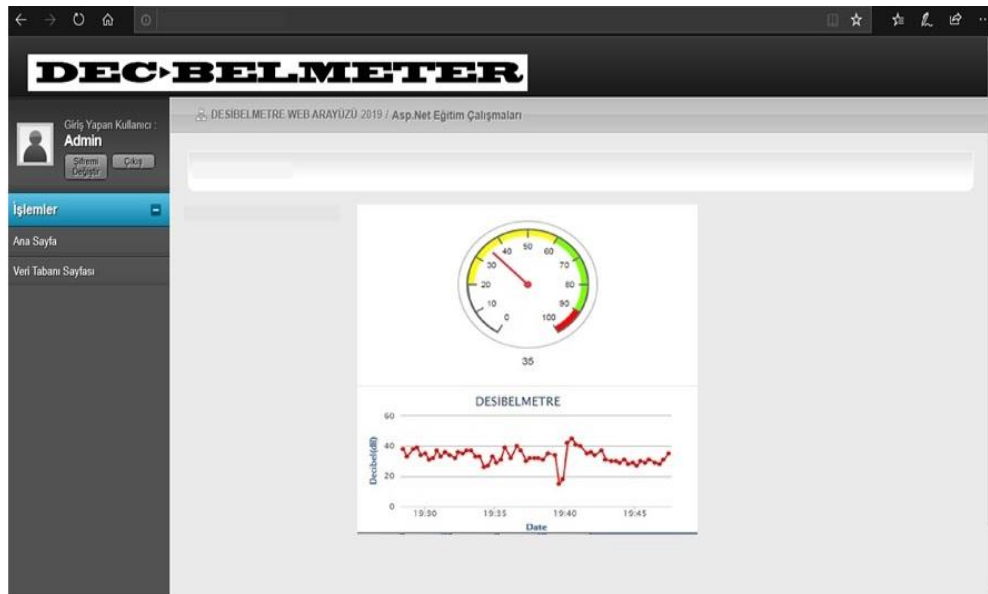


Figure 5. Web Interface Design Home Page

In short, the design of a web interface is a subject that requires separate efforts and attention. What needs to be done is to put forward a design that will address the code and purpose to be designed. Fig. 6 shows Web interface design database page.

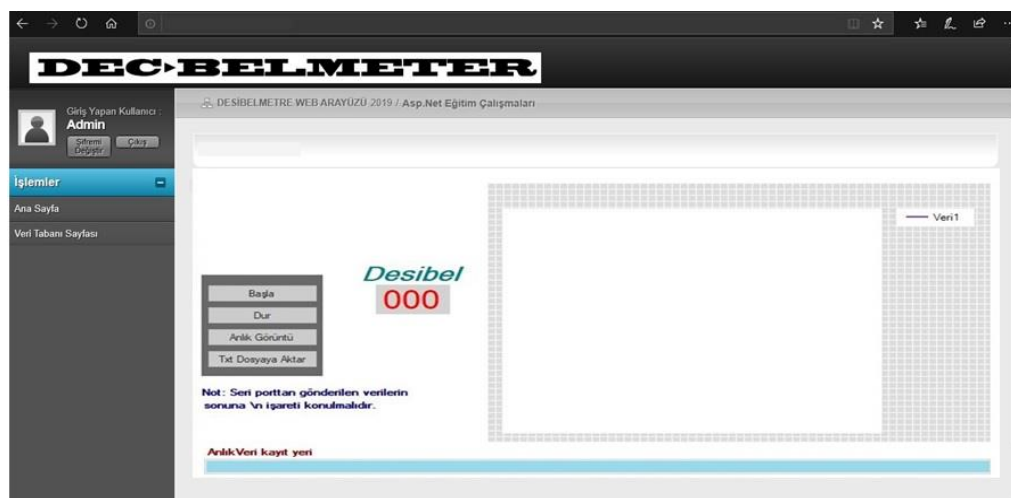


Figure 6. Web Interface Design Database Page

## 4.2 Programming the Web Interface

The interface to be designed belongs to the web base on the Visual C# platform ASP.NET it has been predicted to be made as a web application. The reason for this ASP.NET the interface is completely useful and the designer is completely independent and the design is able to be used at the highest level of visibility. In addition, depending on the operating performance of systems with a database and fast data exchange ASP.NET the interface should be preferred.

The designed interface consists of a home page and a database page. The snapshot values of the data taken from the master page and the graphical version of the data on the database page are shown as the data record table. This design should be done using the software Master Page structure on the code. The image, scripts, themes, and index files of the prepared web design should be added as items to the prepared solution. Using added design files ASP.NET software architecture is realized with. Fig. 7 shows Web interface programming.

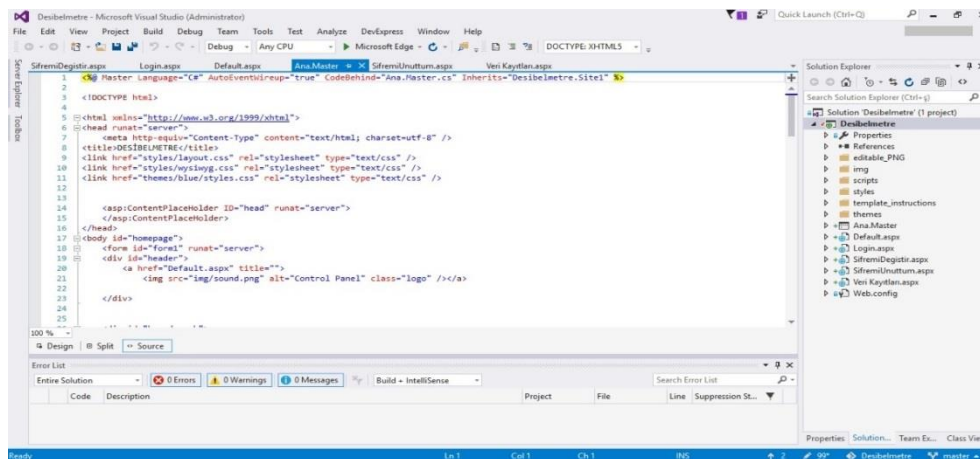


Figure 7. Web Interface Programming

The second stage of encoding is data recording. A database should be used to show which day and which time the data was taken. For this, the SQL structure must be used. This structure should be added to the web server and created as a database.

## 4.3 Opening The Web Interface to Remote Access

ASP.NET the base shows the values taken from the microcontroller in the interface, whose visibility is adjusted with the support of different design programs. However, this view only applies to the computer on which the interface is installed. In order to open the designed interface to access all clients, it is necessary to open the port specified over TCP IPS, where the computer is connected to the internet and the modem provides communication between them. The reason for this is to provide data transmission while at the same time creating the possibility to receive data. In this case, the computer used the data obtained from the microcontroller should be sent to the web address that provides hosting with the purchased ASP.NET. In this process, the purchased website server and any device to access

this interface are set to client. Fig. 8 shows Web server where the web interface and data will be transferred.

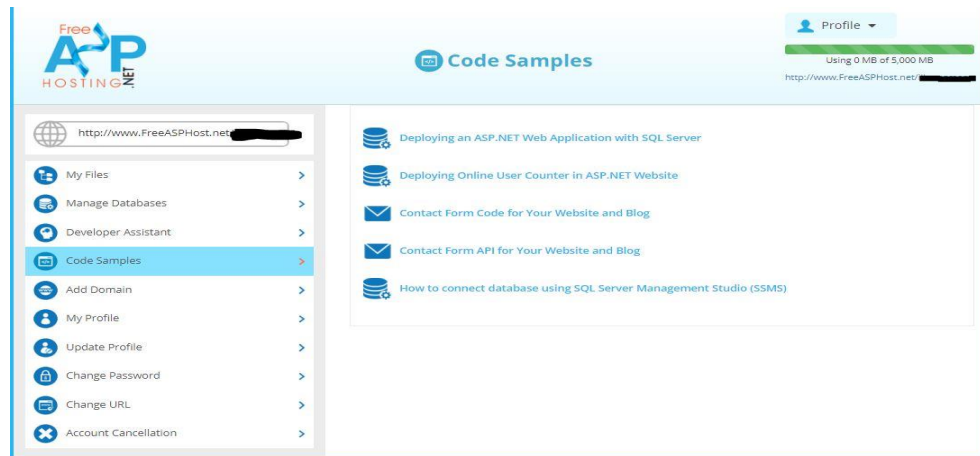


**Figure 8. Web server where the web interface and data will be transferred**

In order to perform this operation, it is necessary to first match the IP address that will be accessible to the microcontroller. Otherwise, the data received will not be able to be displayed in the designed interface. Every 15 seconds the received data must be sent to the website via The opened port. The reason the data is sent every 15 seconds is to prevent accretion in the database.

The process of opening the mapped IP address to clients is called Port Forwarding. This is done from the setting menu of the modem to which the server is connected to the internet. After the port routing process is done, the domain address that is rented from the hosting companies paying a certain fee must be defined as the server. Thus, both the cloud requirement and security vulnerability needed by the database will be eliminated. The purchased domain is personal and will be accessible to clients in the form of a web site and will be uploaded to this web site. ASP.NET the interface must be set to be continuously available for data retrieval by adding it to the panel page that the hosting company has opened. This process can be done by another methods.

Free and reliable platforms such as the developed tracking system, the ThingSpeak web interface and the pushingbox notification application are available. In this study, an original IoT-based noise monitoring system could be developed using open source software, modular and low cost components as an alternative to studies in the literature.

To summarize, first of all, the data from the sound sensor is processed and converted to dB values. Then, the converted data is transferred to the web server over the IP that has been Port Forwarding. Previously ASP.NET it is transferred to the web server whose interface has been added and paired with the microcontroller. This allows instant access to the data received over the internet. Fig. 9 shows Web interface design block diagram.

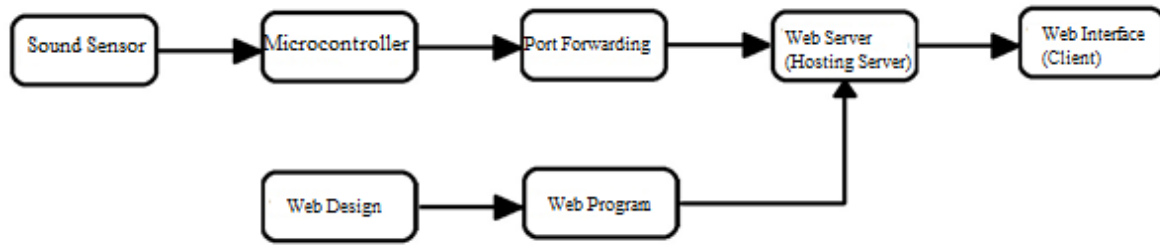


**Figure 9. Web Interface Design Block Diagram**

## 5. Results

In this study, environmental noise tracking system based on web of things was carried out. The study targeted unwanted and disturbing environmental noise problems at every point of life. Noise information can be monitored momentarily in environments where noise level is important, such as city centers, factories, hospitals, schools and entertainment areas. It is aimed to operate the system with a small margin of error, especially in environments where noise change is important. This margin of error can be minimized by replacing the appropriate sound sensor. With this work developed, access can be provided with a web interface created at any time from any place with a device with internet connection. It processes ADC data obtained from the sound sensor used in the designed noise meter and converts it to dB values. This converted data is transferred to the web server over the IP that has been Port Forwarding. Thus, instant access to the data is aimed. In later stages, the system may open an information interface or access to social media applications. Thus, when the noise value exceeds the upper limit or lower limit, an easier, practical solution can be achieved with the improvements included in the system.

As a result of this study, the changes generated by noise and the resulting intensity of people to take measures against it provided a great convenience. It has also been the basis for such studies to be carried out.

## References

- [1] Göçen, R. K., Sarı, E. M., Erman, A. T. (2016). Noisemap: An environmental noise monitoring sensor network. 24th Signal Processing and Communication Application Conference, SIU 2016.
- [2] Çevre ve Orman Bakanlığı Çevre Yönetimi Genel Müdürlüğü. (2011). Çevresel Gürültü Ölçüm ve Değerlendirme Kılavuzu. 3-85.
- [3] Çevre ve Orman Bakanlığı. (2010). “Çevresel Gürültünün Değerlendirilmesi ve Yönetimi Yönetmeliği (2002/49/EC)”, 1-13.
- [4] Biçen, Y., Yaman, O. (2019). An Internet of Things (IoT) based Monitoring System for Oil-immersed Transformers. Balkan Journal of Electrical & Computer Engineering, Vol. 7, No. 3, 226-234.
- [5] Gökrem, L., Bozuklu, M. (2016). Nesnelerin İnterneti: Yapılan Çalışmalar ve Ülkemizdeki Mevcut Durum. Gaziosmanpaşa Bilimsel Araştırma Dergisi, (13), 47-68.

- [6] Postalcıoğlu, S., Kurt, İ. (2018). Web Tabanlı Sıcaklık Takip Sistemi. Kilis 7 Aralık Üniversitesi Fen ve Mühendislik Dergisi, Cilt 2, Sayı 1, 56-63.
- [7] Durgun, M. Web Nesneleri Temelli Ağ Mimarisi Tasarımı ve Uygulaması. Tokat Gaziosmanpaşa Üniversitesi Fen Bilimleri Enstitüsü, Doktora Tezi, Mart, 2019.
- [8] Baytürk, M., Çetin, G. (2013). Gömülü Sunucu ile Tasarlanmış İnternet Tabanlı Sera Otomasyon Sistemi Uygulaması. Bilişim Teknolojileri Dergisi, 6(2), 53-57.
- [9] Candan, Z. Gerçek Zamanlı Sistemlerin Web Üzerinde Kontrolünün Gerçekleştirilmesi. Bahçeşehir Üniversitesi, Fen Bilimleri Enstitüsü, Yüksek Lisans Tezi, 1-65, 2008.
- [10] Dandıl, E. ,Gültekin S. (2017). Web Service-based Automation System for Duration Scheduling and Remote Control of Traffic Signal Lights’ , International Conference on Computer Science and Engineering (UBMK), 948-953.
- [11] Robotik Sistem, Arduino Nedir, 2019.  
[http://www.robotiksystem.com/.arduino\\_nedir\\_arduino\\_ozellikleri.html](http://www.robotiksystem.com/.arduino_nedir_arduino_ozellikleri.html).
- [12] Seed Studio, Grove-Loudness Sensor, 2019. [https://wiki.seedstudio.com/Grove-Loudness\\_Sensor/](https://wiki.seedstudio.com/Grove-Loudness_Sensor/).
- [13] Maker Robotistan, ESP8266 Dersleri 1: Tanıtım ve Güncelleme, 2019,  
<https://maker.robotistan.com/.esp8266-ile-iot-dersleri-1-esp8266-modulunu-guncelleme/>.  
[Accessed:3-mart-2016]
- [14] Güriş, S., Çağlayan, E., Güriş, B. EViews ile Temel Ekonometri. Der yayınları, 2017.
- [15] Ergün, M. SSPS for Windows. Bilimsel Araştırma İstatistik Uygulamaları. Ocak yayınları, 1995.
- [16] Orhunbilge, N. Uygulamalı Regresyon ve Korelasyon Analizi. Nobel Akademik Yayıncılık, 2017.

## INTEGRATION OF WIND POWER PLANTS TO THE GRID AND REACTIVE POWER SUPPORT

*Onur TAKIR<sup>1\*</sup>, Haydar BAYAR<sup>2</sup>, Erkan DURSUN<sup>3</sup>*

*The conversion of wind energy into electrical energy is one of the most environmentally sustainable methods of energy today. According to statistics published by the World Wind Energy Association, the total capacity of wind turbines installed worldwide at the beginning of 2019 exceeded 598 GW. Looking at the situation in Turkey, the number of wind power plants under operation is 180 according to published statistics at January 2019 by the Turkish Wind Energy Association. The total installed capacity of these power plants is 7369.35 MW. By the increasing of wind power capacity, the connection criteria of the power plants which are taken over to the grid become more critical. Although there are systems that are clean, renewable, and reduce external dependence on energy, power quality problems can occur in the grid connections of all wind power plants. In this respect, the grid connection criteria of wind turbines of the countries are essential. The connection requirements of wind turbines in Turkey, on April 22, 2017, revised Turkish Grid Code are determined under Appendix-18. Wind power plants connect to the grid from a medium voltage or high voltage level. At the grid connection point, there are some conditions that the plant must be met like changing wind conditions, switching, fault, etc. These requirements can be summarized as reactive power support, frequency response, contribution to the post-fault system. In this study, the reactive power capacity of a 9x3.6 MW Wind Power Plant to the grid is simulated and investigated.*

*Keywords: Wind power plant, Turkish grid code, reactive power support*

### 1. Introduction

In recent years, with the increasing population growth in the world, the increasing energy demand necessitates the orientation towards alternative energy systems. In this respect, the use of renewable energy sources such as wind, solar, geothermal, and hydroelectric and biomass gains great importance. As of 2017, 23.7% of the electricity consumed around the world is supplied from renewable energy, and wind energy is the third source of this energy [1]. As in the world, interest in renewable energy production in our country continues to increase in recent years. Among renewable energies, wind energy is the sector with the highest investment in the world in terms of installed power and production capacity.

---

<sup>1</sup> Institute of Pure and Applied Science, Marmara University, Kadiköy, Istanbul, Turkey (onurtakir@gmail.com)

<sup>2</sup> The Department of Marine Engineering Operations, Yildiz Technical University, Besiktas, Istanbul, Turkey (hbayar@yildiz.edu.tr)

<sup>3</sup>  <https://orcid.org/0000-0002-4086-938X>

<sup>3</sup> Faculty of Technology, Department of Electrical and Electronics, Marmara University, Kadiköy, Istanbul, Turkey, (erkandursun@marmara.edu.tr)  <https://orcid.org/0000-0002-7914-8379>

As of 2016, the installed capacity of wind power plants in the world is 486.8 GW, and it is predicted that by 2021 there will be 817 GW wind installed power in the world [2].

As of July 2018, 7.7% of Turkey's installed power consists of power plants based on wind energy [2]. According to the International Renewable Energy Agency (IRENA), Turkey's installed capacity of wind power reached 6516 MW in 2017 [3]. Wind energy power plants of 2018 of the share of electricity generation in Turkey are shown in Figure 1.

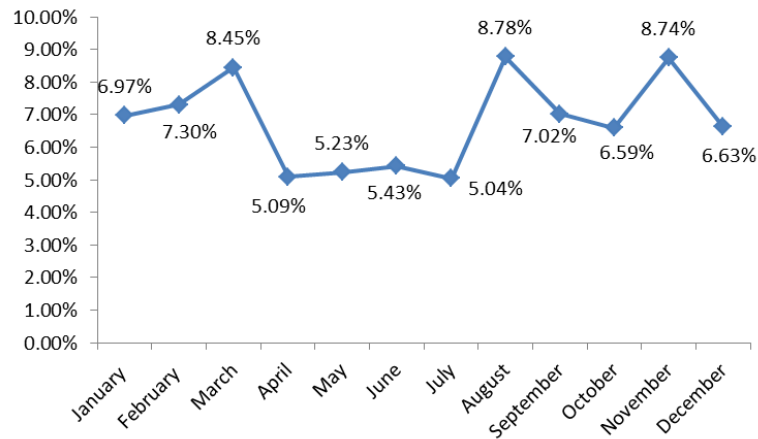


Figure 1. The share of Wind Power Plants in electricity generation in Turkey, 2018

Table 1. Turkey's renewable energy targets and resource-based energy production [MW]

Renewable Energy Type	2015	2017	2019	2023
Hydroelectric	25.526	28.763	32.000	34.000
Wind	5.660	9.549	13.308	20.000
Solar	300	1.800	3.000	5.000
Geothermal	412	559	706	1.000
Biomass	377	530	683	1.000

According to the renewable energy targets shown in Table 1 and targeted by the Ministry of Energy and Natural Resources, it is aimed to increase the wind power installed capacity to 20 GW in 2023. In other words, as of the end of 2017, it is seen that the current installed capacity of wind energy is planned to be doubled. When the wind energy capacity is increased rapidly, the grid connection criteria of the power plants become more critical. The connection requirements of wind turbines in Turkey, on April 22, 2017, revised Turkish Grid Code are determined under Appendix-18. According to the grid criteria in the Electricity Market Grid Regulation, dynamic and static analyzes are needed to provide active power control, frequency response, reactive power capacity, and reactive power support in terms of the effect of wind turbines on the grid [4].

## 2. Contribution of Wind Power Plant to System after Post-Fault

During the period in which the phase-to-phase voltage at the transmission or distribution system connection point remains in zones 1 and 2 given in Figure 2, the relevant generation facilities must remain connected to the grid in case of voltage drops in any phase or all phases.

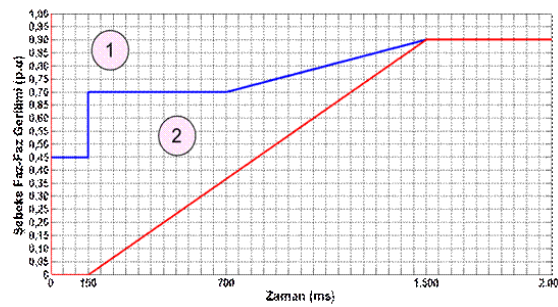


**Figure 2. The line to line voltage in transmission or distribution at a system connection point**

The main purpose shown in Figure 2 is to prevent wind power plants from unnecessarily leaving the system in case of any failure according to the conditions given in the graph and to ensure that the protection priority is given to other protective equipment. According to Figure 2, there are two separate cases [5]. In case 1, phase voltage continues to remain in the system for 150 ms if it drops to 0.45 pu, if the grid voltage goes to 0.70 pu at the end of 150 ms, it will remain in the system for up to 700 ms and finally the grid voltage up to 0.90 pu. If it reaches the pu value, it should remain in the system. 2. In the case of 150 ms mains voltage down to zero, even if the system does not exit, between 150 ms and 1500 ms to 0.90 pu value of the grid voltage increases linearly to reach the wind power must continue to be connected to the interconnected grid. In the cases below zone 2, the wind power plant is not expected to remain connected to the system. The post-fault contribution to the system is entirely related to the design of the controller, which ensures that the wind turbine remains connected to the grid during mains failure. The post-fault contribution to the system also determines how to correct the voltage after the mains failure [6]. In cases where the voltage drop during the fault remains in zone 1, the production plant's active power must be increased by at least 20% of the nominal active power per second immediately after the fault is cleared, to reach the maximum active power value that can be generated. In case the voltage drop during the fault remains in zone 2, the active power of the generation facility should increase by at least 5% of the nominal active power immediately after the fault is cleared and reach the maximum active power value that can be generated. Voltage fluctuations (0.9pu - 1.1pu) up to  $\pm 10\%$  at the grid connection point are normal operating conditions. In case of voltage fluctuations greater than  $\pm 10\%$  in the event of failure in the mains connection point, each wind turbine generator and/or each inverter in the plants shall be capable of inductive or capacitive levels up to 100% of the rated current without exceeding the designed transient ratings and provide maximum reactive current support. This transient should reach the maximum reactive current support value within 60 ms with a 10% error margin and be maintained for 1.5 seconds.

## 2.1. Active Power Control

Active power control can be carried out in emergencies defined in Article 63 of the Electricity Market Grid Regulation in wind generation facilities connected to the transmission system. The active power output of the generation facility should be automatically controlled between 20% and 100% of the available power of the plant under the current conditions with the signals to be sent by the Turkish Electricity Transmission Corporation (TEIAS) when necessary.

## 2.2. Reactive Power Control

Wind power-based generation facilities must be able to operate continuously at each point for reactive power values within the boundaries indicated by dark blue lines in Figure 3 at the transmission or distribution system connection point.

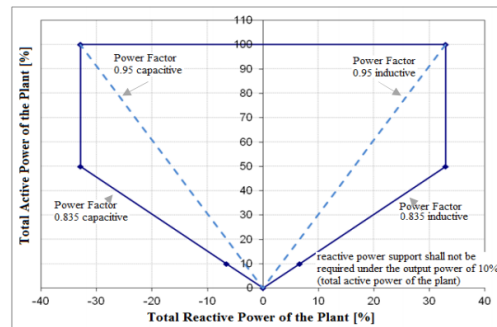


Figure 3. Wind power plant reactive power capacity curve [7]

Wind power plants should react proportionally to changes in grid connection voltage. The voltage drop value should be between 2-7%. The wind power plant under normal operating conditions should start responding to a sudden change in the transmission grid connection voltage within 200 ms at the latest. The reactive output power should reach 90% of the equilibrium value within 1 second.

## 3. Reactive Power Capacity Analysis: A Case Study

In this study, the reactive power capacity of a Wind Power Plant with 9x3.6 MW wind turbines can be provided as an example. According to the reactive power capacity curve of the wind power plant given in Figure 3, the reactive power values that the power plant can supply to the grid are analyzed with EDSA Paladin DesignBase software. EDSA program can perform engineering calculations such as short circuit, relay coordination, arc flash, and load flow [8-10]. Load flow calculations are used to analyze power systems under stable system conditions. In power systems, analyzes are made for the current operating status and planning status. Steady-state is the state in which all variables and parameters in the system operate continuously during the observation period. In load flow analysis, active, reactive power values, current value, voltage, how many lines, and transformers are loaded are analyzed [11-12].

The calculations of the designed power plant were carried out to be connected to the TEIAS transmission line of 154 kV high voltage level. In the power plant, which consists of 9 3.6 MW wind turbines, the voltage of wind turbines is modeled as 0.66 kV. It is planned that the wind turbines joining at 34.5 kV bus bar will connect to the interconnected network with 154 / 34.5 kV TEIAS transformer. For the technical information of the turbines, NORDEX's document "Reactive Power Capability WTG K08 Delta" was used (Figure 4).

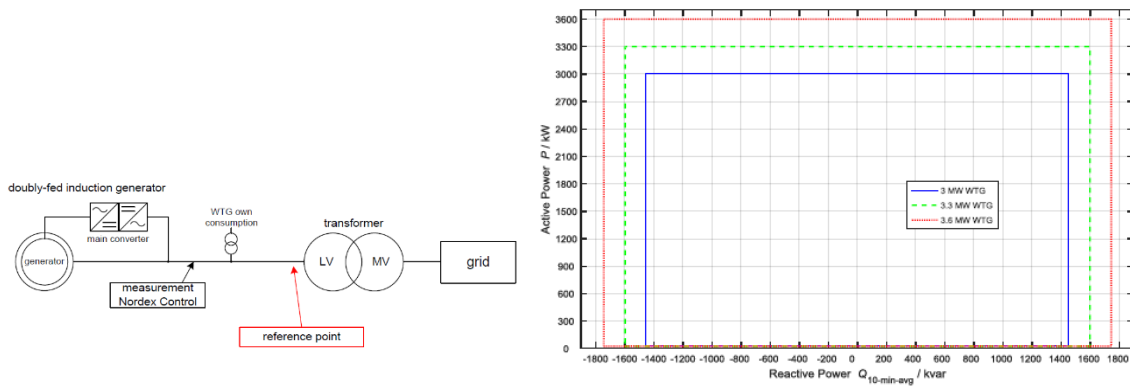


**Figure 4. Nordex 3.6 MW turbine model and turbine active/reactive power change figure**

According to the wind power plant, reactive power capacity curve given in Figure 2, 6 different scenarios were examined. These scenarios are provided in the following Table 2. The scenarios are based on the corner points in the graph given in Figure 2. In other words, the scenarios where the power plant operates at 1 pu, 0,5 pu and 0,1 pu power separately in inductive and capacitive operating conditions are considered.

**Table 2. Load flow analysis scenarios**

Scenarios		NORDEX 3.6 MW	
No		P [kW]	Q [kVar]
1	P <sub>100%</sub> End.	3600	1744
2	P <sub>50%</sub> End.	1800	1744
3	P <sub>10%</sub> End.	360	1744
4	P <sub>100%</sub> Cap.	3600	-1744
5	P <sub>50%</sub> Cap.	1800	-1744
6	P <sub>10%</sub> Cap.	360	-1744

The total active power is  $9 \times 3.6 = 32.4$  MW installed capacity when 9 power plants with 3.6 MW wind turbines are inspected. According to the installed capacity, the inductive or capacitive generation of 10.65 MVar is required in the 32.4 MW and 16.2 MW active power generation range. It must provide reactive power support of 2.14 MVar at 0.1 pu, 3.24 MW active power generation point.

Scenario 1: P = 3600 kW, Q = 1744 kW (Capacitive)

In this scenario, in case of turbines generate 100% active power and capacitive operation, 31,85 MW active power and 11,03 MVar reactive power generation in 154 kV TEIAS bus bar are calculated (Figure 5).

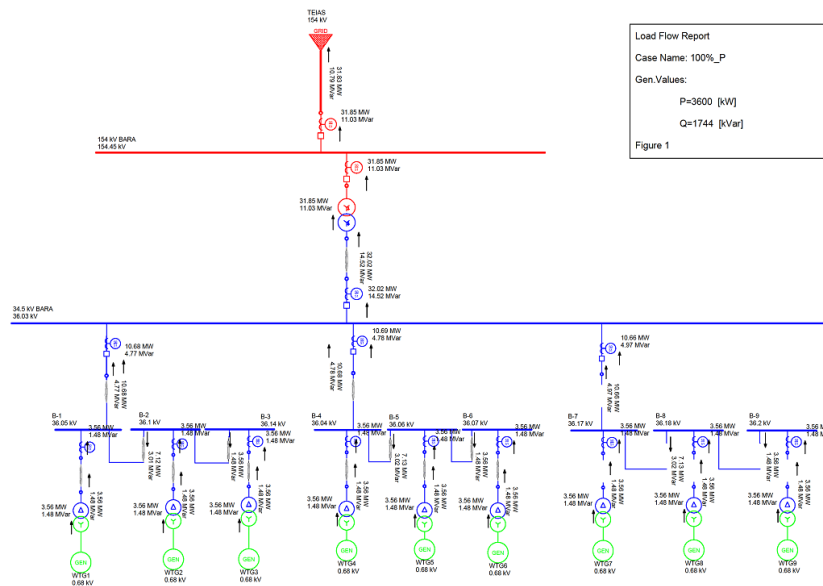


Figure 5. Scenario 1 results

Scenario 2:  $P = 1800 \text{ kW}$ ,  $Q = 1744 \text{ kW}$  (Capacitive)

In this scenario, when the turbines generate 50% active power and capacitive operation, 15.95 MW active power, and 14.37 MVar reactive power generation at 154 kV TEIAS bus bar are calculated (Figure 6).

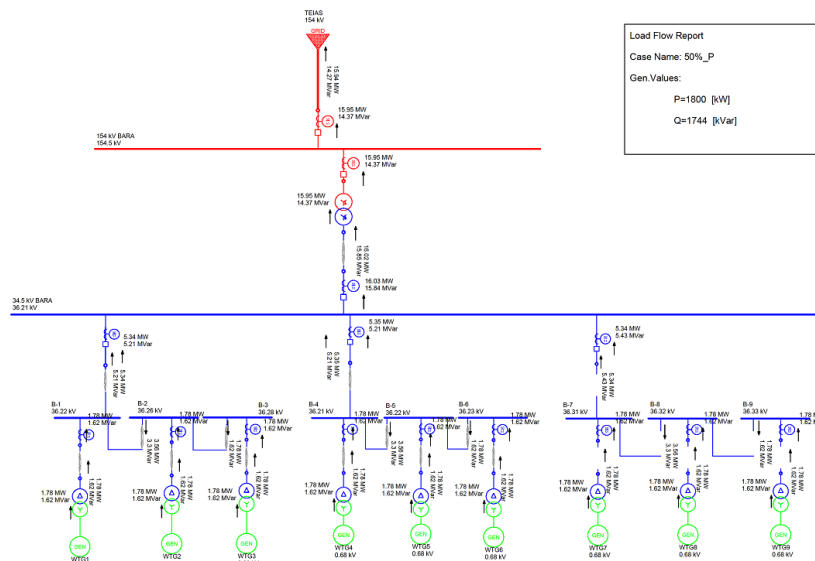


Figure 6. Scenario 2 results

Scenario 3:  $P = 360 \text{ kW}$ ,  $Q = 1744 \text{ kW}$  (Capacitive)

In this scenario, in case of turbines generate 10% active power and capacitive operation, 3.08 MW active power, and 15.42 MVar reactive power generation in 154 kV TEIAS bus is calculated (Figure 7).

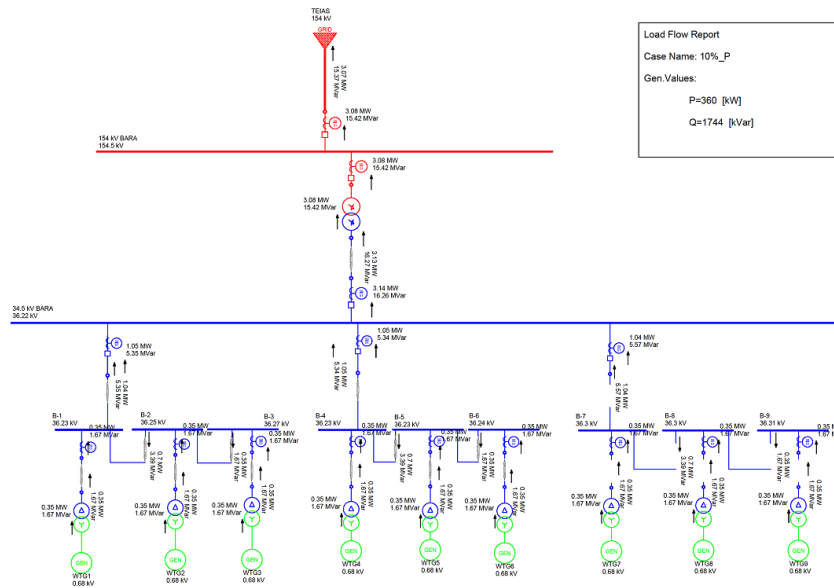


Figure 7. Scenario 3 results

Scenario 4:  $P = 3600 \text{ kW}$ ,  $Q = -1744 \text{ kW}$  (Inductive)

In this scenario, when the turbines generate 100% active power and capacitive operation, 31.75 MW active power and -22.02 MVar reactive power generation at 154 kV TEIAS bus bar is calculated (Figure 8).

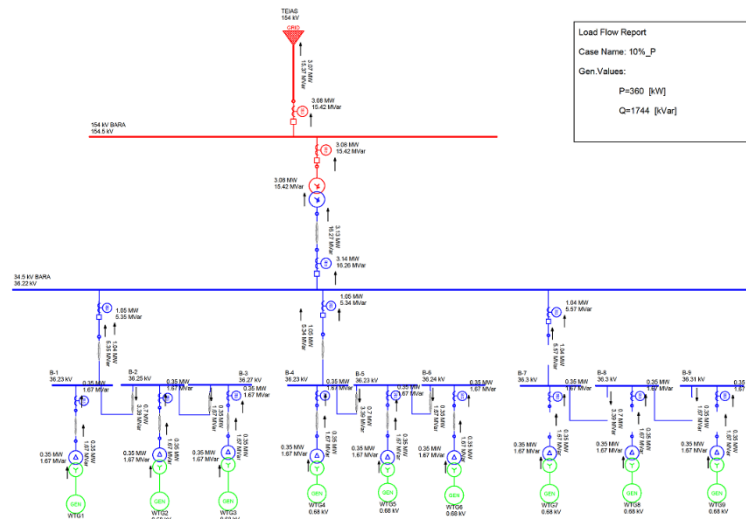


Figure 8. Scenario 4 results

Scenario 5:  $P = 1800 \text{ kW}$ ,  $Q = -1744 \text{ kW}$  (Inductive)

In this scenario, in case of turbines generate 50% active power and capacitive operation, 15,92 MW active power and -17.69 MVar reactive power generation in 154 kV TEIAS bus bar are calculated (Figure 9).

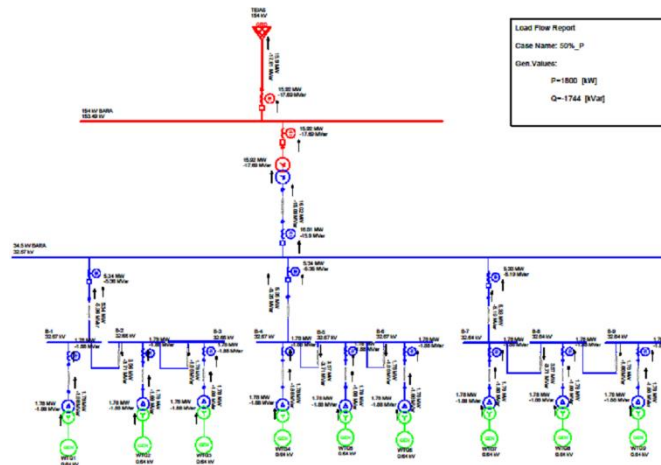


Figure 9. Scenario 5 results

Scenario 6:  $P = 360 \text{ kW}$ ,  $Q = -1744 \text{ kW}$  (Inductive)

In this scenario, in case of turbines generate 10% active power and capacitive operation, 3.07 MW active power and -16.34 MVar reactive power generation in 154 kV TEIAS bus bar is calculated (Figure 10).

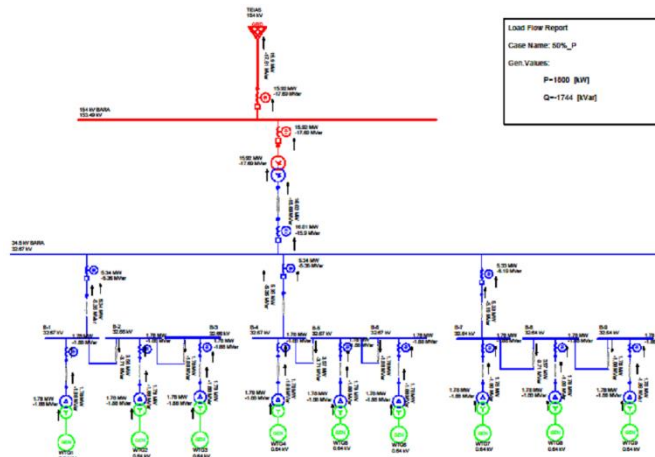


Figure 10. Scenario 6 results

The reactive power capacity curve of the analyzed wind power plant with an installed capacity of 32.4 MW according to 6 different scenarios is shown in Figure 11. As seen in this curve, the wind farm, which is examined as an example, can meet the minimum reactive power support conditions demanded by TEIAS at every point.

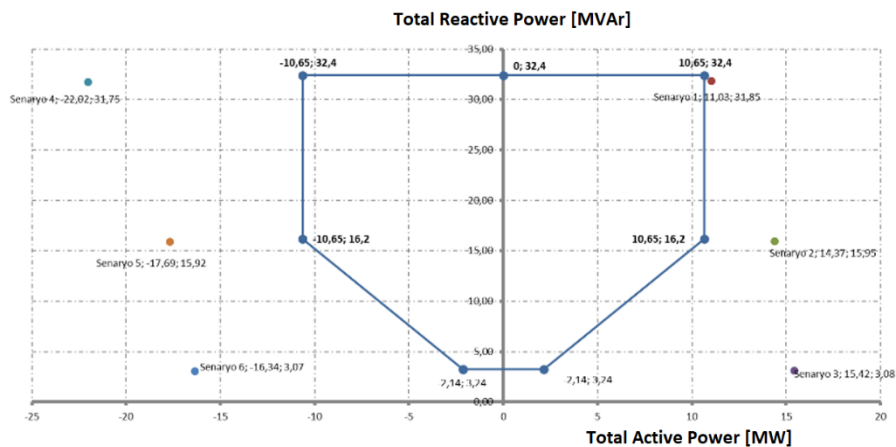


Figure 11. Simulation results for the wind power plant reactive power capacity

#### 4. Conclusions

In this study, the conditions that the 32.4 MW wind power plant to be connected to the interconnected grid at 154 kV voltage level, must comply with the Turkish Grid Code are examined. Load flow analysis of the power plant has been performed and the compliance of the results of the analysis with the Appendix-18 of the Turkish Grid Code has been checked. These analyzes are also required for all wind farms planned to be established. If TEIAS criteria cannot be met according to the results of the analyzes, it may be planned to install a reactor or capacitor feeder in the plant for reactive power support. Load flow analysis, short circuit analysis, harmonic and flicker analysis, dynamic analysis and grounding analysis should be carried out meticulously during the design phase of wind farms. In this way, problems to be encountered in grid connections of wind power plants can be identified and measures can be taken.

#### References

- [1] Republic of Turkey Ministry of Energy and Natural Resources, <http://www.enerji.gov.tr/tr-TR/Sayfalar/Elektrik/> Accessed on May 16, 2019.
- [2] Global Wind Energy Council, <https://gwec.net/publications/global-wind-report-2/global-wind-report-2016/> Accessed on May 10, 2019.
- [3] International Renewable Energy Agency, <https://irena.org/publications/2018/Jul/Renewable-Energy-Statistics-2018/> Accessed on May 26, 2019.
- [4] Turkey Legal Gazette, <http://www.resmigazete.gov.tr/eskiler/2017/04/20170422-8-1.pdf/> Accessed on June 01, 2019.
- [5] Demiroglu, E., Demiroglu, T. (2015). Simulation Modeling for Network Connection Analysis of Wind Power Plants. *Gazi Journal of Engineering Sciences*, 1(3), 351-368.
- [6] Rona, B., Integration of Wind Power Plants to Power System and Analysis According to Grid Regulation. MSc.Thesis, Istanbul Technical University, 2014.
- [7] Uzun, S., et. al (2015). Integration criteria of Turkish wind energy generation plants and assessment of the criteria by analysis. *9th International Conference on Electrical and Electronics Engineering (ELECO)*, Bursa, Turkey, 1039-1042.
- [8] <http://www.poweranalytics.com/introducing-designbase-6-0/> Accessed on June 11, 2019
- [9] Kiliç, H., Khaki, B., Gümüç, B., Yılmaz, M., & Asker, M. E. (2018, November). Stability Analysis of Islanded Microgrid with EVs. In 2018 Smart Grid Conference (SGC) (pp. 1-5). IEEE.
- [10] Yılmaz, M. (2018). Real measure of a transmission line data with load fore-cast model for the future. *Balkan Journal of Electrical & Computer Engineering (BAJECE)*, Vol 6, No 2, pp.141-145.
- [11] Samancıoğlu, G., Wind Basin Planning and Modeling of the Effects of Wind Power Plants to the Network with Digilent Program. MSc.Thesis, Gazi University, 2014.
- [12] Tür, M. R. (2019). The Impact of Emerging Renewable Energy on Capacity Mechanisms in Power Systems and Expert Opinion. *Balkan Journal of Electrical and Computer Engineering*, 7(3), 319-325.

## NUMERICAL ANALYSES OF A STRAIGHT BLADED VERTICAL AXIS DARRIEUS WIND TURBINE: VERIFICATION OF DMS ALGORITHM AND QBLADE CODE

*Abdullah MURATOĞLU<sup>1\*</sup>, M. Sungur DEMİR<sup>2</sup>*

*Wind energy is among the most cost-effective renewable energies. Till date, turbines with different configurations had been designed to harness wind power, each having unique superiorities. Darrieus turbines are one of the mostly investigated vertical axis wind turbines using either experimental or numerical methods. Experimental analyses are time consuming works which requires high amount of effort and expenses. Thus, computational fluid dynamics (CFD) methods have been commonly used by scientists and engineers in order of obtaining detailed performance and illustration of the fluid flow. Contrary to the horizontal axis machines, Darrieus turbines are difficult to be analyzed by CFD algorithms due to high pressure and velocity variations which arise from extreme changes in the angle of attack beyond the stall condition at different azimuthal position of the blades. Therefore, more simplified numerical models are generated employing double multiple streamtube (DMS) theory together with additional improvements. QBlade is one of the mostly used numerical methods based on the lifting line free vortex wake method developed for calculating rotor aerodynamics. The main scope of this study is to design a straight bladed Darrieus turbine ( $D=1028$  mm,  $H=1460$  mm,  $N=3$ ) and to verify the double multiple streamtube theory and QBlade algorithm with the experimental and computational works. Analysis results represented good agreement with the previous studies especially at lower TSR ranges. Compare to the experimental results, an overestimation in the power coefficient is obtained at low free stream speed and high TSR ranges after exceeding the peak point. Sensitivity of the model to the  $Re$  number variations have also been outlined.*

**Key words:** VAWT, Darrieus, experiment, CFD, validation, numerical, QBlade

### 1. Introduction

After the industrial revolution, global energy consumption has been exponentially increased. The reason behind this increment is mainly per capita energy use and population growth. Today, more than 79-80 % of total global energy use is covered from fossil resources [1]. Extreme oil, coal and gas use resulted high carbon dioxide and other greenhouse gas releases. Annual carbon dioxide emission is

<sup>1</sup> Department of Civil Engineering, University of Batman, Batman, Turkey (abdullah.muratoglu@batman.edu.tr)   
<https://orcid.org/0000-0001-8981-5983> (Corresponding author)

<sup>2</sup> Department of Civil Engineering, University of Batman, Batman, Turkey (muhammed.sun@batman.edu.tr)   
<https://orcid.org/0000-0003-3631-6325>

still rising to be above 39.5 Gtons [1]. Global climate change and global warming are the main detrimental consequences of increasing greenhouse gas intensity in the atmosphere. Huge amount of research is provided by scientists and governmental units to solve the climate change problem. Accordingly, majority of the studies reported that the solution is mainly based on decreasing fossil fuel burning, diversification of energy supply [2] and finding more alternative and renewable solutions for energy production. High availability, low cost, sustainability and cleanness of renewable energy resources [3] such as wind, hydro, biomass and solar energy increased attention of researchers to make more R&D and technical feasibility studies.

Wind is defined as moving air that is produced as a result of uneven temperature distribution which is originated from solar radiation and earth's rotation [4]. It is characterized as renewable, interminable environmental friendly source of energy, delivering high power outputs [4]. Today, wind energy is considered as the most cost effective solution among other renewables leading its installed capacity being increased day by day [5]. According to the projections, the global installed capacity of wind energy is estimated to exceed 800 GW, in the next couple of years [5].

Wind energy is mainly classified into two groups according to the orientation of the central shaft. These are vertical axis (VAWT) and horizontal axis wind turbines (HAWT). Horizontal axis turbines are generally preferred for larger-scale applications and commercial installations [6]. On the other hand, vertical axis turbines are employed either for domestic use or at the places where classical HAWTs are not suitable for application, in terms of efficiency or high cost. Basically, literature studies unveil larger power coefficient scores of HAWTs relative to VAWT machines. However, VAWT have several unique advantages over horizontal axis machines. These systems have a number of blades rotating around a central shaft which is perpendicular to the free stream. Therefore, vertical axis devices can produce energy at various and diffuse velocity conditions [7]. Thus they are independent from the flow direction and yaw angle [8]. On the other hand, cyclic variations in the pressure and velocity, high fatigue loads, vibration and noise problems are among the main disadvantages of vertical axis wind turbine configurations [9]. Also, VAWTs have relatively higher cut-out wind speed values which makes them to be practical in majority of the turbulent and harsh flow environments [10]. Again, so called Betz limit can be exceeded in vertical axis machines [11].

VAWT technology can be categorized in two classes, namely drag and lift type of devices. The most popular drag type turbine is known as Savanious turbines having a number of (semicircular) buckets which is activated by the impact of drag force that is driven by the flow [12]. Similarly, Darrieus turbine have been invented by G. J. M. Darrieus to be used for residential purposes at remote zones in order to overcome blade size and rotational speed limits [13]. Unlike the Savanious turbines, Darrieus rotors are mainly activated by the combination of aerodynamic lift and drag forces generated on 2D blade sections (airfoils). Basically, Savanious turbines have relatively lower cut in speed than Darrieus turbines [12]. On the other hand, Darrieus turbines deliver higher efficiency ranges than Savanious turbines. However, the efficiency still remains below the horizontal axis machines [14]. Detailed representation of power coefficient of various horizontal and vertical axis free flow turbines with respect to their tip speed ratio is illustrated in Fig. 1.

There have been various studies on the aerodynamic performance of Darrieus wind or hydrokinetic turbines. The performance of straight bladed Darrieus turbines have been analyzed by Castelli et al. [16] by comparing the computational fluid dynamics (CFD) results with traditional blade element momentum (BEM) theory. Similarly, another study of Castelli et al. [17] provided a model for determining optimal spatial grid node distribution of Darrieus turbines for CFD analyses.

They also validated the numerical simulation results with the experimental data from wind tunnel. Ferreira et al. [18] emphasized the complexity of modelling vertical axis turbines by computational ways due to high velocity and pressure variations at different azimuthal positions of the blade. D'Alessandro et al. [19] developed a mathematical model which analyzes the interaction between flow area and turbine blades in order to analyze the complex flow field around Savanious wind turbines. Scungio et al. [13] investigated wind tunnel performance of a straight bladed micro-scale Darrieus wind turbine at low wind speeds which made of auxiliary airfoiled blades. Rainbird et al. [14] investigated the effect of flow curvature on the performance of Darrieus turbines and they suggested a virtual chamber correction for low order simulation models. Khadir and Mrad [20] numerically investigated the aerodynamic performance of Darrieus wind turbines considering the magnus effect. Ghazalla et al. [21] analyzed Darrieus turbines inside flanged diffuser in order to improve the aerodynamic performance considering different blade sections. Wakui et al. [22] studied on the hybrid configuration of Darrieus and Savanious turbines for standalone wind turbine generator system. Consul et al. [23] investigated the effect of solidity on the performance of vertical axis turbines using numerical approach. Brusca et al. [24] studied the effect of aspect ratio on the performance of straight bladed Darrieus turbines reporting that higher aspect ratios reduces the overall performance.

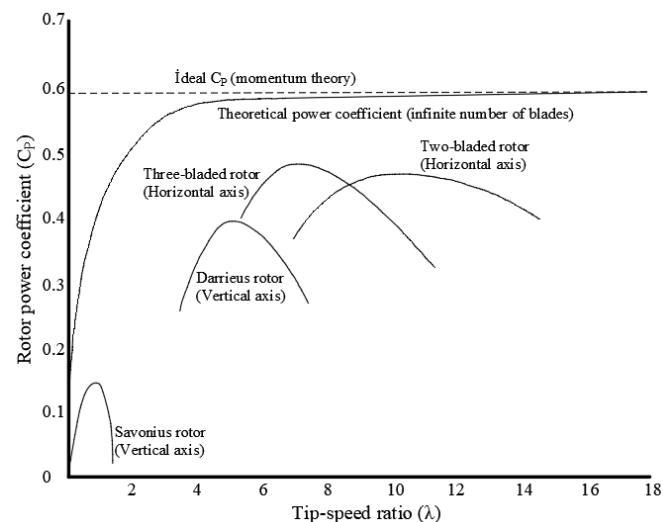


Figure 1. Comparison of vertical and horizontal axis wind turbines in terms of efficiency (Figure is based on [15])

Abovementioned studies reveal that the flow around the Darrieus turbines is quite unsteady necessitating high efforts for CFD modeling. Therefore, employment of more simple numerical models for performance prediction would eliminate the computational effort and expenses of CFD algorithms. QBlade software [25] is a numerical code that have been developed for the design and simulation of horizontal and vertical axis wind and hydrokinetic turbines based on the BEM and double multiple streamtube (DMS) algorithms [26]. The code is developed by Hermann Föttinger Institute of TU Berlin and distributed under General Public License. [27] The model is based on the lifting line free vortex wake (LLFVW) method for calculating the rotor aerodynamics [28]. QBlade runs integrated with the XFOIL code within the graphical user interface and is capable of evaluating airfoil polars and extrapolating the polars for various angles of attack [26]. In the literature, many studies utilized QBlade code for performance analysis or validation of the existing models. Mahmuddin [29] developed a computational method which is based on BEM theory for performance prediction of horizontal axis wind turbines considering tip and root losses by validating the developed

model with QBlade software. Bianchini et al. [28] implemented the virtual camber transformation into the QBlade algorithm. Suresh and Rajakumar [30] reported the aerodynamic analyses for a 2kW small scale HAWT using QBlade algorithm considering different airfoil sections. The effect of Re number on a two bladed HAWT employing QBlade software has been analyzed by Rahimian et al. [31]. Good agreement between BEM and CFD model has been reported. The algorithm has also been used by Akour et al. [32] for determining the power coefficient of a micro wind turbine working under low average wind speed. The code has also been used for verification of 5 MW NREL wind turbine by Barooni et al. [27]. Sensitivity analysis of a Darrieus turbine using Gurney Flaps for power augmentation has been provided using QBlade software for TSR and power curve prediction as a LLFVW model. Smooth and more realistic application of DMS model at uniform interference factors have been attained using QBlade algorithm by Bangsa et al. [33]. Consequently, LLFVW model which is applied by QBlade software have been noted to solve accuracy and convergence problems encountered in VAWTs [34].

The main scope of the present study is to model a three bladed H-shaped (straight) Darrieus turbine via QBlade software and to compare the model outputs with the experimental and computational fluid dynamics results of literature studies [16,17,35,36] employing the similar geometry. For this purpose, the turbine geometry that is generated from NACA 0021 86.5 mm chord length airfoils having radius of 515 mm and height of 1460 mm has been analyzed by QBlade at different free stream speed and tips speed ratio intervals. The modeled geometry and dynamic properties of flow domain are selected to be similar to the abovementioned studies for providing a better comparison and verification.

## 2. Theory and method

### 2.1. QBlade and XFOIL algorithms

QBlade is an open source code that is developed for design and simulation of vertical and horizontal axis wind and hydrokinetic turbines. The model utilizes DMS algorithm for VAWT analyses. The employed blade sections' lift and drag characteristics are evaluated by the XFOIL software which is integrated with QBlade [26]. XFOIL is also an open source interactive algorithm developed for design and analysis of 2D airfoils employing the speed and accuracy of high order panel methods with fully coupled viscous and inviscid interaction method [37]. The performance parameters such as lift, drag, pressure coefficient, etc. of 2D blade sections are evaluated by the XFOIL algorithm. It is a general accepted code that is widely used by the scientific community for aerodynamic analyses [38–40]. In majority of the cases, it becomes impossible to deliver the performance coefficients at high angles of attack beyond the stall conditions using XFOIL, due to the convergence problems. Thus missing data are completed by QBlade software making extrapolations [26] to find out the airfoil performance within  $0^{\circ}$ - $360^{\circ}$  angles of attack in which the airfoils stand at different azimuthal positions.

### 2.2. Aerodynamics forces on Darrieus turbines

A typical vertical cross section of the straight bladed Darrieus turbines is shown in Fig. 2. The relative velocity ( $w$ ) is one of the most important parameters that affects the performance of the complete rotor which is the resultant of both free stream velocity ( $U_{\infty}$ ) and blades' tangential velocity ( $U_t$ ). It varies as a function of the azimuth angle ( $\theta$ ), which is defined as the angle between the blade

and the horizontal axis. Relative velocity acted at an angle of attack ( $\alpha$ ) at different azimuthal position of each blade section generates aerodynamic lift and drag forces which are represented by  $C_L$  and  $C_D$ . Drag force is parallel to the relative velocity vector, while the lift force is at the perpendicular direction. Then, the normal and tangential components of both lift and drag forces can be written as;

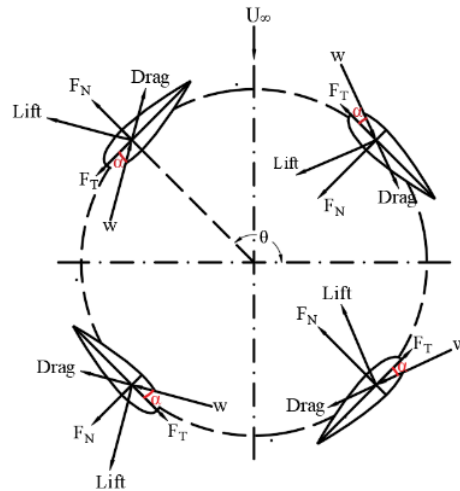


Figure 2. Representation of forces and velocity vectors generated on a typical vertical Darrieus rotor section

$$F_N = \frac{1}{2} \rho w^2 h c (C_n) \quad (1)$$

$$F_T = \frac{1}{2} \rho w^2 h c (C_t) \quad (2)$$

where,  $F_N$  is the normal force to the airfoil chord,  $F_T$  is the tangential force,  $\rho$  is the density,  $w$  is the relative velocity,  $h$  is the blades' height,  $c$  is the chord length,  $C_n$  is the normal force coefficient, and  $C_t$  is the tangential force coefficient. Consequently, normal and tangential force coefficients can be written as follows;

$$C_n = C_L \cos(\alpha) + C_D \sin(\alpha) \quad (3)$$

$$C_t = C_L \sin(\alpha) - C_D \cos(\alpha) \quad (4)$$

### 2.3. DMS theory

In order of being a new and emerging technology, the very first attempts of wind turbine methodology is mainly based on classical propeller theories. Blade element momentum (BEM) method which is originally developed to assess the performance of classical airplane propellers by Glauert [41] has been widely used in the scientific community at the first turbine designs works. Then, single streamtube model has been developed by Templin [42] and it has been extended to be parallel dependent streamtubes by Strickland [43] which is called multiple streamtube theory [44]. Aerodynamic streamtube models are generated considering the conservation of momentum equations and the forces on the turbine blades which are equated to vary in streamwise direction [45]. Contrary to the single streamtube model, DMS theory assumes that the entire rotor is produced from a number of adjacent streamtubes [45]. Double Multiple Streamtube theory is developed as a combination of multiple streamtube method and double actuator disk theories [46]. The method is firstly introduced by Paraschivoiu [47,48]. Multiple streamtube method analyzes the flow considering momentum balance of each streamtube which allows velocity variations at perpendicular directions to the free stream [46].

However, as a disadvantage, multiple streamtube theory is unable to separately analyze upstream and downstream regions. Thus, double actuator disk theory has been proposed which assumes that two actuator disks has been placed sequentially which are connected at the center of turbine [46]. Then, both theories have been combined as double multiple streamtube (DMS) theory. Consequently, the velocity variations can be taken into account between upstream and downstream part of turbine (Fig. 3). The detailed representation of the DMS theory can be provided based on Biadgo at al. [46] as follows;

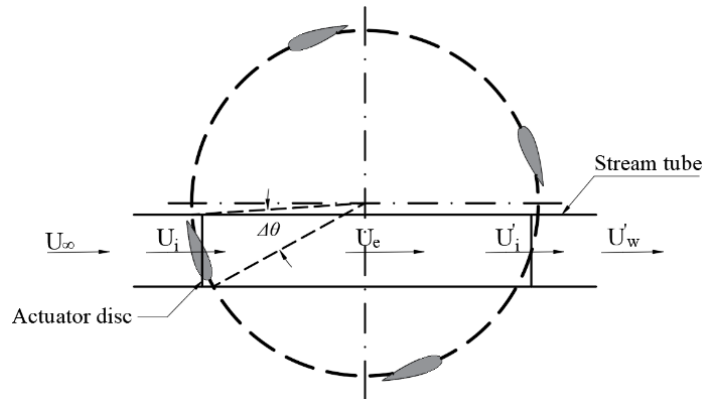


Figure 3. Understanding the DMS theory at a vertical cross section of rotor

DMS assumes that, the streamflow enters to the frontal blades with velocity  $U_i$  and the velocity is induced to the  $U_i'$  at the rear blades. Similarly,  $U_\infty$  is the free steam speed,  $U_e$  is the flow velocity at the center of the turbine and finally  $U_w'$  is the stream speed after the rotor. The induced velocities can be written as;

$$U_i = \frac{U_\infty + U_e}{2} \quad (5)$$

$$U_i' = \frac{U_e + U_w'}{2} \quad (6)$$

The relative velocity vector ( $w$ ) which is primary responsible velocity vector from the turbine's performance becomes a function of turbine's angular velocity and the induced speed. Thus, two different relative velocity functions can be written for the upstream and downstream halves of the rotor, respectively as follows;

$$w = \sqrt{((u_i \sin(\theta))^2 + (u_i \cos(\theta) + \omega R)^2)} \quad (7)$$

$$w' = \sqrt{((u_i' \sin(\theta))^2 + (u_i' \cos(\theta) + \omega R)^2)} \quad (8)$$

Finally, the thrust, torque and power coefficients which are solved for  $w$  and  $w'$ , separately, can be represented as follows;

$$C_T = \frac{2}{\pi} \left( \frac{Bc}{2R} \right) \left( \frac{w}{U_\infty} \right)^2 \left( C_t \frac{\cos \theta}{\sin \theta} - C_n \right) \quad (9)$$

$$C_Q = \left( \frac{Bc}{D} \right) \sum_{i=1}^{N_\theta} \frac{\left( \frac{w}{U_\infty} \right)^2 C_t}{N_\theta} \quad (10)$$

$$C_P = C_Q \lambda \quad (11)$$

where;  $C_T$  the thrust coefficient,  $B$  is the number of blades,  $R$  is the rotor radius,  $w$  is the tangential velocity component,  $U_\infty$  is the free stream velocity,  $C_t$  is the tangential force coefficient,  $C_n$  is the normal force coefficient,  $D$  is the turbine diameter,  $C_Q$  is the torque coefficient and  $\lambda$  is the tip speed ratio.

## 2.4. Numerical setup

The model setup for the present study is produced based on the experimental and CFD analyses provided by Castelli et al. [16,17], Castelli and Benini [35] and Battisti et al. [36]. Details of geometrical and dynamic configurations of abovementioned studies and present study were listed in Tab. 1. The experimental and computational domains that have been reported by Castelli et al. (2010) [17] and Battisti et al. (2018) were illustrated in Fig. 4.

**Table 1. Geometrical and dynamic details of the model and literature studies for experimental, computational and numerical validation**

Features/type	Sym.	Battisti et al. (2018) [36]	Castelli et al. (2010) [17]	Castelli et al. (2011) [16]	Castelli and Benini (2012) [35]	Present study
		Wind tunnel experiment	Wind tunnel experiment	CFD analysis	CFD analysis	Numerical analysis
Rotor diameter (mm)	$D$	1028	1030	1030	1030	1028
Rotor height (mm)	$H$	1460	1456.4	1030	1030	1460
Airfoil type	-	NACA 0021	NACA 0021	NACA 0021	NACA 0021	NACA 0021
Number of blades	$N$	3	3	3	3	3
Chord length (mm)	$c$	85	85.8	85.8	85.8	85
Aerodynamic center	-	0.5c	0.5c	0.5c	0.5c	0.5c
Rotor solidity	$\sigma$	0.25	0.25	N/A	N/A	0.25
Frontal area (m <sup>2</sup> )	$A$	1.5	N/A	N/A	N/A	1.5
Rotational velocity (rpm)	$\Omega$	400	N/A	N/A	N/A	400
Free stream velocity (m/s)	$U_\infty$	6-16	9 m/s	9 m/s	N/A	6-16
Tip speed ratio	$\lambda$	3.8-1.4	0.6-1.2	0.8-3.3	2.6-4.1	3.8-1.4

## 3. Results and discussion

Castelli et al. (2010) [17] studied on the numerical validation of a straight bladed Darrieus VAWT (Tab. 1) and they provided experimental results for a wind tunnel having 4000 x 3840 mm continuous test section which can be used for verification of numerical analyses (Fig. 4a). Experimental results were reported for free stream speed of 9 m/s at various tip speed ratios considering no blockage correction. CFD analysis results were provided for the same geometrical details by Castelli et al. (2011) [16] using SST k- $\omega$  turbulence model at various  $y^+$  values for different wall functions. Again, Castelli and Benini [35] were provided CFD analyses at different tilting conditions. Model 0 of the abovementioned study which having zero tilt angle were used for validation of this study.

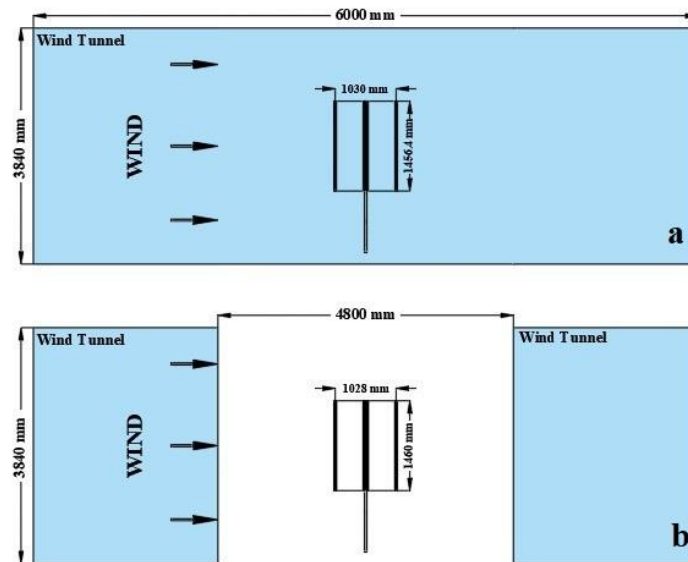


**Figure 4. Illustration of experimental and computational setup reported by Castelli et al. (2010) [17] and Battisti et al. (2018) [36] (b)**

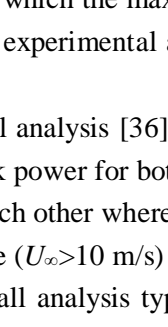
Consequently, Battisti et al. [36] reported wind tunnel experiment results of a straight bladed Darrieus turbine (Tab. 1) inside an open test section (free-jet configuration) at low turbulence intensity ( $<1\%$ ) wind tunnel facility (4000x3840x6000 mm) in order to provide experimental benchmark data for researchers. Turbine's performance at steady 400 rpm rotational speed for the freestream velocity varying between 6-16 m/s were provided. The geometrical blockage ratio is defined as 1.5 % by Battisti et al. [36]. However no blockage correction was reported for the experimental analysis. All experimental analyses are reported to be provided at Bovisa's low turbulence facility and Politecnico di Milano wind tunnel which is situated in Milan.  $C_P$ - $TSR$  curves facilitate to compare the behavior of analyses that is provided using different methods eliminating also the geometrical considerations. The dynamic properties of the flow environment that is inputted to the QBlade software is summarized in Table 2. Comparison of power coefficient vs. tip speed ratio relationships of abovementioned literature studies and the present study has been provided in Fig. 5.

It should be noted that, both experimental studies [17,36] have similar behavior together with slight changes at the turbine geometry that is reported in Tab. 1. The discrepancies are estimated to be sourced from the wind tunnel characteristics and sensitivity of the measurement equipment. The experimental analysis that is delivered by Battisti et al. [36] exhibits very low power coefficients at higher values of  $TSR$  (3-4), while the behavior of other computational and numeric analysis are consistent approximating to about 0.2-0.3. CFD analysis that is reported by Castelli et al. (2011) [16] shows relatively higher overall pressure coefficients (which is provided at  $Re=300 \times 10^3$ ) while the shape of  $C_P$ - $TSR$  curve (bell shape) is very similar to the experiment that is conducted by [36]. It is predicted that, this behavior is a result of higher  $Re$  number which has also been discussed later.

In this study, various numerical analyses have been performed at different  $Re$  numbers. The green dotdash line represents the analysis at multiple  $Re$  number in which the blade sections have been assigned different  $Re$  numbers which is based on Battisti et al. [36]. Numerical results that are provided by QBlade for this curve is quite consistent at lower  $TSR$  ( $<2.5$ ). However, QBlade analyses for multiple  $Re$  numbers exhibit deteriorating performance at higher  $TSR$  ranges, for this study. Therefore, the performance of the rotor at  $Re=80000$  and  $Re=100000$  has also been included in Fig. 5. It is observed that, more or less consistent results have been provided by QBlade software especially at

low Re number ( $Re=80000$ ). Consequently, we reveal that, the suitable and accurate representation of Re number is significantly important while making numerical analysis with QBlade algorithm.

**Table 2. Dynamic properties of QBlade analyses of present study**

Property	Parameter	QBlade view
Free stream velocity	6-16 (m/s)	
Rotational speed	400 (rpm)	
TSR	1.4-3.6	
Reynolds number	$80 \times 10^3 - 200 \times 10^3$	
Viscosity	$1.55 \times 10^{-5}$ ( $m^2/s$ )	
Air density	1.155 ( $kg/m^3$ )	

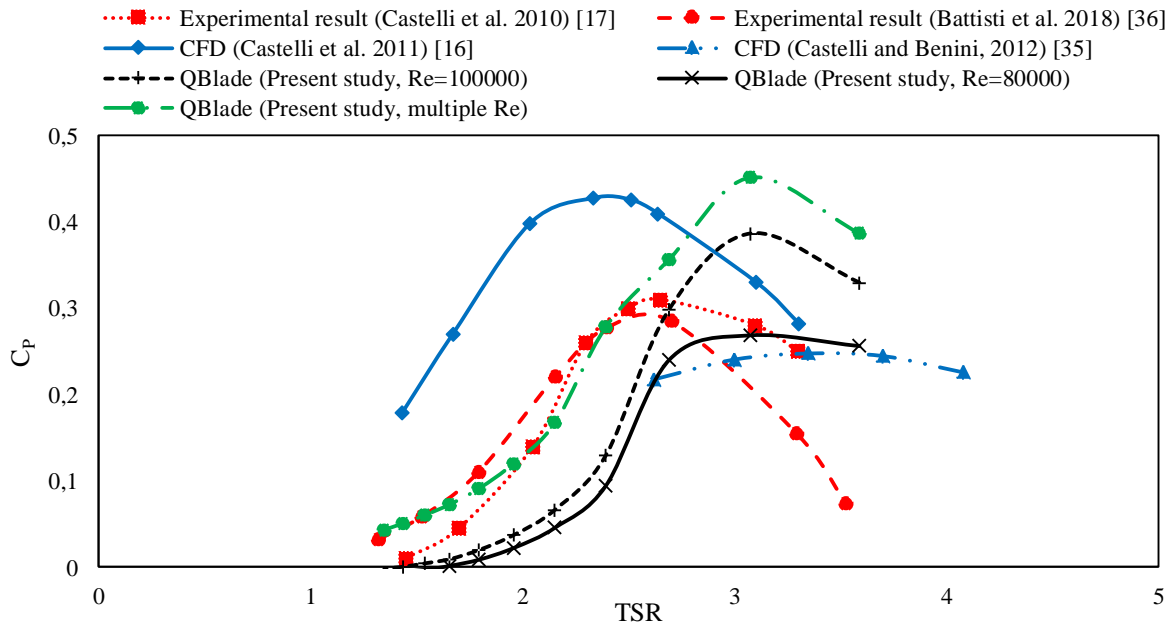


**Figure 5. Efficiency comparison of experimental, computational and numerical (present study) results at different TSR**

On the other hand, while experimental and computational studies have a bell-shaped  $C_p$ -TSR curve, QBlade analyses deliver rather straight or inclined linear behavior at right hand side of the curve. It has also been observed that, QBlade have overestimations in which the maximum  $C_p$  value is shifted toward to the right side at higher TSR values relative to other experimental and computational studies.

The power output vs. free stream speed curves for experimental analysis [36] and present study have been provided in Fig. 6 for 400 rpm rotational velocity. The peak power for both analyses having similar geometric and dynamic configurations are approximating to each other where, the right and left side of the curves should be more discussed. Right hand of  $P-U_\infty$  curve ( $U_\infty > 10$  m/s) represents smaller TSR amounts ( $< 2.15$ ) having very low power coefficient ranges for all analysis types (experimental, computational, numerical) which is less important than the region  $U_\infty < 10$  m/s. It is obvious that, lower free stream speed ranges at LHS deliver high efficiency ranges of Darrieus turbines which should be noticed for higher power output. We realized that,  $5 < U_\infty < 10$  velocity range is very important at 400 rpm rotational velocity in which TSR is between 2.15 and 4.3. In this region  $C_p$ -TSR curves which are discussed above can provide more accurate information for validation of QBlade analyses.

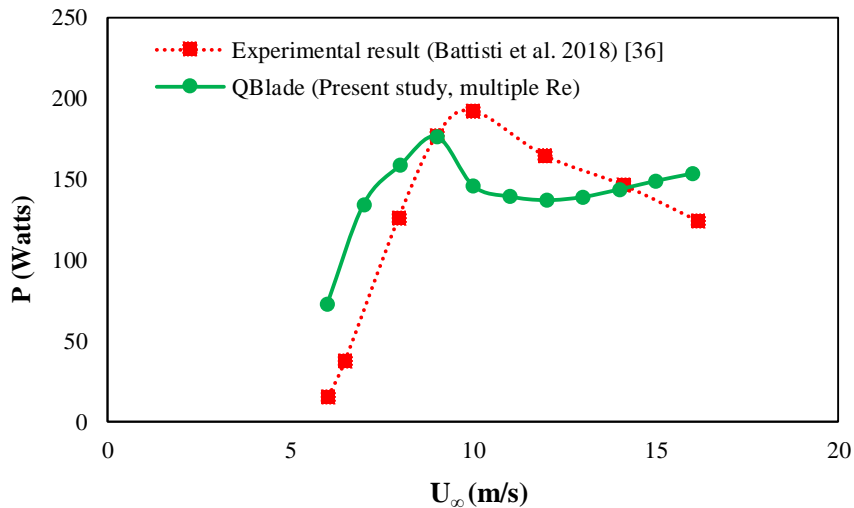


Figure 6. Output power vs. free stream speed comparison of experimental work [36] and this study

In order to assess the sensitivity of Reynolds number, Darrieus turbine performance results of QBlade algorithm for various Re numbers have been provided and summarized in Fig. 7. Again, it is observed that, higher Re numbers increases the overall power output and efficiency of Darrieus turbines by shifting the  $P-U_\infty$  and  $C_p-TSR$  curves towards upward direction. Also, the maximum  $C_p$  is observed at slightly higher TSR values.

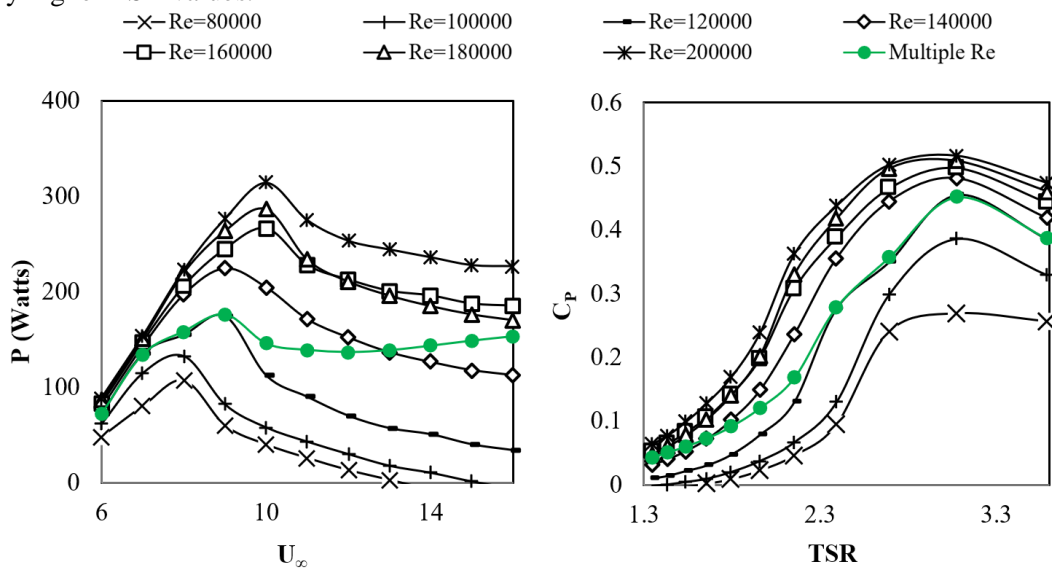


Figure 7.  $P-U_\infty$  and  $C_p-TSR$  curves of QBlade analyses at various Re numbers

Generated torque is a function of blade length. Therefore, the geometry having the same rotor height is needed for comparison the algorithm's output with reference studies. None of the above studies explicitly mention from the torque values for 1460 mm rotor height, thus we could not provide a detailed comparison for torque values. Nevertheless, QBlade algorithm outputs for torque fluctuations of overall three blades at different azimuthal position have been illustrated in Fig. 8. It is observed that, at 9 m/s steady wind speed, higher Re number shows explicitly higher torque outputs, as expected. Also, importance of the azimuthal position is clearly seen from the figure, in which, negative angles of attack deliver deteriorating performance. Thus, pitch regulation mechanism is suggested to maximize the power output from each blade by rotating the blades around their own axis to capture ideal angle of attack.

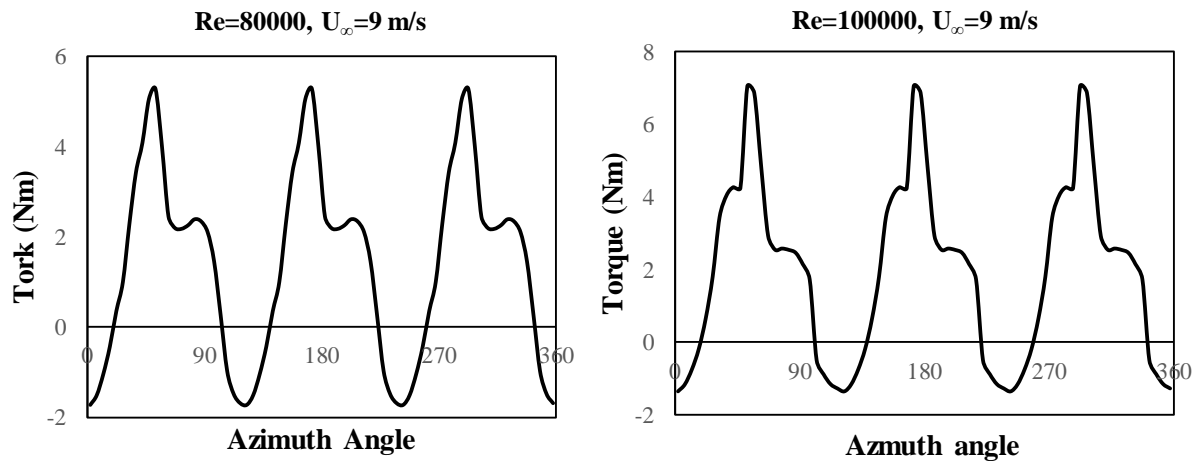


Figure 8. QBlade algorithm outputs for torque fluctuations of three bladed rotor

#### 4. Conclusion

In this paper, the DMS theory which is exploited by QBlade algorithm in order of finding the performance of vertical axis wind turbines has been tested and verified comparing with the experimental and computational results of similar rotor geometry. The proposed turbine geometry has been numerically analyzed by the QBlade code at different free stream and rotational velocity conditions. Overall, the analysis results have been found to have a good agreement (Fig. 6), however special attention should be made at suitable specification of Re number. Because higher Re numbers increases the overall power output and efficiency of Darrieus turbines (Fig. 7). QBlade algorithm has a module facilitating to introduce Re number for each blade segment. On the other hand, the rotor geometry analyzed in this study at the specified free stream conditions exhibited relatively higher power coefficient at high TSR values after the maximum power coefficient (Fig. 5). Authors suggest that, special attention should be paid for the results generated at this region of  $C_p$ -TSR curve at relatively lower free stream speed values. Consequently,  $P$ - $U_\infty$  curves are also found to be consistent together with non-significant discrepancies.

#### References

- [1] Kalair, A.R., Abas, N., Ul Hasan, Q., Kalair, E., Kalair, A., Khan, N. (2019). Water, energy and food nexus of Indus Water Treaty: Water governance. *Water-Energy Nexus*. 2 (1), 10–24.
- [2] Sims, R.E.H. (2004). Renewable energy: a response to climate change. *Solar Energy*. 76 (1–3), 9–17.
- [3] Lian, J., Zhang, Y., Ma, C., Yang, Y., Chaima, E. (2019). A review on recent sizing methodologies of hybrid renewable energy systems. *Energy Conversion and Management*. 199 112027.
- [4] Chaurasiya, P.K., Warudkar, V., Ahmed, S. (2019). Wind energy development and policy in India: A review. *Energy Strategy Reviews*. 24 342–357.
- [5] Ghasemian, M., Ashrafi, Z.N., Sedaghat, A. (2017). A review on computational fluid dynamic simulation techniques for Darrieus vertical axis wind turbines. *Energy Conversion and Management*. 149 87–100.
- [6] Aslam Bhutta, M.M., Hayat, N., Farooq, A.U., Ali, Z., Jamil, S.R., Hussain, Z. (2012). Vertical axis wind turbine – A review of various configurations and design techniques. *Renewable and Sustainable Energy Reviews*. 16 (4), 1926–1939.

- [7] Muratoglu, A., Yuce, M.I. (2017). Design of a River Hydrokinetic Turbine Using Optimization and CFD Simulations. *Journal of Energy Engineering*. 143 (4), 04017009.
- [8] Kirke, B.K., Lazauskas, L. (2011). Limitations of fixed pitch Darrieus hydrokinetic turbines and the challenge of variable pitch. *Renewable Energy*. 36 (3), 893–897.
- [9] Jagtap, M., Navale, L. (2017). Twist Angle Analysis of Helical Vertical Axis Wind Turbine (Vawt) Using Q-Blade. *International Journal of Research Publications in Engineering and Technology*. 3 (8), 2454–2475.
- [10] Hosseini, A., Goudarzi, N. (2019). Design and CFD study of a hybrid vertical-axis wind turbine by employing a combined Bach-type and H-Darrieus rotor systems. *Energy Conversion and Management*. 189 49–59.
- [11] Khan, M.J., Bhuyan, G., Iqbal, M.T., Quaiocoe, J.E. (2009). Hydrokinetic energy conversion systems and assessment of horizontal and vertical axis turbines for river and tidal applications: A technology status review. *Applied Energy*. 86 (10), 1823–1835.
- [12] Kim, S., Cheong, C. (2015). Development of low-noise drag-type vertical wind turbines. *Renewable Energy*. 79 199–208.
- [13] Scungio, M., Arpino, F., Focanti, V., Profili, M., Rotondi, M. (2016). Wind tunnel testing of scaled models of a newly developed Darrieus-style vertical axis wind turbine with auxiliary straight blades. *Energy Conversion and Management*. 130 60–70.
- [14] Bianchini, A., Balduzzi, F., Rainbird, J.M., Peiró, J., Graham, J.M.R., Ferrara, G., et al. (2015). On the influence of virtual camber effect on airfoil polars for use in simulations of Darrieus wind turbines. *Energy Conversion and Management*. 106 373–384.
- [15] Eric, H. (2006). Windmills and Windwheels. In *Wind Turbines*, Springer Berlin Heidelberg, Berlin. 1–21.
- [16] Raciti Castelli, M., Englaro, A., Benini, E. (2011). The Darrieus wind turbine: Proposal for a new performance prediction model based on CFD. *Energy*. 36 (8), 4919–4934.
- [17] Raciti Castelli, M., Ardizzon, G., Battisti, L., Benini, E., Pavesi, G. (2010). Modeling Strategy and Numerical Validation for a Darrieus Vertical Axis Micro-Wind Turbine. 409–418.
- [18] Ferreira, C.J.S., Bijl, H., Bussel, G. van, and Kuik, G. van (2007). Simulating Dynamic Stall in a 2D VAWT: Modeling strategy, verification and validation with Particle Image Velocimetry data. *Journal of Physics: Conference Series*. 75 012023.
- [19] D'Alessandro, V., Montelpare, S., Ricci, R., Secchiaroli, A. (2010). Unsteady Aerodynamics of a Savonius wind rotor: a new computational approach for the simulation of energy performance. *Energy*. 35 (8), 3349–3363.
- [20] Khadir, L., Mrad, H. (2015). Numerical investigation of aerodynamic performance of darrieus wind turbine based on the magnus effect. 9 (4), 383–396.
- [21] Ghazalla, R.A., Mohamed, M.H., Hafiz, A.A. (2019). Synergistic analysis of a Darrieus wind turbine using computational fluid dynamics. *Energy*. 116214.
- [22] Wakui, T., Tanzawa, Y., Hashizume, T., Nagao, T. (2005). Hybrid configuration of darrieus and savonius rotors for stand-alone wind turbine-generator systems. *Electrical Engineering in Japan (English Translation of Denki Gakkai Ronbunshi)*.
- [23] Consul, C., Willden, R., Ferrer, E., McCulloch, M. (2009). Influence of Solidity on the Performance of a Cross-Flow Turbine. in: Proc. 8th Eur. Wave Tidal Energy Conf. , Uppsala, Sweden pp. 484–493.
- [24] Brusca, S., Lanzafame, R., Messina, M. (2014). Design of a vertical-axis wind turbine: how the aspect ratio affects the turbine's performance. *International Journal of Energy and Environmental Engineering*. 5 (4), 333–340.
- [25] Qblade (2018). Wind turbine design and simulation. *Hermann Föttinger Institute of TU Berlin*.
- [26] Marten, D., Wendler, J., Pechlivanoglou, G., Nayeri, C.N., Paschereit, C.O. (2013). Qblade: An Open Source Tool for Design and Simulation of Horizontal and Vertical Axis Wind Turbines. *International Journal of Emerging Technology and Advanced Engineering*. 3 (3), 264–269.

- [27] Barooni, M., Ale Ali, N., Ashuri, T. (2018). An open-source comprehensive numerical model for dynamic response and loads analysis of floating offshore wind turbines. *Energy*. 154 442–454.
- [28] Bianchini, A., Marten, D., Tonini, A., Balduzzi, F., Nayeri, C.N., Ferrara, G., et al. (2018). Implementation of the “Virtual Camber” Transformation into the Open Source Software QBlade: Validation and Assessment. *Energy Procedia*. 148 210–217.
- [29] Mahmuddin, F. (2017). Rotor Blade Performance Analysis with Blade Element Momentum Theory. *Energy Procedia*. 105 1123–1129.
- [30] Suresh, A. and Rajakumar, S. (2019). Design of small horizontal axis wind turbine for low wind speed rural applications. *Materials Today: Proceedings*.
- [31] Rahimian, M., Walker, J., Penesis, I. (2018). Performance of a horizontal axis marine current turbine– A comprehensive evaluation using experimental, numerical, and theoretical approaches. *Energy*. 148 965–976.
- [32] Akour, S.N., Al-Heydari, M., Ahmed, T., Khalil, K.A. (2018). Experimental and theoretical investigation of micro wind turbine for low wind speed regions. *Renewable Energy*. 116 215–223.
- [33] Bangga, G., Dessoky, A., Lutz, T., Krämer, E. (2019). Improved double-multiple-streamtube approach for H-Darrieus vertical axis wind turbine computations. *Energy*. 182 673–688.
- [34] Liu, J., Lin, H., Zhang, J. (2019). Review on the technical perspectives and commercial viability of vertical axis wind turbines. *Ocean Engineering*. 182 608–626.
- [35] Castelli, M.R. Benini, E. (2011). Effect of Blade Inclination Angle on a Darrieus Wind Turbine. *Journal of Turbomachinery*. 134 (3).
- [36] Battisti, L., Persico, G., Dossena, V., Paradiso, B., Raciti Castelli, M., Brighenti, A., et al. (2018). Experimental benchmark data for H-shaped and troposkien VAWT architectures. *Renewable Energy*. 125 425–444.
- [37] Muratoglu, A. (2014). Design and simulation of a riverine hydrokinetic turbine, Ph.D. thesis, University of Gaziantep, 2014.
- [38] Morgado, J., Vizinho, R., Silvestre, M.A.R., and Páscoa, J.C. (2016). XFOIL vs CFD performance predictions for high lift low Reynolds number airfoils. *Aerospace Science and Technology*. 52 207–214.
- [39] Zhang, S., Li, H., Abbasi, A.A. (2019). Design methodology using characteristic parameters control for low Reynolds number airfoils. *Aerospace Science and Technology*. 86 143–152.
- [40] Yirtici, O., Cengiz, K., Ozgen, S., Tuncer, I.H. (2019). Aerodynamic validation studies on the performance analysis of iced wind turbine blades. *Computers & Fluids*. 192 104271.
- [41] Glauert, H. (1963). Airplane Propellers. vol. Aerodynamic Theory Volume IV. WF Durand.
- [42] Templin, R.J. (1974). Aerodynamic performance theory for the NRC vertical-axis wind turbine. *NASA STI/Recon Technical Report N*. 76.
- [43] Strickland, J.H. (1975). The Darrieus Turbine: A Performance Prediction Method Using Multiple Stream Tubes. in: Sand75-0431, p. 94550.
- [44] Saber, E., Afify, R., Elgamal, H. (2018). Performance of SB-VAWT using a modified double multiple streamtube model. *Alexandria Engineering Journal*. 57 (4), 3099–3110.
- [45] Paraschivoiu, I., Delclaux, F. (1983). Double multiple streamtube model with recent improvements (for predicting aerodynamic loads and performance of Darrieus vertical axis wind turbines). *Journal of Energy*. 7 (3), 250–255.
- [46] Biadgo, A.M., Simonović, A., Komarov, D., Stupar, S. (2013). Numerical and analytical investigation of vertical axis wind turbine. *FME Transactions*. 41 (1), 49–58.
- [47] Paraschivoiu, I. (2002). Wind turbine design: with emphasis on Darrieus concept. Polytechnic International Press, Canada.

- [48] Paraschivoiu, I (1982). Aerodynamic loads and performance of the Darrieus rotor. *Journal of Energy*. 6 (6), 406–41

## INVESTIGATION OF MECHANICAL AND THERMAL BEHAVIOR OF BASALT CUTTING WASTE (BCW) ADDED CLAY BRICK

Şermin KOÇYİĞİT<sup>1\*</sup>, Vedat Veli ÇAY<sup>2</sup>

*Porous clay bricks produced by adding 5%, 10%, 15% and 20% by weight of Basalt Cutting Waste (BCW) were manufactured by semi-dry pressing process. BCW (Karacadağ, Diyarbakir, Turkey) was added to brick raw material as an additive in order to increase porosity and strength. The chemical composition and thermal behaviors of raw materials were investigated and SEM analysis was performed. Brick mixes containing different proportions of BCW were formed and then fired at 900 and 1000° C for two hours. Porosity, water absorption, compressive strength, thermal conductivity and microstructure of the samples were examined. It was observed that the porosity ratios were increased by up to 34% with the addition of BCW, however, compressive strength (at least 28 MPa) decreased. However, the compressive strength was found to be higher than the required standards. The thermal conductivity of samples with the addition of 20% BCW decreased from 0.98 up to 0.72 W / mK compared to the reference sample, which also corresponds to a reduction of 26.5% in proportion to the reference sample along with the increase in porosity. The increase in firing temperature also affected the mechanical and physical properties of the samples. In conclusion, this study revealed that the brick samples produced could be evaluated and used as insulating materials by adding BCW to building materials in construction applications.*

**Key words:** *Clay brick, Basalt, Physical properties, Mechanical properties, Thermal conductivity*

### 1. Introduction

Recently, energy consumption of the buildings all over the world has become the most important problem. The energy consumed for the buildings in the world is generally used for heating and cooling. This consumption rate is approximately one third of the energy used in the world [1,2]. In this context, many countries in the world aim to reduce energy consumption in buildings. It is surely known that both economic and environmental concerns come to the forefront in the realization of these targets. Due to these concerns, it is most profitable and preferred solution is to improve thermal insulation properties in order to reduce energy consumption in buildings [3]. Approximately 30% of energy or heat loss in buildings passes through walls. [4-6]. The bricks used in walls are the most common construction

<sup>1</sup> Department of Construction Technology, Technical Sciences Vocational School, Dicle University, Diyarbakir, Turkey, (sermin.kocyigit@dicle.edu.tr)  <https://orcid.org/0000-0002-7283-8967>

<sup>2</sup> Department of Airframes and Powerplants, School of Civil Aviation, Dicle University, Diyarbakir, Turkey (vcay@dicle.edu.tr)  <https://orcid.org/0000-0002-2770-4038>

materials. Bricks should have good thermal insulation behaviors as well as mechanical properties. Fired clay bricks, which are the most well-known type of bricks and among the oldest known construction materials, are preferred because of their simple and reliable construction technique, relatively low cost and low maintenance cost, physical properties [7]. In addition, the bricks also offer a comfortable moisture environment with mechanical and thermal properties in buildings. [8]. The quality of the brick is highly dependent on the properties and composition of the raw materials, the production procedure, the firing method, and the temperature and time [9-11] The sintering process in clay bricks increases the strength of bricks. Sintering is the binding mechanism of clay particles and it can only be achieved under the influence of heat [12]. Furthermore, the thermal performance of bricks depends on the geometry of the pores formed in the brick [13,14]. If the porous structure of clay bricks is improved by appropriate methods, they may have a significantly lower thermal conductivity and permeability properties, which means that a lower heat loss can be achieved on the walls of homes [15,16]. Bricks can be formed with micropores by adding various organic and inorganic pore-forming additives (such as closed pores) to brick raw material mixtures before firing [17]. Some different pore-forming materials such as wood sawdust, polymers, leather residues, organic residues, coal dust, powder limestone, paper sediment and mineral additives providing thermal decomposition were commonly used .Heat resistant porous materials such as diatomite, zeolite, vermiculite and perlite were also utilized in ceramic bricks. [5,6,18–20].

Basalt is among the volcanic rocks in the classification of natural stones. Basalt, which is a dark gray and black volcanic rock that is mainly composed of feldspar and found in nature with crystalline and dense pulp or glassy nature, is widely available with various properties in Diyarbakır and Afyon provinces and in the Thrace region in Turkey [21].

Basalt deposits in Diyarbakır-Karacadağ cover large areas in the Southeastern Anatolia Region of Turkey. The basalt flow from the Karacadağ volcano, which provides the formation of these basalt stones, is widespread in an area of approximately 80 meters thick and 10.000 m<sup>2</sup>, especially in three regions of Diyarbakır [22]. Large basalt plateaus with a diameter of 120-130 km are observed in the regions on the way to Diyarbakır-Şanlıurfa in the west, Diyarbakır-Elazığ in the north and Diyarbakır-Mardin in the east. [23]. Basalt blocks are cut and sized according to the areas of usage. Basalt powders, which are characterized as waste, are formed during this cutting process. These waste powders are stored by business owners in an area that is not operational. The high abrasion resistance, low thermal conductivity, and resistance to acid and frost of the Diyarbakır-Karacadağ basalt have ensured the diversification of the areas of usage and have led to an increase in the studies related to this material. The geological, petrographic, tectonic and basalt-marble properties of different regions basalts of Turkey have been investigated with the studies conducted to date [24-29]. However, it was determined that there were no studies regarding the utilization of waste basalt cutting powders in the literature. Thus, the aim of this study was to determine of feasibility of using the waste basalt powder in production of clay brick samples and the effects on physical and mechanical properties and thermal conductivity of bricks.

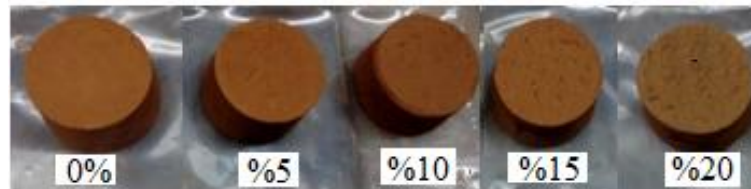
## 2. Mterials and Methods

In this study, it was aimed to produce brick samples from clay mixtures with BCW addition in order to be used as an insulating material. The mechanical and thermal behaviors of BCW additive in powder form in ratios of 5%, 10%, 15%, 20% by weight in clay bricks were examined.

**Table 1. Mixture proportions.**

Mix code	Firing temperature/time	Brick clay(wt.%)	Basalt(wt.%)
S0	900 <sup>o</sup> C/2h	100	0
S1	900 <sup>o</sup> C/2h	95	5
S2	900 <sup>o</sup> C/2h	90	10
S3	900 <sup>o</sup> C/2h	85	15
S4	900 <sup>o</sup> C/2h	80	20
P0	1000 <sup>o</sup> C/2h	100	0
P1	1000 <sup>o</sup> C/2h	95	5
P2	1000 <sup>o</sup> C/2h	90	10
P3	1000 <sup>o</sup> C/2h	85	15
P4	1000 <sup>o</sup> C/2h	80	20

The mixture ratios are presented in Tab. 1. The clay raw material was obtained from the brick manufacturer and the BCW was obtained from the basalt processing plant (in Diyarbakır, Turkey). Clay and BCW were first subjected to pretreatments such as drying, grinding and sieving. Raw materials with a particle size of less than 150  $\mu\text{m}$  were used for the production of bricks. They were mechanically mixed in a laboratory mixer with sprayed water for approximately 15% of total weight for 30 minutes to obtain homogeneity and density in the mixtures.

**Figure 1. Brick production**

For each test, brick samples with  $\text{Ø}=3\text{cm}$ ,  $h=2\text{cm}$  sizes were semi-dry pressed to a mold with a hydraulic press under a pressure of 10 MPa and kept at room temperature overnight. The samples were dried in the furnace at 40<sup>o</sup> C for 20 hours and then at 100<sup>o</sup> C for 18 hours. After drying, the samples were fired in a laboratory electric furnace (Protherm PLF12 / 15) at a rate of 5<sup>o</sup>C/min for 2 hours at 900<sup>o</sup>C and 1000<sup>o</sup>C. The samples fired at 1000<sup>o</sup>C are presented in Fig. 1. Then, the water absorption, porosity, compressive strength and thermal conductivity values of these samples were measured. The measurements of thermal conductivity values were performed using the C-Therm TCi Thermal Conductivity Analyzer [9].

## 2.1. Thermal conductivity measurements

Although the thermal conductivity analyzer measure with an error of less than 0.4%, the mathematical discussion of the error was examined in this study. Because the error is important on the thermal performance of the material. The basic procedure for examining and minimizing the error in thermal measurements is presented below:

- At least three different samples are tested under three different thermal and moisture conditions of each material.
- Each test consists of at least ten thermal measurements.
- The characteristic thermal conductivity value is obtained for ninety tests under three different thermal and moisture conditions, considering the average value in each sample.

### 3. Results and Discussion

#### 3.1. Characterization of the raw material

The chemical compositions of clay and BCW raw material made by XRF analysis are presented in Tab. 2.

**Table 2. Chemical composition of raw material (wt.%).**

Oxides	Clay	BKA
SiO <sub>2</sub>	59.9	46.04
Al <sub>2</sub> O <sub>3</sub>	16.1	13.89
Fe <sub>2</sub> O <sub>3</sub>	7.3	4.89
CaO	2.08	9.12
MgO	2.12	8.76
K <sub>2</sub> O	2.33	1.04
Na <sub>2</sub> O	0.81	3.64
SO <sub>3</sub>	-	-
Loss on ignition	9.36	12.62

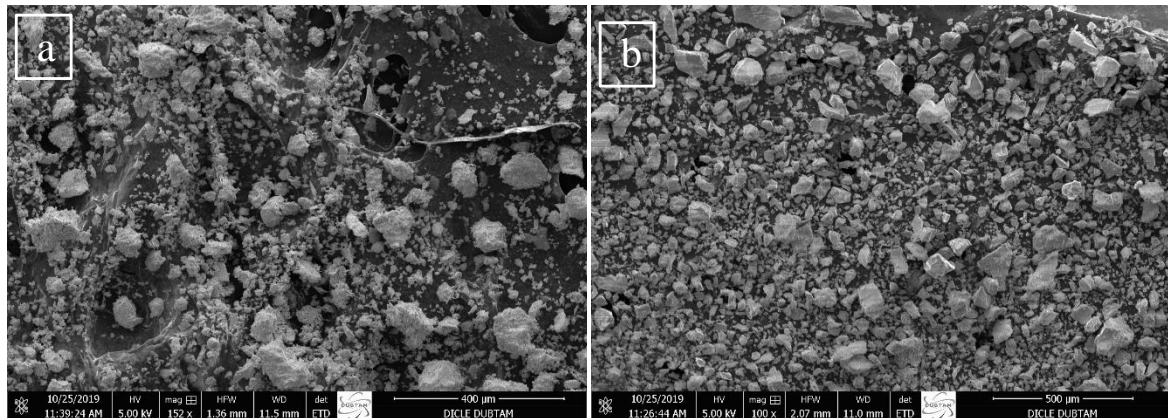


**Figure 2. Raw material morphologies a) clay, b) BCW**

SEM images of clay and BCW raw materials after sieving are presented in Fig. 2. Brick clay contains aluminum, iron, calcium, magnesium and potassium oxides as well as a large silica fraction. Basalt, which is one of the volcanic stone masses, is the most important stone of the gabbro family with its dark color, microlithic or glassy texture and homogeneous structure. The composition of the basalt includes basic feldspar such as augite microliths, enerphit and labrador, magnetite and olivine granules, and also sometimes substances such as ilmenite and hornblende.

### 3.2. Characterization of the fired samples

#### 3.2.1. Apparent porosity

The porosity values of the produced bricks are presented in Fig. 3. As it is seen in Figure 3, the porosity ranged from 28.4% to 33.8%. The lowest porosity was obtained at P0.

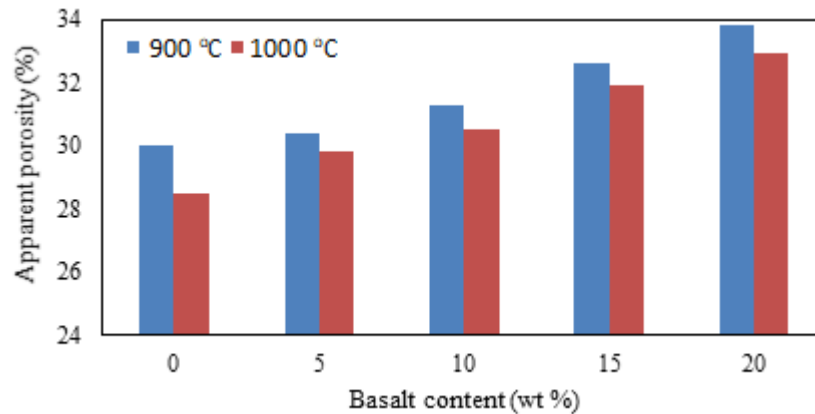


Figure 3. Apparent porosity of the produced bricks.

The highest porosity was observed in S4. As it is seen in Fig. 3, the difference between the two reference bricks (S0 and P0) was 5.1%. When the porosities of S1, S2, S3 and S4 were compared with S0, they were higher by 1.3%, 4.3%, 8.7% and 12.6%, respectively. When the porosities of P1, P2, P3 and P4 were compared with P0, porosity ratios were higher by 4.8%, 7.3%, 12.1% and 15.7%, respectively.

As it is understood, the addition of BCW in the brick had a significant effect on the porosity of the samples since it increased the porosity slightly at both temperatures. When each group containing the same BCW ratio was examined to see the effect of the fire temperature, the largest difference was found to be 5.1% between S0 and P0. As it is seen in Fig. 3, the effect of temperatures in the bricks containing BCW was negligible. The porosity of the brick increased slightly due to the release of CO<sub>2</sub> gas during decomposition and the lack of full adhesion of the BCW. The increase in the porosity of the brick helps improve thermal insulation properties. In cement based composites, it is necessary to increase porosity to obtain high thermal insulation performance. Therefore, air entraining agent and expanded polystyrene (EPS) are used in the buildings. However, their use increases the cost. Furthermore, EPS loses its function when it is exposed to fire. The increase in the porosity of both cement-based and clay-based composites generally leads to a decrease in strength. However, the bricks containing BCW do not show significant strength loss.

### 3.2.2. Water absorption

The water absorption values of the produced bricks are presented in Figure 4. As it is seen in Fig. 4, water absorption values ranged from 16.1% to 20.4%. The lowest water absorption value was obtained in P0 with the lowest porosity and the highest bulk density. The highest water absorption value was observed in S4 with the highest porosity and the lowest bulk density.

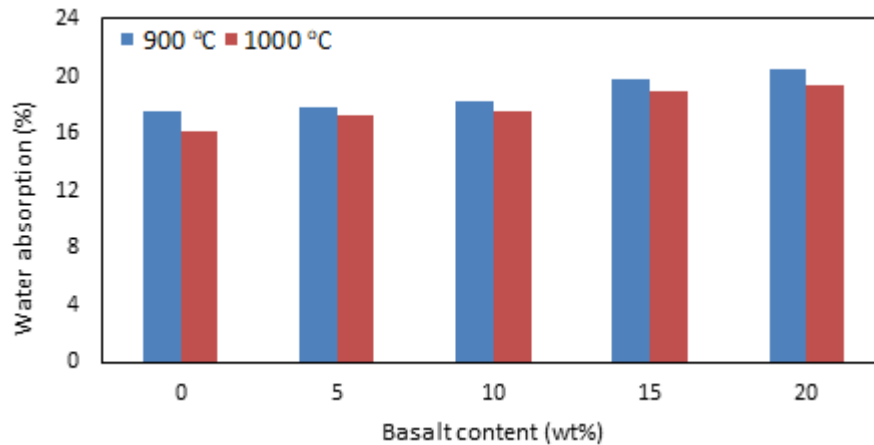


Figure 4. Water absorption of the produced bricks.

### 3.2.3. Compressive strength

Compressive strength is the most important property of construction materials. In many countries, clay bricks are allowed up to be used up to three storeys in building applications. Therefore, it is known that bricks should have a minimum compressive strength of 7 MPa according to Turkish and relevant European Standards (TS EN 771-1). As it is seen in Fig. 5, the compressive strength of the samples produced was decreased depending on the concentration of BCW in the brick for both temperatures.

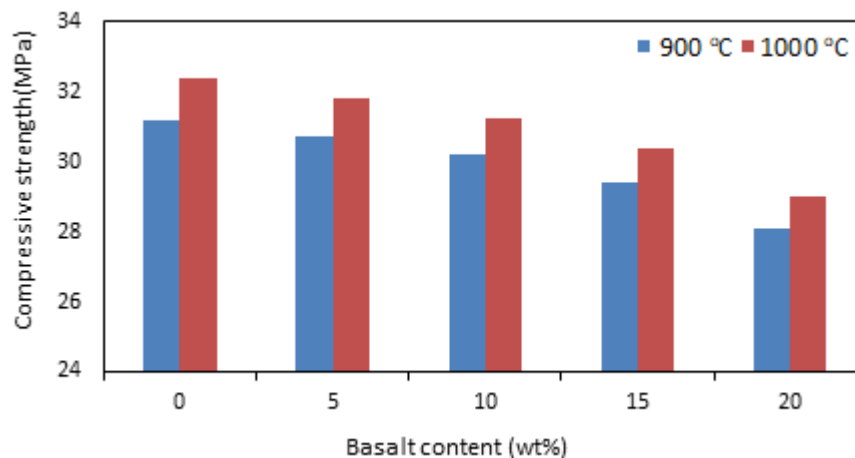


Figure 5. Compressive strength of the produced bricks.

Compressive strength values ranged from 28,1 MPa to 32,4 MPa. The highest strength samples observed in the samples produced were observed in P0 (32.4 MPa) and S0 (31.2 MPa) reference samples. Among the samples, the lowest strength values were observed in S4 (28.1 MPa) and P4 (28.9 MPa) with a concentration of 20% BCW. The compressive strengths of S1, S2, S3 and S4 containing BCW were found to be lower by 1.5%, 3.2%, 5.8% and 10%, respectively, compared to S0. The compressive strengths of P1, P2, P3 and P4 containing BCW were found to be lower by 1.8%, 3.6%, 6.3% and 11.5%, respectively, compared to B1. With this comparison, it was understood that BCW had a significant effect on the compressive strength of the clay brick, and that the effect of temperature was low. Although the bricks lost their strength, all bricks still had high compressive strength. The reason underlying the loss of pressure is related to the porosity of the brick. The values obtained are very suitable for structural applications even in earthquake zones. When density and compressive strength are evaluated together, the bricks produced provided superior values compared to lightweight concrete. When the relationship between porosity and compressive strength was examined, compressive strength decreased while porosity increased. Furthermore, it can be concluded that BCW utilization rate in the samples may increase by more than 20%. Many lightweight concrete containing perlite, vermiculite and expanded polystyrene (EPS) for insulation purposes generally have low compressive strength and are not sufficient for structural applications [30,31]. The bricks with BCW have the thermal insulation and durability required for structural applications. Nevertheless, further studies should be carried out by adding some additives (vermiculite, pumice, perlite, etc.) to the sample to see the effects of mineral additives such as BCW on the properties of bricks.

### 3.2.4. Thermal conductivity

The thermal conductivity results of the bricks produced are presented in Figure 6. The thermal conductivity values of the reference samples (S0 and P0) were 0.98 and 1.12 W/m K, respectively. The thermal conductivity value of the samples decreased to 0.72 W/m K (sample S4) depending on the amount of BCW added to the clay brick mixture.

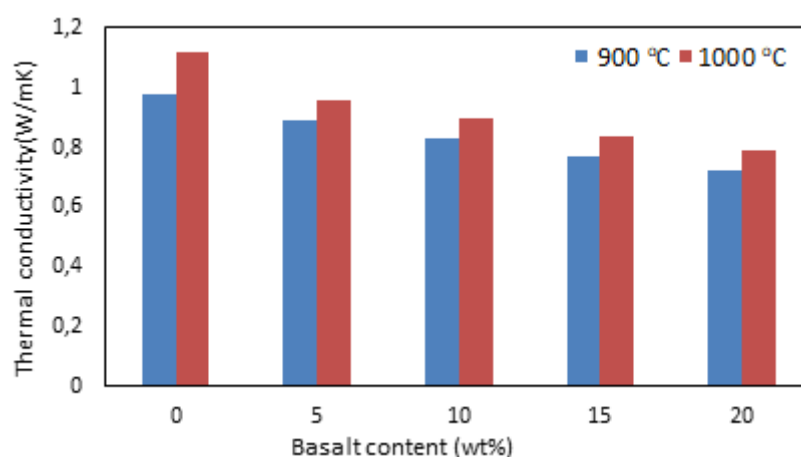


Figure 6. Thermal conductivity of the produced bricks.

Fig. 6 also shows a comparison of thermal conductivities in each group and at each temperature. The thermal conductivity values of S1, S2, S3 and S4 containing BCW were found to be lower by 9.18%, 15.3%, 21.4% and 26.5%, respectively, compared to S0. The thermal conductivity values of P1, P2, P3 and P4 containing BCW were found to be lower by 14.17%, 19.73%, 25% and 29.6%, respectively,

compared to P0, which was due to the increased porosity of the brick. These results indicated that the thermal performance of the bricks should be improved by the use of additional pore-forming materials in the brick.

### 3. Conclusions

In this study, the usability of BCW in brick production was examined. Clay brick samples with different proportions of BCW were produced. The key results of the use of BCW in the production of fired clay bricks are as the following.

- The bulk brick density decreased to  $1.73 \text{ g / cm}^3$  at  $900^\circ \text{ C}$  and up to  $1.82 \text{ g / cm}^3$  at  $1000^\circ \text{ C}$  with BCW depending on its content in the mixture.
- Although lower density was observed at  $900^\circ \text{ C}$ , the effect of temperature on bulk density was smaller and negligible. It is extremely important to reduce the bulk density of the bricks in order to decrease the dead building load. The reduction of the dead load decreases the sections of the load bearing elements of the building.
- BCW had a significant effect on sample porosity. The addition of BCW increased the porosity of fired bricks up to 34%. The effect of temperature changes on brick porosity was insignificant. The increase in the amount of BCW in the bricks resulted in an increase in the thermal insulation performance of the bricks.
- Water absorption of the bricks increased depending on the increase in the amount of BCW. There was a close relationship between water absorption and brick porosity. Higher porosity led to higher water absorption.
- The bricks with 5-20% BCW added to the brick clay had a compressive strength of 28.08-32.38 MPa above 7 MPa as required by the standard. Compressive strength is very important for load bearing elements of walls. The compressive strength of the samples with the addition of BCW was found to be lower compared to the compressive strength of the reference brick at both temperatures. Moreover, it was observed that all bricks with the addition of BCW were found to have greater strength than 18 MPa, which can be used in structural applications, meeting the disaster regulation for a building material that meets the requirement of TS EN 771.
- The addition of BCW increased the thermal performance of bricks. The thermal conductivity of the brick was related to porosity. Nevertheless, thermal insulation performance of bricks could be improved by the use of additional pore-forming materials in the brick. Therefore, further studies on different BCW concentrations, combinations and pore-forming agents should be carried out to see the effects of structural composites on both physical, physico-mechanical and thermal performance. The raw materials of the produced samples and the microstructures of the composites are very important to achieve the desired results. As it was clearly understood from the test results in this study, the bricks containing BCW have superior properties compared to lightweight concrete containing BCW, which clearly indicates the high potential for the use of BCW in clay. Furthermore, it is necessary to study the combination of different additives and the properties of BCW bricks.

## References

- [1] Balaras, C.A., Droutsa, K., Argiriou, A.A., Asimakopoulos, D.N. (2000). Potential for energy conservation in apartment buildings. *Energy and Buildings*, 31 (2), 143–154.
- [2] EN832 Standard. Thermal Performance of Buildings: Calculation of Energy Use for Heating – Residential Buildings CEN, Brussels, Belgium, 1998.
- [3] del Coz Díaz, J., García Nieto, P.J., Suárez Sierra, J.L., Penuelas, Sánchez, I. (2008). Non-linear thermal optimization and design improvement of a new internal light concrete multi-holed brick walls by FEM. *Applied Thermal Engineering*, 28 (8), 1090–1100.
- [4] Sutcu, M. Akkurt, S. (2009). The use of recycled paper processing residues in making porous brick with reduced thermal conductivity, *Ceramics International*. 35 (7), 2625–2631.
- [5] Sutcu, M., del Coz Díaz, J.J., Álvarez Rabanal, F.P., Gencel, O., Akkurt, S. (2014). Thermal performance optimization of hollow clay bricks made up of paper waste. *Energy and Buildings*. 75 96–108.
- [6] Sutcu, M. (2014). Influence of expanded vermiculite on physical properties and thermal conductivity of clay bricks. *Ceramics International*. 41 (2). 2819–2827.
- [7] Gencel, O. (2015). Characteristics of fired clay bricks with pumice additive. *Energy and Buildings*, 102, 217-224.
- [8] Ashmarin, A.G., Vlasov, A.S. (2005). Wall ceramics from zeolite-bearing argillaceous materials, *Glass and Ceramics*, 62 (9–10), 314–316.
- [9] Akpınar, E. K., Koçyigit, F. (2016). Thermal and mechanical properties of lightweight concretes produced with pumice and tragacanth. *Journal of Adhesion Science and Technology*, 30(5), 534-553.
- [10] Koçyigit, Ş., Çay, V.V. (2017). Mechanical properties of the composite material produced by the mixture of expanded perlite, waste marble dust and tragacanth. *European Journal of Technique*, 8(2), 124-133.
- [11] Gencel, O., Sutcu, M., Erdogmus, E., Koc, V., Cay, V.V., Gok, M. S. (2013). Properties of bricks with waste ferrochromium slag and zeolite. *Journal of cleaner production*, 59, 111-119.
- [12] Dondi, M., Mazzanti, F., Principi, P., Raimondo, M., Zanarini, G. (2004). Thermal conductivity of clay bricks. *Journal of Materials in Civil Engineering*, 16(1), 8-14.
- [13] Görhan, G., Şimşek, O. (2013). Porous clay bricks manufactured with rice husks. *Construction and Building Materials*, 40, 390-396.
- [14] Raut, S. P., Ralegaonkar, R. V., Mandavgane, S. A. (2011). Development of sustainable construction material using industrial and agricultural solid waste: A review of waste-create bricks. *Construction and Building Materials*, 25(10), 4037-4042.
- [15] Al-Hazmy, M. M. (2006). Analysis of coupled natural convection–conduction effects on the heat transport through hollow building blocks. *Energy and Buildings*, 38(5), 515-521.

- [16] Cay, V. V., Sutcu, M., Gencel, O., Korkut, T. (2014). Neutron radiation tests about FeCr slag and natural zeolite loaded brick samples. *Science and Technology of Nuclear Installations*, Volume 2014, 5 pages
- [17] Rimpel, E., Rehme, F. (2001). Development of extruded high-thermal insulating bricks. *ZI International*, 54(12), 36-41.
- [18] Zhang, L. (2013). Production of bricks from waste materials – a review, . *Construction and Building Materials*, 47 643–655.
- [19] Valášková, M., Martynková, G. S., Smetana, B., Študentová, S. (2009). Influence of vermiculite on the formation of porous cordierites. *Applied Clay Science*, 46(2), 196-201.
- [20] Koksall, F., Gencel, O., Brostow, W., Lobland, H. H. (2012). Effect of high temperature on mechanical and physical properties of lightweight cement based refractory including expanded vermiculite. *Materials Research Innovations*, 16(1), 7-13.
- [21] Uz, B. (2001). Sert Mermer Grubuna Bir Örnek; Diyarbakır Karacadağ Bazaltlarının Mermer Açısından İncelenmesi. Türkiye III. Mermer Sempozyumu Bildiriler Kitabı. Afyon, 43-53.
- [22] Işık, N., Yıldız, S., Keleştemur, O. (2008). Investigation of the Mechanical Properties of Basalt Stones in the Diyarbakır-Karacadağ. *Science and Eng. J of Fırat Univ*, 20(4), 617-626.
- [23] KAHVECİ, A. E., KadayıfÇi, A. (2013). Investigation structural properties of basalt stone in diyarbakir region. *Uluslararası Teknolojik Bilimler Dergisi*, 5(3), 56-69.
- [24] Hassan, M.Y. (2001). Basalt Rock as an Alternative Raw Material in Portland Cement Manufacture. *Materials Letters*, 50, 172–178.
- [25] Al-Harhi, A.A., Al-Amri, R.M., Shehata, W.M. (1999). The Porosity and Engineering Properties of Vesicular Basalt in Saudi Arabia, *Engineering Geology*, 54, 313–320.
- [26] Franzone, J.G. (1980). Geology Geotechnical Properties and Vesicular Rock Classification of Lousetown Basalt And Lattices Truckee Area California, M.Sc. Thesis, Unpublished University of Nevada.
- [27] Tugrul, A., Gurpinar, O. (1997). A Proposed Weathering Classification for Basalt and Their Engineering Properties (Turkey), *Bulletin of Engineering Geology and the Environment*, 55, 139-149.
- [28] Houston, E. C., Smith, J. V. (1997). Assessment of Rock Quality Variability due to Smectitic Alteration in Basalt Using X-Ray Diffraction Analysis. *Engineering Geology*, 46, 19-32.
- [29] Korkanç, M., Tuğrul, A. (2005). Evaluation of Selected Basalts from the Point of Alkali-Silica Reactivity. *Cement and Concrete Research*, 35, 505-512.
- [30] Cha, J., Seo, J., Kim, S. (2012). Building materials thermal conductivity measurement and correlation with heat flow meter, laser flash analysis and TCi. *Journal of thermal analysis and calorimetry*, 109(1), 295-300.
- [31] Shannag, M. J. (2011). Characteristics of lightweight concrete containing mineral admixtures. *Construction and Building Materials*, 25(2), 658-662.
- [32] Schackow, A., Effting, C., Folgueras, M. V., Güths, S., Mendes, G. A. (2014). Mechanical and thermal properties of lightweight concretes with vermiculite and EPS using air-entraining agent. *Construction and Building Materials*, 57, 190-197.

## PANTOGRAPHY APPLICATION WITH REAL-TIME PLC BASED ON IMAGE PROCESSING IN GANTRY ROBOT SYSTEM

İrem KÖSE<sup>1</sup>, Sıtkı ÖZTÜRK<sup>2</sup>, Melih KUNCAN<sup>3\*</sup>

*Programmable Logic Controllers (PLC) is one of the indispensable products of automation industry. PLCs, which are widely used in many fields of programming, make our lives easier in daily life. In this study, after determining the coordinates of the image taken from the camera with the help of image processing algorithm, the servo drives of cartesian machine are controlled and processed in X-Y plane with Rexroth PLC in real time. In this application, it is aimed to obtain the image again by subtracting the boundary coordinates of the image taken with the camera in MatLab environment. To achieve this goal, the servo drives of the cartesian machine were controlled and the application was realized. Two different methods were applied for the image taken in Matlab environment. The skeleton of the image was taken for the first method and then the boundary coordinates were determined. For the second method, the contour of the image was first extracted. The coordinates of the contour image were not directly used. These coordinates have been tried to be optimized.*

*In this study, it is aimed to draw a desired image by drawing border coordinates in Matlab with Rexroth PLC on a cartesian machine. As a result of the test studies, it was seen that the drawing process was carried out properly (according to the coordinates received) as a result of the analysis and measurement processes (metric caliper and measurement methods).*

Key words: *Rexroth PLC, MatLab, Image Processing, Skeleton, Contour*

### 1. Introduction

A digital image is formed by the conversion of the light energy (analog signal) reflected by the objects into a digital signal by the sensor. The basic component of an image is pixels. A numerical image is expressed by a matrix of MxN sized pixels. For grayscale images, the image consists of different grayscale values. Gray value ranges are expressed as {0,1,2, ..., 255}.

---

<sup>1</sup> Department of Electronics and Communication Engineering, Kocaeli University, Kocaeli, Turkey, (koseirem1@gmail.com)  
<https://orcid.org/0000-0001-9679-3137>

<sup>2</sup> Department of Electronics and Communication Engineering, Kocaeli University, Kocaeli, Turkey, (sozturk@kocaeli.edu.tr)  
<https://orcid.org/0000-0003-3804-5581>

<sup>3\*</sup> Department of Electrical and Electronics Engineering, Siirt University, Siirt, Turkey, (melihkuncan@siirt.edu.tr)  
<https://orcid.org/00000-0002-9749-0418>

The acquisition of information from the images and interpretation of these information forms the basis of the image processing area by processing and analyzing the digitized images by means of developed methods such as video camera and scanner. Examples of image processing applications are industrial quality / production controls from factory automation applications, counting of blood cells from medical applications, character recognition from computing applications, face recognition from security applications, and production of intelligent weapons from military applications. In recent years, it has been seen in the literature that there are many different studies using image processing techniques for automation and production sectors.

Today, digital image processing and image recognition technology is used in many different fields. Another area of use of this technology is, of course, industry. Production is rapidly automated thanks to the robot and artificial intelligence technique developed especially in the assembly industry. The identification of the smooth shapes used in the industry and the definition of the positions and areas of rotation of these shapes will pave the way for new industrial applications.

The variety of applications with image processing is increasing day by day. Plate reading systems, face recognition applications, fingerprint recognition applications, iris recognition applications such as applications that are commonly used today are examples of image processing [1-3].

Another recent topic is the robots. When we talk about robot, the first thing that comes to mind is humanoid machines that think and decide like human beings. This shows that the design of robots is inspired by the structure of living things.

When robot is mentioned, humanoid robots come to mind first. The structure of Cartesian robots is different from that of humanoid robots. Cartesian robots consist of axes perpendicular to each other. Gantry robots are also a kind of cartesian robot. What distinguishes Gantry robots from cartesian robots is that they have two bearing axes. This robot configuration is the robot design with the most limited mobility.

In a cartesian coordinate system, the location of the coordinate system center is the center of the junction of the first two links. The center does not move except for the movements towards the center of the robot, ie the center of the robot is fixed. Cartesian robots consisting of three linear axes are widely used in industrial applications and for manufacturing purposes. Cartesian robots have applications such as packaging, logistics, milling, laser, plasma, oxy acetylene cutting machines, water jet cutting, electro erosion [4-10].

In this study, digital image processing and cartesian robot are combined in this system and real time processing (writing) application is realized with PLC control.

In the first stage of the application, the image taken with the camera was processed in Matlab environment. Two different methods were used to edit this image. For the first method, the image was converted to a black and white image. Then the skeleton of the image was taken and in this way boundary coordinates were obtained. In the second method, the image was passed through a threshold value and the contour of the black and white image obtained in this way was taken and the coordinates were obtained. Optimization process was performed for the obtained coordinates.

In the second stage of the application, the coordinate values were transferred to Rexroth PLC. A series was defined in the program and position information was obtained. The end information of the index was checked with 0. When the sequence is over, the sprung system connected to the relay goes up, ie the relay is deactivated. And the engines for the next series have taken position. Thanks to the

control of servo motors according to the specified coordinates (X and Y), real-time processing (writing operation) was performed on the cartesian robot.

## 2. Test Setup

The mechanism used in the application consists of a cartesian robot that can move in two axes and a pneumatic vacuum holder that can move in the vertical axis. As a result of the processing and evaluation of the image taken from the camera by the computer, the letters are positioned in the horizontal and vertical coordinates. The movement of the robot in the X and Y axes is provided by two servo motors. Each motor is driven by its own drive. These drives are controlled by 1 Rexroth PLC. These PLCs can communicate with the computer via RS232 serial bus and receive commands related to the tasks of the robot and make restrictions on the current situation. Figure 1a shows a solid model showing the movement of the gantry robot in the X (vertical) - Y (horizontal) and Z (vertical) axes. The solid model of the test apparatus is shown in Figure 1b and the computer connection of the X and Y axes in Figure 2 is shown in the block diagram. Figure 3 and Figure 4 show the experimental setup.

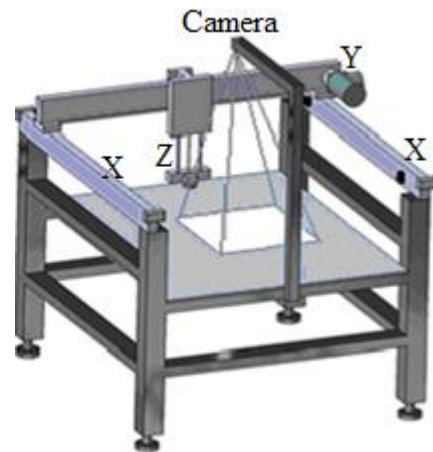
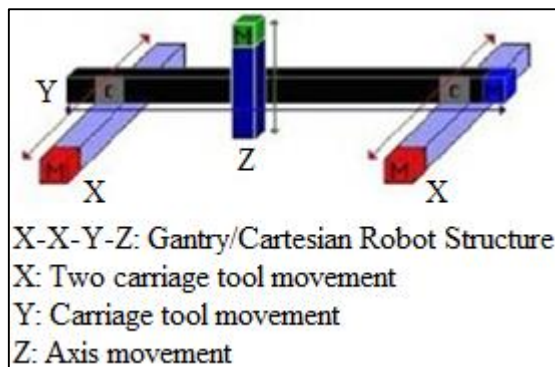


Figure 1a. Solid model of the gantry robot

Figure 1b. Solid model of the experimental setup

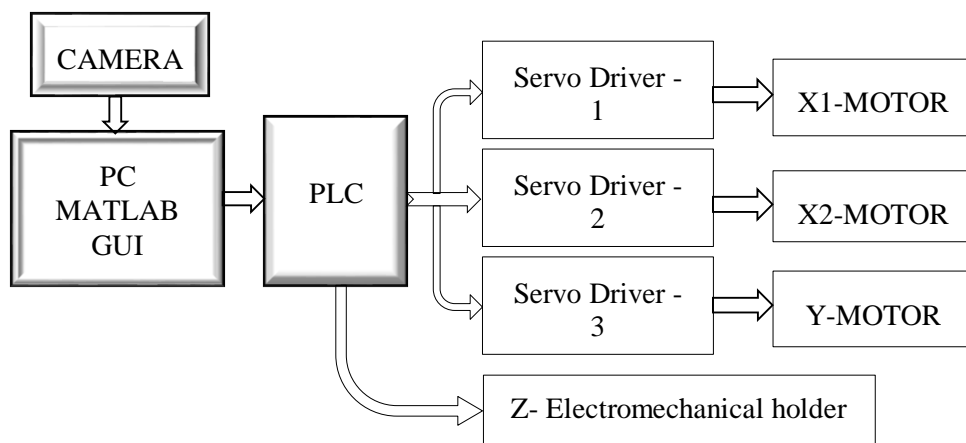
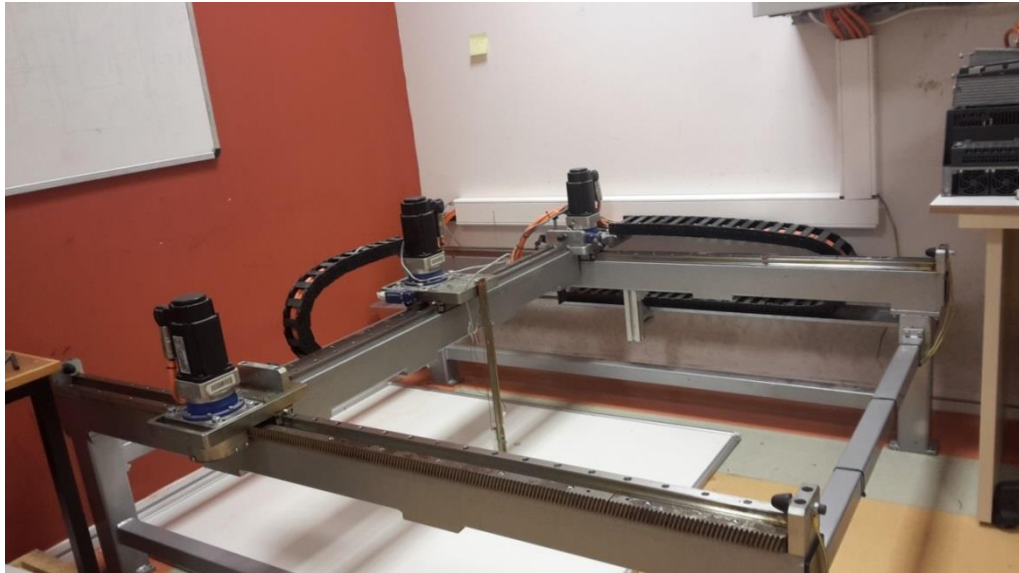


Figure 2. Computer connection of X and Y



**Figure 3. The experimental setup**



**Figure 4. The experimental setup**

### **3. Image Processing Method**

In this section, it has been studied on the recognition of the coordinates of the center points in MATLAB by using digital image processing techniques independently of the rotation and size of the geometric shapes. Image processing techniques were used to extract the boundary coordinates of the image taken with the camera. Two methods are used to extract boundary coordinates. The first method is the skeletal extraction technique, which is a morphological procedure. In the second method, the contour of the image is taken and the coordinates are obtained after an optimized operation. In the Matlab environment, the x-y boundary coordinates of the object in the image obtained by processing and evaluating the image taken from the camera are sent to the PLC and the drawing of the object is realized.

### 3.1. Obtaining a Coordinate by Skeleton

Matlab contains many morphological functions. Skeleton retrieval from these morphological functions removes pixels from the boundaries of objects, but does not allow the object to break apart. The remaining pixels form the image skeleton [11-12]. The general steps of the algorithm of the proposed method are shown in Figure 5.

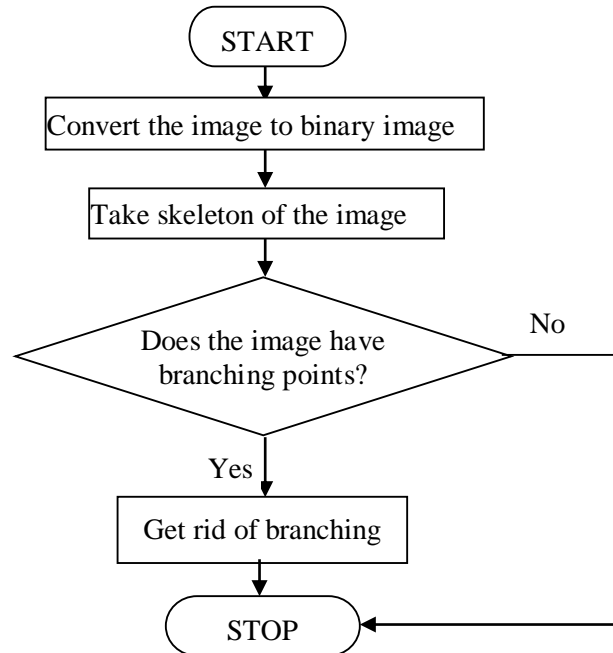


Figure 5. Algorithm of suggested method

The mathematical expression of the skeletal function can be explained as follows:

A's skeleton is defined by 'erosions ( $\ominus$ )' and 'openings ( $\circ$ )' operations [2].

$$S(A) = \bigcup_{k=0}^K S_k(A) \quad (1)$$

$$S_k(A) = (A \ominus kB) - (A \ominus kB) \circ B \quad (2)$$

B is the structuring element seen in Equation (2).  $(A \ominus kB)$  indicates the successive erosion of A.

$$(A \ominus kB) = (\dots((A \ominus B) \ominus B) \ominus \dots) \ominus B \quad (3)$$

The equation in equation (3) is repeated k times. K is the iterative step before A erodes to an empty cluster.

$$K = \max \{k \mid (A \ominus kB) \neq \emptyset\} \quad (4)$$

As a result, the skeleton of A is obtained by combining skeletal subsets. When the disadvantages of this method are evaluated, the skeleton is formed when more points are determined while selecting the points forming the skeleton. However, unnecessarily selected points create unwanted branching points in the image. When the steps in the given algorithm are followed, the creation of the skeletal points of the image is shown in Figure 6. After this step, the boundary

coordinates of the image are taken with the `bwboundaries` command. Creates 6 matrices within the variable. These matrices express each letter sequentially.



**Figure 6. Created skeleton points**

### 3.2. Obtaining a Coordinate by Contour

At this stage, the image is first passed through a threshold level. Then, the gaps in the image are filled with the morphological command `imfill`. In the next step, the contour of the image is taken. Figure 7 shows the contour of the original image.

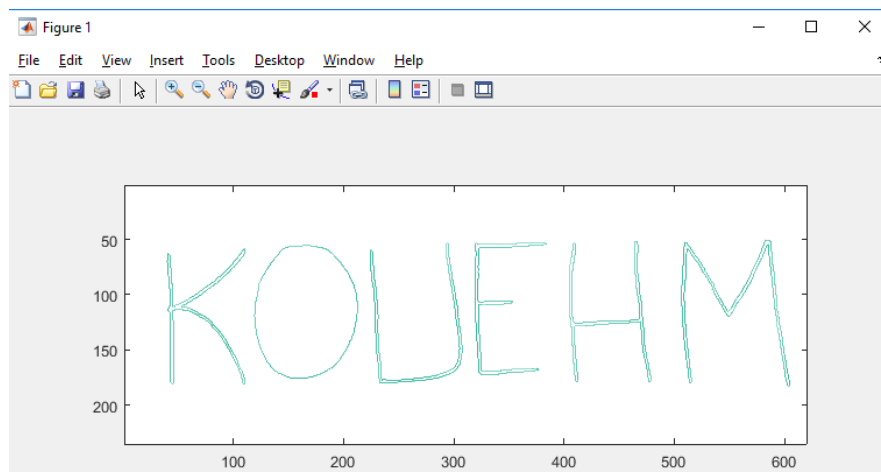


**Figure 7. Contour of original image**

In the second stage of the application, “`polyarea`” function is used. This function returns the polygon fields defined by the X and Y columns if X and Y are matrices of the same size.

The contour obtained in the application was stored in variable C. This variable is divided into x and y coordinates. All rows and columns are transposed and the `polyarea` function is performed in a while loop. Figure 8 shows the “`polyarea`” function.

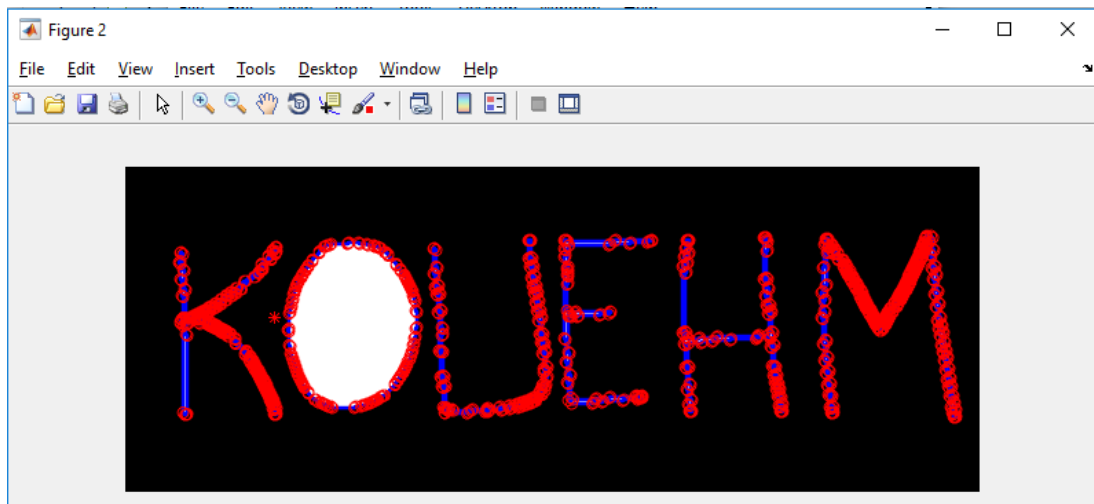


**Figure 8. Processed polyarea method of image**

In this application, another application was tried to be made in order to ensure the optimization of the coordinates received. Certain points are selected from the contour image. These dots are expected to form letters. The most important detail here, the need for too many points, the progress of the ranking is very important for the success of the application. Therefore, this process has been realized by optimizing the points on the image at hand. Figure 9 shows the optimized version of the image.

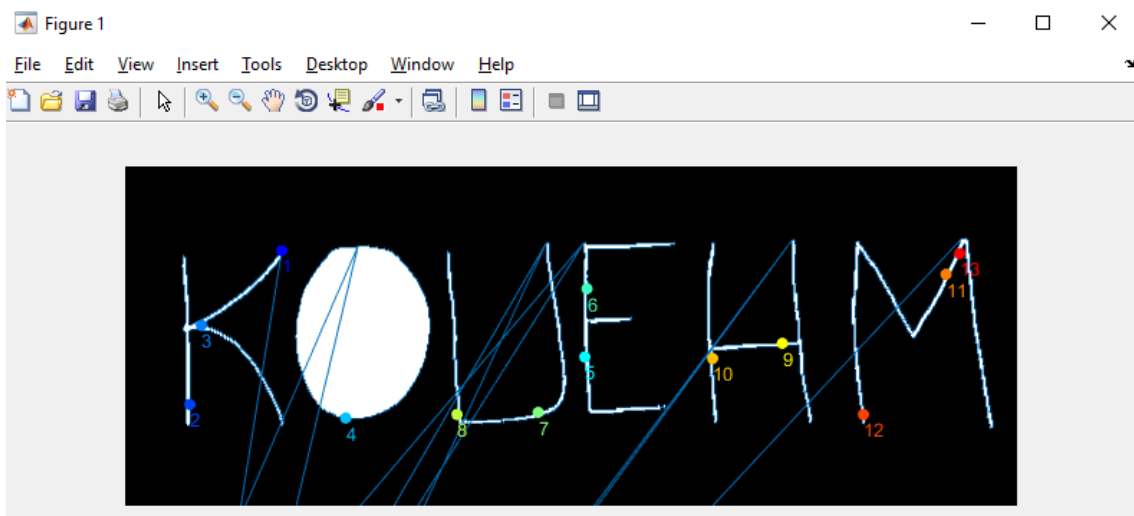


**Figure 9. Image optimized**

### 3.3. Obtaining Coordinates by Eliminating Overhang Pixels

The spur function, which is a morphological process in Matlab, processes the matrix values that are different from neighboring pixels, which may be protrusions, by resembling the neighboring pixel. After applying the spur to the matrix shown in Figure 10, the value different from the neighboring pixels was converted to the neighboring pixels. In this way, the protruding pixel value is removed. In addition, when this function is applied to small objects, the protrusion removes pixels and does not disturb the structure of the object [3]. Therefore, it is thought to be a suitable function for the image used.

0	0	0	0		0	0	0	0
0	0	0	0		0	0	0	0
0	0	1	0	becomes	0	0	0	0
0	1	0	0		0	1	0	0
1	1	0	0		1	1	0	0

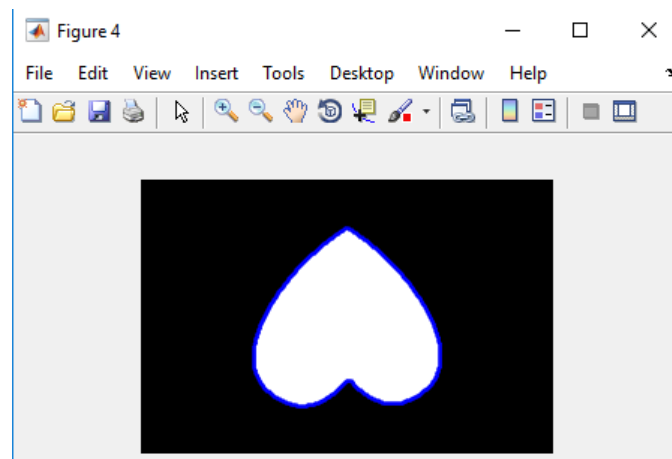
**Figure 10. Spur method**

Figure 11 shows the original image. After converting this image to black and white format, spur function was applied and boundary coordinates were taken by `bwboundaries` command.



**Figure 11. Original image**

Boundary coordinates of the image are given in Figure 12.



**Figure 12. Boundaries of image**

#### 4. Pantograph Application Based on Recommended Techniques

Pantograph application is performed using Rexroth PLC. Rexroth PLC consists of Rexroth servo drives and servo motors. Works on two axes. Communication of the drivers is provided via ethernet. For this purpose, IP scan is performed via ethernet cable connected to the computer. IndraWorks software is used for Rexroth PLCs. IndraLogic provides visualizations for viewing project variables. Geometric elements can be created with the help of visualization. Movement can be provided when used in online mode. Various color and text forms can be applied according to the specified variable values [13-20].

In this section, programming is controlled by the buttons added and the direction of movement of the motor is observed. To add a button to the program, select the appropriate icon from the software interface.

7 objects were used for this programming. It is compared with "k" 8 to see the end of the program. Other commands are used to move position information. When the system is started and "roll-up" is not provided, the roll-up increments the position information for x and y and moves them to the axes with the "move" command. In this way, the letter coordinates are taken. Relay and a spring system are used for the z axis in the scope of operation. The output of the 24 V DC relay is connected to the output of the PLC and the QX0.9 output of the PLC is connected to the input of the relay. When the relay is activated, the spring is pushed and the pen drops down. The relay is deactivated when switching to the other array. The pen comes up. When the position information is received, that is, when the position is started, the pen is turned on and if the AUTO\_START button is pressed, the z axis is activated. The object starts to be drawn.

The result of the programming in this study is shown in Figure 13..



**Figure 13. Result of programming**

## 5. Conclusions and recommendations

It has become a necessity to acquire some images within the developing technology and to arrange these images according to the needs. Various image processing techniques are used in military field, automation, remote sensing. When these techniques and PLC program are used together, the working areas of the PLC are increased and the cost is reduced. For this reason, the technology of the systems made using PLC is increasingly trying to use various artificial intelligence algorithms and image processing techniques instead of manpower.

In this study, it is aimed to draw a desired image by drawing border coordinates in Matlab with Rexroth PLC on a cartesian machine. For this, two methods were used in Matlab. These are skeleton subtraction and subtraction of boundary coordinates using the spur function. After this process, the coordinates received were loaded into Rexroth PLC as position information in sequence with a certain scaling.

As a result of the caliper measurement tests performed on the processing outputs performed on the experimental setup, it was observed that the machining took place almost in an error-free manner

(in coordinates). In the comparisons and evaluations, it is concluded that theoretical results and practical results are in great agreement.

In addition to this, it has been seen that with an image taken from the camera, it is possible to perform operations in image processing area on Matlab and parts processing can be performed in cartesian robots. It has been seen that these processes are developing and can be developed and working in collaboration with electronic devices where image processing can be added to most applications today.

## References

- [1] Özden, M. (2005). Ortalama Kayma Algoritmasının Geliştirilerek Görüntü Dizilerinde Hareketli Nesne Takibi ve Görüntü Kesimleme Amaçlı Kullanılması, Master thesis, Kırıkkale University.
- [2] Karakkoç, Y., Öztürk, S., Kuncan, M. (2012). Hareket Eden Renkli Nesnelerin Takibinin PID ile Gerçekleşmesi. *Otomatik Kontrol Ulusal Toplantısı*, Niğde, Turkey, 281-286.
- [3] Kuncan, M., Kaplan, K., Acar, Fatih., Kundakçı, I. M., Ertunç, H. M. (2016). Fuzzy Logic Based Ball on Plate Balancing System Real Time Control by Image Processing. *International Journal of Natural and Engineering Sciences (IJNES)*, 7(3), 28-32.
- [4] Bakır, A., Güney, Ö. F., Kuncan, M., Ertunç, H. M. (2012). 3 Eksenli Robot Mekanizmasına Monte Edilmiş Bir Kamera Vasıtasıyla Farklı Rotasyon ve Boyutlardaki Geometrik Cisimlerin Tanımlanarak Vakum Tutucu ile Ayrılması. *Otomatik Kontrol Ulusal Toplantısı*, Niğde, Turkey, 606-609.
- [5] Çubukçu, A., Kuncan, M., İmren, M., Erol, F., Ertunç, H. M., Öztürk, S., Kaplan, K. (2015). Object Discrimination and Sorting with Image Processing on 3-Axis Robot Mechanism. *Otomatik Kontrol Ulusal Toplantısı*, Denizli, Turkey, 637-641.
- [6] Horoz, E., Öten, H. F., Kuncan, M., Ertunç, H. M. (2013). Kamera Yardımı ile Ayırt Edilen ve Tanımlanan Cisimlerin 3 Eksenli Robot Mekanizması ile Taşınması. *Otomatik Kontrol Ulusal Toplantısı*, Malatya, Turkey, 1236-1240.
- [7] Cuşkun, Y., Duman, F., Basik, H., Gün, F., Kaplan, K., Ertunç, H. M. (2016). Image processing based multi-purpose 4-axis robot mechanism. *In 2016 National Conference on Electrical, Electronics and Biomedical Engineering (ELECO) IEEE*, Bursa, Turkey, 247-251.
- [8] Sevim, D., Genç, Ç. (2009). Bir Programlanabilir Mantık Denetleyicinin Web Tabanlı Olarak Uzaktan Eğitimi Ve Uygulaması. ISSN:1306-3111 e-Journal of New World Sciences Academy 2009, Volume: 4, Number: 4.
- [9] Genç, Ç., Sevim, D. (2018) Web Tabanlı Programlanabilir Lojik Kontrol Eğitim Materyali. *1<sup>st</sup> International Engineering and Technology Symposium ( 1<sup>st</sup> IETS)* 03- 05 May, Batman, Turkey.
- [10] Sevim, D., Genç, Ç. (2018). Programlanabilir Lojik Denetleyici ile Eğitimde Geleneksel yöntem ile modern yöntemin karşılaştırılması. *1<sup>st</sup> International Engineering and Technology Symposium ( 1<sup>st</sup> IETS)* 03- 05 May, Batman, Turkey.
- [11] Morphological Operations, <https://www.mathworks.com>, (ziyaret tarihi: 09.08.2019).
- [12] Morphological Image Processing, <https://www.slideshare.net>, (ziyaret tarihi: 09.08.2019).

- [13] Mofidul, R. B., Sabbir, M. S. H., Podder, A. K., Rahman, M. S. (2019). Design and Implementation of Remote Controlling and Monitoring System for Automatic PLC Based Packaging Industry. *In Proc. of 1st International Conference on Advances in Science, Engineering and Robotics Technology (ICASERT)*, 1-5.
- [14] Bargal, N., Deshpande, A., Kulkarni, R., Moghe, R. (2016). PLC based object sorting automation. *Int Res J Eng Technol (IRJET)*, 3(07).
- [15] Tailor, D., Kamani, V., Ghetiya, A., & Bhatiya, N. (2017). Object sorting and stacking automation with PLC. *International Journal of Engineering and Technology (IJET)*, 9(3).
- [16] Jha, S. V., Jaiswal, A. G., Jadhav, I. B., Patel, R. V. (2019). Plc Based Object Sorting Machine On Their Height.
- [17] Kulkarni, B., Satpute, M. A., Soundattikar, S. A. (2016). Image Processing and PLC based Automated Biscuit Sorting System. *International Conference on Recent Innovation in Engineering and Management*.
- [18] Erol, F., Emren, M., Öztürk, S., Kuncan, M. (2015). Real Time PI Implementation on Liquid Level Control by means of PLC. *Otomatik Kontrol Ulusal Toplantısı*, Denizli, Turkey, 506-511.
- [19] Chakraborty, K., De, P., Roy, I. (2016). *Industrial Applications of Programmable Logic Controllers and Scada*. Anchor Academic Publishing.
- [20] Thirumurugan, P., Aravind, R., Kumar, M. A., Manjunath, S. D., Kalaiselvan, R. (2018). Automatic sorting in process industries using PLC. *Global Research and Development Journal for Engineering*, 3(3).

## PRODUCTION OF AA7075/B<sub>4</sub>C COMPOSITE MATERIALS BY THE SEMI-SOLID STIRRING METHOD

*Rifat YAKUT<sup>1\*</sup>, Nilhan ÜRKMEZ TAŞKIN<sup>2</sup>*

AA7075 aluminum alloy was reinforced with B<sub>4</sub>C particles to produce aluminum composite materials. In the production of AA7075/B<sub>4</sub>C composite materials, the semi-solid mixing method was used for homogenous reinforcement dispersion and low-pressure solidification. For determination of the mechanical properties of the obtained samples, three-point bending, compression and hardness tests were performed. Additionally, the microstructure, reinforcement matrix interface and chemical structure of the produced composite material were investigated by scanning electron microscopy (SEM), energy dispersive X-ray spectrometry (EDS) and X-ray diffraction (XRD) analyses. As a result, it was observed that, by using the semi-solid mixing method, the reinforcing powders could be distributed homogeneously into the matrix, both chemical and mechanical bonding could be facilitated between the matrix and the reinforcing material, and this mixing technique could be easily used in production of particle-reinforced metal composites. As the reinforcement rate increased, bending strength increased, but there was a reduction in comparison to the non-reinforced aluminum alloy. As the reinforcement rate increased, compressive strength was observed to decreased, while the mean hardness value increased.

Key words: Aluminum, B<sub>4</sub>C, Metal Matrix Composites, Semi-Solid Stirring

### 1. Introduction

Studies on metal matrix composite materials (MMCs) began in the late 1950s with the aim of maintaining the superior characteristics of metallic materials and improving their structural properties [1]. These materials may be used in different areas based on their intended use [2]. These materials are advanced materials which show superior properties due to ceramic reinforcements that are dispersed into metals or metal alloys. They have found a broad area of application especially in the aerospace and automotive industries. Ceramics such as SiC, Al<sub>2</sub>O<sub>3</sub>, C, SiO<sub>2</sub>, MgO, TiC, TiB<sub>2</sub> and B<sub>4</sub>C are the leading types of reinforcements incorporated into MMCs to improve their mechanical properties. Among these reinforcements, B<sub>4</sub>C has been a subject to many fields recently due to its superior physical and chemical properties, and it is a highly strategic material for Turkey, with its rich boron resources [3, 4, 5, 6, 7]. Due to the characteristics of metal matrix composite (MMC) materials

<sup>1</sup> Department of Energy Systems Engineering, University of Batman, Batman, Turkey, (rifat.yakut@batman.edu.tr)  
 <https://orcid.org/0000-0003-0059-3785>

<sup>2</sup> Department of Mechanical Engineering, University of Trakya, Edirne, Turkey, (nilhanurkmez@gmail.com)  
 <https://orcid.org/0000-0003-2251-3889>

consisting of a metal matrix and ceramic reinforcements such as high strength, lightness, high abrasion resistance and good thermal expansion coefficients, their usage areas in the automotive, aviation and defense industries are increasingly more frequent [8]. High-tech ceramics, polymers, metals and composites that entered the world's economy with a high market share in the second half of the twentieth century are high-added-value materials [9]. In recent years, particularly aluminum MMCs (Al-MMCs) have been widely investigated and are used in new industrial applications. The widespread use of aluminum as a matrix material is increasing due to its low density and low cost [10, 11, 12]. Moreover, aluminum is an attractive material for production of MMCs due to its corrosion resistance, low electrical resistance and perfect mechanical properties [13, 14]. Production and use of MMCs are increasing with technological advancements, especially in the automotive industry and the aerospace and aviation sectors. By combining the desired properties of two or more identical or different groups of materials one in the form of at least one metal and metal alloy and the other in the form of continuous fiber, capillary crystal or particle, superior MMCs may be produced [15, 16, 17, 18, 19]. MMCs are high-tech materials which can display superior properties such as high tensile strength, high modulus of elasticity, abrasion, compression and creep strength, ability to maintain its stability at high temperatures, ductility and toughness, low specific gravity, low sensitivity to thermal shocks and high electrical and thermal conductivity [20].

## 2. Research Significance

Due to their low density, high melting temperatures, high elasticity and high strength properties, B<sub>4</sub>C ceramic powders are highly preferred in production of high-strength aluminum-based composite materials. In this study, it was firstly aimed to increase the wettability of B<sub>4</sub>C ceramic powders by the AA7075 Aluminum alloy by using the semi-solid stirring method and heat treatment of B<sub>4</sub>C powders. It was targeted to minimize problems such as non-uniform reinforcement distribution in the matrix, agglomeration of the reinforcements and rejection of reinforcement from mixture and improve the properties of the composite material by the using semi-solid stirring method.

## 3. Material And Method

### 3.1. Matrix Material

The AA7075 alloy was selected as the matrix material the production of B<sub>4</sub>C-reinforced composite materials. The density of this alloy is 2.8 (g/cm<sup>3</sup>), and it has high strength. Copper is the main alloying element in this alloy, where magnesium, chromium and zirconium are additional alloying elements. Tables 1-2 show the properties of the AA7075 aluminum alloy [21].

**Table 1. Mechanical characteristics of AA7075 alloy**

Heat Treatment	Tensile Strength, Rm MPa	Elongation Strength %	Shear Modulus MPa	Elasticity Modulus GPa
T651	572	11	331	72
T7351	503	13	303	72
T7651	503	13	303	72

**Table 2. Chemical composition of AA7075 alloy**

Weight %	Weight %	Si	Fe	Cu	Mg	Mn	Cr	Zn	Ti
Minimum	Minimum	-	-	1.2	2.1	-	0.18	5.1	-
Maximum	Maximum	0.4	0.5	2	2.9	0.3	0.28	6.1	0.2

### 3.2. Reinforcement Materials

Due to its lightness and superior mechanical properties, B<sub>4</sub>C is used as the reinforcing material to increase the abrasion and impact resistance of materials [22]. The B<sub>4</sub>C material is among the advanced-technology ceramics of today with its characteristics such as high melting temperature, high hardness, high abrasion strength, low density and superior resistance against chemical substances. Its hardness values do not decrease even at temperatures around 1300°C [23]. Table 3 shows the properties of B<sub>4</sub>C reinforcing materials.

**Table 3. Some mechanical and physical characteristics of B<sub>4</sub>C materials [21].**

Reinforcement Material	B <sub>4</sub> C
Density (x10 <sup>3</sup> kgm <sup>3</sup> )	2.52
Thermal Expansion Coefficient (10 <sup>-6</sup> C <sup>-1</sup> )	6.08
Melting Point (°C)	2420
Compression Strength (MPa)	2900
Elasticity Modulus (GPa)	460
Knoop Hardness	2800

### 3.3. Composite Material Production by the Method of Semi-Solid Stirring

The temperature of the melting furnace (Figure 1 (a)) was kept constant in the range of 700 °C-720 °C. The nitrogen gas introduction setup was installed by means of the mechanism to allow nitrogen gas to be emitted onto the molten metal. After the matrix material was put into a SiC crucible where melting and mixing processes were performed, it was increased to the semi-solid temperature range, and the reinforcement material, heated up to 220 °C, was added with a speed of 5 gr/min. The B<sub>4</sub>C reinforcement was mixed into the matrix at constant temperature by using steel bars with specially profiled stirrers. Homogeneous mixing of the matrix material and reinforcement in the matrix material was ensured without any flocculation by mixing at a low speed by the mixer at a semi-solid temperature. After the reinforcement process was completed, a homogenization process was carried out by applying high-speed mixing to the semi-solid melt for a short time. After the mixing and homogenization processes, the lowest temperature range that provided fluidity was selected as the casting temperature, and the mixture was removed from the melting unit and transferred to the steel molds which had previously been heated to 540-550 °C (Figure 1 (b)). The mold cap of the melted steel mold was closed, put under a pressure tray and compressed under a pressure process that was started within a few seconds. After applying compressive pressure under 10 MPa for 3-4 seconds, the whole mold was removed from the press, the composite material was allowed to cool in the mold for 15 minutes, and it was removed from the mold and left for cooling at the ambient temperature. The removal process of the prismatic metal matrix composite specimen material from the mold is shown in Figure 1 (c). AA7075/B<sub>4</sub>C composite materials were produced by adding B<sub>4</sub>C reinforcement into the semi-solid aluminum alloy in the ratios specified in Table 4. Temperature measurements were performed by two K-type thermocouples. One of the thermocouples contacted the furnace's interior, and the other was dipped into the mixture in the crucible. Three specimens were produced for each reinforcement ratio. Control specimens were produced under the same production conditions but without reinforcements.



**Figure 1. Experiment details from the AA7075/B<sub>4</sub>C composite production process**

Three-point bending test (TS-205), compression (TS EN ISO 6506-1) and hardness specimens (ASTM-E9) were prepared in accordance with the relevant standards. All specimens were produced with Wire Electrical discharge machining (WEDM) in Hema Industrial Inc. Figure 2 (a), (b), (c) shows the test sample types and preparation details.

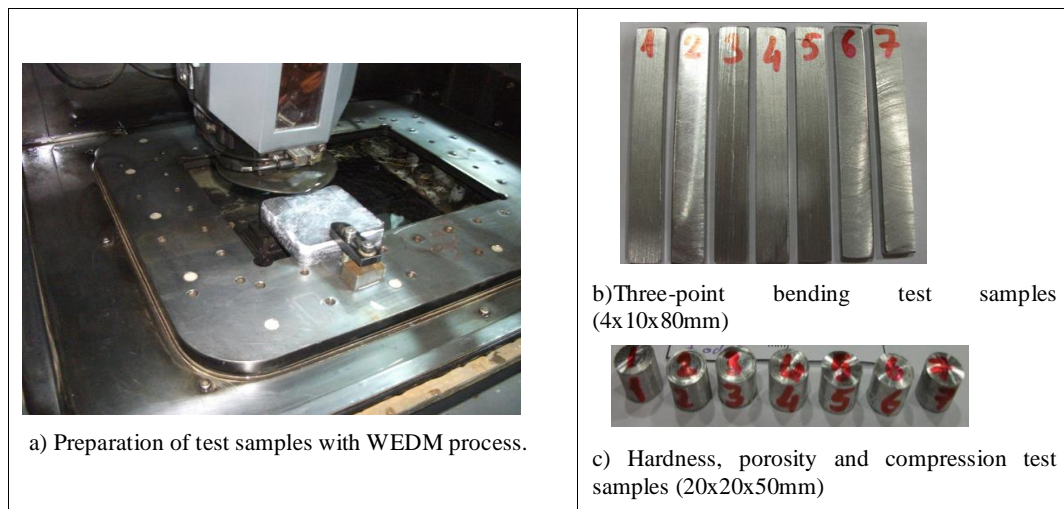


**Figure 2. Test sample types and preparation details**

#### 4. Result And Discussion

In this study, due to its widespread use in industrial fields, the AA7075 aluminum alloy was selected as the matrix material in particular. The B<sub>4</sub>C material selected as the reinforcing material was mixed into the semi-solid aluminum alloy, and composites with different reinforcing ratios were obtained. The effects of the reinforcing ratios of the obtained composites on mixing performance and mechanical properties were investigated.

#### 4.1. Specific Weight and Porosity Measurement Results

The density of the B<sub>4</sub>C-particle-reinforced samples was calculated according to the Archimedes principle. The variation of the theoretical and experimental densities of the samples produced depending on the particle ratio is given in Table 4.

**Table 4. Theoretical, specific gravities and porosity ratios of the samples**

Material	%B <sub>4</sub> C (by Volume)	Theoretical Specific Weight (g/cm <sup>3</sup> )	Experimental Specific Weight (g/cm <sup>3</sup> )	% Porosity
AA7075	-	2.80	2.74	2.0
10% B <sub>4</sub> C-90% AA7075	10	2.77	2.50	9.8
20% B <sub>4</sub> C-80% AA7075	20	2.74	2.43	11.4

It was observed that, as the volumetric reinforcement ratios increased, the experimental specific gravities of the composite materials decreased. Specific weight and porosity experiments were carried out at the Marmara Research Center of TÜBİTAK, and the theoretical and experimental specific weight results of the experiment specimens were compared. As a result of this comparison, the porosity levels were found to be high. This was thought to be due to the length of mixing time and low application rate of compression pressure.

#### 4.2. Mechanical Test Results

##### 4.2.1. Three-Point Bending Test

In this study, three composite materials were produced from each reinforcement ratio to be used in the experiments, and additionally, to make a comparison, three test specimens were produced from the non-reinforced composite material under the same production conditions. Three-point bending tests were applied to these test samples. The bend strength of the samples was calculated with the help of the equation specified in the ASTM B528-05 standard.

When the three-point bending test results of the non-reinforced AA7075 aluminum alloy were examined, the mean bending strength was found to be 268 N/mm<sup>2</sup>. When the three-point bending test results applied to the 10% and 20% by volume particle-reinforced AA7075/B<sub>4</sub>C composites were examined, it was seen that the mean bending strength of the 10% reinforced composites was 194.6 N/mm<sup>2</sup>, and the mean bending strength of the 20% reinforced composites was 206.3 N/mm<sup>2</sup> (Figure 3). As the reinforcement ratio increased, bending strength increased, but due to the high porosity rates, there was a reduction in comparison to the non-reinforced aluminum alloy.

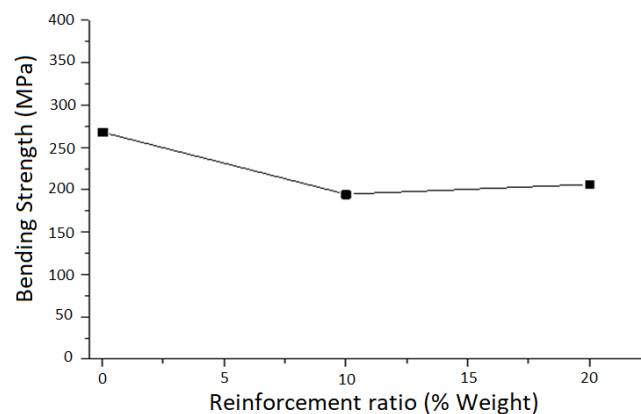


**Figure 3. The effect of reinforcement ratio on bending strength in AA7075/B<sub>4</sub>C composites**

#### 4.2.2. Compression Experiments

When the compression test results of the AA7075 non-reinforced aluminum alloy were examined, it was seen that the mean compressive strength was 500 N/mm<sup>2</sup>. When the compression test results applied to the 10% and 20% by volume particle-reinforced AA7075/B<sub>4</sub>C composites were examined, it was observed that the mean compression strength of the 10% reinforced composites was 493.7 N/mm<sup>2</sup>, and similarly, the mean compression strength of the 20% reinforced AA7075/B<sub>4</sub>C composites was found to be 360 N/mm<sup>2</sup> (Figure 4). It was seen that there was a decrease in compression strength after increasing the B<sub>4</sub>C reinforcement ratio to 20% by volume.

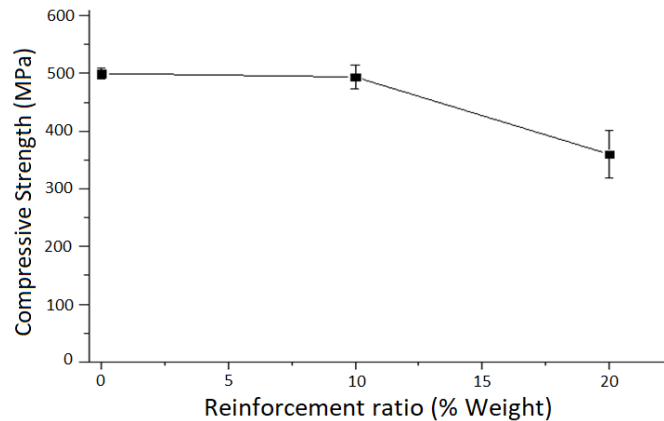


**Figure 4. The effect of reinforcement ratio on compression strength in AA7075/B<sub>4</sub>C composites**

#### 4.2.3. Hardness Experiments

When the hardness test results of the non-reinforced AA7075 aluminum alloy were examined, the mean hardness was found to be 70 BSD. When the hardness test results applied to the 10% and 20% particle-reinforced AA7075/B<sub>4</sub>C composites were examined, the mean hardness of the 10% reinforced composites was found to be 107 BSD, while it was 127 BSD for the 20% reinforced composites (Figure 5). In the study, as the reinforcement material had a good wettability by aluminum, it was seen that the mean hardness value increased as the reinforcement ratio increased.

In their study, Hasırcı and Gül (2010) produced averagely 25- $\mu$ m-sized Al by means of powder metallurgy, they produced 10% and 20% B<sub>4</sub>C-reinforced B<sub>4</sub>C/Al composites, and they investigated the change in hardness depending on the reinforcement volume ratio. They found the results of approximately 46 HV for the 10% B<sub>4</sub>C-Al reinforced composite and about 55 HV for the 20% B<sub>4</sub>C-Al reinforced composite [2]. Since the hardness values of composites produced by powder metallurgy are less than 80 HV and 76 BSD, which is the lowest hardness value in hardness conversion tables, no exact comparison could be made with the hardness values found in this study. However, the fact that the hardness values in this study were seen in the hardness conversion tables shows that the hardness values of the composites produced by powder metallurgy were lower than the hardness values in this study.

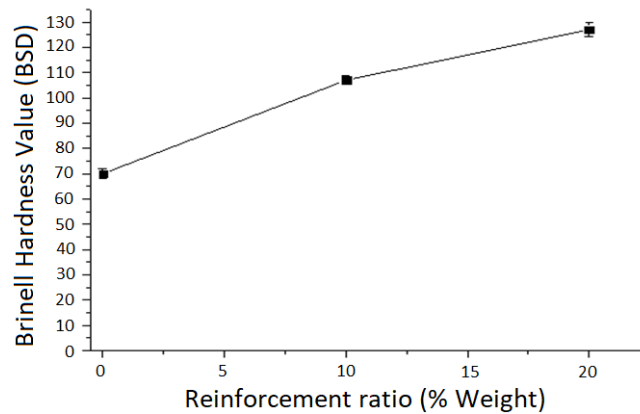
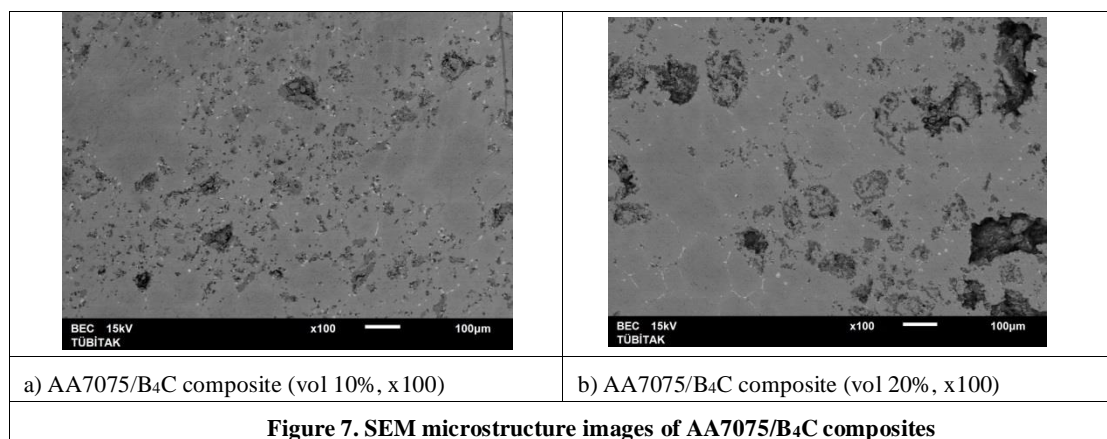


Figure 5. Change in BSD values of AA7075/B<sub>4</sub>C composites by reinforcement ratio

#### 4.2.4. Microstructure Examinations

Whether there is a mechanical or chemical bond between the reinforcement phase and the matrix in the composite materials produced may be understood by examining whether the reinforcement phase is homogeneously dispersed in the matrix. The microstructures of the test samples were examined by SEM images taken at different magnification rates.

The SEM microstructure images of the 10% and 20% B<sub>4</sub>C-reinforced AA7075/B<sub>4</sub>C composites are given in Figure 7. In the composites shown in Figure 7 (a) and (b), it is seen that the reinforcing material was homogeneously distributed, and while looking at x40 and x2500 magnifications, it is seen that the B<sub>4</sub>C particles were wetted well by aluminum. When the images are examined, it is observed that the B<sub>4</sub>C particles were well-surrounded by aluminum, and there were no images related to pores and flocculation. This shows that the reinforcement was distributed homogeneously in the matrix, and a mechanical bond was formed between the reinforcing material and the matrix material.



In the EDS analysis given in Figure 8, it was observed that the reaction products formed at the interface of the matrix material with the reinforcement. Thus, the formation of a chemical bond was confirmed. We observed Al peaks that represented the aluminum constituting the matrix material, B and C peaks that constituted the B<sub>4</sub>C material and O peaks that confirmed the reaction products.





## 7. References

- [1] Toptan, F., Production of High Wear Resistant B<sub>4</sub>C Particle Reinforced Aluminium Matrix Composites, Yıldız Technical University, Department of Metallurgical and Materials Engineering, Ph.D. Thesis, İstanbul, 2011.
- [2] Hasırcı, H. ve Gül, F. (2010). Investigation of abrasive wear behaviours in B<sub>4</sub>C/Al composites depending on reinforcement volume Fraction, *SDU International Technologic Science*, 2 (1), 15-21.
- [3] Akın, G., Production Of Boron Carbide Reinforced Aluminium Matrix Composites Using Powder Metallurgy Method And Investigation Of Their Mechanical Properties, İstanbul Technical University, Institute of Science And Technology, Master of Science Thesis, İstanbul, (2006).
- [4] Pul, M. (2019). The Effect on Mechanical Properties of Reinforcement Amount at B<sub>4</sub>C + TiB<sub>2</sub> Reinforced Al 2024 Based Composites Produced by Powder Metallurgy, *International Journal of Engineering Research and Development*, 11 (1), 87-99.
- [5] Taşcı, U., Gökmeşe, H., Bostan, B. (2013). AA 2014 Al Matrisli B<sub>4</sub>C Parçacık Takviyeli Kompozitlerin Mikro Yapı ve Aşınma Davranışının İncelenmesi, *Gazi Üniversitesi Fen Bilimleri Dergisi Part:C, Tasarım ve Teknoloji*, 1 (4), 161-168.
- [6] Karabulut, H., Effect of Mechanical Alloying Duration on Composite Properties In Production Of Al<sub>2</sub>O<sub>3</sub>, SiC And B<sub>4</sub>C Particulate Reinforced Composite By Powder Metallurgy Method, Gazi University, Institute of Science And Technology, Ph.D. Thesis, Ankara, 2011.
- [7] Topcu, İ., Dikici, M., İpek, C., Investigation of Wear Properties of Ceramic Reinforced Aluminum Based Metal Matrix Composites, 6th International Symposium on Innovative Technologies in Engineering and Science 09-11 November 2018 (ISITES2018 Alanya – Antalya - Turkey)
- [8] Motorcu, A. R., and Ekici, E., (2016) Evaluation of drilling Al/B<sub>4</sub>C composites with carbide drills, *Pamukkale University Journal of Engineering Sciences*, 22(4), 259-266
- [9] Pul, M., Calin, R., Citak, R. (2011). An Investigation of Surface Quality of Turning in Al matrix MgO Reinforced Composite Materials, *Journal of the Faculty of Engineering and Architecture of Gazi University*, 26 (1), 81-88.
- [10] Arslan, D., Gürü, M. (2013). Production of Boron Carbide by Mechanochemical Method and Investigation of Usability on The Aluminium Based Composite Material, *Journal of the Faculty of Engineering and Architecture of Gazi University*, 28 (4), 875-883.
- [11] Çolak, N. Y., Turhan, H. (2016). The Investigation of Microstructure and Mechanical Properties of AlSi/B<sub>4</sub>C Composites Produced by Using Powder Metallurgy Method, *Science and Eng. J of Fırat Univ*, 28 (2), 259-266.
- [12] Çelik, Y. H., Kılıçkap, E., Yenigün, B. (2018). The Effect of Contact Pressure and B<sub>4</sub>C Ratio on Hardness and Wear Behaviours in Al-Matrix Composites Produced by PM Method, *Science and Eng. J of Fırat Univ.*, 30 (1), 33-40.
- [13] Tosun, N., Kuru, C., Altıntaş, E. (2010). Investigation Of Surface Roughness In Milling With Air And Conventional Cooling Method, *Journal of the Faculty of Engineering and Architecture of Gazi University*, 25 (1), 141-146.
- [14] Tuncer, N., Tasdelen, B., Arslan, G. (2011). Effect of Passivation And Precipitation Hardening On Processing And Mechanical Properties Of B<sub>4</sub>CAI Composites, *Ceramics International*, 37 (7), 2861-2867.

- [15] Motorcu, A. R., Ekici, E. (2016). Evaluation of drilling Al/B<sub>4</sub>C composites with carbide drills, *Pamukkale University Journal of Engineering Sciences*, 22 (4), 259-266.
- [16] Gökmen, U. (2016). Joining of Al 2024 Based B<sub>4</sub>C/SiC Particle-Reinforced Hybrid Composites with TIG Welding, *Çukurova University Journal of the Faculty of Engineering and Architecture*, 31 (1), 69-77.
- [17] Seçilmiş, K., Investigation of Wear Behaviors of Al Matrix Composites Reinforced With Different B<sub>4</sub>C Rate Produced by Powder Metallurgy Methods, Batman University, Institute of Science And Technology, Master of Science Thesis, Batman, (2017).
- [18] Ahlatçı, H., Candan, E. ve Çimenoğlu, H. (2003). The Effect of SiC Size on The Wear Behaviour Of 60 Vol % SiC-Al Composites, *İTÜ dergisi/d mühendislik*, 2 (3), 37-42.
- [19] Ekici, E., The manufacture of aluminium matrix composites with B<sub>4</sub>C reinforcing element and addition of graphite and the analysis of mechanical features and their machinability on milling, Gazi University, Institute of Science And Technology, Ph.D. Thesis, Ankara, 2012.
- [20] Atik, E., Ünlü, B.S., Sen, O., Çavdar, U. (2006). Investigation of Wear Strenght and Mechanical Properties of Particle Reinforced AlSi12CuNiMg Composites, *C.B.U. Journal of Science*, 2 (2), 75-87.
- [21] Ürkmez, N., Production of AlMg3/SiCp composites and investigations of variations in mechanical properties, Yıldız Technical University, Institute of Science And Technology, Ph.D. Thesis, İstanbul, 2004.
- [22] Yakut, R., and Ürkmez Ürkmez T., (2018), Production of AA7075 / B<sub>4</sub>C / SiC Hybrid Composite Materials By Semi-Solid Stirring Method, *1st International Engineering And Technology Symposium (1st Iets) 03–05 May*, Batman / Turkey
- [23] Akgün Kayral, S., (2017). Production Of Tib2-B<sub>4</sub>C Composite Powders by The Carbide Boronizing Process, *Engineering Sciences (NWSAENS)*, 12 (3), 141-148

## INVESTIGATING THE UTILIZATION OF WASTE GLASS POWDER, COLEMANITE ORE WASTE AND SUGAR FACTORY FILTER CAKE IN GYPSUM-LIME BASED MORTARS

*Muhammed Yasin DURGUN<sup>1</sup>*

*The wastes generated by the recent industrial developments threaten the future of the world. Therefore, researches on the recycling of the industrial wastes in various ways are increasing day by day. In this study, glass powder, a waste of glass industry, colemanite ore waste, a by-product of boron industry and filter cake, one of the wastes of sugar factories, were used. The evaluation of these wastes in gypsum and lime based mortars has been investigated. In this study, 10, 20 and 30% of the waste materials were used instead of gypsum. Unit weights, ultrasonic pulse velocities, apparent porosities and thermal conductivity coefficients of the gypsum-lime based mortars were determined. Compressive strength and bending strength tests were performed to determine the mechanical properties. The results indicated that the use of wastes negatively affected the mechanical properties while improving the thermal properties.*

*Keywords: gypsum, lime, waste glass powder, colemanite ore waste, sugar factory filter cake*

### 1. Introduction

Gypsum is one of the most preferred building materials in the world. It is used frequently due to its good acoustic performance, fire prevention, moisture balance of building elements and natural, organic and environmentally friendly properties [1]. Besides, it is easy and cheap to produce. However, the fact that the plaster is very brittle and non-resistant to cracking makes it difficult to use as exterior material [2]. For this reason, in some applications, it has been aimed to improve some mechanical properties by adding reinforcing materials such as various fibers or aggregates into gypsum mixtures and it has even been made available as plates [3].

Lime is one of the most traditional binders used in the world for centuries. In the last few decades, it has attracted more attention due to its mechanical strength, modulus of elasticity and water vapor permeability. At the same time, it has become one of the alternative binders for cement due to its more embodied energy and greenhouse gas emission. Thus, research on lime products, lime-based mortars and injections have increased [4, 5].

Today, to reduce environmental hazards arising from the production of Portland cement, researches have focused on obtaining economic binders using industrial by-products and wastes (blast furnace slag, silica fume, fly ash) and natural resources (natural pozzolans, lime, gypsum, calcined clays). Because the factors that triggered global warming have become one of the most fundamental problems [6]. The use of some industrial wastes as mineral additives with Portland cement has become

<sup>1</sup> Department of Civil Engineering, Bartın University, Bartın, Turkey, (mydurgun@bartin.edu.tr)  <https://orcid.org/0000-0003-4656-9430>

Received: 18 November 2019; Accepted: 25 December 2019

Doi: <https://doi.org/10.36222/ejt.648038>

very popular for this purpose. In this way, energy consumption is reduced, the economy is provided, ecological balance and natural resources are protected [7].

Gypsum is a material that hardens when it reacts with water. The water used in gypsum mixtures can be divided into two parts. The first part is the part necessary for the gypsum to be hydrated. The second part is the part that necessary for achieving the workability. The second part of the water constitutes a large part of the water added to the mixture and will then leave the structure in the air voids, depending on age and drying. The use of high amounts of water causes negativity in terms of mechanical properties [8].

In the literature, it is seen that the use of different additives to improve the physico-mechanical and hydrophobic properties of gypsum-containing mixtures to keep their structure together against deterioration. For example, Wang et al. [9], evaluated the use of metakaolin in gypsum-lime mixtures, while Morsy et al. [6] evaluated the use of fly ash as well as metakaolin in gypsum-lime mixtures. Demir and Başpınar [10] investigated the use of silica fume and expanded perlite in fly ash-lime-gypsum mixtures. Gourav and Reddy [11] produced bricks from gypsum-lime mixtures containing fly ash and investigated their structural performance. Neto et al. [12] conducted studies on the use of blast furnace slag in gypsum and lime mixtures and del Rio Merino et al. [13] worked on the evaluation of ceramic wastes in gypsum mixtures. Khalil et al. [14] used rice husk ash together with slag to improve the properties of gypsum-lime mixtures. In another study, Aubert et al. [15] examined the rate of gypsum and lime consumption in lime-gypsum mixtures using natural pozzolan, silica powder, and waste paper sludge ash.

As can be seen, it has been paid attention that the additives used in the studies are waste and / or show pozzolanic properties. Thus, it is aimed to obtain improved and / or economical products. Pozzolan is the general name of natural of inorganic materials that react in the presence of calcium hydroxide (lime) and water and harden [16]. For this reason, the pozzolanic properties of the additives used to make the idea that they can contribute to the strength. The fact that the material is waste, contributes to environmental protection and enables a more economical mixture to be produced.

According to data from the year 2017, 1.331.265 tonnes of glass packaging is manufactured in Turkey. 23% of the marketed portion of these produced packages was recycled [17]. According to 2016 data, these values are 99% in Sweden, 98% in Switzerland, 96% in Belgium and 85% in Germany [18]. Waste glasses are generally stored in solid waste landfills if they cannot be recycled. This causes environmental problems [19]. For this reason, recent studies on the potential of glass wastes in the concrete and cement industry are being conducted frequently. Various researchers are being conducted on the use of waste glass in the aggregate form [20], filler material [21], geopolymer raw material [22] and concrete admixture [23]. Researchers have reported that even if used in small proportions, finely ground glass powder may exhibit more pozzolanic activity than fly ash, which is very common in use [24].

Turkey, as is known, has about 72% of boron known reserves around the world. Boron is a precious mineral used in industry, energy, and medicine. Turkey is the world's second-largest boron and components manufacturer after the United States. The most common boron minerals are colemanite, ulexite, and tincal. These minerals are subjected to various processes in production sites and turned into boric acid and borates in plants. Some by-products are generated from this production and these wastes cause environmental pollution. Colemanite ore wastes resulting from colemanite processing are collected in ponds close to the facility and create a risk of pollution by mixing with underground water resources [25]. For this reason, studies on the evaluation of colemanite ore wastes

in the cement and concrete industry have shown that the wastes contribute to the concretes later age strength. Olgun et al. [26], in their study in cement production by using colemanite ore waste instead of gypsum, obtained positive results and reported that a denser microstructure was obtained.

Approximately 65-70% of the world's sugar production is met by sugar cane [27]. According to 2013 data, annual sugar cane production is 1.877 Mt. Approximately 104 kg of sugar is obtained from 1000 kg sugar cane harvested after reaching the factory and subjected to various processes, which corresponds to about 13% of the first crop. The remaining parts are treated as sugar factory wastes. Sugar factories have three main wastes. These are sugar cane pulp, molasses, and filter cake. Up to 52% of the total product is liquid waste, 28% is pulp, 3% is molasses and 4% is filter cake [28]. The filter cake is a product produced after the purification of sugar water and is one of the main solid wastes of the sugar industry. The safe storage and disposal of this product have always been an important issue. Random storage may cause occupation of space due to stacking, air pollution and groundwater pollution [29]. The basic chemical component of the filter cake is CaO, which is also main component of the lime-based cement components. Therefore, investigations have been made on the usability of filter cake instead of lime-based raw materials in cement clinker production [30]. Li et al. [31, 32] examined the hydration characteristics of the product by using filter cake instead of lime-based materials in clinker production and obtained positive results up to certain ratios. It is also seen in the literature that filter cake is used in fields such as soil improvement [33], light foam concrete production [28] and brick production [34].

In this study, waste glass powder (WGP), colemanite ore waste (COW) and sugar factory filter cake (SFC) were used in 10, 20 and 30% ratios in gypsum-lime based mixtures. The unit weights, ultrasonic pulse velocity values, bending and compressive strengths, apparent porosity values and thermal conductivity coefficients of the produced samples were examined and the evaluability of these waste materials in gypsum applications was investigated. By this way, it is aimed to preserve gypsum sources and to evaluate waste materials in the gypsum-based mixtures.

## 2. Materials and Methods

### 2.1. Materials

WGP used in the study was taken from the waste powders of a glass factory operating in the Kahramanmaraş region. COW was obtained from Bigadiç Boron Plant's wastes. The SFC was taken from Elbistan sugar factory wastes. All wastes obtained was milled in the ball mill and sieved to a size of less than 30 microns. The gypsum used as the main material is commercially obtained, has a specific surface value of 4280 m<sup>2</sup>/g and a density of 2.91 g/cm<sup>3</sup>. The lime used in the study was commercially obtained meets with TS EN 459-1. Chemical analysis and images of waste materials used are given in Table 1 and Fig. 1., respectively.

**Table 1. Chemical and physical properties of waste materials.**

Compound (%)	Waste Glass Powder	Colemanite Ore Waste	Sugar Factory Filter Cake
<i>Chemical analysis results</i>			
SiO <sub>2</sub>	72.65	34.15	2.55
Al <sub>2</sub> O <sub>3</sub>	0.76	9.96	0.83
Fe <sub>2</sub> O <sub>3</sub>	0.19	5.67	0.35
CaO	9.36	12.05	37.66
MgO	4.16	-	1.21
SO <sub>3</sub>	0.21	-	0.21
Na <sub>2</sub> O + K <sub>2</sub> O	12.88	-	0.39
B <sub>2</sub> O <sub>3</sub>	-	19.06	-
Loss on ignition (%)	-	9.68	54.87
<i>Physical analysis results</i>			
Density (g/cm <sup>3</sup> )	2.75	2.41	2.07
Fineness	< 30 µm	< 30 µm	< 30 µm

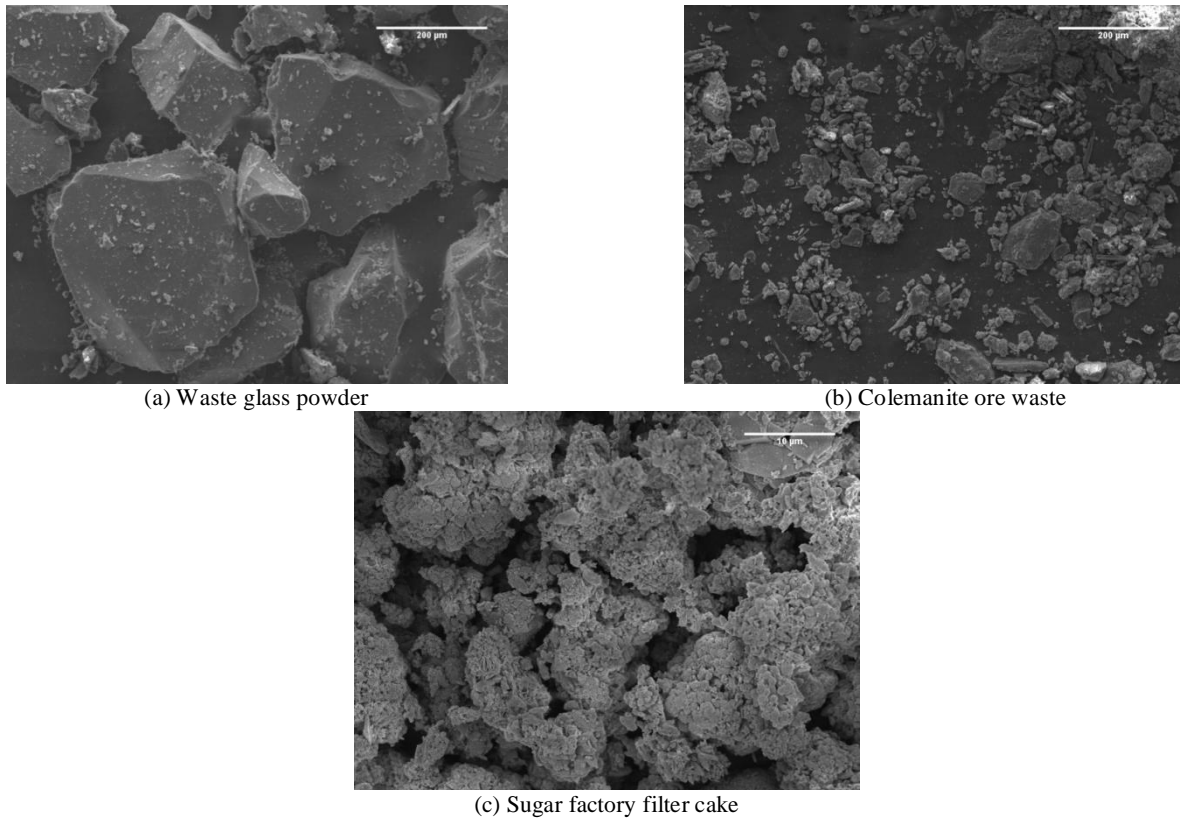


**Figure 1. Images of waste glass powder, colemanite ore waste and sugar factory filter cake.**

As fine aggregate standard CEN sand with a density of  $2.63 \text{ g/cm}^3$  and water absorption of % 1.50 was used. The grain distribution of the standard CEN sand is given in Figure 2.

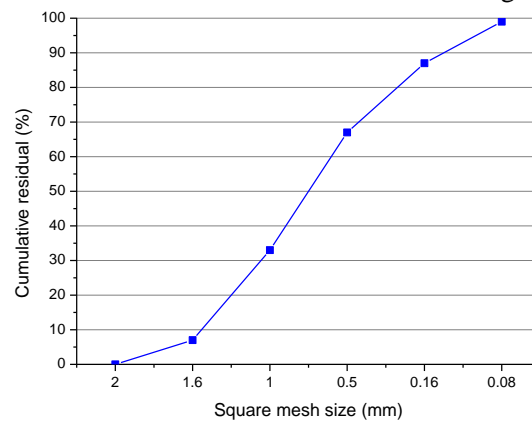


**Figure 2. Grain distribution of standard CEN sand.**

## 2.2. Methods

The mix design used in the study is given in Table 2. In the table, codes for reference sample, WGP, COW and SFC are “R”, “GP”, “CW” and “FC”, respectively. All waste materials were used in 10, 20 and 30% by weight instead of gypsum. The mixtures were prepared according to EN 13454-2. Water was poured into the bowl and then gypsum-lime was added. The materials mixed for 30 s at low speed and the sand added and then mixed 30 more seconds. Finally, the materials mixed for 60 s at high speed. The fresh mixes were cast into molds of 40x40x160 mm and vibration was applied for 30 seconds. The samples were removed from the molds after 24 hours and kept at  $23 \pm 2 \text{ }^\circ\text{C}$  and approximately 50% humidity for 28 days.

**Table 2. Mix design of waste containing gypsum-lime based mortars (g).**

Code	Gypsum	Lime	Fine Aggr.	WGP	SFC	COW	W/B <sup>1</sup>
R	675	225	1350	0	0	0	0.60
GP10	607.5	225	1350	67.5	0	0	0.60
GP20	540	225	1350	135	0	0	0.60
GP30	472.5	225	1350	202.5	0	0	0.60
CW10	607.5	225	1350	0	0	67.5	0.60
CW20	540	225	1350	0	0	135	0.60
CW30	472.5	225	1350	0	0	202.5	0.60
FC10	607.5	225	1350	0	67.5	0	0.60
FC20	540	225	1350	0	135	0	0.60
FC30	472.5	225	1350	0	202.5	0	0.60

<sup>1</sup> Water/binder ratio

At the end of this period, the samples were kept in the oven at 40 °C for 24 hours and free moisture was removed. The samples were then subjected to unit weight, ultrasonic pulse velocity (UPV) (ASTM C597), thermal conductivity (ASTM D7984), compressive strength, and bending strength tests (TS EN 13279-2). Some samples were saturated with water and the amount of water absorption was determined, as well as the apparent porosity values were measured using the Archimedes method (ASTM C20).

### 3. Results and Discussion

#### 3.1. Unit Weights

The unit weights of the samples are shown in Figure 3.

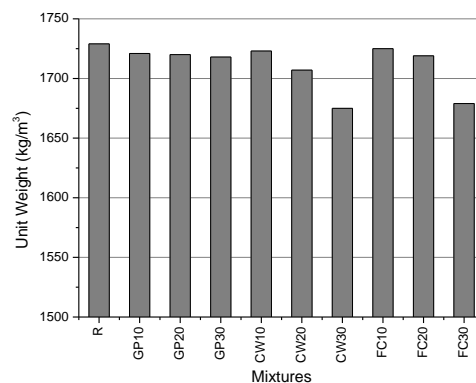


**Figure 3. Unit weight results.**

The unit weight values varied between 1675 – 1729 kg/m<sup>3</sup>. The highest value was obtained from the sample R, which does not contain any waste material. The lowest value was obtained from 30% COW containing sample. From Figure 3, it can be obviously seen that waste incorporation decreased the unit weights of the gypsum-lime based samples. The effect of COW and SFC is more effective than WGP, especially at higher percentages. The unit weight decreased %3.1 at most, which is obtained from CW30. It can be concluded that waste addition decreased the unit weight but the level of the reduction is not very significant. The reason of the decrease of the unit weight can be related to the reactions of the waste materials. It is believed that due to unreacted particles, sufficient development in the paste phase does not occur and a more porous structure formed. This situation discussed again in section 3.3. and 3.5.

#### 3.2. Ultrasonic Pulse Velocity

Ultrasonic pulse velocity (UPV) results are given in Figure 4. The relation between UPV and apparent porosity of the samples is given in Figure 5.

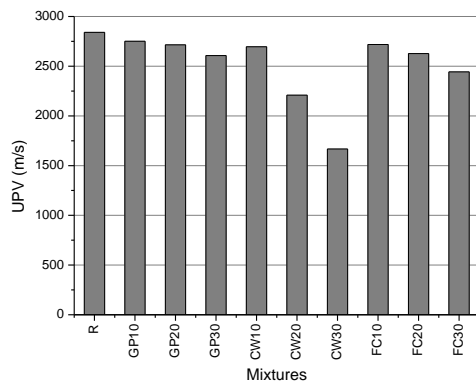


Figure 4. Ultrasonic pulse velocity results.

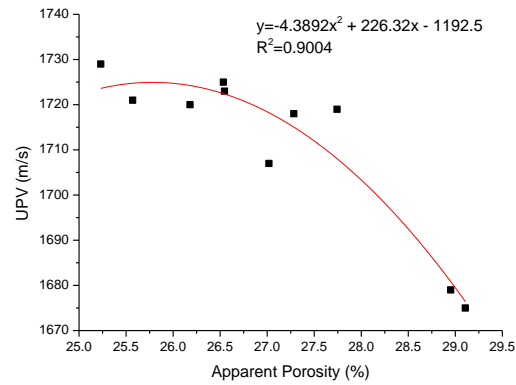


Figure 5. Apparent porosity and UPV relation.

The ultrasonic pulse velocity values varied between 1667 – 2841 m/s. The highest value obtained from sample R and the lowest value obtained from CW30. The UPV values of all waste added gypsum-lime based mortars decreased compared to R. However, the decrement in WGP and SFC is not as significant as COW containing samples. Especially higher amount of COW incorporation, 20% and 30%, changed the value 11% and 32%. It is known that the ultrasonic pulse velocity is strongly related to the pore structure of the material. The velocity of the ultrasonic waves in the body is slowed down by the high amount of voids, and it is higher in low-void bodies. The results can be evaluated that as the increase in the amount of COW, the pore structure increases. As can be seen from Figure 5, there is a strong relation between them and while the porosity increases the UPV decreases.

### 3.3. Apparent Porosity

The apparent porosity values of the samples are given in Figure 6.

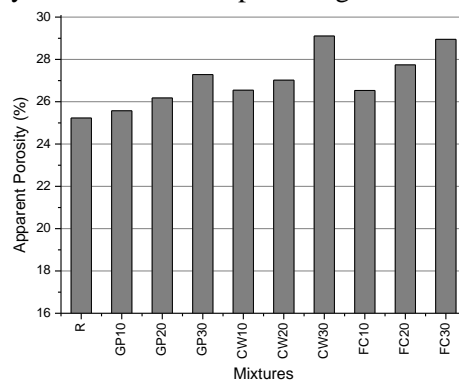


Figure 6. Apparent porosity of the samples.

The porosity values of gypsum-lime based mortars varied between 25.2% - 29.1%. Tesch and Middendorf [35] studied porosity values of many different gypsum-lime based mortars at different storage conditions and found that the values obtained varied between approximately 17% – 34%. As can be seen from Figure 6, the highest porosity value obtained from the CW30 sample. The lowest porosity value belongs to sample R. In section 3.2. it was mentioned about the relation between porosity and UPV. According to the results, all waste containing samples have higher porosity value than the R sample. Samples containing WGP have lower porosity value than other waste groups. With the increase of COW and SFC, the porosity value increased. Especially at 30% of addition, the highest porosity values obtained.

These results can be related to the reactions of waste materials. WGP is a pozzolanic material. It is expected to react with lime and occur C-S-H gels in the structure. C-S-H gels are the main phase of

cementitious materials, which provide the strength of the matrix. The chemical composition of COW and SFC is probably not sufficient for their participation in chemical reactions. Therefore, they create more voids in the structure. From the view of strength, the increment in pore amount is not desired, but from the view of thermal conductivity, high porosity is the desired situation.

### 3.4. Water Absorption

The water absorption values of the samples are shown in Figure 7. Figure 8 shows the relation between apparent porosity and water absorption.

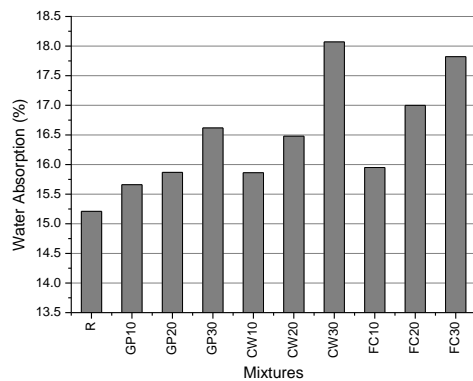


Figure 7. Water absorption values of the samples.

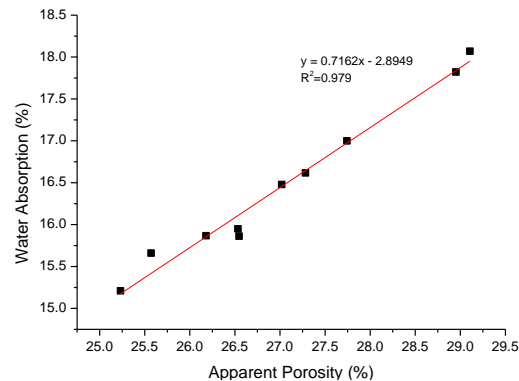


Figure 8. Apparent porosity and water absorption relation.

The water absorption values varied between 15.2% - 18.1%. The lowest value obtained from the sample R. It can be seen that water absorption values increased with the increase of waste content. The highest water absorption value obtained from CW30. SFC additive was also found to increase water absorption values, especially when used at high amounts. These results can be related to the pore structure of the material. As seen in section 3.3., high water absorption values were obtained from samples with high porosity. The  $R^2$  value is very high, which indicates a strong correlation between these two parameters.

### 3.5. Compressive Strength

The results of compressive strength tests are given in Figure 9. The compressive strength results varied between 7.5 MPa – 19.1 MPa. The compressive strengths of the samples were gradually reduced with the addition of waste additives. The highest value belongs to sample R. According to Turkish standards on gypsum plasters [36], various compressive strength limits are specified for different types of gypsum plasters.

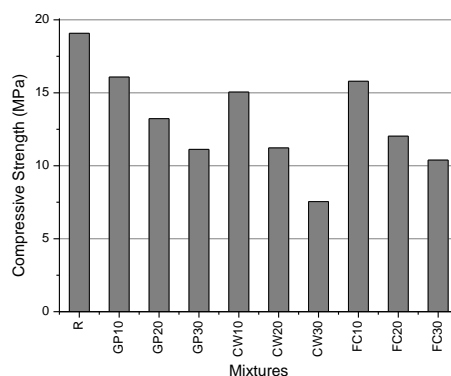


Figure 9. Compressive strength values of samples.

For most gypsum plaster types, it is considered sufficient to have a compressive strength over 2 MPa, while for some types of gypsum plasters this limit increases up to 6 MPa at most. On the other hand, the highest lower limit for compressive strength of limes for structural application is 5 MPa, according to the Turkish standards conforming European norms [37]. As can be seen from Figure 9, the compressive strength values of all the gypsum-lime based mortars are over 6 MPa. However, CW30, which has the lowest compressive strength value has a compressive strength loss of 60.7%. The closest result to the reference sample was obtained from the G10 sample. This sample showed a decrease of 15.7% compared to the sample R.

It is a known fact that porosity has a significant effect on the mechanical properties of the materials. Compressive strength is one of the most important mechanical properties of the structural material. An increase in porosity decreases compressive strength. In the literature, many experimental studies have been conducted on this subject and theoretical equations have been generated. In the studies carried out on gypsum plasters, the relationship between the porosity and compressive strength has been presented experimentally and theoretically [38, 39]. In the light of these data, it will be more meaningful to evaluate the compressive strength results together with porosity results given in section 3.3. It is seen that the amount of pores formed by the use of waste additives significantly affected the compressive strength results.

### 3.6. Bending Strength

The results of bending strength tests are given in Figure 10. The bending strength results varied between 3.4 MPa – 5.7 MPa. The trend of the results is similar to the compressive strength results. The highest value belongs to R sample and the lowest obtained from CW30. Morsy et al. [6] performed bending tests on metakaolin – fly ash – lime – gypsum containing sample and the results varied between 2.2 MPa – 4.1 MPa. In another study performed by Vimmrova et al. [40] on gypsum – lime – metakaolin binders, the highest bending strength value was 5.8 MPa. In general, it can be seen that WGP containing samples gave higher bending strength values than other waste containing groups. This may be partly due to the pozzolanic nature of the WGP. Besides, as it can be seen from the results of unit weight, UPV and porosity, the pore-forming effects of other wastes are thought to have a negative effect on bending strength results as the effect on the compressive strength results.

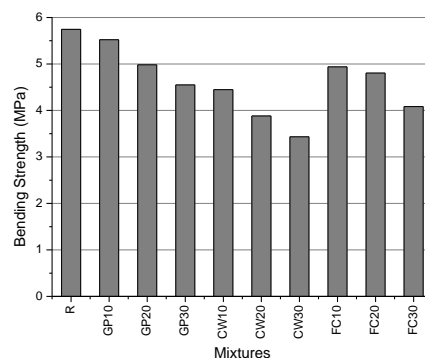
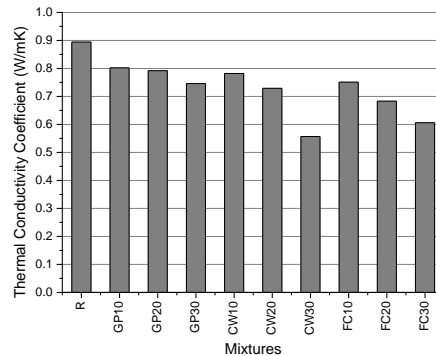


Figure 10. Bending strength values of samples.

### 3.7. Thermal Conductivity

The thermal conductivity coefficients of samples are given in Figure 11. Thermal conductivity decreased with the addition of wastes. The R sample has a thermal conductivity of 0.894 W/mK. The lowest value belongs to the CW30 sample, which is 0.557 W/mK. The closest value to the R sample

obtained from GP10, which is 0.802 W/mK. It can be seen that from the figure, waste addition decreased the thermal conductivity coefficient between 10.3% and 37.7%. The increment in the thermal performance of the sample is related to a decrease in unit weight and an increase in porosity with the addition of wastes. The microstructure of a material strongly affects the thermal conductivity [41]. Vimmarova et al. [40] investigated the thermal performance of gypsum – lime – metakaolin binders and the values changed between 0.198 – 0.348 W/mK. The results are quite low, but it should be noted that the water/binder ratio used in the study ranged from 0.7 to 0.85. Another study [42] based on diatomite added gypsums, which is a very low density and porous material, reported that the thermal conductivity values varied between 0.348 – 0.497 W/mK.



**Figure 11. Thermal conductivity coefficients of samples.**

### 3.8. Scanning Electron Microscopy

To examine the microstructure of samples, SEM micrographs were taken from some samples. Figure 12 shows the SEM micrographs.

The micrographs were taken from every 10% and 30% waste containing sample besides sample R. In these micrographs two basic points are examined. The first one is the porosity and the compactness of the matrix phase and the second one is the quality of the adherence between the aggregate particles and the matrix. From Figure 12a, it can be seen that the matrix phase and the adherence between the matrix and the aggregate are quite denser. This denser structure appears to be looser in the waste added samples. Particularly in the case of COW-containing samples, it can be seen that needle-like gypsum crystals have a much more separate structure. When the adherence condition of the samples examined, it is seen that the aggregate-matrix interface is much looser in samples containing COW and there are significant gaps between aggregates and the paste phase. In samples containing WGP, it can be seen that the paste is more compact and the aggregates are better covered by the paste phase.

## 4. Conclusions

In this study, the use of some waste material in gypsum-lime based mortars was experimentally investigated. According to the data obtained, the following conclusions can be drawn;

- Waste addition slightly decreased the unit weight. In this way a more lightweight product obtained.
- Ultrasonic pulse velocity values decreased with the increase of the waste amount. This is related to the amount of the pores in the body. This finding also confirmed by the results of the apparent porosity test. The highest porosity obtained from CW30.

- Water absorptions of the samples increase by the increase in waste amount. This is also related to the pore structure.
- The highest compressive and bending strength was obtained from sample R. Waste addition decreased the mechanical properties. This is related to the loose microstructure of the matrix and the aggregate-paste interface.
- Waste addition improved the thermal properties of the samples. The thermal conductivity coefficient decreased between 10.3% - 37.7%.

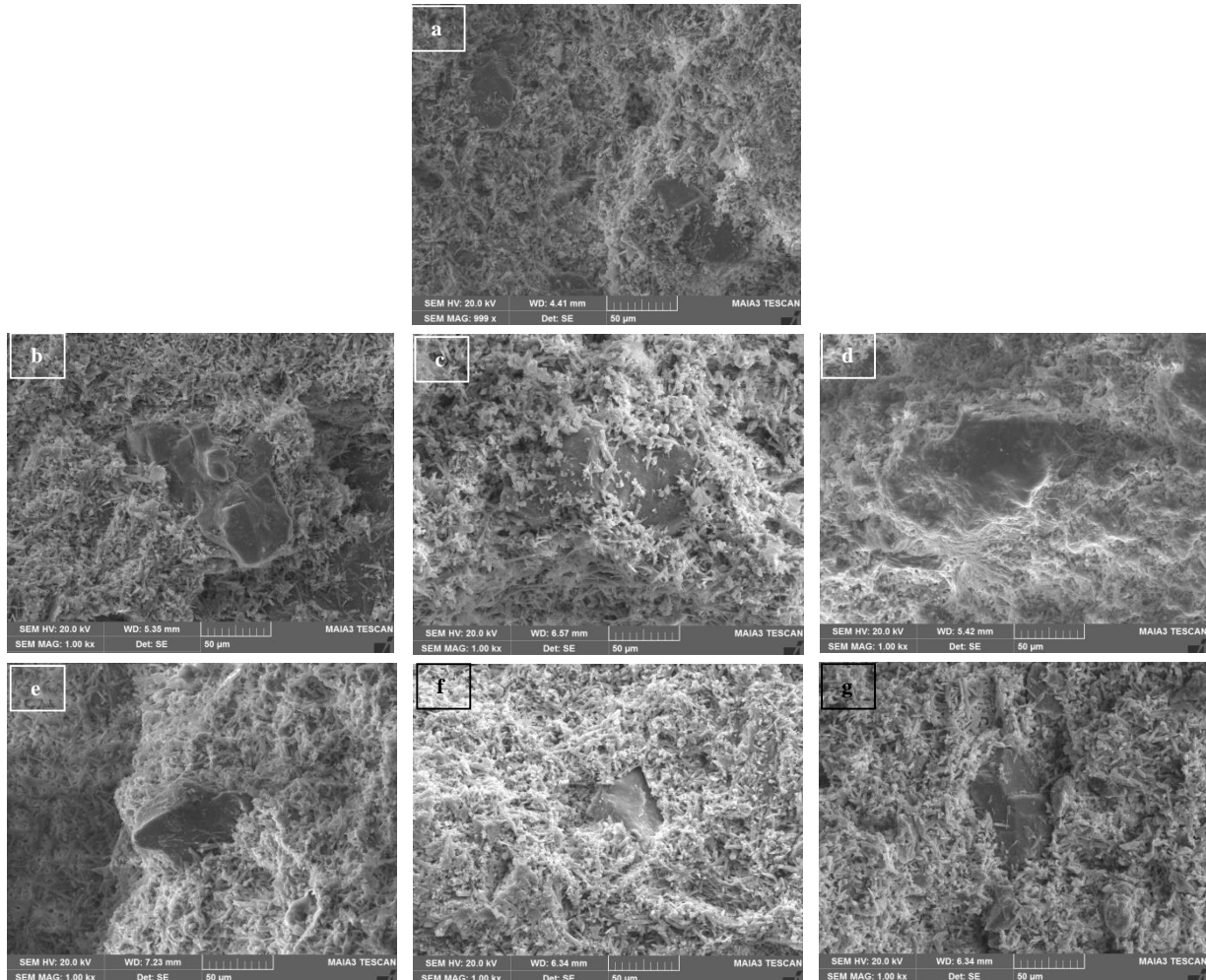


**Figure 12. SEM images of a) R b) G10 c) G30 d) S10 e) S30 f) C10 g) C30**

## References

- [1] Serna, A., del Rio, M., Palomo, J. G., Gonzalez, M., (2012). Improvement of gypsum plaster strain capacity by the addition of rubber particles from recycled tyres, *Construction and Building Materials*, 35, 633-641.
- [2] Biçer, A., Kar, F., (2017). Thermal and mechanical properties of gypsum plaster mixed with expanded polystyrene and tragacanth, *Thermal Science and Engineering Progress*, 1, 59-65.
- [3] Gencil, O., del Coz Diaz, J. J., Sütçü, M., Köksal, F., Alvarez Rabanal, F. P., Martinez-Barrera, B., Brostow, W., (2014). Properties of gypsum composites containing vermiculite and polypropylene fibers: Numerical and experimental results, *Energy and Buildings*, 70, 135-144.
- [4] Barrera-Barbero, M. M., Medina Flores, N., (2018). The effect of polypropylene fibers on graphite-natural hydraulic lime pastes, *Construction and Building Materials*, 184, 591-601.

- [5] Yılmaz, F., Fidan, D., (2017). Effect of wetting-drying cycles on volumetric stability of clayey soil stabilized with lime and perlite, *European Journal of Technique*, 7 (2), 2017-2018.
- [6] Kamnikas, R., Mituzas, J., Kamnikas, A., (2006). The effect of pozzolana on the properties of the finest fraction of separated Portland cement, *Ceramics*, 50, 15-21.
- [7] Morsy, M. S., Alsayed, S. H., Salloum Y. A., (2012). Development of eco-friendly binder using metakaolin-fly ash-lime-anhydrous gypsum, *Construction and Building Materials*, 35, 772-777.
- [8] Khalil, A. A., Abdel kader A. H., (2010). Preparation and physicomechanical properties of gypsum plaster-agro fiber waste composites, *Journal of InterCeram: International Ceramic Review*, 21, 62-67.
- [9] Wang, Y., Shui, Z., Gao, X., Huang, Y., Yu, R., Ling, G., (2019). Chloride binding behaviors of metakaolin-lime hydrated blends: influence of gypsum and atmospheric carbonation, *Construction and Building Materials*, 201, 380-390.
- [10] Demir, İ., Başpınar, M. S., (2008). Effect of silica fume and expanded perlite addition on the technical properties of the fly ash-lime-gypsum mixture, *Construction and Building Materials*, 22, 1299-1304.
- [11] Gourav, K., Reddy, B. V. V., (2018). Out-of-plane flexure behavior of fly ash-lime-gypsum brick masonry walls, *Engineering Structures*, 173, 241-250.
- [12] Neto, A. A. M., Cincotto, M. A., Repette, W., (2010). Mechanical properties, drying and autogenous shrinkage of blast furnace slag activated with hydrated lime gypsum, *Cement and Concrete Composites*, 32, 312-318.
- [13] Del Rio Merino, M., Astorqui, J. S. C., Saez, P. V., Jimenez, R. S., Cortina, M. G., (2018). Eco plaster mortars with addition of waste for high hardness coatings, *Construction and Building Materials*, 158, 649-656.
- [14] Khalil, A. A., Tawfik, A., Hegazy, A. A., El-Shahat, M. F., (2014). Effect of some waste additives on the physical and mechanical properties of gypsum plaster composites, *Construction and Building Materials*, 68, 580-586.
- [15] Aubert, J. E., Segui, P., Husson, B., Measson, M., (2012). A method developed to quantify lime and gypsum consumed by mineral additions, *Cement and Concrete Composites*, 34, 874-880.
- [16] Massazza, F., (1998). "Pozzolana and Pozzolanic Cements" in *Lea's Chemistry of Cement and Concrete*, Butterworth-Heinemann, 471-635.
- [17] PAGÇEV, Atık İstatistikleri. <http://www.pagcev.org/atik-istatistikleri>. 2007. Accessed: 07.09.2019.
- [18] Lu, J. X., Zheng, H., Yang, S., He, Pingping, Poon, C. S., (2019). Co-utilization of waste glass cullet and glass powder in precast concrete products, *Cons. Built. Mat.*, 223, 210-220.
- [19] Du, H., Tan, K. H., (2017). Properties of high volume glass powder concrete, *Cement and Concrete Composites*, 75, 22-29
- [20] Ling, T. C., Poon, C. S., (2014). Feasible use of large volumes of GGBS in 100% recycled glass architectural mortar, *Cement and Concrete Composites*, 53, 350-356.
- [21] Vaitkevicius, V., Serelis, E., Hilbig, H., (2014). The effect of glass powder on the micro-structure of ultra high performance concrete, *Construction and Building Materials*, 68, 102-109.
- [22] Redden, R., Neithalath, N., (2014). Microstructure, strength, and moisture stability of alkali activated glass powder-based binders, *Cement and Concrete Composites*, 45, 46-56.
- [23] Durgun, M. Y., Sevinç, A. H., (2019). High temperature resistance of concretes with GGBFS, waste glass powder, and colemanite ore wastes after different cooling conditions, *Cons. Built. Mat.*, 196, 66-81.

- [24] Papadakis, V. G., Tsimas, S., (2002). Supplementary cementing materials in concrete Part I: efficiency and design, *Cement and Concrete Research*, 32, 1525-1532.
- [25] Sevim, U. K., (2011). Colemanite ore waste concrete with low shrinkage and high split tensile strength, *Materials and Structures*, 44, 187-193.
- [26] Olgun, A., Kavas, T., Erdogan Y., Once G., (2007). Physico-chemical characteristics of chemically activated cement containing boron, *Building and Environment*, 42, 2384-2395.
- [27] Ochoa, G. P. A., Eras, J. J. C., Gutierrez, A. S., Hens, L., Vandecasteele, C., (2010). Residue from sugarcane juice filtration (filter cake): Energy use at the sugar factory, *Waste and Biomass Valorization*, 1, 407-413.
- [28] Makul, N., Sua-iam, G., (2016). Characteristics and utilization of sugarcane filter cake waste in the production of lightweight foamed concrete, *Journal of Cleaner Production*, 126, 118-133.
- [29] Yaduvanshi, N. P. S., Yadav, D. V., (1990). Effect of sulphation press mud and nitrogen fertilizer on biomass, nitrogen economy and plant composition in sugarcane and soil chemical properties, *The Journal of Agricultural Science*, 114 (3), 259-263.
- [30] Neha, G., Sumit, T., Chandrajit, B., (2011). Characterization of press mud: a sugar industry waste, *Fuel*, 90, 389-394.
- [31] Li, H., Xu, J., Wu, J., Xu W., Xu, Yan, (2012). Influence of sugar filter mud on formation of Portland cement clinker, *Journal of Wuhan University of Technology*, 28 (4), 746-750.
- [32] Li, H., Xu, W., Yang, X., Wu, J., (2014). Preparation of Portland cement with sugar filter mud as lime-based raw material, *Journal of Cleaner Production*, 66, 107-112.
- [33] James, J., Pandian P. K., (2016). Geoenvironmental application of sugarcane press mud in lime stabilization of an expansive soil: a preliminary report, *Australian Journal of Civil Engineering*, 14 (2), 114-122.
- [34] Mansoor, A. M., Visgai, P., Sumeha, P. S., Swathi, K., Sowmiya, R., (2017). Utilization of sugar mill waste in manufacturing of bricks, *International Journal of Engineering Research and Technology*, 5 (13), 1-5.
- [35] Tesch, V., Middendorf, B., (2006). Occurrence of thaumasite in gypsum lime mortars for restoration, *Cement and Concrete Research*, 36, 1516-1522.
- [36] TS EN 13279-1, Gypsum binders and gypsum plasters – Part 1: Definitions and requirements, February 2009, Turkish Standards Institute, Ankara.
- [37] TS EN 459-1, Building lime – Part 1: Definitions, specifications and conformity criteria, 2015, Turkish Standards Institute, Ankara.
- [38] Bu, J., Tian, Z., (2016). Relationship between pore structure and compressive strength of concrete: Experiment and statistical modeling, *Sadhana*, 41 (3), 337-344.
- [39] Schiller, K. K., (1971). Strength of porous materials, *Cement and Concrete Research*, 1 (4), 419-422.
- [40] Vimmrova, A., Keppert, M., Michalko, O., Cerny, R., (2014). Calcined gypsum-lime-metakaolin binders: Desing of optimal composition, *Cement and Concrete Composites*, 52, 91-96.
- [41] Sevim, D., Fidan, Ş., Polat, S., Oktay, H., (2017). Experimental and articial neural network based studies on thermal conductivity of lightweight building materials, *European Journal of Technique*, 7 (1), 33-41.
- [42] Gencil, O., del Coz Diaz, J. J., Sutcu, M., Koksall, F., Alvarez Rabanal, F. P., Martinez-Barrera, G., (2016), A novel lightweight gypsum composite with diatomite and polypropylene fibers, *Construction and Building Materials*, 113, 732-740.

## CONDENSATION ANALYSIS OF THE INSULATION OF WALLS IN MARDIN PROVINCE ACCORDING TO DIFFERENT LOCATIONS

*Fatih UNAL<sup>1\*</sup>*,

*In this study, condensation and vapor diffusion caused by different positioned insulation in the wall were analyzed for Mardin province. In the analysis, according to the 2008 standard of TS 825, the MATLAB calculation program was used with the Glaser graphing method and graphical user interface (GUI). Extruded polyurethane foam was used as the insulation material and normal unreinforced concrete was chosen as the wall. Evaporation and condensation values were determined by creating 6 different wall models with the same insulation thickness of 20 cm and an unreinforced concrete wall was covered with 2 cm plaster on the inside with a 3 cm thickness on the outside. The data obtained for 2 cm and 4 cm insulation thicknesses are presented in tables and the results are interpreted for Mardin province. Consequently, it was seen that the worst wall structure in terms of condensation and evaporation was obtained in the middle insulated wall and later in the interior insulated wall structure. The externally insulated wall did not show any condensation.*

*Keywords: Condensation and vapor diffusion, Glaser graphic method, TS 825 Standard, Insulation*

### 1. Introduction

Turkey is a foreign dependent country in terms of energy sources. Therefore, any kind of energy efficiency research has great importance for our country. If insulation materials are used correctly and in sufficient quantities, materials, energy, and costs will be saved [1]. The outer walls of the buildings, which form a border between the interior spaces, remain under the influence of constantly changing climatic conditions. In order to provide comfort conditions according to the changing climatic conditions, it is necessary to insulate the walls of the structures in appropriate ways. The use of insulation in buildings is important both to meet comfort requirements and to reduce initial installation costs and so to reduce energy consumption. Additionally, insulation comfort conditions are provided by preventing energy consumption and condensation from occurring. Thus, moisture and mold problems that shorten the life of the structure are prevented due to condensation. Sweating occurs according to summer and winter comfort conditions and conditions of use. Sweating or condensation forms on surfaces corresponding to the temperature at which the water vapor in the air releases moisture. If the water vapor in the air does not condense on the surface of the building material, it enters the building material without sweating. At this point, as soon as the partial pressure

---

<sup>1</sup> Department of Mechanical Program, Mardin Artuklu University, Mardin, TURKEY, (fatihunal@artuklu.edu.tr)   
<https://orcid.org/0000-0001-6660-9984>

of the water vapor emitted to the building material is equal to the water vapor saturation pressure, it begins to condense in the inner layers. The condensation of water vapor in the air passing through the structure causes paint deterioration, mold, fungus growth, and odor. Condensation increases heat loss by increasing the total heat transfer coefficient of the material and disrupts the structure of the material [2].

When the studies in the literature are examined, Umaroğulları et al. [3] calculated some insulated and uninsulated wall sections using the WUFI@2D-3 computer program for reinforced concrete wall elements in Edirne province where the outdoor conditions change and the indoor environment is considered constant. Kavas [4] researched condensation control in terms of internal surface temperature and also studied the applicability of the sections and insulation materials, which are recommended in the thermal insulation regulation to determine whether the sections were suitable for thermal comfort.

Freezing is the condensation of water vapor in the structure causing mold, loss of adhesion, and corrosion. Water vapor passing through the structure may also carry chemicals that will damage the structure. Therefore, Akman [5] stated that in most of the demolished structures, steel reinforcements rust and the element loses its bearing quality. Bircan [6] designed a computer program and studied the process of vapor diffusion in building materials. Yuksek [7], analyzed the adequate thermal conductivity values using a reinforced concrete skeleton structure in the 3rd-degree-day zone for the determination of suitable thicknesses and condensation tests of the TS 825 by using different structural components in the vertical structural elements of the structure. Using the program designed with TS 825 method, Ozel and İlgin Beyazıt [8] stated that the worst wall in terms of condensation is in the inner wall and then in the inner and middle insulated walls respectively.

Unlike other studies, this study was analyzed with software developed by Turkey's 2nd degree-days in the region at the outer walls of buildings located in Mardin province for condensation and vapor diffusion of the TS 825 standard. For the designated structures, condensation and vapor passage were examined for each of the insulated walls from inside, middle, and outside sections. Additionally, extruded polystyrene foams with 2 cm and 4 cm thicknesses were used as insulation materials and also unreinforced concrete was used as the wall material.

## 2. Humidity control with TS 825 method

The water vapor diffused through the dry air was calculated by the Fick Law correlation  $W_y$  ( $\text{kg}/\text{m}^2\text{h}$ ). The vapor diffusion flow rate (flow) in the wall block was calculated by Equation 1.

$$W_y = \delta_o x \frac{P_i - P_d}{s_{d.T}} \quad (1)$$

The vapor diffusion obtained from a non-condensing building element is given in Figure 1. The difference between the amount of moisture transported from the interface where the condensation is present and the amount of moisture transported is the amount of condensation.

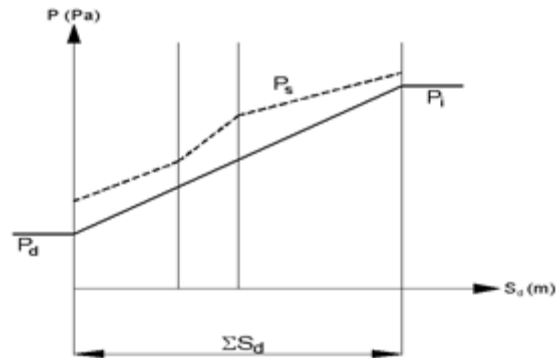


**Figure 1. Vapor diffusion in a building element without condensation.**

The amount of condensation can be calculated using Equation 2.

$$W_t = \delta_o \left( \frac{P_i - P_{sw}}{S_{d,T} - S'_{d,sw}} - \frac{P_{sw} - P_d}{S'_{d,sw}} \right) \quad (2)$$

Water vapor diffusion equivalent air layer thickness is calculated by Equation 3:

$$S_d = \mu * d \quad (3)$$

In this equation,  $\mu$  expresses the water vapor diffusion resistance factor and  $d$  is the thickness of the layer (m).

The partial pressures were calculated by multiplying the relative humidity and saturated vapor pressure values corresponding to the internal and external temperatures. The partial pressure  $P$  (Pa) was calculated by Equation 4 and the saturated vapor pressure  $P_s$  (Pa) was calculated by Equation 5-7.

$$P = P_s * \varphi \quad (4)$$

$$P_s = a \left[ b + \frac{T}{100^\circ\text{C}} \right]^n \quad (5)$$

$$T \leq 0^\circ\text{C} \Rightarrow P_s = 610,5e^{\frac{21,875T}{265,5+T}} \quad (6)$$

$$T \geq 0^\circ\text{C} \Rightarrow P_s = 610,5e^{\frac{17,269T}{237,3+T}} \quad (7)$$

For preparation and interpretation of the graph of the building shell element for the condensation period, the amount of condensation water, water vapor diffusion equivalent air layer thickness, the difference between indoor and outdoor temperature, internal and external surface temperatures and internal temperatures, saturated vapor pressure values and partial vapor pressure values should be determined [9-11]. For this purpose, the amount of heat passing through the building component was calculated with the help of Equations 8-15.

$$q = \alpha_d * (T_d - T_{dy}) \quad (8)$$

$$T_1 = T_{yi} - R_1 * q \quad (9)$$

$$T_2 = T_1 - R_2 * q \quad (10)$$

$$q = \alpha_i * (T_i - T_{iy}) \quad (11)$$

$$T_{iy} = T_i - \frac{q}{\alpha_i} \quad (12)$$

$$T_n = T_{n-1} - R_n * q \quad (13)$$

$$q = U * A * (T_i - T_d) \quad (14)$$

$$U = \frac{1}{\frac{1}{\alpha_i} + \frac{d_1}{\lambda_1} + \frac{d_2}{\lambda_2} + \dots + \frac{d_n}{\lambda_n} + \frac{1}{\alpha_d}} \quad (15)$$

In the above equations: The internal and external surface temperatures are given as  $T_{iy}$  and  $T_{dy}$  ( $^{\circ}\text{C}$ ), respectively.  $T_i$  and  $T_d$  indicate indoor and outdoor temperatures ( $^{\circ}\text{C}$ ), respectively.  $R_n$  is defined as  $1/(d_n/\lambda_n)$ .  $\alpha$  is the internal heat transfer coefficient (W/mK) and  $\alpha_d$  is the external heat transfer coefficient (W/mK). The total heat transfer coefficient of the structural component is given as  $U$  (W/m<sup>2</sup>K), the thermal conductivity coefficient of the component forming layer is given as  $\lambda$  (W/mK) and the thickness of the component forming layer is given as  $d$  (m).

### 3. Condensation and diffusion examined wall models

In this study, amounts of condensation and evaporation were calculated by using 2 cm and 4 cm extruded polyurethane insulation materials on the inner, middle, and outer parts of the unreinforced concrete wall. Schematic shapes of wall structures examined are given in this section and condensation and vapor diffusion graphics are presented for 2 cm insulation thickness per unit area in January for Mardin province.

#### 3.1. Internal insulated wall model

The internal insulated wall model examined in the study is given in Figure 2. As seen in the figure, the effect of condensation inside the structure was examined by placing insulation material on the inner surface of the wall. When Figure 3 is examined, condensation was started at a point in the midpoints of the insulation layer and condensation occurred in more than half the area of the brick wall.

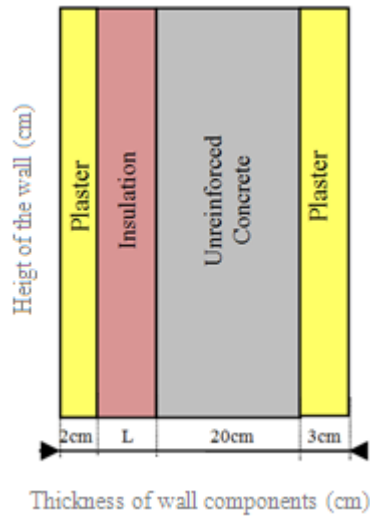


Figure 2. Internally insulated wall.

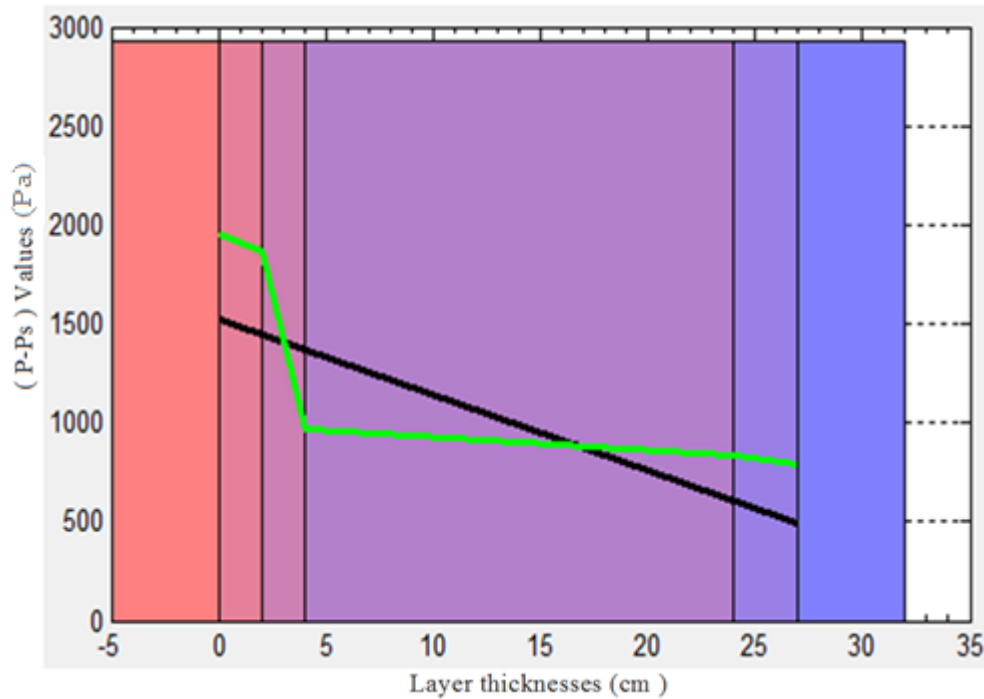


Figure 3. Vapor diffusion on 2 cm insulated wall from inside.

3.2. Middle insulated wall model

The medium insulated wall model examined in the study is given in Figure 4. As shown in the figure, the solution made as the insulation material was placed in the middle of the unreinforced concrete wall. The vapor diffusion change in the middle insulated building block is shown in Figure 5. As seen in the figure, condensation occurs in one-third of the area covering the first part of the concrete wall near the end of the insulation and the second piece of the non-reinforced concrete wall.

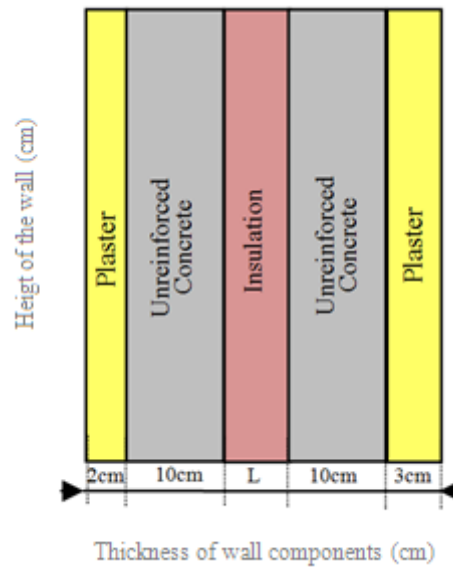


Figure 4. Middle insulated wall.

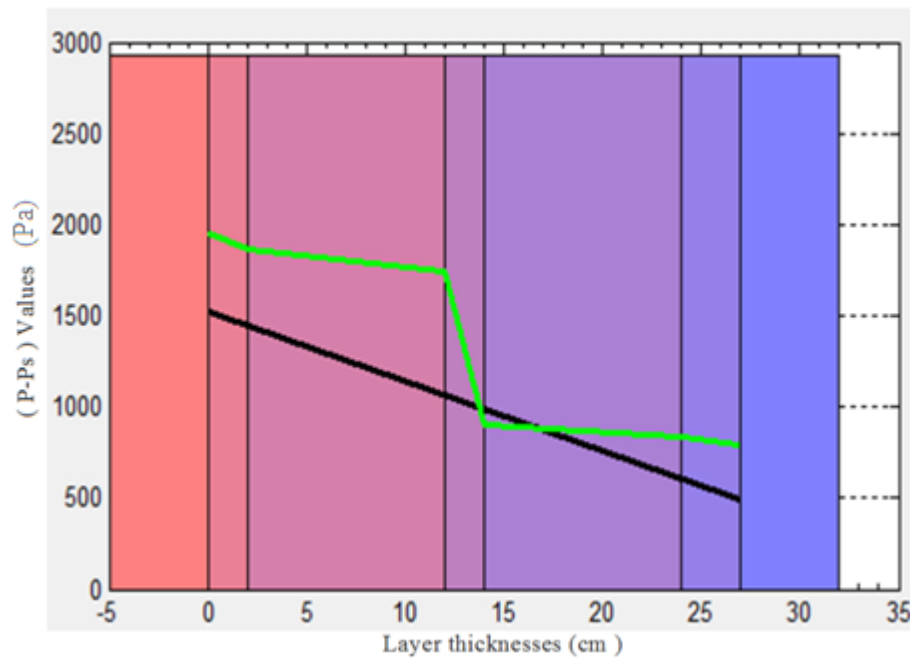


Figure 5. Vapor diffusion on 2 cm insulated wall in the middle.

### 3.3. Externally insulated wall model

The externally insulated wall model used in the study is given in Figure 6. As shown in the figure, the placed wall was covered with 2 cm of internal and 3 cm of external plasters. Then, a wall model was created by placing extruded polyurethane insulation materials with 2 cm and 4 cm thicknesses on the outer surface of the 20 cm thick unreinforced concrete wall. Figure 7 shows the variation of the vapor diffusion for the wall thickness. As seen in this figure, no condensation occurred, but there was a risk of condensation between the insulation layer and the plaster on the outer surface towards the endpoint of the insulation.

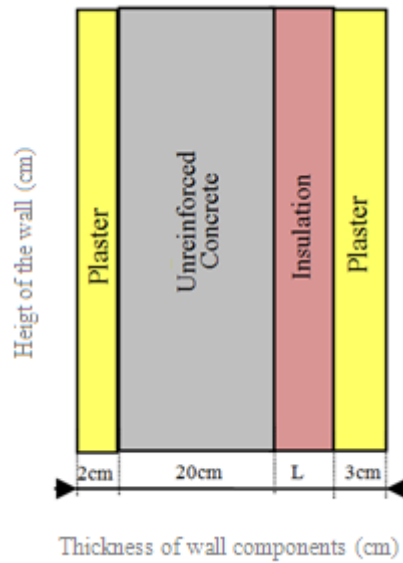


Figure 6. Externally insulated wall.

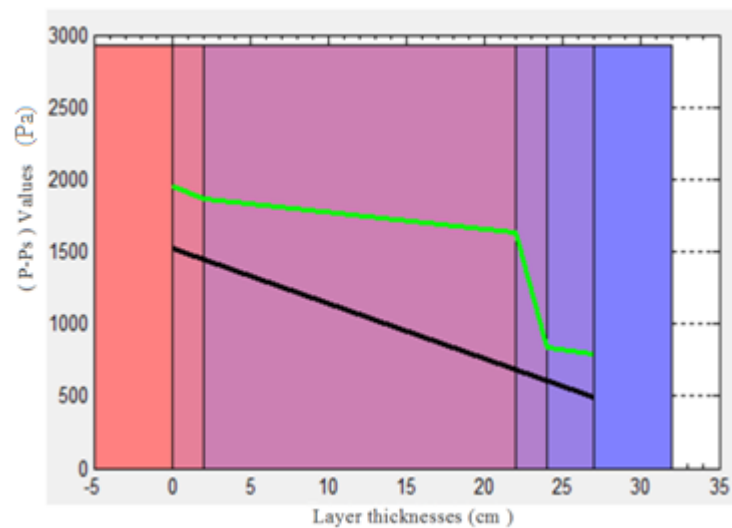


Figure 7. Vapor diffusion on external 2 cm insulated wall.

#### 4. Results and discussion

In this study, condensation and vapor diffusion analysis of different insulation models of wall structures were performed for Mardin province, which located in Turkey's 2nd degree-days area. For this purpose, a computer program prepared according to TS 825 Standard was used. The building block was examined as a 20 cm wide unreinforced concrete wall, extruded polystyrene foam insulation material of 2 cm, 4 cm, and 6 cm thickness, and 2 cm gypsum plaster from inside and 3 cm gypsum plaster from outside. Analyzes were made according to this building block and the results obtained were given in Table 1.

**Table 1. Condensation and evaporation amounts for 3 different insulation positioning situations with 2 cm, 4 cm, and 6 cm insulation thickness for Mardin province.**

Wall Insulation Thickness	Unreinforced Concrete Wall	Internal Insulated Wall	Center Insulated Wall	Externally Insulated Wall
	+ Extruded Polyurethane Foam			
2 cm Insulated Wall	$W_v$ (kg/m <sup>2</sup> )	0,088153	0,20538	0,178079
	$W_t$ (kg/m <sup>2</sup> )	0,04515	0,14648	-
4 cm Insulated Wall	$W_v$ (kg/ m <sup>2</sup> )	0,079482	0,17346	0,160562
	$W_t$ (kg/ m <sup>2</sup> )	0,00254	0,06836	-
6 cm Insulated Wall	$W_v$ (kg/m <sup>2</sup> )	0,072364	0,15012	0,146184
	$W_t$ (kg/ m <sup>2</sup> )	0,00994	0,03751	-

When the data obtained for 3 different locations and three different insulation thicknesses of the insulation model in Mardin are examined;

- In the analyzes made for the internally insulated wall model;

As a result of the calculation made by using 2 cm insulation material according to the TS 825 method, it was calculated that the amount of condensation water is 0.04515 kg/m<sup>2</sup> in months when the amount of condensation water can be seen all year. Moreover, the amount of water vapor carried from the wall is 0.088153 kg/m<sup>2</sup> and since this amount is 0.043006 kg/m<sup>2</sup> more than the amount of water condensed on the wall during the year, the total amount of condensed water evaporates during the year. As a result of the calculation made according to the TS 825 method by using 4 cm insulation material, it was calculated that the amount of condensing water was 0,00994 kg/m<sup>2</sup>. Furthermore, since the amount of water vapor carried from the wall is 0.079482 kg/m<sup>2</sup>, this amount is 0.07694 kg/m<sup>2</sup> more than the amount of water condensed on the wall during the year and the total amount of water condensed during the year evaporates. As a result of the calculation made according to the TS 825 method by using 6 cm insulation material, it was determined that the amount of condensing water was 0,00994 kg/m<sup>2</sup>. Besides, since the amount of water vapor carried from the wall is 0,072364 kg/m<sup>2</sup>, this amount is 0.062426 kg/m<sup>2</sup> more than the amount of water condensed on the wall during the year and the total amount of water condensed during the year evaporates. According to the results, the best insulation thickness for the internally insulated wall model was found to be 4 cm.

- In the analysis made for the middle insulated wall model;

As a result of the calculation made according to the TS 825 method by using 2 cm insulation material, it was calculated that the amount of condensing water was 0,14648 kg/m<sup>2</sup> in the whole year. In addition to this, the amount of water vapor carried from the wall is 0,20538 kg/m<sup>2</sup> and since this amount is 0,058903 kg/m<sup>2</sup> more than the amount of water condensed on the wall during the year, the total amount of condensed water evaporates during the year. As a result of the calculation made according to the TS 825 method by using 4 cm insulation material, it was calculated that the amount of condensing water was 0,06836 kg/m<sup>2</sup>. Furthermore, since the amount of water vapor carried from the wall is 0,17346 kg/m<sup>2</sup>, this amount is 0,1051 kg/m<sup>2</sup> more than the amount of water condensed on the wall during the year and the total amount of water condensed during the year evaporates. As a result of the calculation made according to the TS 825 method by using 6 cm insulation material, it was determined that the amount of condensing water was 0,03751 kg/m<sup>2</sup>. Additionally, since the amount of water vapor carried from the wall is 0,15012 kg/m<sup>2</sup>, this amount is 0,112608 kg / m<sup>2</sup> more than the amount of water condensed on the wall during the year and the total amount of water condensed

during the year evaporates. According to the results, the best insulation thickness for the middle insulated wall model was found to be 6 cm.

- In the analysis made for the external insulated wall model;

As a result of the calculation made according to the TS 825 method by using 2 cm insulation material, the amount of water vapor carried from the wall throughout the year was 0,178079 kg/m<sup>2</sup>. When a similar analysis was performed for 4 cm insulation thickness, the amount of water vapor carried from the wall was 0.160562 kg/m<sup>2</sup>. In the analysis made for 6 cm insulation thickness, it was calculated that 0,146184 kg/m<sup>2</sup> water vapor was evaporated. According to the results, the best insulation thickness for the external insulated wall model was found to be 6 cm.

As a result, for all three insulation thickness; The best insulation position is externally insulated and the worst insulation position is determined as the middle insulated wall model. In the evaluation made in terms of problems such as mold, moisture and paint deterioration, it was determined that the insulation position where the condensation did not occur and the natural structure of the structure did not deteriorate was an external wall model.

### Nomenclature

d: Layer Thickness Forming Component m

D: Diffusion constant cm<sup>2</sup>sn<sup>-1</sup>

P: Partial Water Vapor Pressure Pa

P<sub>s</sub>: Saturated Water Vapor Pressure Pa

S<sub>a</sub>: Water Vapor Diffusion Equivalent Air Layer Thickness m

q: Heat Transfer Amount W

T<sub>i</sub> : Indoor Temperature °C

T<sub>d</sub>: Outdoor Temperature °C

T<sub>iy</sub>: Internal Surface Temperature °C

T<sub>dy</sub>: Outer Surface Temperature °C

U: Total Heat Transfer Coefficient of Component W(m<sup>2</sup>K)<sup>-1</sup>

W<sub>γ</sub>: Amount of Steam Flow (Flow) kgm<sup>-2</sup>

W<sub>c</sub>: Amount of condensation, kgm<sup>-2</sup>

λ: Heat conduction coefficient of the material W(mK)<sup>-1</sup>

α<sub>i</sub>: Internal Heat Transfer Coefficient W(m<sup>2</sup>°C)<sup>-1</sup>

α<sub>d</sub>: External Heat Transfer Coefficient W(m<sup>2</sup>°C)<sup>-1</sup>

μ: Vapor diffusion resistance factor μ

φ: Relative Humidity %

δ<sub>o</sub>: Steam Transmission Coefficient of air kg(msPa)<sup>-1</sup>

### References

- [1] Kallioglu, M.A., Bati, Z.A, Karakaya H., Durmuş A. (2016). Environmental and economic analysis of optimum heat insulation thickness in energy saving, *European Journal of Technic*,6(2),160-169
- [2] Heperkan H.A., Bircan M.M., Sevindir M.K. (2001). Vapor diffusion and condensation in building materials, *V. National Installation Engineering Congress and Exhibition, İzmir, TURKEY*, 461-469

- [3] Umaroğulları F., Zorer Gedik, G., Mihlayanlar, E. (2011). Condensation Control of Insulated and Uninsulated Concrete Walls in the Periodic Regime: The Case of Edirne. *megaronjournal*, 6(1), 13-20
- [4] Kavas, E., Thermal Protected Wall Sections in Eastern Anatolia Region and Condensation Control (Erzurum Case), Master Thesis, Yıldız Technical University, İstanbul, TURKEY, 1997
- [5] Akman, S., *Building damage and repair principles*, TMMOB Publications, İstanbul, TURKEY, 2000
- [6] Bircan, M.M., Computer program for the examination of the vapor diffusion process in building materials and condensation calculation, Mater Thesis, Yıldız Technical University, İstanbul, TURKEY, 1999
- [7] Yüksek İ., Sıvacılar S.( 2017). Thermal Efficiency of Different Types Covered Walls TS 825 A Comparative Study on Conditions in Turkey. *Politeknik Journal*, 20 (2), 291-302
- [8] Özel, M, İlgin Beyazıt, N . (2018). Condensation Analysis According to Different Location of Insulation in Wall. *Dicle University Journal of Engineering Faculty(DÜMF)*, 9 (2), 785-794
- [9] Glaser, H. (1959). Graphisches Verfahren zur Untersuchung von Diffusionsvorgängen, *Kaltetechnik 11*, Heft 10/59, 345-349
- [10] Anon., DIN 4108, Warmeschutz im Hochbau, Beuth Verlag GmbH, Berlin, 1981
- [11] Anon., TS 825 Thermal Insulation Rules in Buildings, Turkish Standard Draft, Ankara, 2008

## DETERMINING EFFECTS OF HEAT TRANSFER FINS ON THE SOLIDIFICATION PROCESS OF PCM AND NANO-PCM WITH A RECTANGULAR COOLER

*Besir KOK<sup>1\*</sup>, Mert GÜRTÜRK<sup>2</sup>*

*In this study, the performances of the heat transfer fins during the solidification processes of PCM and nano-PCMs( $Al_2O_3$  -  $CuO$ ) were investigated. These two situations were considered for both with and without fins. Two different heat transfer fins were considered in the study. The investigation was carried out using both experimental (for Base-PCM) and numerical methods. The results showed that the effects of heat transfer fins were limited due to the overcooling effect of PCMs. The solidification process of Base-PCM in the heat storage tank ended in 10 minutes, while the solidification time of the PCM was determined as 11 minutes by using the Fin 1 design. The solidification process in the heat storage tank with nano-PCM ( $CuO$ ) was realized in 13 minutes with the Fin 1 design.*

Key words: PCM; Fin; TES; Solidification

### 1. Introduction

In the literature, there are many studies designed and examined for the solidification process of PCM in the TES. For example, heat transfer fluid was passed through a cylindrical cooler placed in a cylindrical heat storage tank. The solidification process of PCM which is in the liquid phase between the cooler and heat storage walls was investigated. The temperature and liquid mass fraction values of PCM were discussed in that study. In the study, corrugated heat transfer fins were designed to improve the solidification process of PCM [1]. When the studies in the literature are examined, it is seen that the most commonly used heat transfer fin type is rectangular. In one of those studies, rectangular heat transfer fins were used to accelerate the solidification time of a PCM in the liquid phase. By changing the placement of those fins in the heat reservoir, many parameters were considered during the solidification of the PCM. These parameters are temperature fields, current lines and solid fraction. All those values were taken into consideration in the solidification process of PCM based on time [2]. In many studies examined in the literature, it is seen that heat storage geometry is cylindrical. Innovative fins were designed to the solidification of PCM, which is in the liquid phase, in a cylindrical heat reservoir. Many parameters were considered examining the effects of those fins and PCM on the solidification process. Those parameters such as solidification time, temperature distribution, total solidification time were examined [3]. Many numerical methods are used to examine the solidification process of PCM. It is seen that different strategies are followed in those methods. Approaches such as the use of adaptive mesh structure and porosity evaluation of the surface between solid and liquid phase PCM are adopted. Using the adaptive mesh structure, contour of values such as the solidification process, total energy, solid fraction in a TES were formed and examined [4]. In some studies, the solidification process of PCM was examined by considering the heat storage design. In one of those

<sup>1</sup> Technical Vocational School, Firat University, Elazig, Turkey, ([besirkok@gmail.com](mailto:besirkok@gmail.com))  <https://orcid.org/0000-0001-7241-952X>

<sup>2</sup> Department of Energy Systems Engineering, Technology Faculty, Firat University, Elazig, Turkey, ([m.gurturk@gmail.com](mailto:m.gurturk@gmail.com))   
<https://orcid.org/0000-0003-0380-5704>

studies, the solidification process of PCM in thermal energy storage, which is a triplex tube, was investigated [5]. The same researchers conducted a similar study to accelerate the melting time of PCM [6]. In a similar heat store, a study was carried out considering the natural convection occurring during the solidification process. In the study, the solidification process of PCM, which is in the liquid phase, between heat reservoir and heat transfer fins made from aluminum was examined. The parameters such as liquid fraction, minimum temperature value, average temperature value, which depend on time, were considered [7]. As mentioned before, it is emphasized that there are many studies on various heat transfer fin designs during the solidification process of PCM. In one of those studies, various analyses were carried out considering the variable thickness parameters of the heat transfer fins. In those analyses, parameters such as solidification time, solid fraction and temperature contour were examined [8]. In the fin designs studied so far, the heat transfer fins have a non-porous structure. Studies were conducted on the effects of heat transfer fins, which have a foam structure, on the solidification process of PCM [9]. In the last study discussed in the introduction part of the study, the effects of V shape heat transfer fins on the solidification process of PCM were investigated. The researchers examined the solidification process of PCM in the heat reservoir with a numerical study [10].

In this study, the effects of heat transfer fins placed in the heat storage tank, which is rectangular geometry, on the solidification process of PCM were investigated. However, the effects of the fins designs on the solidification process of the PCM and nano-PCM were examined in this study.

## 2. Material and Methods

Two different heat transfer fins were considered. The effects of these designed fins on the solidification process of PCM were investigated. The effects of the designed Fin 1 are compared with the effects of the heat transfer Fin 2 placed throughout the heat reservoir, which are highly preferred in the literature, to the melting of the PCM. In this study, by adding nanoparticle particles to PCM, the thermophysical properties of paraffin wax were changed. The main purpose of nano-material adding into PCM is to obtain PCMs with poorer thermophysical properties. For this reason, many nano-PCM studies have been investigated and it is seen that mixing high amounts of nanomaterial with PCM has a bad effect on the heat storage property of PCM. The experimental study was used to determine the validation process of the numerical model. The solidification of PCM in the heat storage was experimentally carried out. The flow diagram of the experimental setup used in the experiments is shown in Fig. 1.

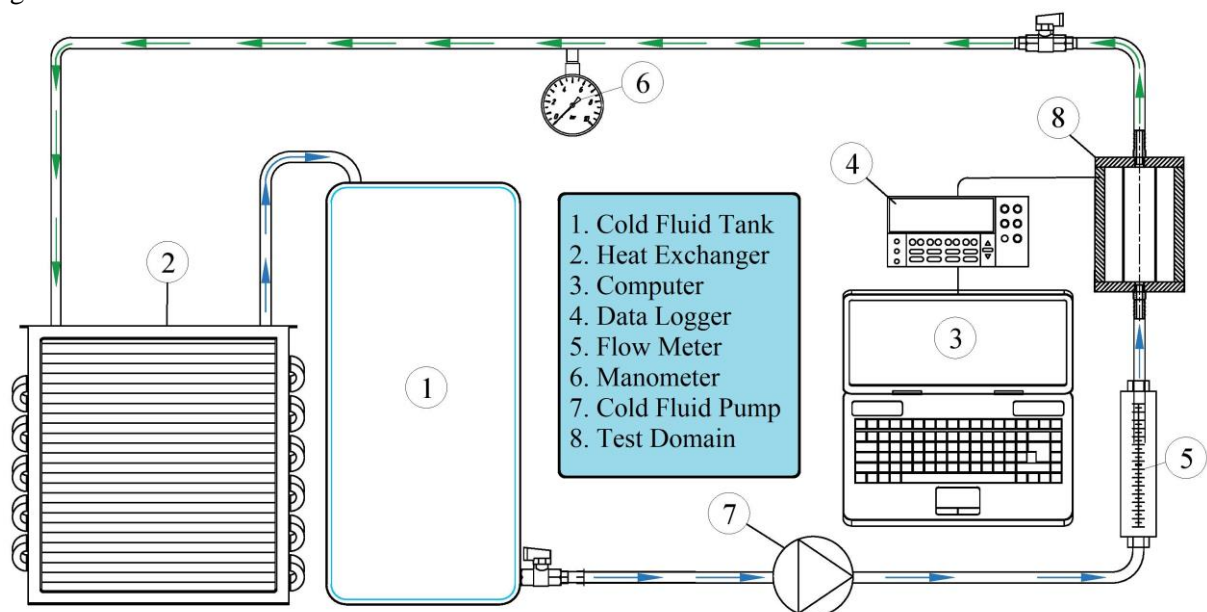


**Figure 1. Experimental setup**

During the discharge process of the thermal energy in the heat reservoir, water was sent by a circulation pump. The heated water in the TES is sent back to the cold water tank before being sent to the heat storage tank. The desired water temperature value is provided again by the cooling system. In the experiment setup, the measured temperature values were transferred to the computer with a datalogger. The flow rate of the circulating water in the system is 2.5 kg/s. The flow rate is controlled by a flow meter. Detailed drawings and boundary conditions of the test domain

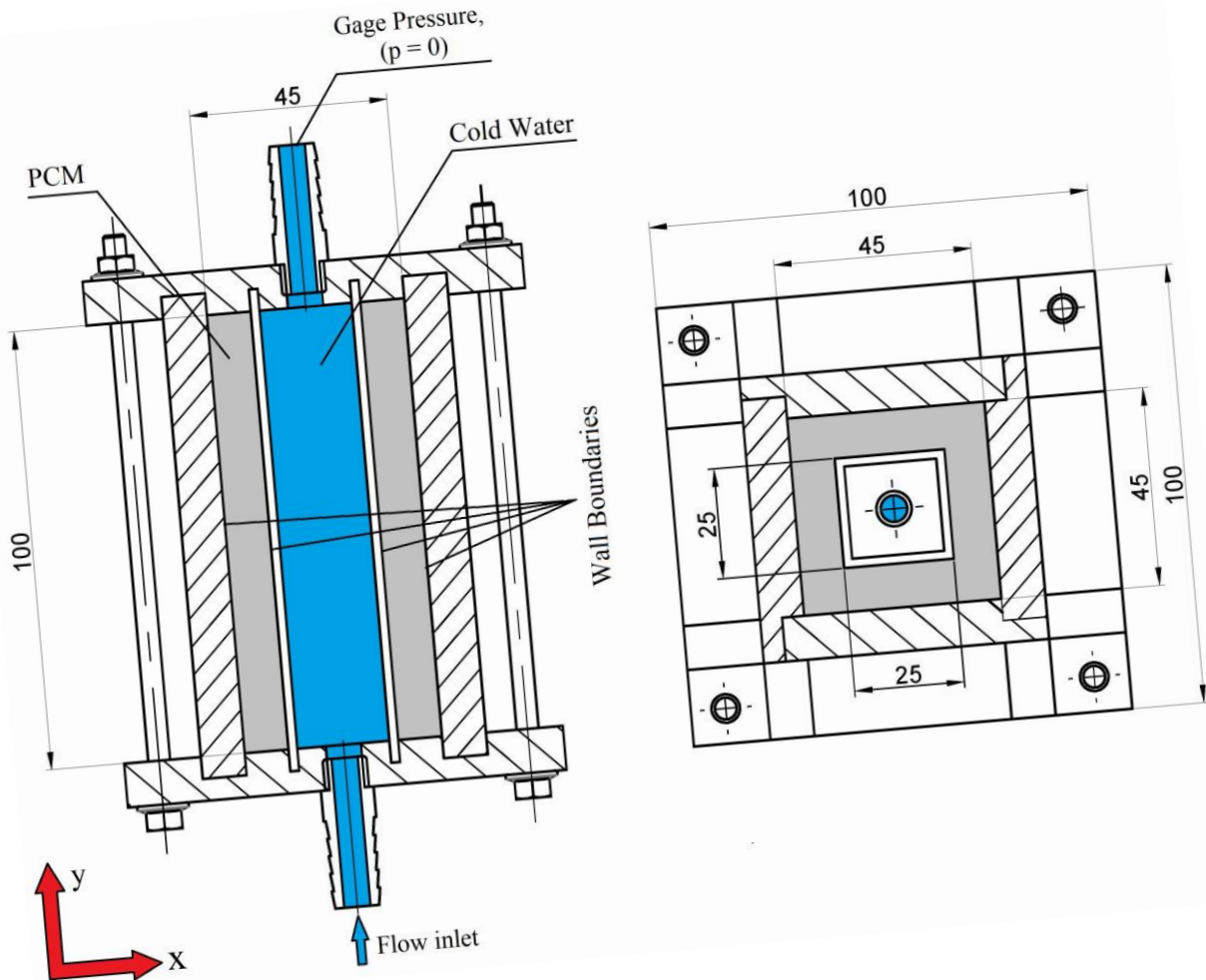


**Figure 2. Detailed drawings and boundary conditions of the test domain**

The figure shows the dimensions of the test domain. All dimensions are in millimeters. The cooler is rectangular and the refrigerant passes through this channel. There is PCM in the liquid phase in between the rectangular cooler and walls of the heat storage tank. The heat transfer fins considered in the scope of the study are shown in Fig. 3. The Fin 2 design shown in Fig. 3 is the most widely used heat transfer fin-type in the literature.

The heat conductive coefficient of PCM used in the experiments was determined by using KD2pro device. PCM (paraffin wax) used in the study has a heat conduction coefficient of  $0.3 \text{ W / m} \cdot \text{K}$  for the solid phase and  $0.095 \text{ W / m} \cdot \text{K}$  for the liquid phase. The heat conduction coefficient was measured experimentally using KD2'pro instrument. The instruments used in all measurement applications were first calibrated and then necessary measurements were made. The error rate of the device used to determine the thermal conductivity value is 0.0287. The melting temperature of the paraffin wax varies between 52 and 55 °C. The viscosity and density of PCM

used in the experiments were determined by the following equations. The density, the heat capacity, the viscosity, the thermal conductivity of the nano-PCMs are determined by using equations in Table 1.

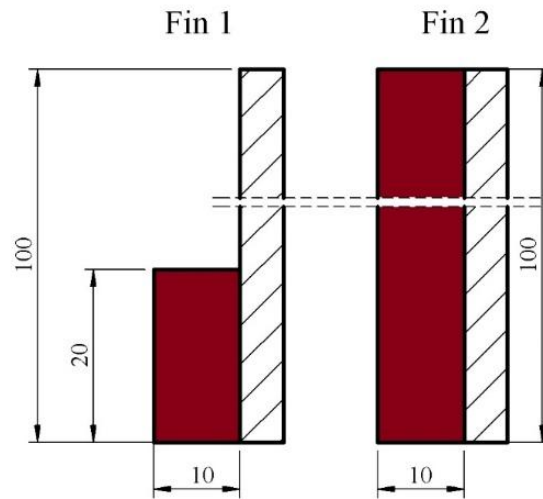


Figure 3. Heat transfer fins considered in the scope of the study

Table 1. Used equations

The density (PCM) [11, 12]	$\rho = \frac{750}{0.001(T - 319.15) + 1}$
The viscosity (PCM) [11, 12]	$\nu = 0.001 \exp\left(-4.25 + \frac{1790}{T}\right)$
The density (nano-PCMs) [13]	$\rho_{nPCM} = (1 - \Phi)\rho_{PCM} + \Phi\rho_p$
The heat capacity (nano-PCMs) [11]	$(\rho C_p)_{nPCM} = (1 - \Phi)(\rho C_p)_{PCM} + \Phi(\rho C_p)_p$
The viscosity (nano-PCMs) [11]	$\mu_{nPCM} = \frac{\mu_{nPCM}}{(1 - \Phi)^{2.5}}$
The thermal conductivity (nano-PCMs) [11]	$\frac{k_{nPCM}}{k_{nPCM}} = \frac{k_p + 2k_{PCM} - 2\Phi(k_{PCM} - k_p)}{k_p + 2k_{PCM} + \Phi(k_{PCM} - k_p)}$

Table 2 presents the density, specific heat capacity, thermal conductivity and viscosity values for base-PCM, Nano 1 - PCM (Paraffin Wax + Al<sub>2</sub>O<sub>3</sub>) and Nano 2 - PCM (Paraffin Wax + CuO). The table shows these properties for 25 °C (solid phase) and 70 °C (liquid phase). However, these values were calculated at 5 °C intervals between 25 °C and 85 °C and the boundary conditions were defined for these values in the program.

Table 2. Thermophysical properties of Base and Nano PCMs

	Nano Particles		Base-PCM (Paraffin Wax)		Nano 1 - PCM (Paraffin Wax + Al <sub>2</sub> O <sub>3</sub> )		Nano 2 - PCM (Paraffin Wax + CuO)	
	Al <sub>2</sub> O <sub>3</sub>	CuO	Solid (25°C)	Fluid (70°C)	Solid (25°C)	Fluid (70°C)	Solid (25°C)	Fluid (70°C)
<b>ρ(kg/m<sup>3</sup>)</b>	2702	8933	766	732	862.8	830.5	1174.4	1142
<b>Cp(J/kg K)</b>	903	385	2140	2580	1946.3	2307.2	1472.5	1721.5

<b>k(W/m K)</b>	237	401	0.3	0.095	0.3471	0.11	0.3473	0.11
<b><math>\mu</math>(kg/m s)</b>	-	-	-	$2.6 \times 10^{-3}$	-	$3 \times 10^{-3}$	-	$3 \times 10^{-3}$

The enthalpy of the phase change material is calculated by using Eq. (1) [14].

$$LH = h + \Delta LH \quad (1)$$

$h$  indicates the sum of the sensible enthalpy and  $LH$  is the latent heat.

$$\frac{\partial}{\partial t}(\rho H) + \nabla \cdot (\rho \vec{v} LH) = \nabla \cdot (k \nabla T) + S \quad (2)$$

where  $\rho$ ,  $\vec{v}$  and  $S$  are density, fluid velocity and source term, respectively. ANSYS FLUENT solve numerically continuity, momentum and energy equations by meant the finite volume method. The SIMPLE algorithm uses a relationship between velocity and pressure corrections to enforce mass conservation and to obtain the pressure field [14].

In this study, a rectangular cooler was placed in a rectangular heat tank. The PCM in the liquid phase was left to the volume remaining between the heat storage tank and the cooler.

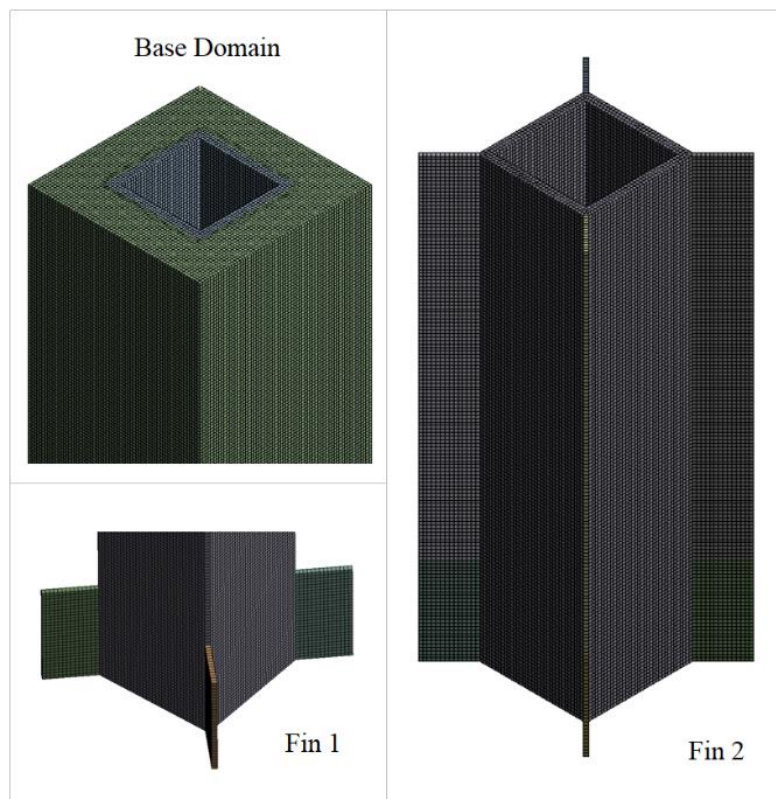


**Figure 4. Mesh structure**

The solidification process of PCM in the liquid phase was investigated by passing cold water through the rectangular cooler. The numerical method was used in the analysis and the mesh structure of the geometry was formed. Illustrations of the mesh structures formed are shown in Fig. 4. Fig. 4 shows mesh structures of the special heat transfer Fin 1 designed, Base-PCM (without fin) and heat transfer Fin 2 which is preferred in the literature. It is seen that the formed mesh structures are homogeneous and have a smooth transition between the mesh structures. A suitable mesh structure for CFD analysis of the problem has been obtained with the optimization of these different element numbers and mesh models. The liquid fraction values obtained for the different mesh structures and element numbers are given in Fig. 5.

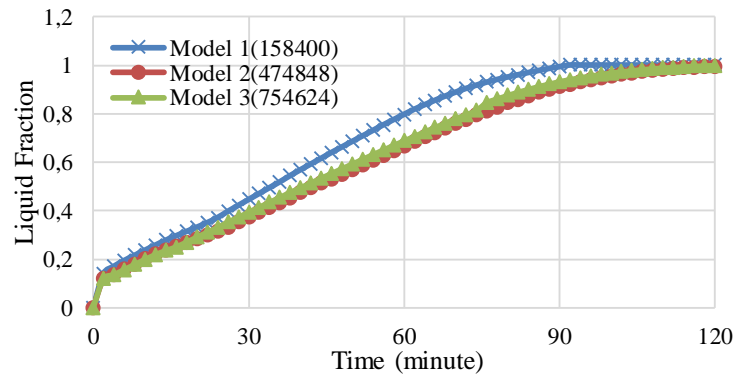


**Figure 5. Comparison of CFD models created according to different network structures and to liquid fraction values**

The data obtained from numerical and experimental measurements were taken into consideration and validation of the numerical model was performed. In Fig. 6, the temperature values obtained from numerical and experimental studies are compared with each other.

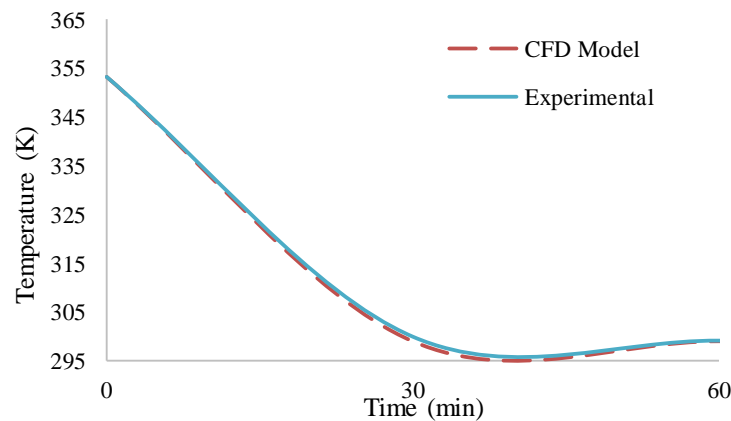


**Figure 6. Comparison of temperature values of both experiment and numerical measurements**

The results obtained from experimental and numerical analyses are very close to each other. This proves the reliability of the numerical model. The results obtained from the verification study of the numerical model show the accuracy of the method followed in the creation of the numerical model. Base\_Al<sub>2</sub>O<sub>3</sub>, Base\_CuO, Fin 1, Fin 2 ve Fin 1\_CuO numerical models were created by using the same method.

### 3. Results and Discussion

The solidification of the PCM is important as well as the melting of the PCM. Many studies have been conducted examining the discharge process of thermal energy during the solidification process of PCM. In this study, the effects of the specially designed fin on the solidification process of Base-PCM and nano-PCM were investigated by numerical analysis. Heat storage tank (without fin) was considered for three different situations. These three different situations are Base-PCM, Base\_Al<sub>2</sub>O<sub>3</sub> and Base\_CuO. Fig. 7 below shows the mass fraction obtained from the solidification process in the thermal energy storage in these three cases.

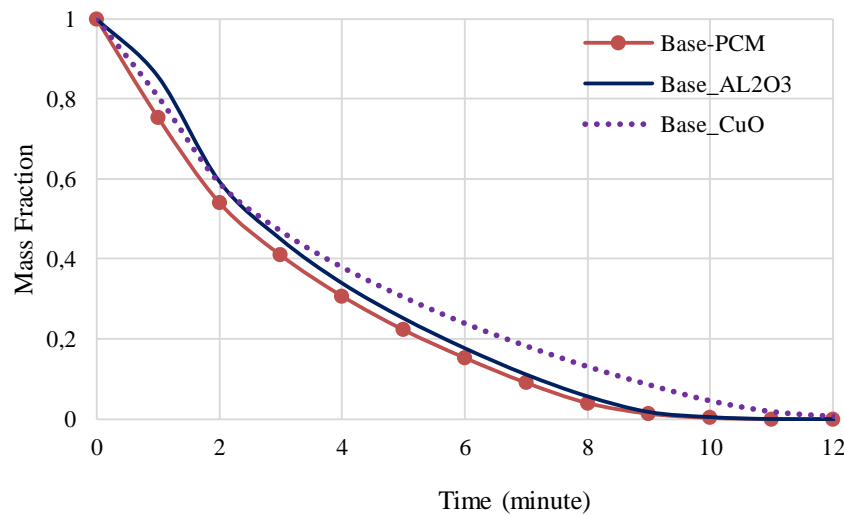


**Figure 7. Base-PCM and nano\_PCMs (CuO and Al<sub>2</sub>O<sub>3</sub>) solidification process in a thermal energy storage**

The figure shows the time-varying mass fraction for Base-PCM and nano-PCMs. In Fig. 7, the value 1 in the y-axis shows that the whole of PCM in the thermal heat store is in the liquid phase. 0 indicates that the whole of PCM is in the solid phase. The data obtained show that Base-PCM performed best. The solidification process was realized with Base-PCM in the shortest time. In the literature, it has been emphasized that the main purpose of using nano-PCM is to improve the thermophysical properties of PCM. The use of CuO at more than 1% causes negative effects on the thermophysical properties of PCMs [12]. In the solidification process, similar results were obtained in the literature. When the graph in Fig. 7 is examined, the worst solidification process is obtained with Base\_CuO. In this study, numerical models have been formed and the solidification processes of Base-PCM, Fin 1 and Fin 2 were examined. The results are shown in Fig. 8.

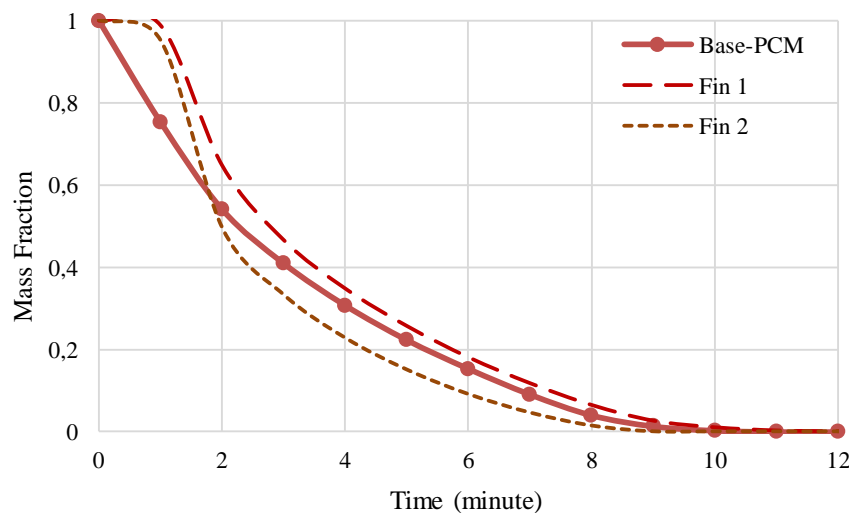


**Figure 8. Time-dependent variation of the solidification process of PCM in thermal energy tanks with and without fins**

As shown in Fig. 8, the Fin 2 design performed best in solidifying paraffin wax. The absence of heat transfer fins in the Base PCM model increases the discharge time of the energy stored in the PCM. This relates to the area of the cooling surface during the transfer of heat. Heat transfer fins in the thermal energy discharge process of PCMs perform better because they increase the surface area of the cooling

or heating surface. The worst in the solidification process was obtained with Fin 1. Fig. 9 shows the values for the solidification process in the cases of Base\_CuO, Fin 1\_CuO and Base-PCM.

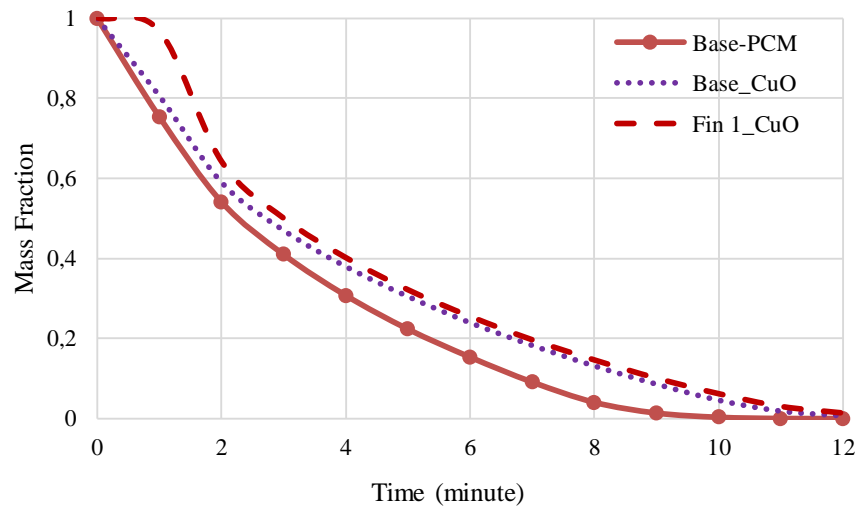


**Figure 9. Time-dependent variation of the solidification process of Base\_CuO, Fin 1\_CuO and Base-PCM**

When the solidification processes in Fig. 9 were examined, Base-PCM showed the best performance. Solidification in Base-PCM ended in 10 minutes. Solidification times of Fin 1\_CuO and Base\_CuO are 13 minutes. The solidification process of PCMs refers to the process of discharging thermal energy. The absence of a heat transfer fins in the PCM model increases the discharge time of the thermal energy stored in the PCM. This complicates the discharge of energy from the PCM in regions away from the cooling surface. High concentrations of nano-PCM (CuO) have negative effects on cooling. The non-fin Base-PCM model performed better during the solidification process of the PCM. Although the Fin 1\_CuO model had heat transfer fins, the solidification process took longer than the Base\_PCM model in Fig. 9. The energy stored as both sensible and latent heat is discharged during the solidification process of the PCM. As can be seen in many sources in the literature, it has been reported that overcooling occurs during the solidification process of PCM. As seen in this study, it was observed that PCM and nano\_PCM solidified under the effects of overcooling in a very short period of time.

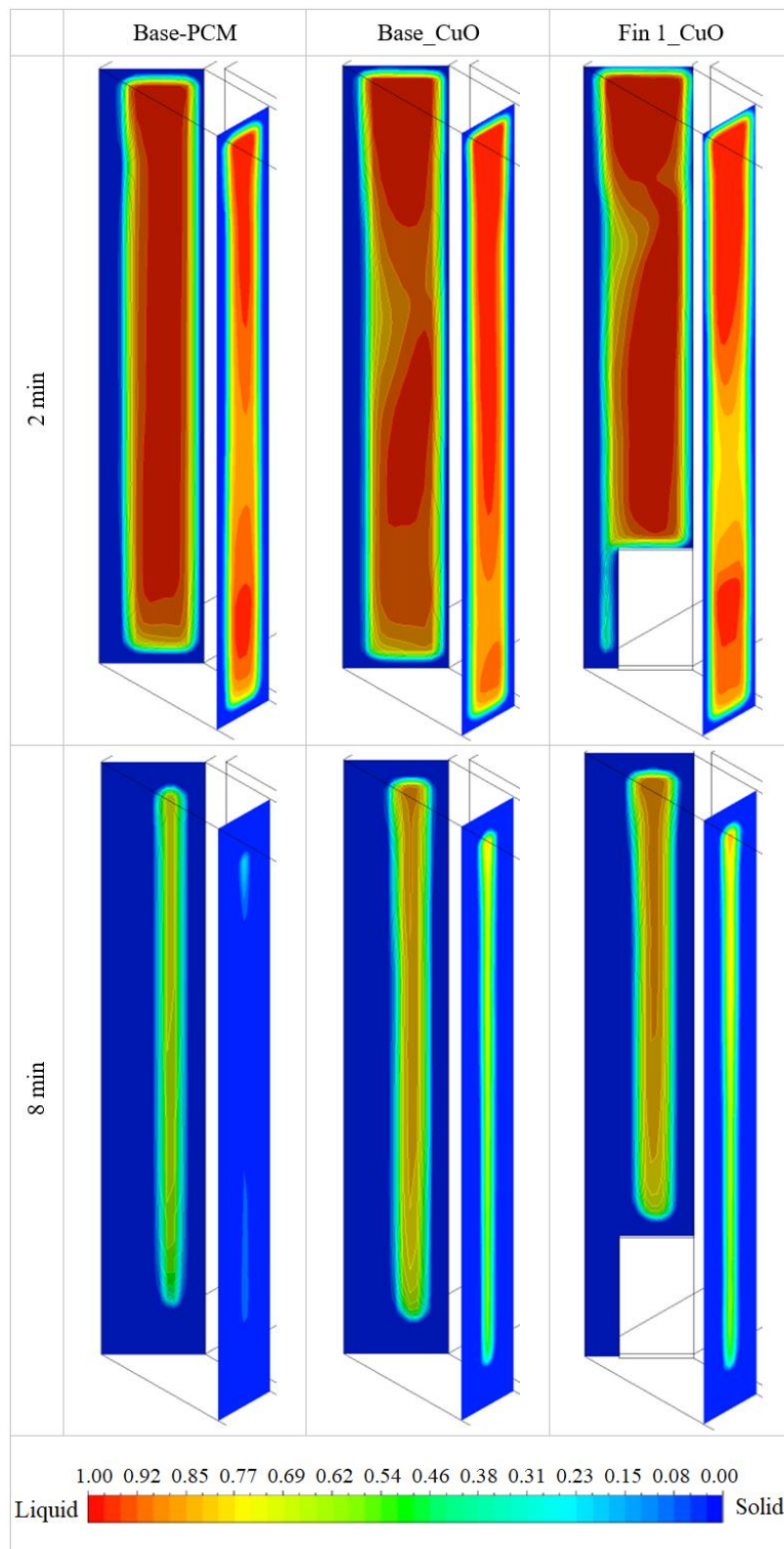


**Figure 10. Solidification process of Base-PCM, Base\_CuO and Fin 1\_CuO**

The solidification process of Base-PCM, Base\_CuO and Fin 1\_CuO, which solidify in a very short period of time, on two different planes in the heat storage are shown in Fig. 10. In parallel with the graph of Fig. 9, the values in Fig. 10 are similar. It can be said that the heat transfer Fin 1 has no effect on the solidification process. In general, there is no significant difference between the best performing and the worst-performing models during the solidification process. The main reason for this is the effects of overcooling. This can be better illustrated in Fig. 11.

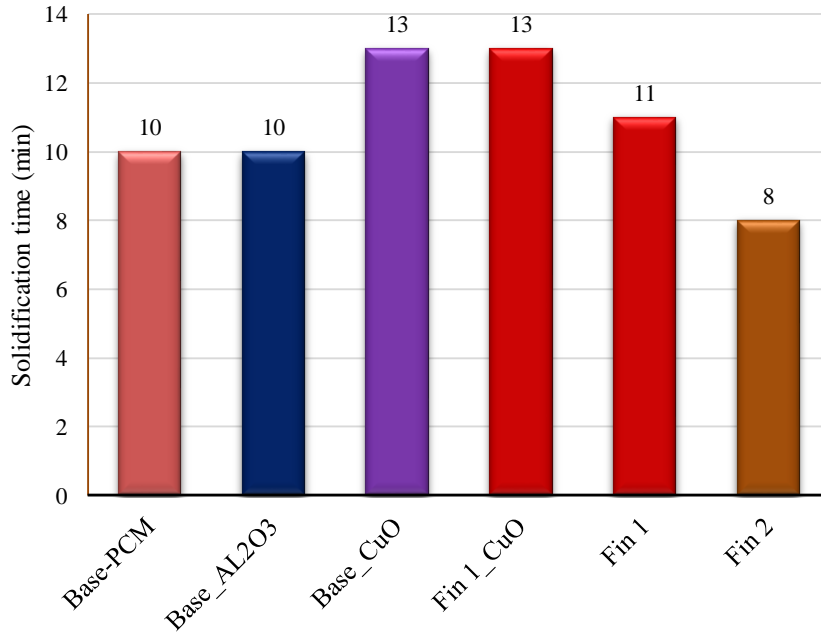
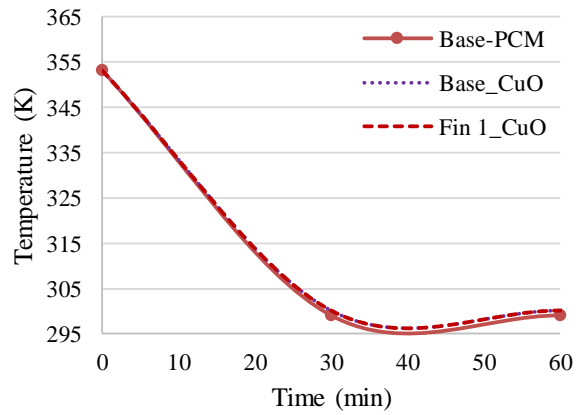
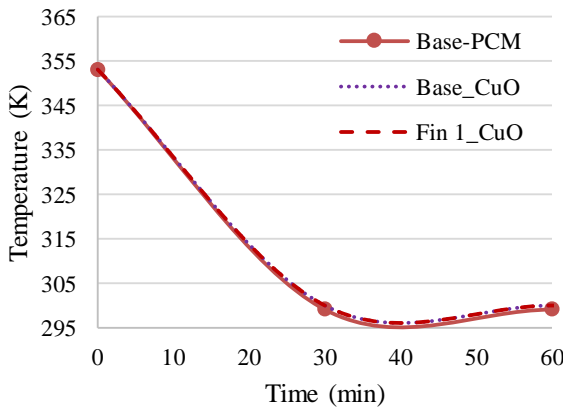


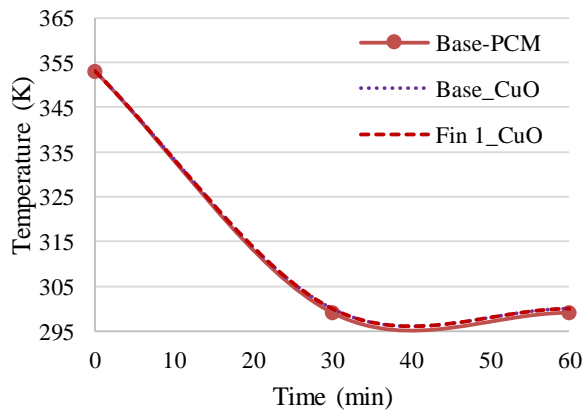
**Figure 11. Solidification time of all models**

When the data obtained are examined, it is seen that the effects of the special heat transfer fins in the solidification process of PCM are limited. When the data on the solidification process in Fig. 11 is examined, the best solidification was obtained with Fin 2 at 8 min, while the worst solidification process was at 13 minutes with Base\_CuO and Fin 1\_CuO. As shown in Figs 8-11, the Base\_PCM model performed better than Base\_CuO, Fin 1\_CuO and Fin 1 models.



**Top**

**Middle**



**Bottom**

### Figure 12. Temperature values at different point of the thermal energy storage

The difference between the best and the worst is only 5 minutes due to the effects of overcooling. The data examined up to this part of the article is related to the discharge process of the latent heat of the PCM. Sensible heat discharge of PCMs is obtained by considering temperature graphs. Fig. 12 shows the temperature graphs of Base-PCM, Fin 1\_CuO and Base\_CuO. Fig. 12 shows the temperature values at different points within the thermal energy storage. There is almost no difference between the temperature values for all three cases. The discharge time of the sensible heat in the Thermal Energy Storage (TES) ended at about 40. Min. When parameters in Fig. 12 are considered, it is understood that there is no difference between the temperature values at different points in the TES. As with latent heat, the effects of overcooling can be seen during the discharge of sensible heat. As a result, Fin 1 has a limited effect on the solidification process of PCM and nano-PCM. This comment can be observed in the process that occurs during the discharge of both sensible and latent heat.

#### 4. Conclusion

In this study, the effects of these fins on the solidification process of PCM were investigated.

- The effect of Fin 1 on the solidification processes of PCM and 1% prepared nano-PCM (CuO) was very limited.
- With the Fin 1 design, the solidification of the nano-PCM (CuO) was achieved in 13 minutes. This process showed that the latent heat of nano-PCM with Fin 1 was discharged at 13 min, but the sensible energy of the nano\_PCM with Fin 1 was discharged at 40 min.
- The solidification process of Base-PCM ended in 11 min by using Fin 1. The solidification process of Base-PCM is 10 minutes. In view of these two conditions, the Fin 1 design has not a positive contribution to the solidification process of paraffin wax.
- The findings show that the effects of heat transfer fins may be limited due to the overcooling effect of PCM and nano-PCM. However, it should be emphasized that this may also vary according to the size of the thermal heat store and the amount of PCM.

#### Nomenclature

B	liquid fraction
$C_p$	specific heat capacity (J/kg · K)
g	gravity (m/s <sup>2</sup> )
h	enthalpy (J/kg)
k	thermal conductivity (W/m · K)
L	length (m)
LH	laten heat (J/kg)
S	source term
T	temperature (K)
t	time (s)
$\vec{v}$	velocity (m/s)
$\nu$	viscosity (Ns/m <sup>2</sup> )
Greek letters	
$\mu$	viscosity (Ns/m <sup>2</sup> )
$\rho$	density (m <sup>3</sup> /kg)

$\Phi$  particle concentration

Subscripts

ref reference

PCM phase change material

nPCM nano phase change material

p pressure

## References

- [1] Aly KA, El-Lathy AR, Fouad MA (2019) Enhancement of solidification rate of latent heat thermal energy storage using corrugated fins. *J Energy Storage* 24:100785 . doi: 10.1016/j.est.2019.100785
- [2] Jmal I, Baccar M (2018) Numerical investigation of PCM solidification in a finned rectangular heat exchanger including natural convection. *Int J Heat Mass Transf* 127:714–727 . doi: 10.1016/j.ijheatmasstransfer.2018.08.058
- [3] Liu S, Peng H, Hu Z, et al (2019) Solidification performance of a latent heat storage unit with innovative longitudinal triangular fins. *Int J Heat Mass Transf* 138:667–676 . doi: 10.1016/j.ijheatmasstransfer.2019.04.121
- [4] Sheikholeslami M (2018) Numerical modeling of nano enhanced PCM solidification in an enclosure with metallic fin. *J Mol Liq* 259:424–438 . doi: 10.1016/j.molliq.2018.03.006
- [5] Mahdi JM, Nsofor EC (2018) Solidification enhancement of PCM in a triplex-tube thermal energy storage system with nanoparticles and fins. *Appl Energy* 211:975–986 . doi: 10.1016/j.apenergy.2017.11.082
- [6] Mahdi JM, Lohrasbi S, Ganji DD, Nsofor EC (2018) Accelerated melting of PCM in energy storage systems via novel configuration of fins in the triplex-tube heat exchanger. *Int J Heat Mass Transf* 124:663–676 . doi: 10.1016/j.ijheatmasstransfer.2018.03.095
- [7] Sefidan AM, Sojoudi A, Saha SC, Cholette M (2017) Multi-layer PCM solidification in a finned triplex tube considering natural convection. *Appl Therm Eng* 123:901–916 . doi: 10.1016/j.applthermaleng.2017.05.156
- [8] Hosseinzadeh K, Alizadeh M, Tavakoli MH, Ganji DD (2019) Investigation of phase change material solidification process in a LHTESS in the presence of fins with variable thickness and hybrid nanoparticles. *Appl Therm Eng* 152:706–717 . doi: 10.1016/j.applthermaleng.2019.02.111
- [9] Yang X, Niu Z, Bai Q, et al (2019) Experimental study on the solidification process of fluid saturated in fin-foam composites for cold storage. *Appl Therm Eng* 161:114163 . doi: 10.1016/j.applthermaleng.2019.114163
- [10] Alizadeh M, Hosseinzadeh K, Shahavi MH, Ganji DD (2019) Solidification acceleration in a triplex-tube latent heat thermal energy storage system using V-shaped fin and nano-enhanced phase change material. *Appl Therm Eng* 163:114436 . doi: 10.1016/j.applthermaleng.2019.114436
- [11] Valan Arasu A, Sasmito AP, Mujumdar AS (2011) Thermal performance enhancement of paraffin wax with AL<sub>2</sub>O<sub>3</sub> and CuO nanoparticles - A numerical study. *Front Heat Mass Transf* 2:1–7 . doi: 10.5098/hmt.v2.4.3005
- [12] Iachachene F, Haddad Z, Oztop HF, Abu-Nada E (2019) Melting of phase change materials in a trapezoidal cavity: Orientation and nanoparticles effects. *J Mol Liq* #pagerange# . doi: 10.1016/j.molliq.2019.03.051
- [13] Khodadadi JM, Hosseinizadeh SF (2007) Nanoparticle-enhanced phase change materials (NEPCM) with great potential for improved thermal energy storage. *Int Commun Heat Mass Transf* 34:534–543 . doi: 10.1016/j.icheatmasstransfer.2007.02.005
- [14] (2013) ANSYS Fluent Theory Guide

## EFFECT OF FORMING HISTORY ON CRASHWORTHINESS OF A SPOT-WELDED AND DOUBLE-HAT ELLIPTICAL THIN-WALLED TUBE

Hüseyin BEYTÜT<sup>1</sup>, Selçuk KARAGÖZ<sup>2\*</sup>, Serkan ÖZEL<sup>3</sup>

*Thin-walled structures (TWTs) are widely used in automotive and aerospace industries due to their easy formability, high energy absorption capacity, low cost, and lightweight advantages. In this study, considering the forming history, the crashworthiness of spot-welded and double-hat shaped elliptical TWT was numerically investigated under dynamic axial load, by the finite element method (FEM). In addition, a bead-shaped trigger mechanism was added to the TWT to reduce the peak crushing force. Non-uniform thickness distribution (thickening or thinning of some elements), plastic strain and work hardening may occur during forming. To investigate the effect of the forming history on crashworthiness, the sheet metal was formed by single-acting deep-drawing process and forming data were mapped to the TWT. The results showed that forming history has an effect on the crashworthiness of the tube. With deep-drawing results mapped to the tube, energy absorption decreased by 5.218% and peak crushing force decreased by 3.614%. Numerical simulations were conducted by using the nonlinear finite element codes RADIOSS/explicit.*

**Keywords:** *Crashworthiness; Thin-Walled Tubes; Forming History; Finite Element Method; Deep-Drawing.*

### 1. Introduction

Due to high competition, strict safety norms and increase in accident rates, the crashworthiness of TWTs are becoming more important these days. Since TWTs undergo large plastic deformation in a very short period during the accidents, their behavior is more complicated. Therefore, understanding how TWTs behave in the event of a possible accident is extremely critical in terms of passenger and goods safety.

In the years when FEM and computer technology have not been developed so far, researches have focused mainly on theoretical and experimental studies [1-4]. With the development of FEM and computer technology, dynamic analyzes can be made by using FE codes and thanks to these, time and money can be saved.

---

<sup>1</sup>Department of Mechanical Engineering, Bitlis Eren University, Bitlis, Turkey, (hbeytut@beu.edu.tr)  <https://orcid.org/0000-0001-8751-2225>

<sup>2\*</sup>Department of Mechanical Engineering, Bursa Technical University, Bursa, Turkey, (selcuk.karagoz@btu.edu.tr)  <https://orcid.org/0000-0002-1987-5750>

<sup>3</sup>Department of Mechanical Engineering, Bitlis Eren University, Bitlis, Turkey, (sozel@beu.edu.tr)  <https://orcid.org/0000-0003-0700-1295>

In recent years, many studies have been conducted by researchers to improve the energy absorption capability of the TWTs. The studies are mainly focused on the effect of geometric configurations (different cross-section, conical, tapered) and materials [5-11].

TWTs under the dynamic axial load can undergo global (Euler type) or progressive (accordion, diamond) buckling. Since global buckling usually occurs from the center with single folding, energy absorption is limited [12]. Length, diameter, and thickness are the most important geometric parameters that determine the deformation mode [13, 14]. Thus, these parameters should be considered during the design of TWTs.

The absorbed energy (AE) in the course of plastic deformation, is found by the area under the force versus displacement curve which obtain by crash test. Generally, the peak crushing force (PCF) occurs at the first reaction force and it is one of the disadvantages of TWTs used for energy absorption. PCF should be low in terms of passenger and goods safety. In addition, since PCF occurs in a very short time, the effect on AE is limited. The studies have shown that by adding the trigger mechanism (hole, groove, hollow), the initial folding was start easier and the PCF decreased [15, 16].

TWTs can be produced by sheet metal forming methods such as deep-drawing, hydroforming and extrusion. Plastic deformation occurs during forming of thin-walled tube and plastic deformations produce work hardening. During the forming process, thickness variations, residual stresses, work hardening, plastic strain occur. Studies have shown that the forming history has a serious effect on crash performance [17-19]. Therefore, the forming history should be taken into account when evaluating the crash performance of the TWT.

Dutton et al. [20] examined the effect of forming parameters. They formed a s-rail structure by hydroforming and mapped the forming results (thickness, residual stress and plastic strain) to the impact analysis. They found forming history effect the crashworthiness and it was important to consider the forming history to obtaining a real crash condition. Gümrük and Karadeniz [21] numerically investigated the effects of deep-drawing process on the crashworthiness of top-hat thin-walled structure. They also found that the thickness variations and plastic strains significant effect the crashworthiness. Lee et al. [22] numerically investigated the influence of back stresses during forming processes of s-rail structure on crashworthiness. S-type structure produced by deep-drawing and tube formed by hydroforming processes. They found that to obtain a more reliable impact test, the back stresses during forming process should be taking into account. Krusper [23] examined the influences of the forming history on the crash performance for a simple hat profile structure. He found that plastic strain and thickness distribution had an important role in the crash response. Williams et al. [24] experimentally and numerically investigated the influence of the hydroforming process on the crashworthiness of EN-AW5018 aluminum alloy. They concluded that the energy absorption capability of the hydroformed aluminum tubes decreased by mapped the forming history to the structure. Kim et al. [25] Numerically examined the effect of plastic strain and thickness distribution on crashworthiness on a full vehicle. They found that forming effects have effect the deceleration pulse and deformation mode.

Crash analysis of TWTs can be performed either quasi-static or dynamic depending on applied load [26]. Thought most of the studies about the crashworthiness of TWT have been conducted using quasi-static tests, it is important to also take into consideration the dynamic high-speed impact response of TWTs.

In this paper, the impact response of spot-welded elliptical thin-walled tube under dynamic axial load was investigated. Besides, the bead-shaped trigger mechanism was added to the tube to reduce the

peak crushing force and to obtain a more stable deformation mode. To investigate the effect of forming history on crashworthiness, the TWT was produced by single-acting deep-drawing method. After deep-drawing process, thickness variations, plastic strain, and stresses were mapped to the tube and dynamic analysis was repeated. RADIOSS used as solver and explicit and nonlinear FE codes used.

## 2. Material and Methods

Double-hat shaped elliptical TWT was design with bead-shaped trigger mechanism (fig. 1). All dimension is in millimeter.

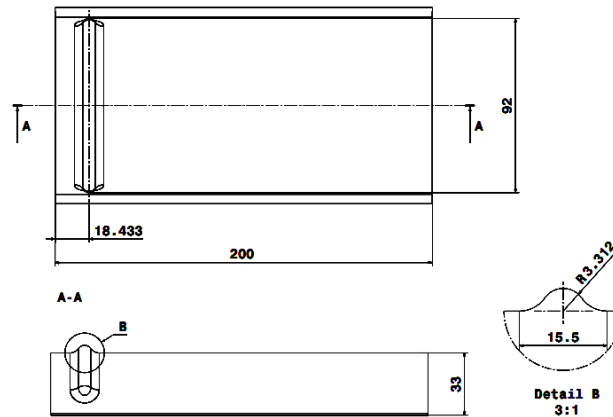


Figure 1. Details of bead-shaped trigger mechanism and TWT.

The parts of TWT were joined by using twenty-four spot welds. The tube has 1.5 mm wall thickness ( $t$ ), 200 mm length ( $L$ ), 33 mm semi-minor axis ( $a$ ) and 46 mm semi-major axis ( $b$ ). The radial ratio is ( $a/b$ ) 0.717. While the sides of added trigger mechanism is concave, the middle is convex. By adding the trigger mechanism, it is aimed to reduce peak crushing force and obtain more stable deformation mode.

### 2.1 Material Characterization

Since reducing vehicle weight affects fuel consumption and emission rates, the use of aluminum and magnesium alloys, which may be alternative to steel in recent years, has increased. In this paper, Al6061 was used as TWT material with Young's module  $E=69$  GPa, density  $\rho = 2.7$  gr/cm<sup>3</sup> and Poisson ratio  $\nu=0.33$ . Since under axial dynamic impact, strain-rate effects and inertia force have significant effect on crashworthiness [27-29], Johnson-Cook material model [30] was utilized to obtain more realistic impact results. The Johnson-Cook material model expressed as follow.

$$\sigma = (A + B\varepsilon_p^n) \left(1 + C \ln \frac{\dot{\varepsilon}_{pl}}{\dot{\varepsilon}_o}\right) \left(1 - \left(\frac{T-T_a}{T_m-T_a}\right)^m\right) \quad (1)$$

Where  $\sigma$  is flow stress,  $A$  is yield stress,  $B$  is hardening parameter,  $\varepsilon_p$  is plastic strain,  $n$  is hardening exponent,  $\dot{\varepsilon}_o$  is references strain rate,  $\dot{\varepsilon}_{pl}$  is plastic strain-rate,  $C$  is strain rate coefficient and can be found with split Hopkinson (Kolsky) pressure bar test [31]. In this study the thermal effect is neglected. Johnson-Cook parameters of Al6061 are given in Table 1.

Table 1. Johnson-Cook parameters [32].

A (MPa)	B (MPa)	n	C	$\dot{\varepsilon}_o$ (s <sup>-1</sup> )
314	114	.42	.002	1

## 2.2 Finite Element Model and Deep-Drawing Process

Double-hat elliptical TWT consists of two parts. The parts were joined by using twenty-four spot welds. 4-node shell elements of type quad were utilized with 3 mm mesh size (in the region of the trigger mechanism, smaller size elements were used) for TWTs and 1D spring elements for spot welds. Five integration points across the thickness were chosen to avoid the hourglass mode and obtain good accuracy in the crash simulation. “Nodes to Surface Contact” between the tube and rigid-wall is defined with 0.2 friction coefficient and self-contact algorithm is used (to avoid penetration between the surfaces during folding), provided by RADIOSS. 250 kg mass was added to the end of the tube and moved a speed of 10 m/s to a rigid wall. The tube is restricted to all degrees of freedom except for the axis of speed y (fig. 2).

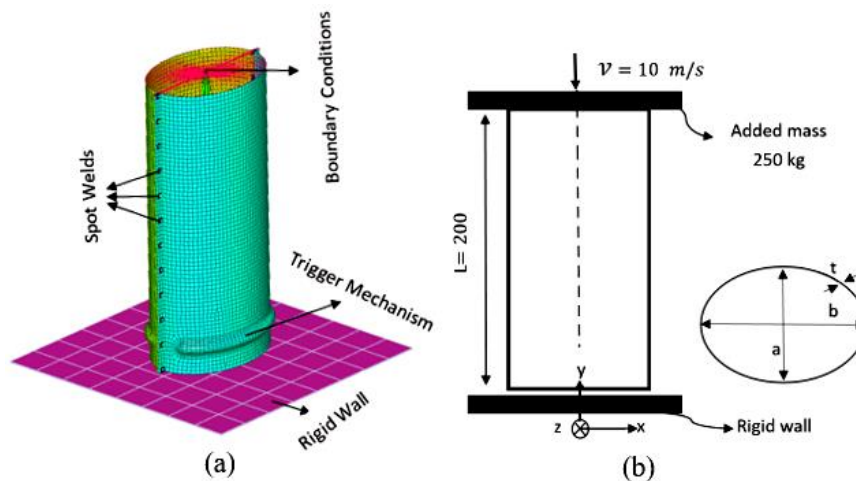


Figure 2. a) Finite element model b) schematic diagram of TWT.

The model was meshed by using HyperMesh software. Time step is  $1.77\text{E-}4$  and  $1.98\text{E-}7$  for unmapped and with mapped TWTs respectively. Therefore, the analysis of the mapped tube lasted longer. The dynamic simulation was conducted using RADIOSS/Explicit software.

In order to examine the effect of forming history on impact performance, the tube was formed by the single-acting deep-drawing method. Die and punch are defined as rigid.  $3 \times 3 \text{ mm}$  quad mesh type was utilized with Adaptive mesh. Therefore, mesh size decreased in the regions where the stresses were higher. The die and the punch, form the blank together. Blank was placed between die and punch and the blank is forced into the die for creating the desired shape. FE model of deep-drawing process and after deep-drawing analysis, the appearance of the sheet metal is shown in figure 3. HyperForm software was used for deep-drawing analysis.

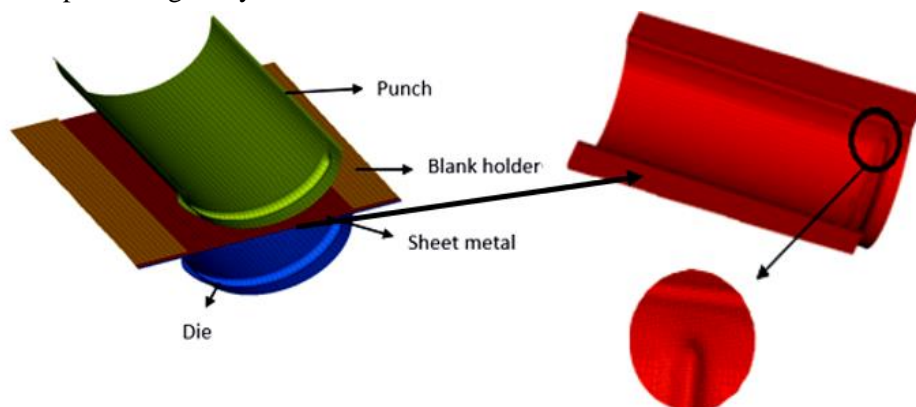


Figure 3. Finite element model of deep-drawing process.

### 2.3. Model Validation

Zarei and Kröger [33] experimentally performed the impact test of a cylindrical TWT. With the purpose of validating the FEM, a cylindrical TWT of the same dimensions was designed, the finite element model was generated and impact analysis was performed. A good agreement was obtained on deformation shapes of the TWTs at a 75.5 mm crush distance (fig. 4). In the experimental study, the mean crushing force value was 13.03 kN while 11.04 kN by FEM (the difference is 15.27 percent). This difference was acceptable, as the forming history had a significant impact on the crashworthiness of TWTs [34-36].

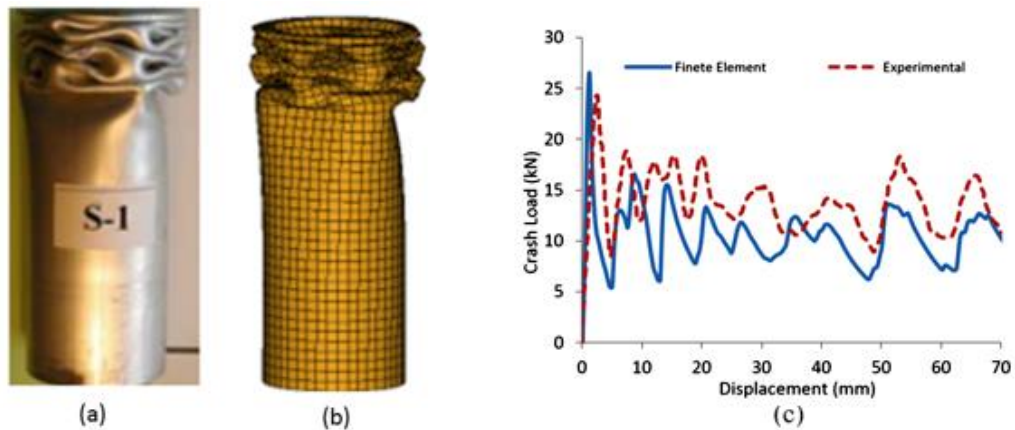


Figure 4. Comparison deformation shape at 75.5 mm crush distance a) Experimental b) Finite Element c) Comparison crash load versus displacement

### 3. Results and Discussion

After deep-drawing analysis, thickness variations, stresses, and plastic strain were occurred in the sheet metal (fig. 5). In particular, thinning is concentrated in the region where the trigger mechanism is located. The wall thickness value, which was initially 1.5 mm, ranged from 1.569 mm to 1.106 mm. After the results were mapped to the tube, the thickness varied between 1.554 and 1.107. This difference, which did not affect the results, was due to the decrease in the size of sheet metal elements after deep-drawing analysis.

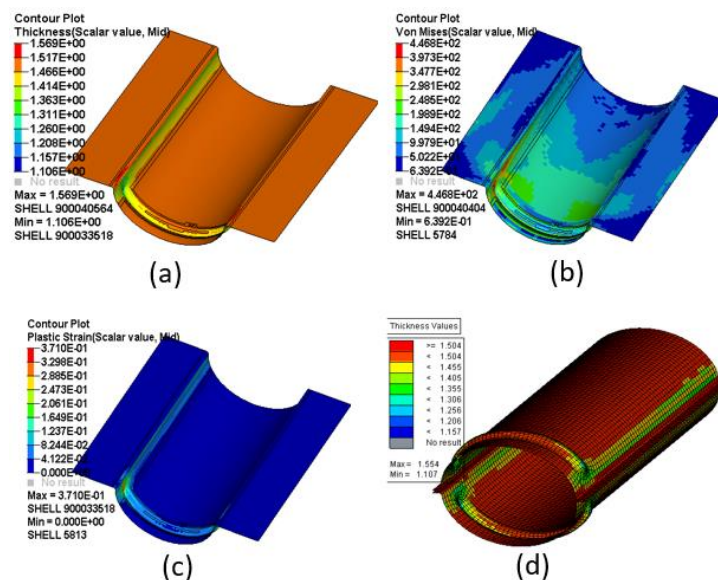


Figure 5. Deep-drawing results a) thickness variations b) Von Mises stress c) plastic strain d) elliptical TWT which deep-drawing results were mapped.

In the tubes, the first folding occurred in the region where the trigger mechanism was added. Progressive deformation mode occurred for both and deformation modes of the tubes differed in the course of impact (fig. 6).

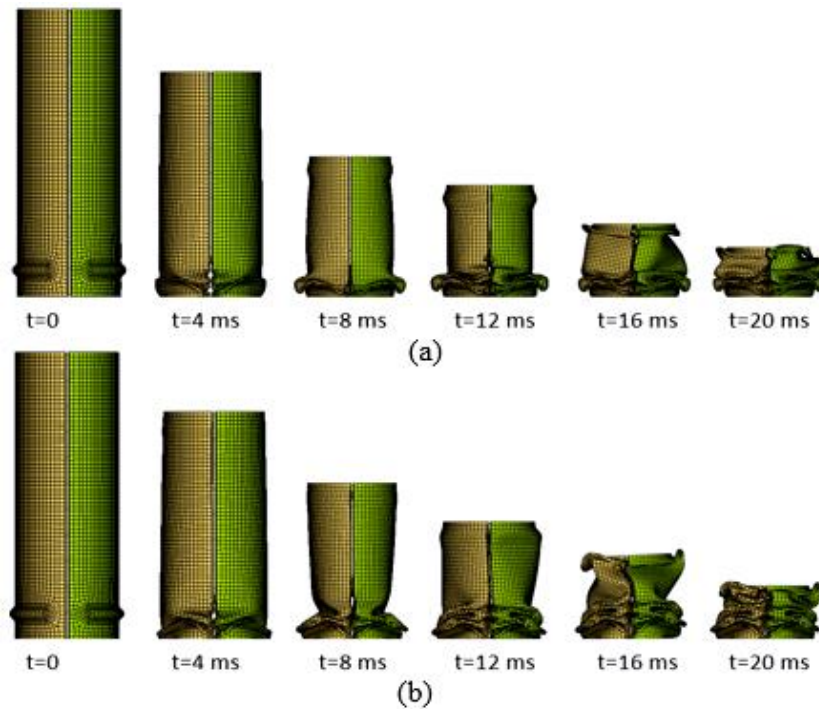


Figure 6. Comparison of deformation mode during impact a) unmapped b) mapped.

With the mapped forming history, the PCF was 62.346 kN with a decrease of 3.614% from 64.6878 kN (fig. 7). Due to the thinning in the location of the trigger mechanism during the deep-drawing process, the first folding was occurred easier and the first reaction force was lower. The AE was 7063.86 J with a decrease of 5.218% from 7452.68 J (fig. 8). The crush distance was 156 mm for both tubes.

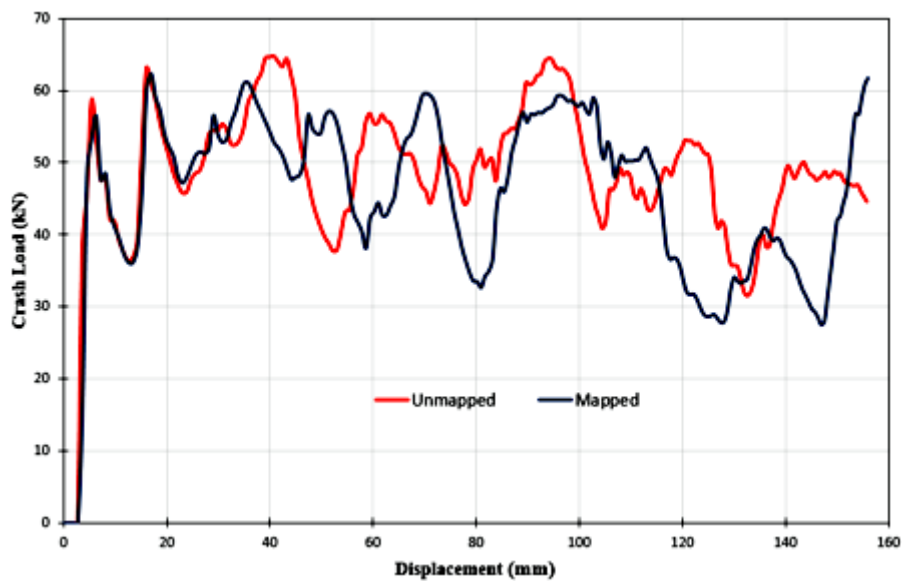


Figure 7. Crash load versus displacement.

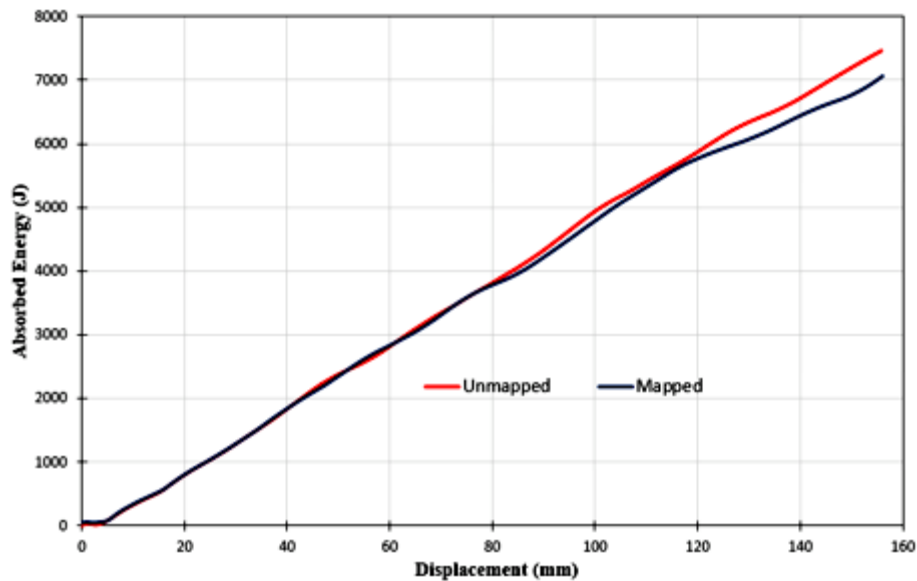


Figure 8. Absorbed energy versus displacement.

It is important to check whether the energy balance is ensured after the analysis in terms of the accuracy of the FE model. For obtain a good energy balance, the total energy must be constant throughout the analysis and must be equal to the sum of the absorbed energy, kinetic energy, contact energy and the hourglass energy. In addition, zero or negligible amount of hourglass energy is important in terms of the accuracy of the analysis.

The thin-walled tube with a velocity of 10 m/s and a 250 kg added mass has 12500 J kinetic energy at the beginning of crash. The kinetic energy of the tube started to fall with the crash. The amount of energy absorbed must be equal or too close to the loss in kinetic energy. At the end of the analysis, the absorbed energy was 7063 J, the kinetic energy was 5369 J, the total energy was 12433 J, the hourglass energy was zero and contact energy was 63 J. The results showed that a good energy balance was obtained (fig. 9)

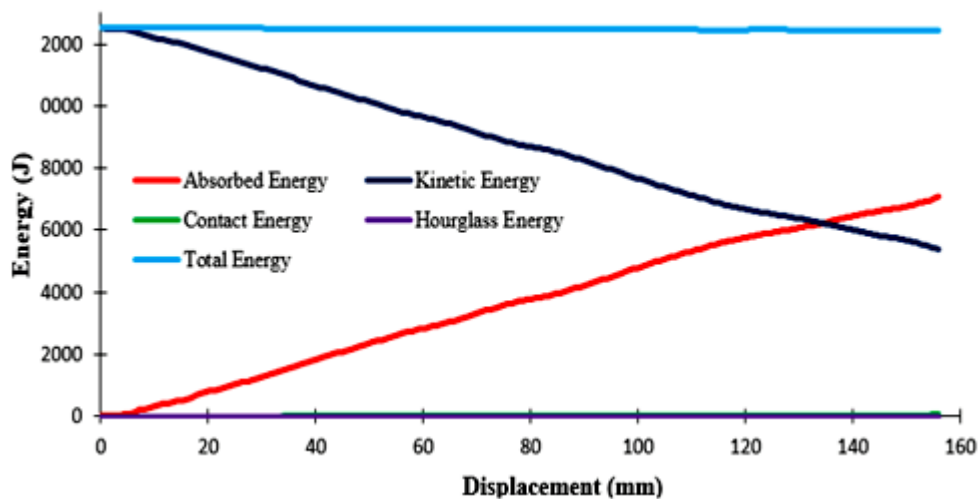


Figure 9. Energy balance of unmapped TWT.

#### 4. Conclusion

With the addition of the trigger mechanism, the PCF, which usually occurs at the first reaction force, has occurred in subsequent force fluctuations. Especially in the region where the trigger mechanism is located and in the corners of sheet metal, thickness variations, residual stresses and plastic strain were occurred during forming process. With the results were mapped the tube, the deformation mode was changed in the course of impact and AE decreased by 5.218%, PCF decreased by 3.614%. The results showed that the forming history has effect on crash performance of the TWTs. Therefore, in terms of providing a realistic crash atmosphere and obtaining accurate results, forming history should be taking into account.

#### 5. Future works

In this study, only one trigger mechanism was added to the tube. A new study can be done by changing the number or position of the trigger mechanism. In addition, the tube was shaped by deep-drawing method, the effects of other sheet metal forming methods on crash performance can be investigated. To investigate which forming result (wall thickness, plastic strain, residual stress) is most effective on crashworthiness, the results can be mapped one by one to the TWT.

#### References

- [1] Abramowicz, W. and N. Jones,(1984) Dynamic axial crushing of square tubes. *International Journal of Impact Engineering*. 2(2): p. 179-208, doi:10.1016/0734-743X(84)90005-8.
- [2] Alexander, J.M.,(1960) An approximate analysis of the collapse of thin cylindrical shells under axial loading. *The Quarterly Journal of Mechanics and Applied Mathematics*. 13(1): p. 10-15, doi:10.1093/qjmam/13.1.10.
- [3] Pugsley, A.,(1960) The large-scale crumpling of thin cylindrical columns. *The Quarterly Journal of Mechanics and Applied Mathematics*. 13(1): p. 1-9, doi:10.1093/qjmam/13.1.1.
- [4] Wierzbicki, T. and W. Abramowicz,(1983) On the Crushing Mechanics of Thin-Walled Structures. *Journal of Applied Mechanics-Transactions of the Asme*. 50(4a): p. 727-734, doi:10.1115/1.3167137.
- [5] Li, Z.G., H.F. Yang, X.W. Hu, J.F. Wei, and Z.T. Han,(2018) Experimental study on the crush behavior and energy-absorption ability of circular magnesium thin-walled tubes and the comparison with aluminum tubes. *Engineering Structures*. 164: p. 1-13, doi:10.1016/j.engstruct.2018.02.083.
- [6] Mamalis, A.G., D.E. Manolacos, M.B. Ioannidis, P.K. Kostazos, and G. Hassiotis,(2001) Finite element simulation of the axial collapse of thin-wall square frusta. *International Journal of Crashworthiness*. 6(2): p. 155-164, doi:10.1533/cras.2001.0169.
- [7] Nia, A.A. and J.H. Hamedani,(2010) Comparative analysis of energy absorption and deformations of thin walled tubes with various section geometries. *Thin-Walled Structures*. 48(12): p. 946-954, doi:10.1016/j.tws.2010.07.003.

- [8] Sun, G.Y., Z. Wang, H. Yu, Z.H. Gong, and Q. Li,(2019) Experimental and numerical investigation into the crashworthiness of metal-foam-composite hybrid structures. *Composite Structures*. 209: p. 535-547, doi:10.1016/j.compstruct.2018.10.051.
- [9] Tarlochan, F., F. Samer, A.M.S. Hamouda, S. Ramesh, and K. Khalid,(2013) Design of thin wall structures for energy absorption applications: Enhancement of crashworthiness due to axial and oblique impact forces. *Thin-Walled Structures*. 71: p. 7-17, doi:10.1016/j.tws.2013.04.003.
- [10] Zheng, G., S.Z. Wu, G.Y. Sun, G.Y. Li, and Q. Li,(2014) Crushing analysis of foam-filled single and bitubal polygonal thin-walled tubes. *International Journal of Mechanical Sciences*. 87: p. 226-240, doi:10.1016/j.ijmecsci.2014.06.002.
- [11] Dindar, Ç., H. Beytüt, and S. Karagöz,(2019) Effect of Heat Treatment and Cross Section on the Crashworthiness of 51CRV4 Spring Steel. *Uludağ University Journal of The Faculty of Engineering*. 24(2): p. 477-488, doi:10.17482/uumfd.477569.
- [12] Andrews, K.R.F., G.L. England, and E. Ghani,(1983) Classification of the Axial Collapse of Cylindrical-Tubes under Quasi-Static Loading. *International Journal of Mechanical Sciences*. 25(9-10): p. 687-696, doi:10.1016/0020-7403(83)90076-0.
- [13] Abramowicz, W. and N. Jones,(1997) Transition from initial global bending to progressive buckling of tubes loaded statically and dynamically. *International Journal of Impact Engineering*. 19(5-6): p. 415-437, doi:10.1016/S0734-743x(96)00052-8.
- [14] Lima, R.M., Z.N. Ismarrubie, E.S. Zainudin, and S.H. Tang,(2012) Effect of length on crashworthiness parameters and failure modes of steel and hybrid tube made by steel and GFRP under low velocity impact. *International Journal of Crashworthiness*. 17(3): p. 319-325, doi:10.1080/13588265.2012.661238.
- [15] Estrada, Q., D. Szwedowicz, A. Rodriguez-Mendez, M. Elías-Espinosa, J. Silva-Aceves, J. Bedolla-Hernández, et al.,(2019) Effect of radial clearance and holes as crush initiators on the crashworthiness performance of bi-tubular profiles. *Thin-Walled Structures*. 140: p. 43-59, doi:10.1016/j.tws.2019.02.039.
- [16] Marzbanrad, J., A. Abdollahpoor, and B. Mashadi,(2009) Effects of the triggering of circular aluminum tubes on crashworthiness. *International Journal of Crashworthiness*. 14(6): p. 591-599, doi:10.1080/13588260902896458.
- [17] Huh, H., K.P. Kim, S.H. Kim, J.H. Song, H.S. Kim, and S.K. Hong,(2003) Crashworthiness assessment of front side members in an auto-body considering the fabrication histories. *International Journal of Mechanical Sciences*. 45(10): p. 1645-1660, doi:10.1016/j.ijmecsci.2003.09.022.
- [18] Karagoz, S. and A.R. Yildiz,(2017) A comparison of recent metaheuristic algorithms for crashworthiness optimisation of vehicle thin-walled tubes considering sheet metal forming effects. *International Journal of Vehicle Design*. 73(1-3): p. 179-188, doi:10.1504/ijvd.2017.10003410.
- [19] Oliveira, D.A., M.J. Worswick, R. Grantab, B.W. Williams, and R. Mayer,(2006) Effect of forming process variables on the crashworthiness of aluminum alloy tubes. *International Journal of Impact Engineering*. 32(5): p. 826-846, doi:10.1016/j.ijimpeng.2005.06.006.

- [20] Dutton, T., S. Iregbu, R. Sturt, A. Kellicut, B. Cowell, and K. Kavikondala,(1999) The effect of forming on the crashworthiness of vehicles with hydroformed frame siderails. *SAE transactions*: p. 3354-3360.
- [21] Gümrük, R. and S. Karadeniz,(2009) The influences of the residual forming data on the quasi-static axial crash response of a top-hat section. *International Journal of Mechanical Sciences*. 51(5): p. 350-362.
- [22] Lee, M.-G., C.-S. Han, K. Chung, J.R. Youn, and T.J. Kang,(2005) Influence of back stresses in parts forming on crashworthiness. *Journal of materials processing technology*. 168(1): p. 49-55.
- [23] Krusper, A.,(2003) Influences of the forming process on the crash performance-finite element analysis. *Unpublished master's thesis. Chalmers University of Technology, Göteborg*.
- [24] Williams, B., D. Oliveira, M. Worswick, and R. Mayer, *Crashworthiness of high and low pressure hydroformed straight section aluminum tubes*. 2005, SAE Technical Paper.
- [25] Kim, H., S. Hong, S. Hong, H. Huh, K. Motors, and K.-d. Kwangmyung-Shi.(2004) The evaluation of crashworthiness of vehicles with forming effect. in *4th European LSDYNA Users' Conference*.
- [26] Ma, J. and Y. Yan,(2013) Quasi- static and dynamic experiment investigations on the crashworthiness response of composite tubes. *Polymer Composites*. 34(7): p. 1099-1109, doi:10.1002/pc.22518.
- [27] Calladine, C. and R. English,(1984) Strain-rate and inertia effects in the collapse of two types of energy-absorbing structure. *International Journal of Mechanical Sciences*. 26(11-12): p. 689-701, doi:10.1016/0020-7403(84)90021-3.
- [28] Harrigan, J.J., S.R. Reid, and C. Peng,(1999) Inertia effects in impact energy absorbing materials and structures. *International Journal of Impact Engineering*. 22(9-10): p. 955-979, doi:10.1016/S0734-743x(99)00037-8.
- [29] Karagiozova, D.,(2001) Inertia effects on some crashworthiness parameters for cylindrical shells under axial impact. *International Journal of Crashworthiness*. 6(4): p. 561-572, doi:10.1533/cras.2001.0198.
- [30] Johnson, G.R.,(1983) A constitutive model and data for materials subjected to large strains, high strain rates, and high temperatures. *Proc. 7th Inf. Sympo. Ballistics*: p. 541-547.
- [31] Kolsky, H.,(1949) An investigation of the mechanical properties of materials at very high rates of loading. *Proceedings of the physical society. Section B*. 62(11): p. 676, doi:10.1088/0370-1301/62/11/302.
- [32] Lesuer, D.R., G. Kay, and M. LeBlanc, *Modeling large-strain, high-rate deformation in metals*. 2001, Lawrence Livermore National Lab., CA (US).
- [33] Zarei, H.R. and M. Kroger,(2006) Multiobjective crashworthiness optimization of circular aluminum tubes. *Thin-Walled Structures*. 44(3): p. 301-308, doi:10.1016/j.tws.2006.03.010.

- [34] Huh, H., K.P. Kim, S.H. Kim, J.H. Song, H. Kim, and S. Hong,(2003) Crashworthiness assessment of front side members in an auto-body considering the fabrication histories. *International Journal of Mechanical Sciences*. 45(10): p. 1645-1660.
- [35] Kim, K.P. and H. Huh.(2003) Collapse analysis of auto-body structures considering the effect of fabrication. in *Key Engineering Materials*. Trans Tech Publ.
- [36] Lee, S.-H., C.-S. Han, S.-I. Oh, and P. Wriggers,(2001) Comparative crash simulations incorporating the results of sheet forming analyses. *Engineering Computations*. 18(5/6): p. 744-758.

## DYNAMIC ANALYSIS OF UNIFORM AND NON-UNIFORM CROSS-SECTION CANTILEVER SANDWICH BEAMS

*Mesut HÜSEYİNOĞLU<sup>1\*</sup>, Murat ŞEN<sup>2</sup>, Osman YİĞİD<sup>3</sup>, Orhan ÇAKAR<sup>4</sup>*

*In this study, an analytical solution for dynamic analysis of uniform and non-uniform cross-section cantilever sandwich beam is presented. The sandwich beam was assumed to be an Euler-Bernoulli beam and formed with a thin core and two thin skin layers. So the shear deformations and rotational effects were neglected. The equivalent flexural rigidity was obtained for the entire sandwich structure. Some implementations for the solution method are given and the results are compared with numerical solutions. The usability of the Euler-Bernoulli Beam Theory for thin layered uniform or non-uniform sandwich beams is investigated. The solutions obtained from analytical and numerical solutions are in good agreement.*

Key words: *Natural Frequency, Sandwich Beam, Mode Shape, Vibration*

### 1. Introduction

Sandwich structures have a very wide usage from aircrafts to automotive, marine, storage and transportation. Due to their light weight, high bending stiffness and damping capability, they are preferred in many engineering applications. Generally a sandwich structure is combined with two elastic thin skin layers and a viscoelastic core layer. Using the advantages of light weight, vibration isolation and flexural strength properties of these structures come forward in mechanical and structural engineering. These advantages make researchers focus on these structures and a lot of papers have been published on this topic for the last decade. Some of them are the studies of analytical approaches when the big amount of them are numerical and experimental analysis. Khalili *et al.* [1] investigated the free vibrations of three layer sandwich beams by using dynamic stiffness method considering different density, thickness and shear modulus of core materials for various boundary conditions. Rabinovitch and Hamed [2] made a study on dynamic behavior of sandwich beams with viscoelastic soft core. They took into account the shear and transverse effects for sandwich beams by utilizing the Maxwell and Kelvin-Voigt models for viscoelasticity. A model was formulated by Palmeri and Ntotsios [3] for dynamic analysis of sandwich beams by using mathematical derivation of generalized Maxwell model of shear type viscoelastic layer for the core and consisting of two parallel Euler-Bernoulli elastic beams. Irazu *et al.* [4] made a study on the sandwich structures with viscoelastic adhesive films. They

<sup>1</sup>Department of Mechanical Engineering, Dicle University, Diyarbakır, Turkey, ([mesuth@dicle.edu.tr](mailto:mesuth@dicle.edu.tr))  <https://orcid.org/0000-0002-6130-6658>

<sup>2</sup>Department of Mechanical Engineering, Fırat University, Elazığ, Turkey, ([msen@firat.edu.tr](mailto:msen@firat.edu.tr))  <https://orcid.org/0000-0002-3063-5635>

<sup>3</sup>Department of Mechanical Engineering, Fırat University, Elazığ, Turkey, ([oyigid@firat.edu.tr](mailto:oyigid@firat.edu.tr))  <https://orcid.org/0000-0002-1798-1250>

<sup>4</sup>Department of Mechanical Engineering, Fırat University, Elazığ, Turkey, ([cakaro@firat.edu.tr](mailto:cakaro@firat.edu.tr))  <https://orcid.org/0000-0001-6947-3875>

characterized the sandwich structure and the viscoelastic films by using standard experimental dynamic tests by obtaining loss factor, storage modulus and shear complex modulus. A method was presented by Sakiyama *et al.* [5] so as to analysis the vibration characteristics of a three layered sandwich structure combined with elastic or viscoelastic core by using an approach utilizing the solution of differential equations of the flexural behavior of the structure under loading condition. Wang *et al.* [6] analyzed vibration characteristics of three layered sandwich plates with bounded piezoelectric patch actuators and a viscoelastic core. They handled the viscoelastic core as complex layer and variant with frequency and temperature by using the Golla-Hughes-McTavish method to account for the frequency dependent properties of it. Zghal *et al.* [7] gave an approach to deal with the local nonlinearities on the dynamic behavior of such model assembled structures.

Finite element solutions are widely used for sandwich structures [8]–[12]. Zhen and Wanji [13] used a high order zigzag method for vibration analysis of composite beams. They made an elimination for the higher order derivatives of displacement parameters of shear stresses by utilizing the variational principle of Hu-Washizu. Pham *et al.* [14] presented a shear deformable finite element formulation for free and forced vibration analysis of two directional functionally graded sandwich beams which combined with a homogeneous ceramic core layer and two functionally graded skin layers. High order methods are used successfully in many studies [15]–[17].

In sandwich structures, core material, pattern or cell type and geometry effect the dynamic characteristics of structures [18]–[22]. Sun and Thamburaj [23] studied on sound and vibration transmission across a sandwich beam combined with anisotropic layers. They investigated the effects of damping, thickness of the layers and material density on the sound transmission loss. They focused on selecting a core material and geometry to transfer the vibration from the top skin into the shear deformation and in-plane wave in the core for reducing the deflection of the bottom skin of the sandwich beams.

There are also number of analytical or numerical studies on various kinds of functionally graded structures [24]–[35]. Yang *et al.* [36] studied on the resonance frequencies and critical speed of an axially moving sandwich beam and on the relationship between the axially travelling speed and the natural frequencies. Lougou *et al.* [37] developed a double scale asymptotic method which separates the original problem into two small ones to analyze the layered sandwich structures with viscoelastic core.

In this study, an analytical solution for free vibration characteristics of uniform and non-uniform cross-section sandwich beams for fixed-free boundary condition is presented. The sandwich beam was assumed to be a thin Euler- Bernoulli beam. So the shear deformations and the rotational effects were neglected. In the following sections, the methodology, the application and the conclusion parts are given respectively.

## 2. Material and Method

There are two common approaches in vibrations of beams one of which is Euler-Bernoulli beam theory and the second is Timoshenko beam theory. In the former approach the shear deformations and rotational effects are neglected while in the latter approach they are taken in account. Euler-Bernoulli beam theory is suitable for thin beams (the thickness of the beam is very small according to width and length of it). But for thick beams Timoshenko beam theory is more appropriate. In our study, the sandwich beam is considered thin enough to neglect the rotational effects. So, Euler-Bernoulli beam theory is used. Free body diagram of a small part of a simple Euler-Bernoulli beam is given in Figure 1.

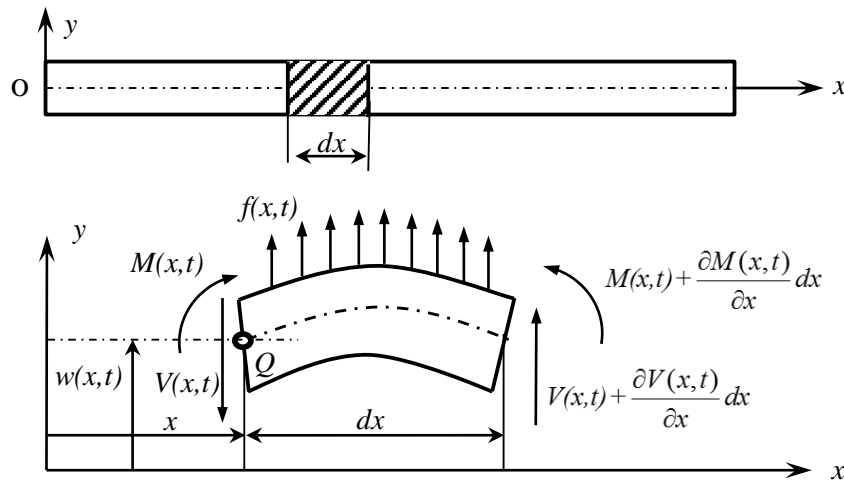


Figure 1. Free body diagram of a small part of a simple Euler-Bernoulli beam.

If a small unit element  $dx$  is handled of an Euler-Bernoulli beam exposed to a distributed load  $f(x, t)$ , the differential equation of motion can be expressed as:

$$f(x, t)dx + \left[ V(x, t) + \frac{\partial V(x, t)}{\partial x} dx \right] - V(x, t) = m(x)dx \frac{\partial^2 w(x, t)}{\partial t^2} \quad (1)$$

Here,  $m(x)$  is the linear mass density (kg/m). The right part of the equation is the inertial force of the small element. By neglecting the rotary inertia if the moments about  $z$  axis trough the point  $Q$  are taken and after summation:

$$\left[ f(x, t)dx \right] \frac{dx}{2} + \left[ V(x, t) + \frac{\partial V(x, t)}{\partial x} dx \right] dx + \left[ M(x, t) + \frac{\partial M(x, t)}{\partial x} dx \right] - M(x, t) = 0 \quad (2)$$

Equation (2) can be obtained and by simplifying it, the equation (3) can be written.

$$\left[ \frac{f(x, t)}{2} + \frac{\partial V(x, t)}{\partial x} \right] (dx)^2 + \left[ V(x, t) + \frac{\partial M(x, t)}{\partial x} \right] dx = 0 \quad (3)$$

Here,  $dx$  is very small and  $(dx)^2$  is almost zero, so the term  $(dx)^2$  can be neglected. So, this expression can be rewritten as in equation (4):

$$V(x, t) = - \frac{\partial M(x, t)}{\partial x} \quad (4)$$

By substitution this expression into equation (1)

$$f(x, t)dx - \frac{\partial^2}{\partial x^2} [M(x, t)] dx = m(x)dx \frac{\partial^2 w(x, t)}{\partial t^2} \quad (5)$$

Also, the relation between the bending moment and the deflection of beam can be expressed by

$$M(x,t) = EI(x) \frac{\partial^2 w(x,t)}{\partial x^2} \quad (6)$$

Here  $EI(x)$  is the flexural rigidity and combined by modulus of elasticity ( $E$ ) of the material and moment of inertia ( $I(x)$ ) of the beam changes through  $x$  direction respectively. Substitution of equation (6) into (5) and to simplify with dividing the equation (5) by  $dx$  yields:

$$\frac{\partial^2}{\partial x^2} \left[ EI(x) \frac{\partial^2 w(x,t)}{\partial x^2} \right] + m(x) \frac{\partial^2 w(x,t)}{\partial t^2} = f(x,t) \quad (7)$$

The equivalent flexural rigidity  $EI(x)$  can be written for  $n$  layers sandwich structure with combination of the layers can be expressed as:

$$EI(x) = E_1 I_1(x) + E_2 I_2(x) + \dots + E_n I_n(x) \quad (8)$$

For three layer symmetric sandwich beam with two face sheets and a core layer, the equation (8) can be rewritten:

$$EI(x) = 2E_f I_f(x) + E_c I_c(x) \quad (9)$$

## 2.1. For uniform cross-section sandwich beams

For uniform cross-section sandwich beams, the linear mass density and the flexural rigidity are constant due to the uniform thickness and width through the length. A uniform cross-section sandwich beam is illustrated in Figure 2.

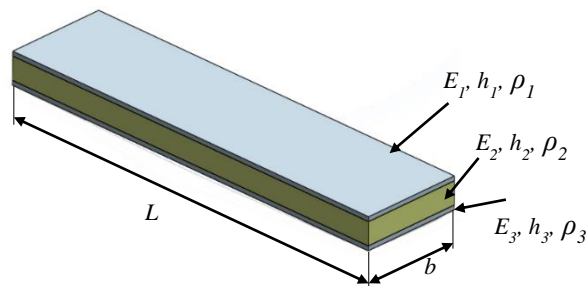


Figure 2. A uniform cross-section sandwich beam.

For uniform cross-section sandwich beams ( $EI(x)$  and  $m(x)$  are constant) the equation (7) can be written as:

$$\frac{\partial^2}{\partial x^2} \left[ EI \frac{\partial^2 w(x,t)}{\partial x^2} \right] + m \frac{\partial^2 w(x,t)}{\partial t^2} = f(x,t) \quad (10)$$

For free vibrations (with no excitation force) and for uniform cross-section beams, simplified equation (11) is obtained, where,  $a^2 = EI/m$

$$a^2 \frac{\partial^4 w(x,t)}{\partial x^4} + \frac{\partial^2 w(x,t)}{\partial t^2} = 0 \quad (11)$$

With the separation of variables the solution can be expressed by equalizing to a constant  $\omega^2$ ,

$$a^2 \frac{X^{IV}(x)}{X(x)} = -\frac{\ddot{T}(t)}{T(t)} = \omega^2 \quad (X^{IV} = \frac{d^4 X}{dx^4}, \quad \ddot{T} = \frac{d^2 T}{dt^2}) \quad (12)$$

This equation can be decomposed spatial and time parts.

$$\ddot{T}(t) + \omega^2 T(t) = 0 \quad T(t) = A \sin \omega t + B \cos \omega t \quad (13)$$

Here,  $A$  and  $B$  can be determined by the initial conditions. By rearranging the equation (12) for spatial equation

$$X^{IV}(x) - \frac{\omega^2}{a^2} X(x) = 0 \quad (14)$$

By defining  $x = Ae^{\lambda x}$  and recalling the equation (11) yields:

$$\beta^4 = \frac{\omega^2}{a^2} = \frac{m\omega^2}{EI} \quad (15)$$

Then general solution of the equation (14) can be calculated in the form as follows:

$$X(x) = c_1 \sin \beta x + c_2 \cos \beta x + c_3 \sinh \beta x + c_4 \cosh \beta x \quad (16)$$

Here  $C_1, C_2, C_3, C_4$  are constant and one can obtain those constants from boundary conditions. The boundary conditions for cantilever beam can be written as follows:

For clamped end at  $x = 0$

$$\begin{aligned} x(0) &= 0 \\ x(0) &= c_1 \sin 0 + c_2 \cos 0 + c_3 \sinh 0 + c_4 \cosh 0 = 0 \\ c_4 &= -c_2 \end{aligned} \quad (17)$$

$$\begin{aligned} x'(0) &= 0 \\ x'(0) &= \lambda c_1 \cos 0 - \lambda c_2 \sin 0 + \lambda c_3 \cosh 0 + \lambda c_4 \sinh 0 = 0 \\ c_3 &= -c_1 \end{aligned} \quad (18)$$

For free end at  $x = L$

$$\begin{aligned} x''(L) &= 0 \\ x''(L) &= -\beta^2 c_1 \sin \beta L - \beta^2 c_2 \cos \beta L + \beta^2 c_3 \sinh \beta L + \beta^2 c_4 \cosh \beta L = 0 \\ c_1 (\sin \beta L + \sinh \beta L) + c_2 (\cos \beta L + \cosh \beta L) &= 0 \end{aligned} \quad (19)$$

$$\begin{aligned} x'''(L) &= 0 \\ x'''(L) &= -\beta^3 c_1 \cos \beta L + \beta^3 c_2 \sin \beta L + \beta^3 c_3 \cosh \beta L + \beta^3 c_4 \sinh \beta L = 0 \\ c_1 (\cos \beta L + \cosh \beta L) + c_2 (-\sin \beta L + \sinh \beta L) &= 0 \end{aligned} \quad (20)$$

If the last two equalities are written in matrix form

$$\begin{bmatrix} (\sin \beta L + \sinh \beta L) & (\cos \beta L + \cosh \beta L) \\ (\cos \beta L + \cosh \beta L) & (-\sin \beta L + \sinh \beta L) \end{bmatrix} \begin{bmatrix} c_1 \\ c_2 \end{bmatrix} = \begin{bmatrix} 0 \\ 0 \end{bmatrix} \quad (21)$$

For nontrivial solution, the determinant of the first part of the left equation must be zero. For this:

$$\cos \beta_n L \cosh \beta_n L + 1 = 0 \quad n = 1, 2, \dots, n \quad (22)$$

The characteristic equation can be obtained. The first four roots of equation (22) are calculated as:  $\beta_n L = 1.8751, 4.6941, 7.8548, 10.9955$  ( $n=1, 2, 3, 4$ )

With a transformation of  $\beta_n L = \lambda_n$  the natural frequencies equation can be obtained:

$$\omega_n = \frac{\lambda_n^2}{L^2} \sqrt{\frac{EI}{m}} \quad (\text{r/s}) \quad (23)$$

$$f_n = \frac{\lambda_n^2}{2\pi L^2} \sqrt{\frac{EI}{m}} \quad (\text{Hz}) \quad (\omega_n = 2\pi f_n) \quad (24)$$

For a uniform cross-section three layered sandwich beam, the equivalent flexural rigidity and mass density can be expressed as:

$$EI = E_1 \left[ b \frac{h_1^3}{12} + bh_1 \left( \frac{h_1 + h_2}{2} \right)^2 \right] + E_2 b \frac{h_2^3}{12} + E_3 \left[ b \frac{h_3^3}{12} + bh_3 \left( \frac{h_3 + h_2}{2} \right)^2 \right] \quad (25)$$

$$m = \rho_1 A_1 + \rho_2 A_2 + \rho_3 A_3 \quad (26)$$

By using equations (17-22), the mode shapes can be obtained as in equation (27).

$$X(x) = (c_1)_n \left[ \frac{(\sin \beta_n L + \sinh \beta_n L)}{(\cos \beta_n L + \cosh \beta_n L)} (\cos \beta_n x - \cosh \beta_n x) + \sin \beta_n x + \sinh \beta_n x \right] \quad (27)$$

## 2.2. For non-uniform cross-section sandwich beams

For non-uniform cross-section sandwich beams, the linear mass density and the flexural rigidity are not constant, because the width of the sandwich beam is not constant through the length while the length and the total height of the sandwich beam is constant. A non-uniform cross-section sandwich beam is illustrated in Figure 3.

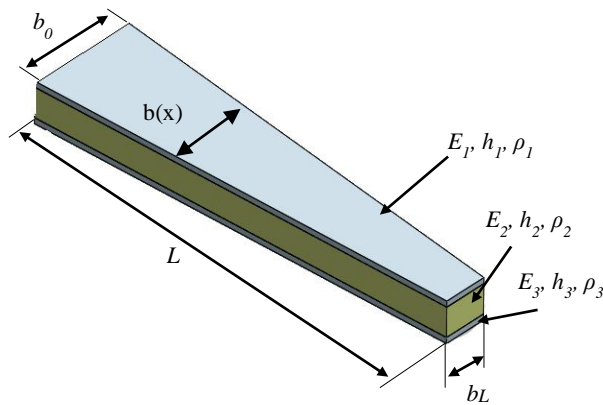


Figure 3. A non-uniform cross-section sandwich beam.

For non-uniform cross-section sandwich beams flexural rigidity ( $EI(x)$ ) and linear mass density ( $m(x)$ ) in equation (7) are not constant and they change through the length. Assuming the total height of the sandwich beam is constant and the width of the beam is changing exponentially through the length as:

$$b(x) = b_0 e^{-\delta x} \quad (28)$$

where  $b_0$  is the width of the beam at the fixed end and  $\delta$  is the non-uniformity parameter. Mass density and the flexural rigidity changes with respect to  $b(x)$ .

$$m(x) = (\rho_1 h_1 + \rho_2 h_2 + \rho_3 h_3) b(x) \quad (29)$$

$$EI(x) = b(x) \left\{ E_1 \left[ \frac{h_1^3}{12} + h_1 \left( \frac{h_1 + h_2}{2} \right)^2 \right] + E_2 \frac{h_2^3}{12} + E_3 \left[ \frac{h_3^3}{12} + h_3 \left( \frac{h_3 + h_2}{2} \right)^2 \right] \right\} \quad (30)$$

Assuming  $m_0 = (\rho_1 h_1 + \rho_2 h_2 + \rho_3 h_3)$  and

$$I_0 = \left\{ E_1 \left[ \frac{h_1^3}{12} + h_1 \left( \frac{h_1 + h_2}{2} \right)^2 \right] + E_2 \frac{h_2^3}{12} + E_3 \left[ \frac{h_3^3}{12} + h_3 \left( \frac{h_3 + h_2}{2} \right)^2 \right] \right\}$$

the mass density and the flexural rigidity simplify as:

$$m(x) = m_0 b(x) \quad (31)$$

$$EI(x) = I_0 b(x) \quad (32)$$

Assuming the solution of the equation (7) to be

$$y(x, t) = y(x) \sin \omega t$$

then after simplification, it reduces to

$$\frac{d^4 y}{dx^4} - 2\delta \frac{d^3 y}{dx^3} + \delta^2 \frac{d^2 y}{dx^2} - \omega^2 \frac{m_0}{I_0} y(x) = 0 \quad (33)$$

Solution of Eq. (33) can be obtained as:

$$y(x) = e^{\frac{\delta}{2}x} [C_1 \cos(ax) + C_2 \sin(ax) + C_3 \cosh(bx) + C_4 \sinh(bx)] \quad (34)$$

where,

$$a = \frac{\sqrt{4\omega_0 + \delta^2}}{2}; \quad b = \frac{\sqrt{4\omega_0 - \delta^2}}{2} \quad (35)$$

Here,

$$\omega_0 = \sqrt{\frac{m_0}{I_0}} \omega^2$$

and  $C_1, C_2, C_3, C_4$ , are constant and can be determined from boundary conditions.

For fixed-free beam boundary conditions are:

$$y(0) = 0; \quad y'(0) = 0; \quad y''(L) = 0; \quad y'''(L) = 0 \quad (36)$$

The natural frequencies of the fixed-free beam can be obtained substituting these boundary conditions into Eq. (34). A characteristic equation for this configuration of beam is obtained as:

$$\begin{aligned} & \frac{ab}{8} - \frac{ab^3}{2} + \frac{a^3b}{2} + ab^5 + a^5b + \cos(aL) \sinh(bL) \left( -\frac{a^3}{4} - \frac{ab^2}{4} + ab^4 + a^3b^2 \right) \\ & + \cos(aL) \cosh(bL) \left( -\frac{ab}{8} + \frac{ab^3}{2} - \frac{a^3b}{2} + 2a^3b^3 \right) \\ & + \sin(aL) \sinh(bL) \left( -\frac{a^2}{16} + \frac{a^4}{4} + \frac{b^2}{16} + \frac{b^4}{4} + 3\frac{a^2b^2}{2} - a^2b^4 + a^4b^2 \right) \\ & + \sin(aL) \cosh(bL) \left( \frac{b^3}{4} + \frac{a^2b}{4} + a^4b + a^2b^3 \right) = 0 \end{aligned} \quad (37)$$

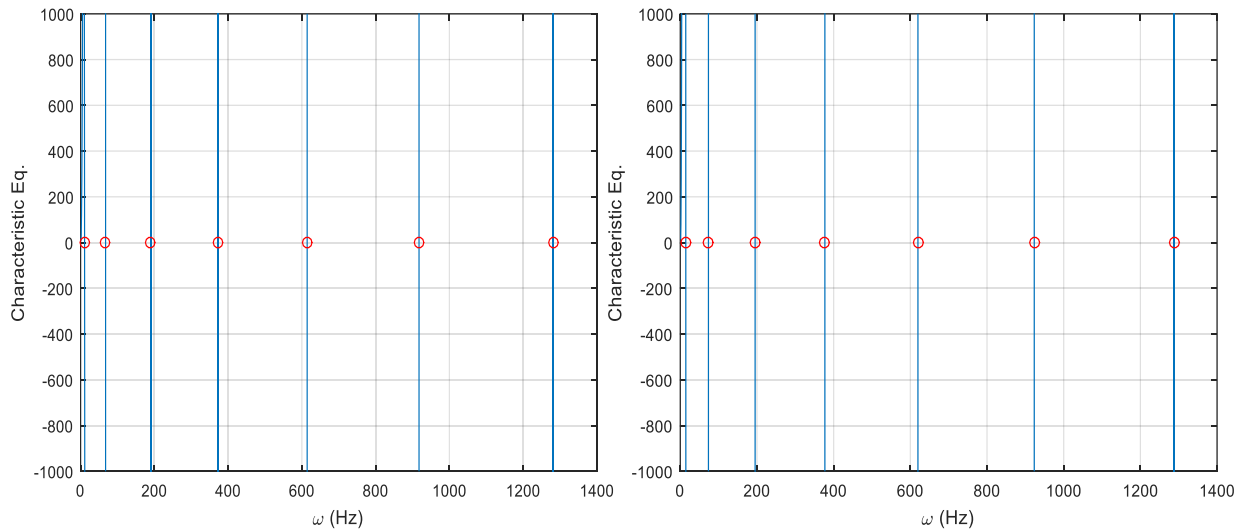
### 3. Applications

In application studies, for both uniform and non-uniform cross-section sandwich beams the natural frequencies were obtained by using presented analytical method and by utilizing numerical approach. The non-uniformity is expressed as a function ( $b(x) = b_0 e^{-2x}$ ) for which the width changes through the length. The numerical studies were made by using ANSYS Wokbech finite element software. For both uniform and non-uniform sandwich beams, the material properties are given in Table 1. The sandwich structures are made by using two aluminum face layers and ABS core layer for both types. The layers of the sandwich beams were assumed to be thin enough as it is supposed to be for Euler-Bernoulli beam theory approach and assumed to remain in contact with each other with perfect connection.

**Table 1. Material properties of uniform and non-uniform cross-section sandwich beams.**

Parameters	Uniform Cross-section	Non-uniform Cross-section
$E_1$ (GPa)	69	69
$E_2$ (GPa)	2	2
$E_3$ (GPa)	69	69
$\rho_1$ (kg/m <sup>3</sup> )	2700	2700
$\rho_2$ (kg/m <sup>3</sup> )	1020	1020
$\rho_3$ (kg/m <sup>3</sup> )	2700	2700
$h_1$ (mm)	1	1
$h_2$ (mm)	1	1
$h_3$ (mm)	1	1
$b$ (mm)	50 (constant)	$b(x) = b_0 e^{-2x}$
$L$ (mm)	500	500

For a few bending modes, the natural frequencies obtained by presented analytical solution are illustrated in Figure 4. (in which the value of the characteristic equation is zero) and the ones obtained by numerical approach are given in Table 2 and Table 3 with percentage difference for both uniform and non-uniform cross-section sandwich beams comparatively.

**Figure 4. Natural frequencies of uniform and non-uniform cross-section sandwich beams.****Table 2. The first five natural frequencies of uniform cross-section sandwich beams for bending vibrations.**

Frequencies (Hz)	Analytical	Numerical (ANSYS)	Difference (%)
1 <sup>st</sup> Frequency	10.81	10.86	-0.46
2 <sup>nd</sup> Frequency	67.73	67.89	-0.24
3 <sup>rd</sup> Frequency	189.60	189.38	0.12
4 <sup>th</sup> Frequency	371.60	369.22	0.64
5 <sup>th</sup> Frequency	614.30	606.48	1.27

**Table 3. The first five natural frequencies of non-uniform cross-section sandwich beams for bending vibrations..**

Frequencies (Hz)	Analytical	Numerical (ANSYS)	Difference (%)
1 <sup>st</sup> Frequency	14.38	14.67	-2.02
2 <sup>nd</sup> Frequency	73.43	74.45	-1.39
3 <sup>rd</sup> Frequency	195.20	195.50	-0.15
4 <sup>th</sup> Frequency	377.10	374.60	0.66
5 <sup>th</sup> Frequency	619.80	610.39	1.52

#### 4. Conclusion

An analytical solution for vibration analysis of uniform and non-uniform cross-section sandwich cantilever beams is presented. The sandwich beams were considered with small thicknesses and they were handled as Euler-Bernoulli beams for which the shear deformations and the rotational effects are ignored. The natural frequencies of both type sandwich structures were obtained by using the presented analytical solution and ANSYS finite element software. It is observed that the analytical and the numerical results are in good agreement with maximum percentage difference as 1.27 for the uniform cross-section and 1.52 for the non-uniform cross-section sandwich beams. According to obtained results, for dynamic analysis of thin layered sandwich beams the presented solution using the Euler-Bernoulli Beam Theory approach is useful and can give good results.

#### References

- [1] Khalili, S.M.R., Nematı, N., Malekzadeh, K., Damanpack, A.R. (2010). Free vibration analysis of sandwich beams using improved dynamic stiffness method. *Composite Structures* 92, 387–394.
- [2] Hamed, E., Rabinovitch, O. (2009). Modeling and dynamics of sandwich beams with a viscoelastic soft core. *AIAA Journal* 47, 2194–2211.
- [3] Palmeri, A., Ntotsios, E. (2016). Transverse vibrations of viscoelastic sandwich beams via galerkin-based state-space approach. *Journal of Engineering Mechanics* 142, 1–12.
- [4] Irazu, L., Elejabarrieta, M.J., Garces, Y. (2015). Dynamic properties of thin sandwich structures: Influence of viscoelastic core. *22nd International Congress on Sound and Vibration, ICSV 2015*.
- [5] Sakiyama, T., Matsuda, H., Morita, C. (1996). Free vibration analysis of continuous sandwich beams with elastic or viscoelastic cores by applying the discrete Green function. *Journal of Sound and Vibration* 198, 439–454.
- [6] Wang, G., Veeramani, S., Wereley, N.M. (2000). Analysis of sandwich plates with isotropic face plates and a viscoelastic core. *Journal of Vibration and Acoustics, Transactions of the ASME* 122, 305–312.
- [7] Zghal, S., Bouazizi, M.L., Bouhaddi, N. (2014). Reduced-order model for non-linear dynamic analysis of viscoelastic sandwich structures in time domain. *MATEC Web of Conferences* 16, 1–4.
- [8] Barbieri, N., Barbieri, R., Winikes, L.C. (2010). Parameters estimation of sandwich beam model with rigid polyurethane foam core. *Mechanical Systems and Signal Processing* 24, 406–415.
- [9] Benjeddou, A., Guerich, M. (2019). Free vibration of actual aircraft and spacecraft hexagonal honeycomb sandwich panels: A practical detailed FE approach. *Advances in Aircraft and Spacecraft Science* 6, 169–187.
- [10] Lashin, M.M.A., Okasha El-Nady, A. (2015). Free Vibration Analysis of Sandwich Beam Structure Using Finite Element Approach. *IOSR Journal of Mechanical and Civil Engineering Ver. I* 12, 2278–1684.
- [11] Huang, Z., Qin, Z., Chu, F. (2016). Vibration and damping characteristics of sandwich plates with viscoelastic core. *Journal of Vibration and Control* 22, 1876–1888.

- [12] Cortés, F., Sarriá, I. (2015). Dynamic analysis of three-layer sandwich beams with thick viscoelastic damping core for finite element applications. *Shock and Vibration* 2015, 1–9.
- [13] Zhen, W., Wanji, C. (2018). Free and forced vibration of laminated composite beams. *AIAA Journal* 56, 2877–2886.
- [14] Pham, V.N., Nguyen, D.K., Gan, B.S. (2019). Vibration Analysis of Two-Directional Functionally Graded Sandwich Beams Using a Shear Deformable Finite Element Formulation. *Advances in Technology Innovation* 4, 152–164.
- [15] Kant, T., Swaminathan, K. (2001). Analytical solutions for free vibration of laminated composite and sandwich plates based on a higher-order refined theory. *Composite Structures* 53, 73–85.
- [16] Arvin, H. (2014). Frequency response analysis of higher order composite sandwich beams with viscoelastic core. *Iranian Journal of Science and Technology - Transactions of Mechanical Engineering* 38, 143–155.
- [17] Nasihatgozar, M., Khalili, S.M.R. (2017). Free vibration of a thick sandwich plate using higher order shear deformation theory and DQM for different boundary conditions. *Journal of Applied and Computational Mechanics* 3, 16–24.
- [18] Rajesh, C., Suresh Kumar, J. (2016). Free Vibration Analysis of various Viscoelastic Sandwich Beams. *Indian Journal of Science and Technology* 9, 1–8.
- [19] Abdel Salam, M., Bondok, N.E. (2010). Free Vibration Characteristics for Different Configurations of Sandwich Beams. *International Journal of Mechanical and Mechanics Engineering* 10, 41–54.
- [20] Purushothaman, V., Guruprasad, V. (2018). Vibration Analysis of Sandwich Beam with Different Core Patterns. *International Journal of Engineering Research & Technology* 6, 2–5.
- [21] Abdel Salam, M., Abd Raboo, S.M., Bondok, N.E., Sayed, E.K. (2013). An Investigation Into Static and Dynamic Characteristics Of Sandwich Beam. *Journal of Applied and Industrial Sciences* 1, 54–65.
- [22] Dai, G., Zhang, W. (2009). Cell size effects for vibration analysis and design of sandwich beams. *Acta Mechanica Sinica* 25, 353–365.
- [23] Thamburaj, P., Sun, J.Q. (2001). Effect of material and geometry on the sound and vibration transmission across a sandwich beam. *Journal of Vibration and Acoustics, Transactions of the ASME* 123, 205–212.
- [24] Çallioğlu, H., Demir, E., Yilmaz, Y., Sayer, M. (2013). Vibration analysis of functionally graded sandwich beam with variable cross-section. *Mathematical and Computational Applications* 18, 351–360.
- [25] Garooschi, M., Barati, F. (2016). Free Vibration Analysis of Sandwich Cylindrical Panel with Functionally Graded Core by Using ABAQUS Software. *Journal of Engineering and Applied Sciences* 11, 920–929.

- [26] Kurpa, L., Shmatko, T., Awrejcewicz, J. (2019). Vibration analysis of laminated functionally graded shallow shells with clamped cutout of the complex form by the Ritz method and the R-functions theory. *Latin American Journal of Solids and Structures* 16, 1–16.
- [27] Di Sciuva, M., Sorrenti, M. (2019). Bending and free vibration analysis of functionally graded sandwich plates: An assessment of the Refined Zigzag Theory. *Journal of Sandwich Structures and Materials* 0, 1–43.
- [28] Ebrahimi, F., Farazmandnia, N. (2018). Vibration analysis of functionally graded carbon nanotube-reinforced composite sandwich beams in thermal environment. *Advances in Aircraft and Spacecraft Science* 5, 107–128.
- [29] Burlayenko, V.N., Sadowski, T. (2019). Free vibrations and static analysis of functionally graded sandwich plates with three-dimensional finite elements. *Meccanica* 7.
- [30] Ramirez, D.A., Cuba, L.M., Mantari, J.L., Arciniega, R.A. (2019). Bending and free vibration analysis of functionally graded plates via optimized non-polynomial higher order theories. *Journal of Applied and Computational Mechanics* 5, 281–298.
- [31] Zenkour, A.M., Abbas, I.A. (2014). 1371. Free vibration analysis of doubly convex/concave functionally graded sandwich beams. *Journal of Vibroengineering* 16, 2747–2755.
- [32] Li, B., Dong, L., Zhu, L., Chen, X. (2015). On the natural frequency and vibration mode of composite beam with non-uniform cross-section. *Journal of Vibroengineering* 17, 2491–2502.
- [33] Tahouneh, V. (2018). Three-dimensional elasticity solution for vibrational analysis of thick continuously graded sandwich plates with different boundary conditions using a two-parameter micromechanical model for agglomeration. *Mechanics of Advanced Composite Structures* 5, 49–66.
- [34] Burlayenko, V.N., Sadowski, T., Dimitrova, S. (2019). Three-Dimensional Free Vibration Analysis of Thermally Loaded FGM Sandwich Plates. *Materials* 12, 1–20.
- [35] Wattanasakulpong, N., Ungbhakorn, V. (2012). Free Vibration Analysis of Functionally Graded Beams with General Elastically End Constraints by DTM. *World Journal of Mechanics* 02, 297–310.
- [36] Yang, X.D., Zhang, W., Chen, L.Q. (2013). Transverse vibrations and stability of axially traveling sandwich beam with soft core. *Journal of Vibration and Acoustics, Transactions of the ASME* 135, 1–5.
- [37] Lougou, K.G., Boudaoud, H., Daya, E.M., Azrar, L. (2016). Vibration modeling of large repetitive sandwich structures with viscoelastic core. *Mechanics of Advanced Materials and Structures* 23, 458–466.

## EVALUATION OF RENEWABLE ENERGY SOURCE ALGAE AS BIODIESEL FEEDSTOCK

*Fevzi YAŞAR<sup>1</sup>*

*World population growth, together with urban development and industrialization, is increasing the world primary energy consumption every passing day. It is known that most of the energy used worldwide is derived from fossil fuels such as coal, oil and natural gas, which are called primary energy sources. In this context, as humanity continues to search for sustainable development and better living conditions, renewable energy production becomes a worldwide priority. Renewable energy has an extremely important place in respect to meeting the energy needs of countries with domestic resources, thus reducing foreign dependencies, by diversifying resources and ensuring sustainable energy use and minimizing the damage to the environment as a result of energy consumption. Within the context of alternative energy policies, agriculture-based biomass energy has found a wide application area all over the world, with environment-friendly, sustainable energy production and environmental management features aimed at development. However, the increasing production of biofuels due to the agricultural potential and technological levels of the countries has brought significant debates with it. In this case, scientists have voiced that algae biomass, defined as third generation, could be an alternative energy source and that they have many advantages. From algae biomass; studies on biofuels such as biodiesel, renewable aviation fuel / bio jet fuel, bio- gasoline / green gasoline, bio-butanol, bioethanol, methane has been widely developed. It is a very important development that the agricultural areas are not used during the cultivation of the algae, and that they can reproduce with great speed even in very small areas.*

*Key words: Renewable energy source, vegetable oils, algae oil, biodiesel feedstock - Word Style TS Abstract*

### 1. Introduction

Energy is one of the most basic and influential requirements of the economic and social development of a country. From this standpoint, "energy security" phenomenon is a vital element of economic security and national security [1]. Energy is an indispensable input for almost all processes necessary for us to sustain our social lives; accordingly, it is used in industry, transportation, residential

---

<sup>1</sup> Vocational School of Technical Sciences, Department of Chemistry and Chemical Process Technology, Batman University, 72100, Batman, Turkey, (fevzi.yasar@batman.edu.tr),  <https://orcid.org/0000-0003-3504-9157>

and commercial sub-sectors. While the energy consumed in the world today is derived from a large number of energy sources, fossil resources such as oil, natural gas and coal account for 87% of these sources [2]. Population and income growth are the main factors causing the increase of world primary energy consumption. Population growth is predicted to have a significant impact on global energy demand growth, depending on emerging industries and urbanization [3]. According to the scenarios, it is predicted that these fuels will continue to be dominant sources despite their relatively decreasing share up to 2040 [4].

### 1.1. The Situation of Petroleum in the World and in Turkey

It is known that most of the energy used in world is derived from fossil fuel sources such as coal, oil and natural gas, which are called primary energy sources, and the increase in primary energy demand is accelerating due to the increase in income and population in the world. It is known that oil has the largest share in the world's primary energy consumption, especially as the main energy source of the transportation sector [5]. When the geographical distribution of oil reserves is assessed, it appears that the entire world is dependent on the Middle East for its oil reserves. Instabilities occurring in the Middle East lead to difficulties in the uninterrupted supply of petroleum, which is a major necessity of the modern world. When geographical distribution of global oil reserves is looked through, the Middle East region draws attention as having 47.66% of world oil reserves. The Middle East is followed by Central and South America with a reserve of 19.23% and North America with a reserve of 13.31%. In addition, the areas, such as Europe and Eurasia, Africa and Asia –Pacific, have the shares of global oil reserves as 9.50%, 7.50% and 2.81%, respectively. In terms of visible / proven oil reserves of the countries, with 300 billion barrels, Venezuela takes place at the first place, and this country is followed by Saudi Arabia with 269 billion barrels, Canada with 171 billion barrels and Iran with 157.8 billion barrels and Iraq with 143 billion barrels. Turkey, by its geopolitical position, is neighbor with countries possessing three-quarters of world's proven oil and natural gas reserves; and takes place in many important projects together with the energy-rich Caspian, Central Asia, Middle East countries as a natural "Energy Center" located in among the consumer markets in Europe, and supports the projects in question. It is envisaged that a significant portion of the world's primary energy demand, which is expected to increase by 40% by 2030, will be met from the resources of the region we are in [6]. At the end of the first six months of 2017, the remaining domestic crude oil reserves are 332.8 million barrels (48 million tons). If no new discoveries are made, the current production level and the total domestic crude oil reserves have an 18 year life span. In the first five months of 2017, approximately 7.7% of consumption was covered by domestic production. Turkey's primary energy consumption in the years 2010-2016 (except for 2008) is constantly rising, the share of primary energy consumption of oil and natural gas hovered around 60%. In 2016, the share of oil and natural gas consumption in primary energy was 57.4%.

In 2016, the total consumption rate of domestic crude oil production was 5.8%. In the first six months of 2017, a total of 1.3 million tons of crude oil was produced; and a total of 150 million tons of crude oil has been produced till present day. Despite the fact that the raw material and energy resource capacities of our country are limited due to the information given above, the continuous and rapid increase in the raw material and energy needs with the use of new technological products entering our lives every day forces humanity to find new alternative energy sources. Alternative sources need to be human-focused, renewable, feasible, and easily obtainable with sustainable economic development and domestic resources for a cleaner environment. For this reason, the use of renewable energy resources in the form of both local and renewable natural resources is of great importance in meeting the energy

needs of both our country and the rest of the world. That is why a tendency has begun to focus on renewable energy sources all over the world both in terms of technological researches and using the energy produced from these sources. Countries concentrate on various renewable energy sources (biomass, solar, wind, hydroelectric, geothermal, wave etc.) depending on their economic, environmental, natural and social characteristics. Within the context of alternative energy policies, agriculture-based biomass energy has found a wide application area all over the world, with environment-friendly, sustainable energy production and environmental management features aiming at development. However, the increased production of biofuels due to the agricultural potential and technological levels of the countries has brought about some significant debates. In this case, scientists have voiced that algae biomass, defined as third generation, could be an alternative energy source, and that they have many advantages. Biomass energy research, which has accelerated in recent years with the effect of rising oil prices, has begun to be seen as a source of energy promising hope. Studies, where biofuels such as biodiesel, renewable aviation fuel / bio jet fuel, bio gasoline / green gasoline, bio-butanol, bioethanol, methane are obtained from algae biomass, have been widely developed. By using algae oils as raw materials in the production of biodiesel, both the biodiesel unit price can be competitive with the petroleum origin diesel fuel and it will be possible to diversify the energy sources of the countries and the countries will be able to get rid of the external dependence in terms of energy. The studies have indicated that biodiesel fuel obtained from renewable sources such as vegetable and animal fats can be used as an alternative to the petroleum diesel and thus is considered as a promising alternative fuel for reducing petroleum dependence and reducing pollution caused by exhaust emissions [7].

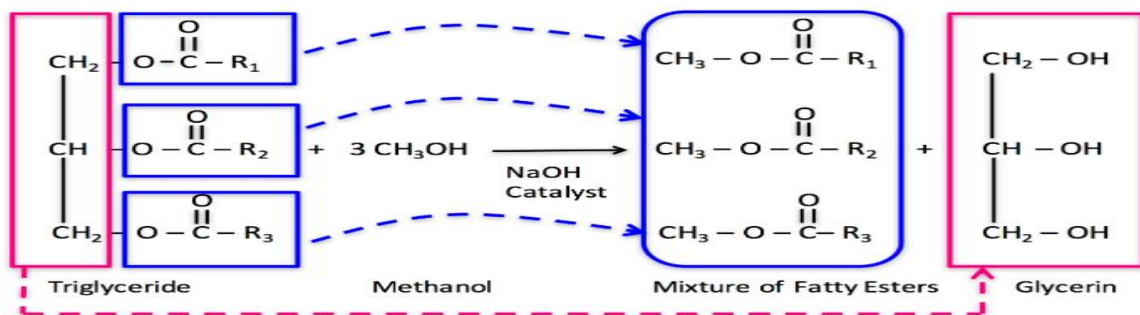
## 2. Biodiesel Production and Properties

To be able to use vegetable and animal oils as alternative fuels in diesel engines, it is necessary to lower the biodiesel viscosities, which are very high, compared to petroleum origin diesel fuel (diesel) [8]. For this purpose, dilution, micro emulsion formation, pyrolysis and transesterification methods are used. In the dilution method, the oil is diluted by mixing with diesel fuel [9]. Depending on the mixture of diesel fuel ratio, the fuel improves in terms of viscosity, evaporation, spraying properties. In micro emulsion formation, it is intended to form micro emulsions with short chain alcohols such as methanol, ethanol or 1-butanol. The micro emulsion is the equilibrium distribution of optically isotropic liquid microstructures with dimensions between 1 and 150 nm, normally formed by the mixing of two immiscible liquids and one or more active substances. In pyrolysis method, however, oil molecules are broken down into smaller molecules in an oxygen-free environment at high temperatures. Pyrolysis process is divided into three parts as hydrocracking, catalytic cracking and thermal cracking. The amount of product produced depends on the method and reaction parameters used. With this method, although the fuel properties of oils approach diesel fuel properties, the most important drawback is high energy consumption. Transesterification is the re-esterification reaction of fatty acids (vegetable oils, domestic waste oils, animal oils) with alcohol (methanol, ethanol, etc.) in the presence of a basic catalyst. In this method, oil molecules enter into a chemical reaction with alcohol at a certain temperature with the help of a catalyst. With this chemical reaction, the fatty acids separate from the triglycerides they are bound to form new esters with alcohols [9].

### 2.1. Reaction mechanism in biodiesel production by transesterification

Transesterification is an ester conversion process that breaks down triglycerides that form vegetable and animal fats, in other words, by taking the glycerol in it and replacing it with the alkyl

radical in the alcohol used. Briefly, glycerol-based triesters are converted to alkyl-based monoesters. With transesterification, the conversion of triglycerides into monoesters results in a molecular weight of about one third, and a major problem, the high viscosity, is greatly reduced. In addition, the volatility feature is also improved [10]. Alcohol: the raw material molar ratio for the stoichiometric transesterification reaction is 3: 1, and since transesterification is a reversible equilibrium reaction, it is necessary to use more alcohol in theory to be able to move the reaction towards the products. For this reason, in practice, alcohol with molar ratios greater than 3: 1 is used. Generally, when 100% excess alcohol (6: 1) is used, the reaction rate and ester conversion are obtained at the highest level. However, increasing the ratio of alcohol more than a certain value does not improve the ester conversion, but prevents the decomposition of glycerol. Moreover, at the end of the reaction, it is necessary to remove the residual alcohol from the reaction environment, which adds extra cost to the system [11]. The alcohol used is very important because it affects both the transesterification reaction and the properties of the biodiesel fuel obtained. Biodiesel is an ester fuel called the alkyl part of the alcohol used in the production. If methanol is used in the reaction, the fuel is defined as the methyl ester; and it is called as ethyl ester fuel if ethanol is used. It also contains the alcohol bonds used in the biodiesel production and thus the fuel properties are affected by this. Among the alcohols used in the transesterification reaction, methanol is preferred because of its low cost and physical-chemical advantages (polar and shortest chain alcohol). Methanol reacts rapidly with triglycerides and the catalyst readily becomes soluble in



methanol. Biodiesel is made through a chemical reaction called transesterification (Fig. 3) where fats and oils are converted into a mixture of fatty acid methyl esters (FAME) in a presence of alcohol with base catalyst.

**Figure 3. Transesterification reaction for biodiesel production [12]**

The base, acid or enzyme (biological) catalyst is used as a catalyst to accelerate the transesterification reaction. Acid and enzyme catalysts are slower than base catalysts [11].

## 2.2. Biodiesel Properties

Biodiesel, like vegetable and animal fats, is a promising alternative diesel fuel derived from renewable sources that contains oxygen and is particularly promising in terms of reducing polluting exhaust emissions [13]. Biodiesel is a methyl or ethyl ester type fuel containing medium chain C16-C18 fatty acid chains. It does not contain toxic wastes, it dissolves rapidly in nature like sugar, and it reduces the need for fertilization by its nitrogen retention feature. The adverse effects on the ozone layer are 50% less than diesel fuel. Biodiesel is an environmentally friendly, anti-toxic, biologically fast and easily degradable fuel that can be obtained from renewable raw materials. At the same time, with low content of sulfur and high flash point, it is a kind of fuel which can be easily stored, and is portable and usable. It also has an excellent lubrication feature. Biodiesel and its diesel fuel mixtures can be used in

diesel engines without any technical modifications or minor changes [14]. This feature raises the quality of petroleum-derived diesel. For example, it reduces the emission values of harmful gases generated by combustion, increases the degree of lubrication on the motors and dissolves accumulators that reduce motor power. Since biodiesel is derived from agricultural crops in general, it does not have an increasing the greenhouse effect as it converts CO<sub>2</sub> into food by photosynthesis and accelerates the carbon cycle in the biological carbon cycle. In other words, biodiesel can be considered as a natural sink for CO<sub>2</sub> emissions. For the biodiesel, the European Union of EN 14214 and the American Standard of ASTM D 6751 are in force. TSA Standard in Turkey has been prepared based on EN 14214 standard. In Table 3, the specifications that the biodiesel produced in Turkey should provide for the TS according to EN 14214 standards are given.

**Table 3. EU (EN 14124: 2013) biodiesel standard [15].**

Properties	Unit	Limit Values	Test Method
Esther content	% (m/m)	96.5	EN 14103
Density (15 ° C)	kg/m <sup>3</sup>	860-900	EN ISO 12185
Kinematic viscosity (40°C) (40°C)	mm <sup>2</sup> /s	3.50-5.00	EN ISO 3104
Flash Point	°C	101 min.	EN ISO 3679
Sulfur content	mg/kg	10 max.	EN ISO 20846
Carbon residue	% (m/m)	0.30	EN ISO 10370
Cetane number		51min.	EN ISO 5165
Sulphate ash content	% (m/m)	0.02 max.	ISO 3987
Water content	mg/kg	500 max.	EN ISO 12937
Total pollution	mg/kg	24 max.	EN 12662
Copper strip corrosion	Corrosion	No 1 max.	EN ISO 2160
Oxidation stability (110 ° C)	Hour	8.0 min.	EN 14112
Acid value	mg KOH/g	0.5 max.	EN 14104
Iodine value	g I <sub>2</sub> /100 g	120 max.	EN 14111
Linolenic acid methyl ester	% (m/m)	12 max.	EN 14103
High unsaturation (≥4 double	% (m/m)	1 max.	EN 15779
Methanol content	% (m/m)	0.20 max.	EN 14110
Monoglyceride content	% (m/m)	0.80 max.	EN 14105
Diglyceride content	% (m/m)	0.20 max.	EN 14105
Triglyceride content	% (m/m)	0.20 max.	EN 14105
Free glycerol	% (m/m)	0.02 max.	EN 14105
Total glycerol	% (m/m)	0.25 max.	EN 14105
Group I Metals (Na + K)	mg/kg	5.0 max.	EN 14108
Phosphor content	mg/kg	4.0 max.	EN 14107

### 3. Advantages and Disadvantages of Using Biodiesel

The most important advantage of using biodiesel as alternative engine fuel is that it can be used in existing diesel powered vehicles. In other words, there is no need to make any changes or additions to the engine construction to use biodiesel as fuel in the engines available. As is known, parallel to the developments in diesel engine technology, the number of vehicles with diesel engines also increases and its use in automobiles is becoming more widespread. Like other alternatives (such as hydrogen, LPG, CNG), since biodiesel does not necessitate an additional system, this makes it an attractive alternative fuel. Biodiesel has many positive features and potentials directly, indirectly and possibly.

### 3.1. Advantages of biodiesel

- Biodiesel-forming C16-C18 methyl esters are easily and rapidly disintegrated. They are biodegradable and non-toxic. According to the tests performed, 99.6% of the biodiesel obtained from the canola was decomposed in 21 days. It is an environmentally friendly alternative energy source, and has edible character, can be produced with local opportunities. When compared to diesel, it does not cause the accumulation of CO<sub>2</sub> in the atmosphere and consequently the greenhouse effect. This is because the resulting CO<sub>2</sub> from the combustion of biodiesel is used by plants where biodiesel is obtained [16].
- It allows making use of used domestic and industrial oils. It can be produced from waste vegetable and animal oils and fats. Assessment of waste materials reduces the amount of waste on the earth. It gives agricultural crops a second surplus value [17].
- Fatty acids and oils containing them in biodiesel have the highest thermal value in all biological materials. This property is the feature of relatively long hydrocarbon chain linked to a single carboxyl group bearing two hydrogen atoms. For this reason, vegetable oils are the closest biomass to liquid fuels and fatty biomaterials with higher heat energy than lean biomass provide a constant potential for biodiesel production [18].
- Biodiesel has a higher ignition rate ( $> 110^{\circ}\text{C}$ ) than petroleum-derived diesel fuel. Although this does not directly affect combustion, it makes biodiesel safer in terms of storage and portability [19].
- Emissions have less carbon monoxide, particulate matter, unburned hydrocarbons and aromatic compounds and almost no sulfur. Furthermore, it is also poor in terms of cancer causing compounds (Aromatics). Since biodiesel does not contain sulfur, it can be used as an oxidation catalyst in biodiesel plants. Thus, harmful emission values can be lowered to even lower levels.
- Biodiesel has a better lubricant than the engine, which prolongs engine life. Because the degree of lubrication is high [20].
- Biodiesel contains 11% oxygen by weight. The higher the oxygen content, the higher the combustion efficiency [16].
- Biodiesel has a very low iodine count, so it does not form any soot [21].
- The fact that it has higher cetane number compared to the diesel provides the engine with the less noise and without knocking operation. Biodiesel can be used in 100% ratio as well as being mixed with diesel fuel at various ratios in any unchanged diesel engines [22].
- Commercial glycerin and potassium fertilizer is obtained from biodiesel as by-product.
- In addition to accelerating the agricultural development of the countries with the impact of agriculture by providing integration of industrialization with agricultural products, new employment opportunities are created with the use of biodiesel, and contributions that cannot be underestimated by the country's economy are realized [21].

### 3.2. Disadvantages of biodiesel

- Biodiesel has a higher flow point than a diesel. The main factor affecting the use of vegetable oils directly as diesel fuel is their high viscosities. Injection systems of modern diesel engines show sensitivity to viscosity changes. The high viscosity spoils atomization of the fuel in the combustion chamber, preventing full combustion by growth in droplet size. Uncompleted combustion leads to deposits in the combustion chamber, in the injectors causing coking and

blockage; besides, it negatively affects the lubricating oil by thickening and gelling it. Another problem with the use of vegetable oils as fuel originates from unsaturated bonds. The fact that unsaturated structures mix into the lubricating oil and are polymerized in this environment causes viscosity increases which are possible to destroy the engine [18].

- Biodiesel is affected more quickly by cold weather than by diesel. It has a higher cloud point in cold weather. Biodiesel containing high amounts of saturated fatty acids can cause blockage of fuel filter and fuel line pipes in winter. This is a limiting factor of biodiesel to be used in cold climate regions. In order to overcome this challenge, use of mixture form is preferred and the problem can be removed by preheating. Biodiesel is low by thermal value. This leads to some power drop in the resultant combustion [16].
- It has a high gel point. It is 0 ° C (32 ° F) for B100 (100% biodiesel) and -26 ° C (-15 ° F) for B20 (20% biodiesel + 80% diesel) [23].
- Another disadvantage of biodiesel is its tendency towards oxidation. Biodiesel in contact with air starts to oxidize rapidly, especially at high temperatures. Biodiesel, however, has a higher flash point. Although this does not directly affect burning, it makes biodiesel safer in terms of storage and portability [23].
- Biodiesel breaks up natural and butyl rubbers in storage, transport and engine equipment and cannot be stored for long periods. In the case of pure (B100) use, the hoses, fittings and gaskets in the fuel equipment in the engine should be replaced with appropriate materials [24].

#### 4. Utilization of Algae Oils in Biodiesel Production

Algae (single-celled microalgae) are living organisms capable of performing microscopic photosynthesis on the land and in the sea. They are regarded as living things that have enabled life to start and be transferred to land by scientists, and they are said to have existed for almost 5 billion years. It is known that about 200,000 to 2-3 million species of algae in the nature have been recorded, and until now, about 30,000 species have been recorded and only a few of them could be commercialized [25]. Algae are rich in carbohydrates, proteins and especially fatty acids. Highly nutritious algae are the most important source of nutrients, vitamins and trace elements for the aquatic creatures. They also provide essential pigments for the development of coloring in fish and other aquatic life. Algae play an important role in protecting the integrity of all ecosystems. Diatoms and other microscopic algae in the oceans produce two thirds of the photosynthetic carbon needed by the entire world. In addition to photosynthetic vitrification carried out by sea algae in the water, it also meets the needs and nutrients and protection of creatures living in the water. Since the end of the 17th century, it has been known that the "potas", which are used to make soap, glass, soda and fertilizer, are obtained from their mineral rich ashes by the burning of brown moss. Bromine and iodine, which are among the chemical substances, have been isolated for the first time from this ash, and it is known that iodine is still obtained from marine algae in Japan. Algae are important food source, especially in eastern Asia. They are rich in A, B1, B2, B6 and C and niacin, iodine, potassium, iron, magnesium and calcium. Some algae varieties are cultivated as "support nutrients" and packaged and sold. Approximately 70 in China and 20 algae types in Japan are used meals [26]. Table 4 gives the lipid content, lipid productivity, volumetric and areal yields of biomass of some algae species used in biofuel production [27].

**Table 4. Lipid content and productivity of different algae species**

Algae species	Lipid content (% Dry Wt.)	Lipid yield (mg/L/day)	Biomass Volumetric yield (mg/L/day)	Biomass Sparse yield (mg/m <sup>2</sup> /day)
Ankistrodesmus sp.	24-31	-	-	11.5-17.4
Chlorella emersonii	25-63	10.3-50	0.036-0.041	0.91-0.97
Chlorella vulgaris	5-58	11.2-40	0.02-0.20	0.57-0.95
Chlorella sp.	10-48	42.1	0.02-2.5	1.61-16.4
Chlorella pyrenoidosa	2	-	2.90-3.64	72.5-130
Chlorella	18-57	18.7	-	3.5-13.9
Dunaliella salina	6-25	116	0.22-0.34	1.6-3.5/20-38
Dunaliella primolecta	23.1	-	0.09	14
Haematococcus	25	-	0.05-0.06	10.2-36.4
Nannochloropsis sp.	12-53	37.6-90	0.17-1.43	1.9-5.3
Porphyridium cruentum	9-18.8	34.8	0.36-1.50	25
Scenedesmus sp.	19.6-21.1	40.8-53.9	0.03-0.26	2.43-13.52
Spirulina platensis	4-16.6	-	0.06-4.3	1.5-14.5/24-51
Spirulina maxima	4-9	-	0.21-0.25	25
Tetraselmis suecica	8.5-23	27-36.4	0.12-0.32	19

#### 4.1. Fuels produced from algae oils

Algae have been produced or evaluated as food additives in animal breeding rather than as an alternative source of energy for many years. As a result of biomass energy research, which accelerated in recent years with the effect of rising oil prices, algae have begun to be seen as a promising source of energy. Despite being successful in laboratory research, pilot and small-scale experiments, the desired yield cannot be achieved in the case of the ideal processes in large-scale local production, if it is not possible to produce ideal processes in the field in the studies targeting to use many algae in nature used as energy source also called third generation biofuel technology. In general, algae can contain about 15-77% oil, albeit varying by species. The fact that algae have high oil content and growth yields compared to other oil plants makes microalgae attractive for biodiesel and biogas production. The production of these fuels from microalgae has the potential to contribute to the prevention of global warming by responding to increasing global energy needs and, in part, by transforming excess carbon dioxide into an efficient product through photosynthesis in the atmosphere. One of the advantages of using mosses as raw materials for biofuels is that different kinds of fuels can be produced. Besides, algae have properties that can meet our needs for biodiesel and biogas as well as ethanol, bio jet fuel, bio-gasoline or other fuels [28].

Below are some types of fuel produced from algae:

- Biodiesel
- Renewable Aviation Fuel / Bio jet Fuel
- Bio gasoline / Green Gasoline,
- Biobutanol
- Bioethanol
- Methane

Biodiesel is a diesel fuel derived from plant or animal lipids (liquid or solid oils). Studies show that some algae types contain 80% more oil of their total dry weight. The majority of algae cells have large-scale biomass production capacities because they are grown with water, CO<sub>2</sub> and dissolved nutrients in the aqueous suspension medium in pools and photo bioreactors. Oil produced from algae can then be used as biodiesel in automobiles [29]. Figure 4 shows the production of bio-fuels and various biofuels resulting from oil extraction from algae grown by using wastewater such as agricultural or sewerage in plants established alongside the power plant.

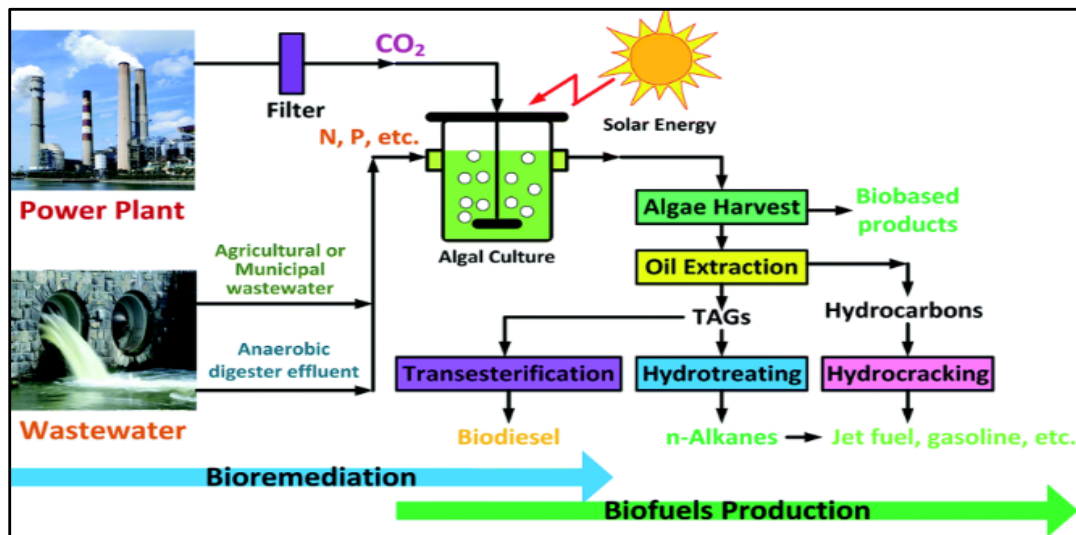


Figure 4. Production of biodiesel from algae biomass grown in wastewater [30]

## 5. Use and Advantages of Seaweed Oil as an Energy Source

The oil obtained from algae can be used directly as a fuel in diesel engines, just like other vegetable oils, and can be converted to biofuels by purification. The algae are observed in the laboratory environment that they increase the amount of oil produced by 40% because they are fed with more CO<sub>2</sub> and organic substances. Seaweed oil, especially used in biodiesel production, can be used as an organic and environmentally friendly fuel. According to oil plants, algae produce organisms that make use of sunlight and CO<sub>2</sub> more effectively, and their cleavage potentials and growth rates are also quite high. Some algae contain up to 60% by their weight of oil and can produce about 55,000-60,000 liters of oil per hectare per day if optimum conditions are met. For these reasons, it is possible to produce mosses in smaller areas, in larger quantities and at lower costs, compared to oil farms that have been cultivated extensively. The advantages of using algae oil as an energy source are given below:

- The fact that biodegradation of CO<sub>2</sub> in industrial flue gases by algae and the transformation of grown algae oil into biodiesel take place reduces the effect of greenhouse gases in the atmosphere [31].
- Because they can be grown photo synthetically, they do not need carbon sources and use carbon dioxide as the energy source of previous consumption products to achieve carbon dioxide neutralization [32].
- Biodegradation of CO<sub>2</sub> in industrial flue gases by algae and the transformation of grown algae and therefore oil into biodiesel reduces the effect of greenhouse gases in the atmosphere [30].
- Because they can develop photo synthetically, they do not need carbon sources and use carbon dioxide as the energy source of previous consumption products to achieve carbon dioxide neutralization [33].
- The lipids accumulated by the microalgae are generally in the form of triacylglycerol (> 80%) and contain fatty acids C16-C18 rich in carbon atoms, which is also evident in the fatty acid distribution of the oil we use. The average lipid content of algae cells varies between 1% and 70%, but there are also 90% lipid-accumulating algae when optimum conditions are met.

## 6. Results and Discussion

The contents of oils used in production of biodiesel and the oil amount obtained per hectare/year and the area as  $m^2$  necessary for one liter biodiesel production and biodiesel amounts obtainable per hectare/year were investigated.

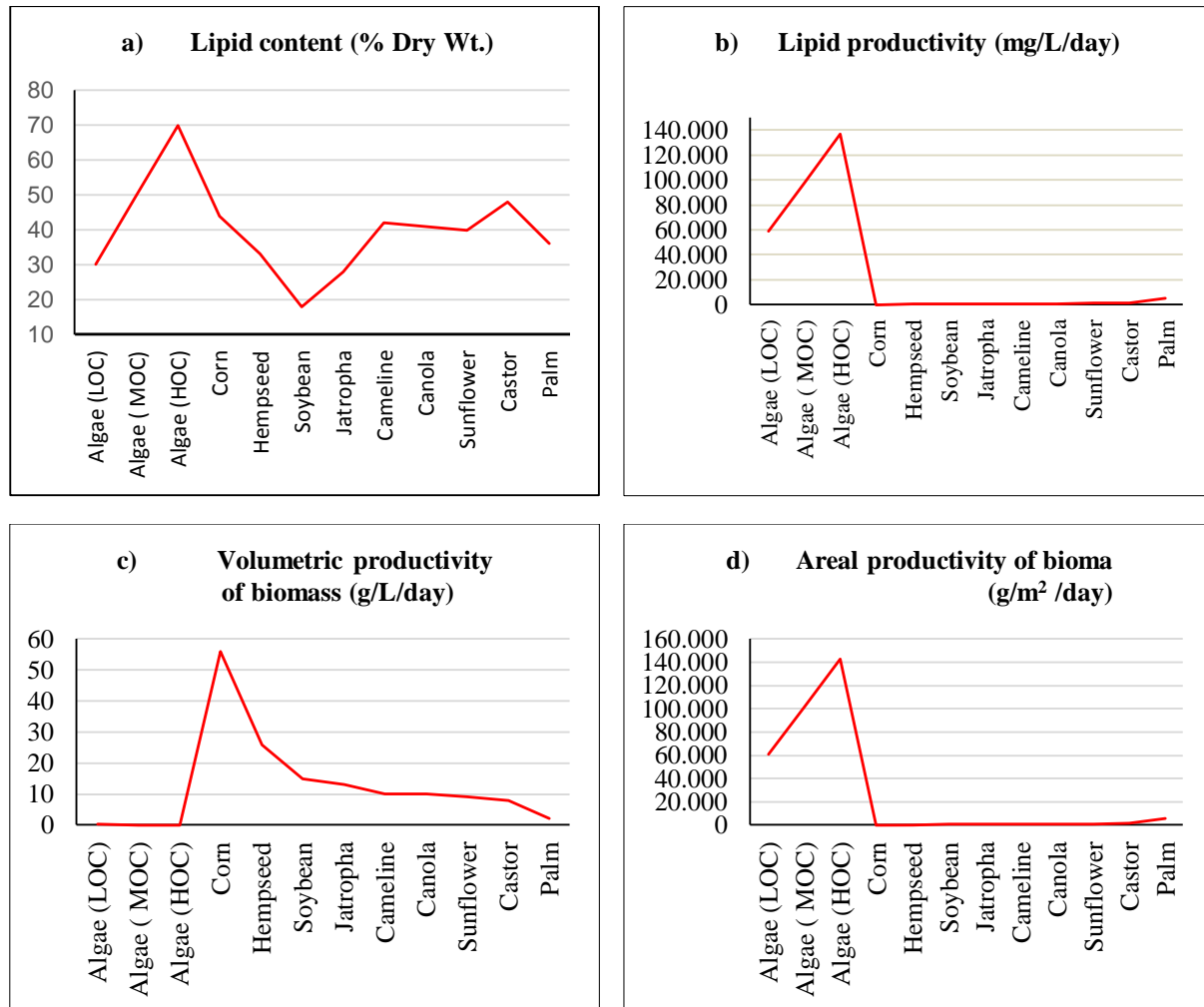


**Figure 5.** Oil content, oil yield, usage area and biodiesel yields of different vegetable oils used in biodiesel production. (LOC: Low oil content, MOC: Medium oil content, HOC: High oil content)

When Figure 1 is examined, it can be seen that algae HOC have the highest oil content with 70%; and this is followed by algae MOC and jute with 50% and 48%, respectively. It is known that algae types such as “*Chlorella emersii*” have quite oil contents in biodiesel production [vv]. When Figure 1b, d) is examined, it is determined that algae (HOC, MOC and LOC) have had higher yields compared to other resources in oil and biodiesel obtained per hectare/year. When Figure 1 c) is examined, it is seen that while Algae HOC necessary to produce 1 liter biodiesel is 0,1m<sup>2</sup>, it is 56 m<sup>2</sup> for maize. This clearly shows that algae are the most appropriate sources for biodiesel production. The density, viscosity and acid values, and some critical fuel properties such as peroxide value, saponification value, total particle matter (TPM) and calorific value of oils to be used in biodiesel production were analyzed in TÜPRAŞ Batman Refinery fuel analysis laboratory and in Batman University Technical Sciences Vocational College, Refinery and Petrochemical Technology Program laboratory. In Table 5. some of the critical properties of various herbal oils were given.

**Table 5. Some critical fuel properties of vegetable oils used in the study**

Oils	Density (kg/m <sup>3</sup> ,15 °C)	Viscosity (mm <sup>2</sup> /s,40 °C)	Acid Value (mg KOH/g)	Iodine Value (g I <sub>2</sub> /100g)	Peroxide Value (meq/kg)	Saponification Value (mgKOH/g)	TPM (%)	Heating Value (kJ/kg)
Algae	916.0	30.43	0.07	105.44	17.35	183.28	7.5	39657
Sunflower	921.7	33.08	0.21	122.68	10.39	192.73	4.0	39873
Soybean	923.3	32.63	0.12	129.65	25.45	195.06	8.0	39633
Canola	919.9	35.78	0.19	110.74	13.45	191.04	2.0	39755
Corn	921.9	34.33	0.26	115.36	6.09	189.72	6.0	39651
Cotton	922.3	33.96	0.19	114.19	9.09	195.27	6.5	39568
Hazelnut	917.1	37.74	0.19	86.91	12.88	188.33	2.5	39710
Olive	917.5	38.93	2.32	81.85	11.39	183.42	5.5	39617

In Figure 6, density, viscosity, acid value and heating value values of different oils used in biodiesel production are compared.

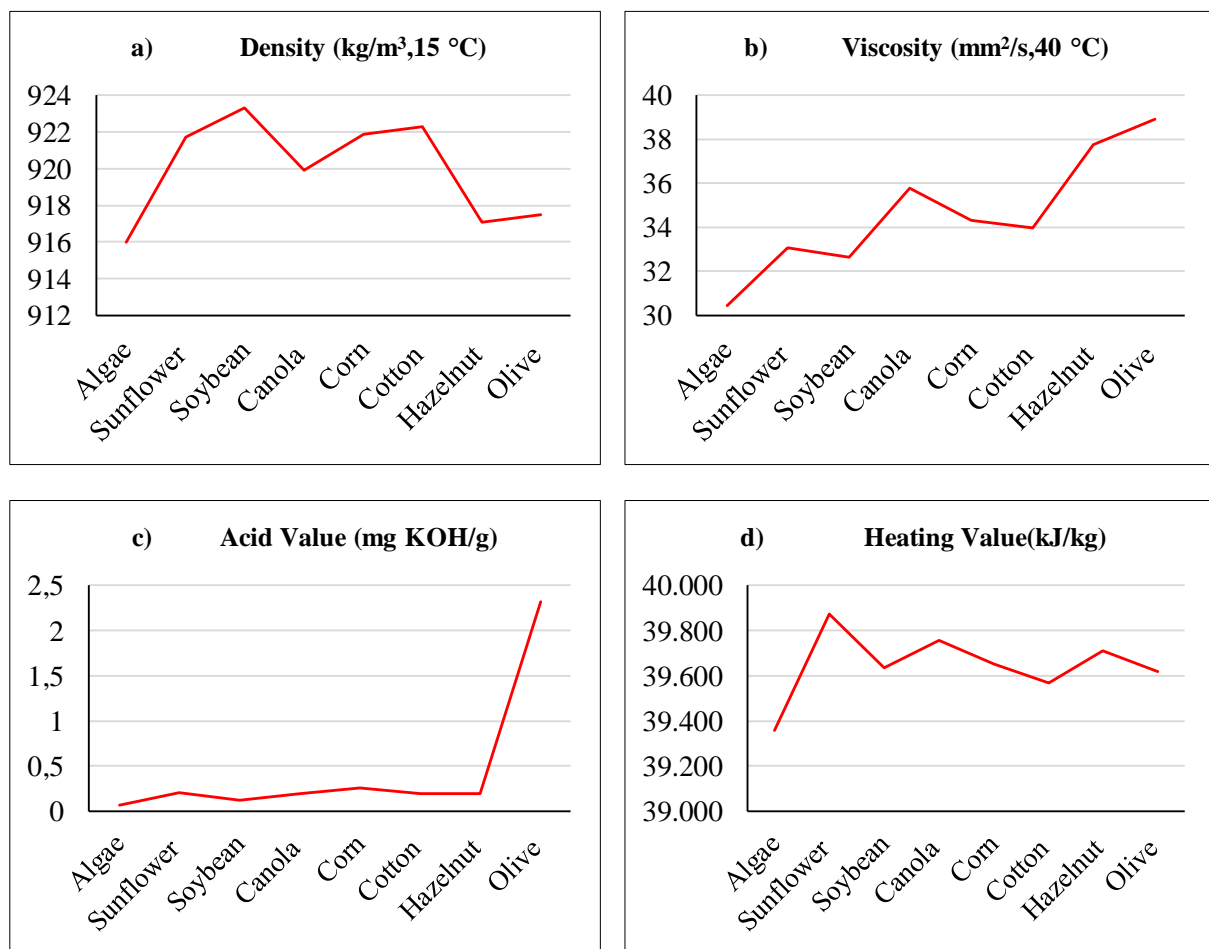


**Figure 6. Density, viscosity, acid value and heating value values of different oils used in biodiesel production are compared**

When Figure 6 a) and b) are examined, it can be comprehend that the source whose density and viscosity values are the lowest is algae ( $916\text{kg/m}^3$ ,  $30,43\text{mm}^2/\text{s}$ ) and that this depends on the distributions of oil acids of the oils. One of the most important properties of oils used in biodiesel production is that of the acid values of the oil. When Figure 6 c) is examined, it can be clearly seen that algae oil has the lowest acid value ( $0,07\text{mgKOH/g}$ ), while olive oil has the highest acid value ( $2,32\text{mgKOH/g}$ ). And, this strengthens the view that algae oil is the most appropriate for biodiesel production. The energy values of fuels change depending on their calorific values. When the other oils used in the study are examined (Figure 6 c)), it is seen that sunflower, canola, hazelnut and algae have had the highest calorific values as  $39.873\text{ kJ/kg}$ ,  $39.755\text{ kJ/kg}$ ,  $39.710\text{ kJ/kg}$  and  $39.657\text{ kJ/kg}$ , respectively.

## 7. Conclusion

Many countries in the world are covering a large part of the energy they need from petroleum and importing the vast majority of that oil, which is a very critical problem, leading to energy dependency. For countries that import vast majority of Fossil-Origin Energy, such as our country, the matter of alternative energy sources, which can be produced with domestic resources, is a very critical issue. The fact that biofuels, which are becoming increasingly important in the world among alternative energy sources, can be used as an alternative to fossil based fuels causes attention to be drawn to this point. Increasingly becoming common throughout the world, biofuels contribute to countries' energy supply and provide alternative income and employment opportunities for producers of biofuel raw materials, especially in rural areas. When alternative fuels come into question in our country, biofuels, especially biodiesel, are at the forefront. With regard to biodiesel; it is foreseen that biodiesel will continue to be popular in the coming years, although there have been considerable criticisms such as the use of agricultural land for energy purposes, rising prices of food and agricultural products, and the tendency to do mono cultivation. The use of vegetable and animal oils with high cooking oil quality in the production of biodiesel means the extra cost for countries that import a large part of their oil needs. Especially in the face of rising food prices, the search for environmentally friendly energy sources has been accelerated without touching existing resources and using agricultural land. In this context, a lot of extensive studies have recently been carried out on the production of biodiesel from different algae species. The fact that some algae species have more fat than field crops and are easier to grow, and are not affected by changing seasons and climatic conditions, and can be grown in high quantities in a short period of time make them advantageous fuels. Nevertheless, the fact that agricultural lands are not used during their growing, and that they can reproduce even in very small areas, and that they do not need fertile soil for their development, and that they can grow in small ponds, and adapt to desert conditions are their most important advantages. When oil contents of the oils used in biodiesel production and oil amount obtained per hectare/year and the area in  $\text{m}^2$  necessary for producing one litre of biodiesel and biodiesel amounts obtainable for per hectare/year are examined, it is seen that algae has been established to have the highest oil content with 70%, which is followed by Algae MOC with 50% and Jute with 48%. In addition, it has been determined that algae (HOC, MOC and LOC) have the highest yield compared with other sources in oil and biodiesel yield obtained per hectare/year. Moreover, it is seen that while Algae HOC needed for 1 litre biodiesel yield is  $0,1\text{m}^2$ , it is  $56\text{m}^2$  for maize. It is clearly seen that alga are the most appropriate source for biodiesel production. When some of the critical values of oils used for biodiesel production are examined, it is seen that the source whose density and viscosity values are the lowest is algae with  $916\text{kg/m}^3$ ,  $30,43\text{mm}^2/\text{s}$ , and also the algae oil has the lowest acid value with  $0,07\text{mgKOH/g}$ , while olive oil has the highest acid value with  $2,32\text{mgKOH/g}$ . It is known

that the energy values of fuels change depending on their calorific values. When the oils used in the study are examined, it can be seen that Sunflower, Canola, hazelnut and Algae have the highest caloric values with 39.873kJ/kg, 39.755kJ/kg, 39.710kJ/kg and 39.657kJ/kg, respectively. When all data and analyses are taken into consideration, it is considered that some types of algae are quite appropriate for biodiesel production.

## References:

- [1] Fadly, F., (2019). Low-carbon transition: Private sector investment in renewable energy projects in developing countries. *World Development*, 122, 552–569.
- [2] Turkey Petroleum Year 2016 *Crude Oil and Natural Gas Sector Report*.
- [3] Zheng, W., Walsh, P.P. (2019). Economic growth, urbanization and energy consumption — A provincial level analysis of China. *Energy Economics*, 80, 153–162.
- [4] Kim, Y.D., Frei, C., 2019. World Energy Scenarios, *World energy council*.
- [5] Zarifi, F., Mahlia, T.M.I., Motasemi, F., Shekarchian, M., Moghavvemi, M. (2013). Current and future energy and exergy efficiencies in the Iran's transportation sector. *Energy Conversion and Management*, 74, 24–34.
- [6] <http://www.enerji.gov.tr/en-TR/Pages/Petrol>, 2108.
- [7] Yaşar, F., (2016). Production of biodiesel from algae oil and its use as an alternative fuel in a diesel engine, *Doctoral Thesis, Batman Institute of Science*, Batman.
- [8] Knothe, G., (2005). Historical perspectives on vegetable oil-based diesel fuels. Book: *The Biodiesel Handbook*.
- [9] Gebremariam, S.N., Marchetti, J.M., (2017). Biodiesel production technologies: review. *AIMS Energy*, 5(3): 425-457.
- [10] Sabancı, A., Oren, M. N., Yasar, B. Ozturk, H., Atala, M., (2010). Evaluation of the agricultural sector in terms of biodiesel and bioethanol production in Turkey, Agricultural Engineering VII. Technical Congress.
- [11] Şanlı, H., (2014). Characterization of waste frying oils and evaluation in biodiesel production, Doctorate Thesis, Kocaeli University. *Institute of Science and Technology*. Kocaeli.
- [12] Singh, K., Kumar, S.P., Blumich, B., (2019). Monitoring the mechanism and kinetics of a transesterification reaction for the biodiesel production with low field H NMR spectroscopy. *Fuel* 243, 192–201.
- [13] Sugoza, I., C. Oner, S. Altun, (2010). The performance and emissions characteristics of a diesel engine fueled with biodiesel and diesel fuel. *Int. J. Eng. Res. Dev.*, Vol. 2.
- [14] Altun, Ş., Yaşar, F., (2013). Biodiesel production from leather industry wastes as an alternative feedstock and its use in diesel engines. *Energy Exploration & Exploitation*, 31 (5), 759-770.
- [15] Knothe, G., (2006). Analyzing biodiesel: Standards and other methods. *Journal of the American Oil Chemists' Society*, 83, 823-833.
- [16] Ögüt, H., Oğuz, H., (2006). The fuel of the third millennium biodiesel. *Book*, 48-49.
- [17] Akin, E., (2005). *Turkey biofuels (biodiesel-bioethanol) report*, Ankara.
- [18] Öztürk, Ö., (2007). Investigation of the effects of biodiesel used without mixing in diesel engines on engine performance, Master Thesis, Yıldız Technical University, *Institute of Science*, Istanbul.
- [19] Mutlu, L., Yavuz, H., Bayrakçeken, H., (2006). Meeting the performance of biodiesel fuels, 9. *Burning Symposium*, 40-49, Kırıkkale.
- [20] Altun, S., Öner, C., (2013). Gaseous emission comparison of a compression-ignition engine fueled with different biodiesels. *Int. J. Environ. Sci. Technol*, 10, 371-376.

- [21] Nişancı, S., (2007). Experimental Investigation of Effects of Biodiesel Fuel Mixtures on Performance and Emission, M.Sc. Thesis, Yıldız Technical University, *Institute of Science*, Istanbul.
- [22] Türkay, S., (2005). Biodiesel production technologies, problems and suggestions on the current situation in biodiesel production workshop in Turkey, December 2, Ankara.
- [23] Aries, M., (2011). Determination of the proper production of biodiesel and biodiesel plants that can be grown and grown technology in Turkey, PhD Thesis, Yildiz Technical University, *Institute of Science and Technology*, İstanbul.
- [24] Artukoğlu, B.D., (2006). Development of biodiesel production and properties from animal waste oils, Graduate Thesis, Gazi University. *Institute of Science*, Ankara.
- [25] [www.mikroalg.com/tag/mikroalg-a](http://www.mikroalg.com/tag/mikroalg-a), March 29, 2018.
- [26] [https://www.academia.edu/Alglerin Ecological Prevention](https://www.academia.edu/Alglerin_Ecological_Prevention), March 20, 2018.
- [27] Mata, T. M., Martins, A. A., Caetano, N. S., (2010). Microalgae for biodiesel production and other applications: A review. *Renewable and Sustainable Energy Reviews*, 14, 217-232.
- [28] [www.en.wikipedia.org/wiki/Algae\\_fuel](http://www.en.wikipedia.org/wiki/Algae_fuel), 19 January 2018.
- [29] Canzer M., Van Gerpen J., (2001). Biodiesel production from oils and fats with high free fatty acids. *T. ASABE.*, 44, 1429-1436.
- [30] Shen, Y., (2014). Carbon dioxide bio-fixation and wastewater treatment via algae photochemical synthesis for biofuels production, *RSC Advances*, 91.
- [31] Wang B, Li Y, Wu N, Lan CQ., (2008). CO<sub>2</sub> bio-mitigation using microalgae. *Applied Microbiology and Biotechnology*, 79 (5), 707-718.
- [32] Lorenz, R.T., Cysewski, G. R., (2000). Commercial potential for haematococcus microalgae as a natural source of astaxanthin. *Trends in Biotechnology*, 18, 160-167.
- [33] Rajvanshi, S., Sharma, M.P., (2012). Microalgae: A potential source of biodiesel, *Journal of Sustainable Bioenergy Systems*, 2, 49-59.

## INVESTIGATION OF MICROSTRUCTURE AND MICROHARDNESS PROPERTIES OF CO AND CR REINFORCED NIAL INTERMETALLIC COMPOUND PRODUCED BY SHS METHOD

*İbrahim BİLİZ<sup>1</sup>, Musa KILIÇ<sup>2\*</sup>, Adem BAKKALOĞLU<sup>3</sup>*

*In this study, the porous samples were manufactured through self-propagating high-temperature synthesis (SHS) by adding 10 % Co and Cr to 50 % Ni – 50 % Al powders. 10 % Co and Cr added 50 % Ni – 50 % Al samples were mixed for 12 hours using a mixer with a rotational speed of 300 rpm and compacted under 100 MPa pressure. The obtained samples were then synthesized by moving them to an argon atmosphere and combusted with the aid of a tungsten electrode. The obtained samples after the combustion reaction were characterized in terms of their microstructure using scanning electron microscope - the backscattered electrons (SEM-BSE). The elemental and phase analysis were carried out using EDS and XRD, respectively. The Energy-dispersive spectroscopy (EDS) results showed that the dominant element was Ni and the presence of Co with Cr was less than that of Al. As a result of XRD analyses, it was determined that NiAl was formed as the dominant phase in the samples and also Ni<sub>3</sub>Al and NiAl<sub>3</sub> phases were formed in low amounts. Both Cr and Co addition increased hardness of NiAl alloy. However, Cr has a greater effect on the increase of hardness values than Co.*

*Key words: SHS, NiAlCo, NiAlCr, Microstructure, Microhardness*

### 1. Introduction

Properties such as resistance to temperature, corrosion resistance at high temperatures and resistance to oxidation, which are among the desired properties in equipment operating at high temperatures are presence in the NiAl intermetallic material [1-3]. Therefore, its produce for mass production and put into use has an important place in industrial sense [4-6]. Reaction synthesis method, which is a low cost, easy to install and use method, which does not require external energy and thus does not cause environmental damage, has started to attract great attention in obtaining NiAl and Ni<sub>3</sub>Al intermetallic compounds [7-9].

Problems such as brittleness, improvement of mechanical properties, limiting the use of NiAl intermetallic alloy cover a significant part of the researches for the development of these materials. The most important of these problems is the brittleness of these materials and thus the restriction of

<sup>1</sup> Department of Metallurgical and Materials Engineering, University of Batman, Batman, Turkey, (ibrahim.biliz@batman.edu.tr)  <https://orcid.org/0000-0002-9090-4905>

<sup>2</sup> Department of Machinery and Manufacturing Engineering, University of Batman, Batman, Turkey, (musa.kilic@batman.edu.tr)  <https://orcid.org/0000-0002-5808-6917>

<sup>3</sup> Department Metallurgical and Materials Engineering, University of Yildiz Technical, İstanbul, Turkey, (ejt@ineseg.org)  <https://orcid.org/0000-0002-7148-2567>

forming [2]. In the researches, Cr, which is indicated to increase toughness and ductility, and Co, which is indicated to increase porosity and hardness, were investigated by adding to NiAl, and the hardness values of the produced samples were investigated [2,5,10, 11]. The aim of this study is to investigate the effect of Co and Cr element added to NiAl powder compound on microstructure and microhardness properties of NiAl. At the same time, microstructure image by SEM-BSE, elemental analysis by EDS and phase components were determined by XRD analysis.

## 2. Materials and Method

Ni, Al, Co and Cr metal powders used in alloy production were obtained from a commercial company. Information on these metal powders is given in Table 1.

**Table 1:** Properties of metal powders used in laboratory

Materials	Purity (%)	Powder Size (mesh)	Melting Temperature (°C)	Specific Weight (gr/cm <sup>3</sup> )
Aluminum	99,99	-325	660	2,700
Nickel	99,99	-325	1453	8,908
Cobalt	99,99	-325	1495	8,920
Chromium	99,99	-325	1875	7,190

In this study, every step of the laboratory studies was carried out in Argon atmosphere. In the glove box, a mixture of Ni and Al element powders prepared in the atomic ratios given in Table 2 and 10% Co and Cr powders were added. The prepared powder mixtures were mixed in the mixing mill at 300 rpm for 12 hours [12]. Table 2 shows the atomic and mass ratios and theoretical densities of Ni, Al, Co and Cr powder mixtures.

**Table 2:** Atomic and theoretical densities of powder mixtures

Mixture Number	Powder Mixture	Atomic Ratio	Weight Ratio	Theoretical Density
1	NiAl	%50Ni- %50Al	%76,74 Ni %23,26 Al	5,804 g/cm <sup>3</sup>
2	NiAlCo(10)	%45Ni - %45Al - %10Co	%65,56 Ni %19,88 Al %14,56 Co	6,11 g/cm <sup>3</sup>
3	NiAlCr(10)	%45Ni - %45Al - %10Cr	%67,45 Ni %20,45 Al %12,10 Cr	5,94 g/cm <sup>3</sup>

The powder mixtures obtained at the end of this process were compressed in a cylindrical mold by cold press with a pressure of 100 MPa. Pre-and post-ignition (raw and synthesized) pictures of compacted 10% alloy doped NiAl raw samples are given in Figure 1.

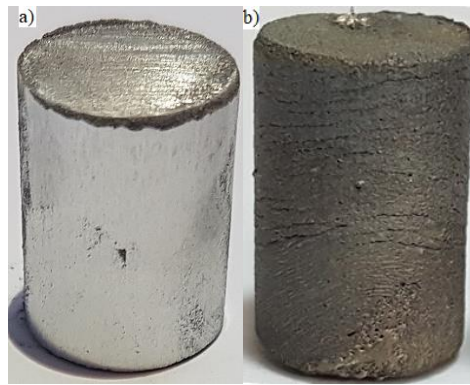


**Figure 1:** a) Raw sample b) Synthesized sample

The device for preheating and igniting the pressed samples in argon atmosphere was designed and produced. Ignition unit consists of preheating chamber, ignition center and chamber, temperature control knob and argon gas inlet-outlet sections. The scheme of the production by SHS method is given in Figure 2.

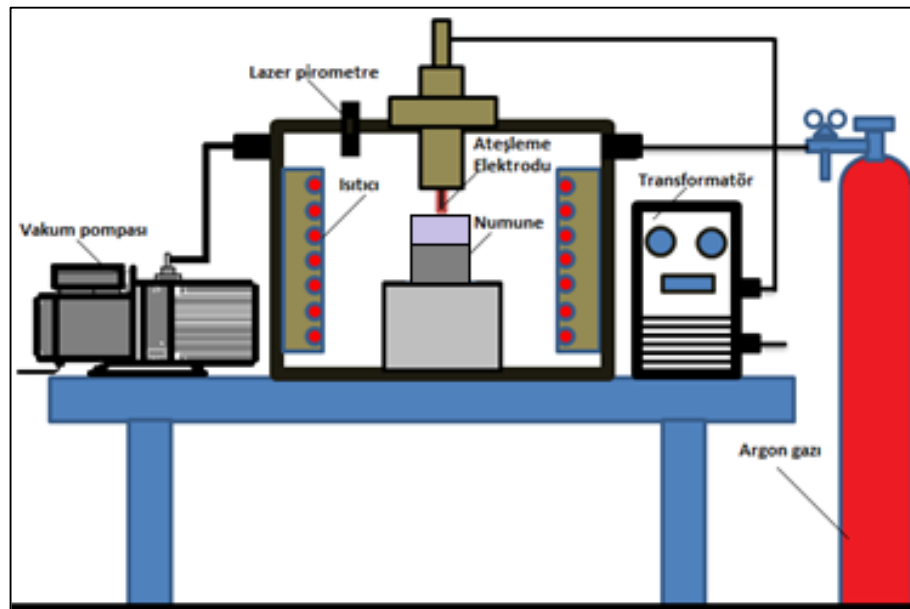


**Figure 2:** The scheme of ignition unit[13]

The external heat, which would allow the self-synthesis of the compacted samples, was given by ignition in the firing chamber under argon atmosphere. Samples were cut on the cutting disc for metallographic analysis after synthesis.

The cut samples were polished using 240, 400, 600, 800, 1000 and 1200 mesh sanders. After pre-polishing, the samples were polished with 1  $\mu\text{m}$  size diamond paste solution for final polishing. For the microstructure analysis of the polished samples, etch of 33 wt% HF, 33 wt% HNO<sub>3</sub>, 33% water solution was used. Leica brand optical microscope, Jeol brand SEM-BSE and EDS elemental analysis devices were used for microstructure analysis of samples after etching. The phase compositions were determined using Cu K $\alpha$  radiation and the sample in horizontal position ( $2\theta$  angles: 10 to 120 ° C) using Rigaku MiniFlex. Shimadzu brand microhardness tester with 20 g (HV<sub>0.02</sub>) loading was used to obtain microhardness values.

### 3. Results and Discussion

In this study, samples were obtained by adding Co and Cr to NiAl powder mixture. Microstructures and microhardness values of these samples were determined. In this method, which is similar to powder metallurgy production methods, porosity decreases as a result of increasing contact of powder particles with pressing [14]. It is thought that the rapid synthesis reaction may increase the pore ratio since there is no time for shrinkage of the samples. In addition, addition of Co and Cr alloy elements changed the porosity rates. As a result of the calculations, the porosity ratio of unalloyed NiAl was determined as 27.17%. However, the NiAl intermetallic material with 10% Co added was 28.25% due to the effect of Co element. However, the addition of 10% Cr reduced this porosity by 9.83% and was found to be 25%. It is found that Co and Cr additive increases microhardness values at different rates.[12] The addition of Co and Cr triggers the formation of NiAl<sub>3</sub> and Ni<sub>3</sub>Al phases. Formation of NiAl<sub>3</sub> and Ni<sub>3</sub>Al changes hardness because the hardest point of Ni<sub>3</sub>Al is almost 500 HV and NiAl<sub>3</sub> harder than Ni<sub>3</sub>Al about 200 HV.

The lowest point of hardness of NiAl as a function of stoichiometry is when Ni/Al is 1 and it is 330 HV [12].The Cr additive reduced the porosity relatively, and the Co additive was found to increase the pore ratio further. These data and the data in the literature support each other. [11,15-19]. Microhardness measurements taken from Cr and Co reinforced samples are given in Figure 3. According to the hardness measurement results, the highest hardness value obtained in the Cr alloyed samples as 578 HV and 523 HV for Co alloyed samples while hardness of NiAl is between 279-339 HV according to studies.[12]The mean hardness of Cr alloyed samples was 77.6 HV harder than the mean hardness of Co alloyed samples. In addition, the value range of the measurements taken in Cr reinforced samples has a narrower range than Co reinforced samples. The reason for this is thought to be that the phases in the structure of Cr reinforced samples are less and the number of phases in Co reinforced samples is higher. In addition, the porosity of the material is one of the factors affecting this situation.

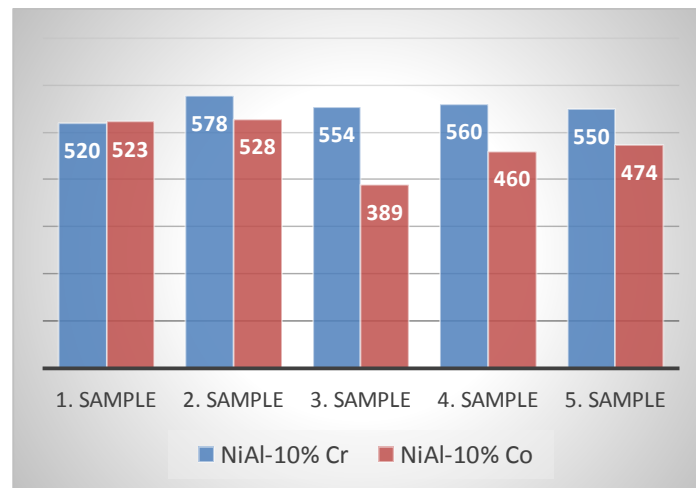


**Figure 3:** Co and Cr reinforced NiAl intermetallic compounds microhardness values

SEM, BSE and optical microscope images and XRD, EDS graphs of Cr and Co reinforced NiAl alloys are given in Figure 4 and Figure 5. The porous structure of the produced materials can be seen in SEM and optical microscope views. The composition ratios of the samples in the EDS results confirm the alloying element ratios in the produced samples.

In the XRD analysis, NiAl and Ni<sub>3</sub>Al phases and low NiAl<sub>3</sub> phases were detected in Cr alloyed NiAl sample. On the other hand, more NiAl phase and low Ni<sub>3</sub>Al and NiAl<sub>3</sub> phases were detected in the Co alloyed NiAl sample

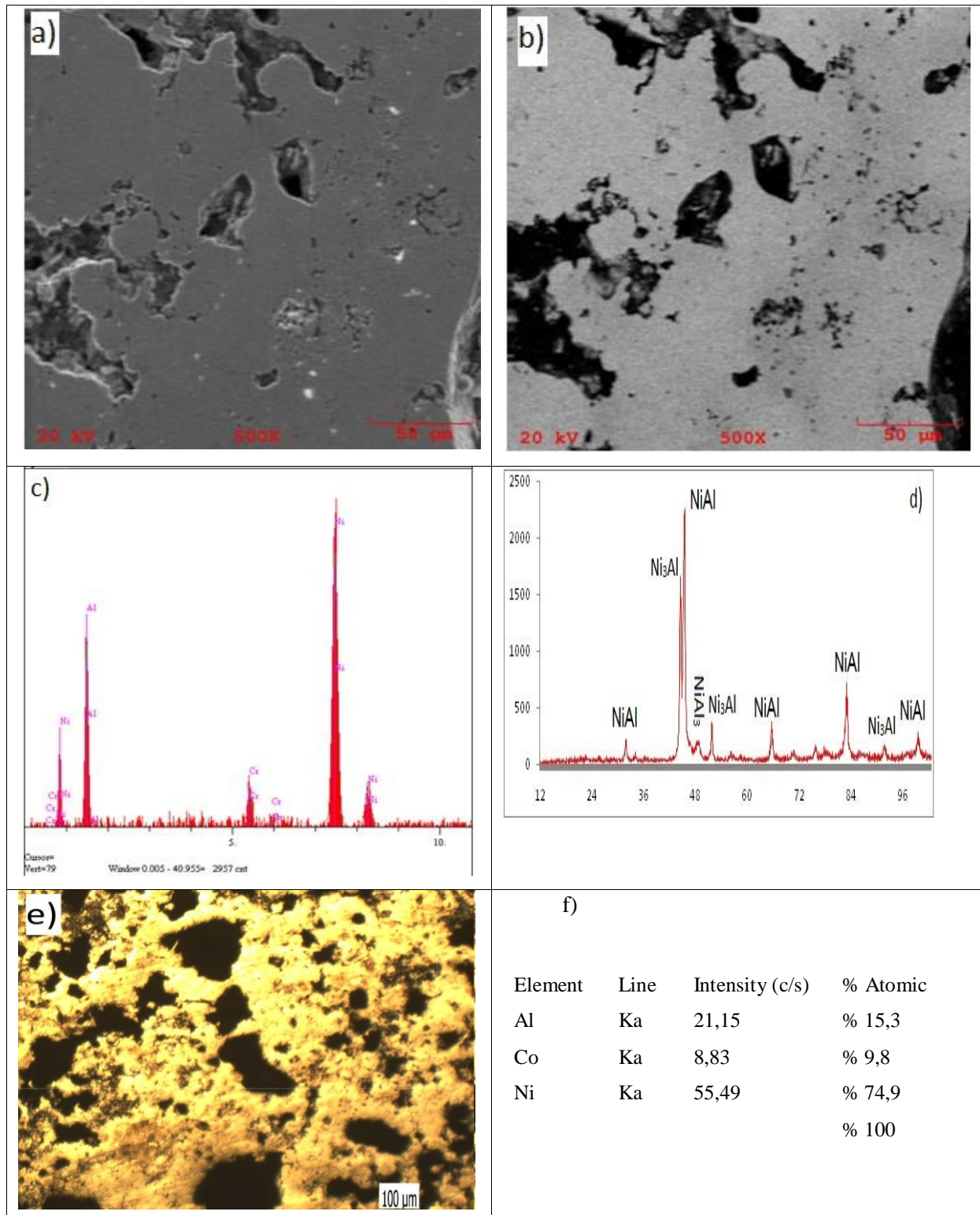


Figure 4: a) SEM, b) BSE, c) EDS graph, d) XRD, e) optical microscope image, f) EDS composition ratios of the Cr reinforced NiAl alloys

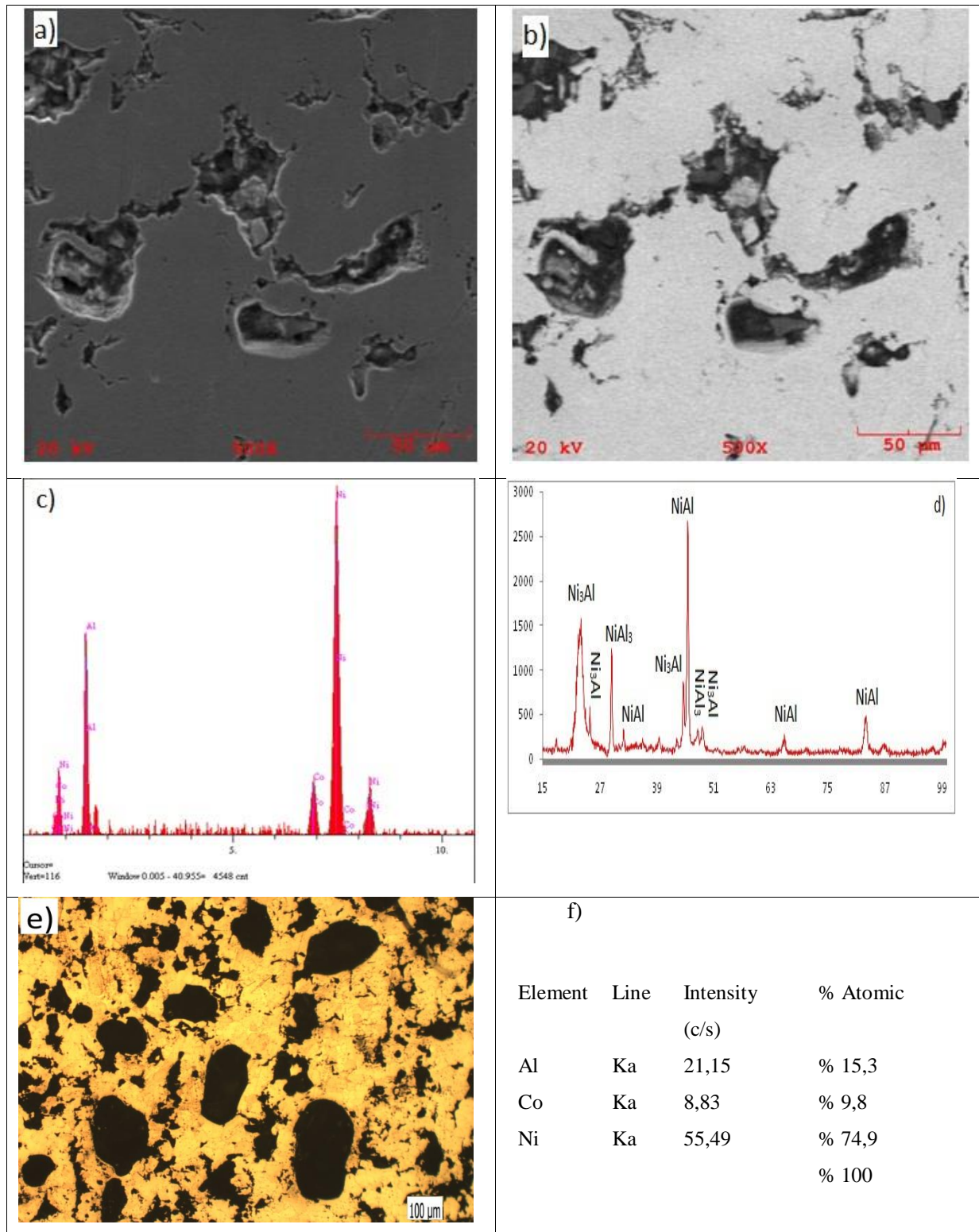


Figure 5: a) SEM, b) BSE, c) EDS graph, d) XRD, e) optical microscope image, f) EDS composition ratios of the Co reinforced NiAl alloys

#### 4. Conclusions

In this study, by using SHS method, 50% Ni-50% Al powders were reinforced with 10% Co and 10% Cr and sample production was carried out and microstructure and microhardness analysis of samples were performed. According to the data obtained;

- It was found that Co and Cr additive increases the microhardness values of NiAl at different rates. The highest hardness of Cr alloy specimens was 578 HV, while Co alloy specimens had 523 HV. The mean hardness of Cr alloy samples was 77.6 HV harder than the mean hardness of Co alloyed samples.
- Based on the optical microscope and SEM-BSE images, the samples produced were found to have high porosity. This porosity is thought to be an important factor in microhardness results.
- The most common NiAl and Ni<sub>3</sub>Al phases and low NiAl<sub>3</sub> phases were determined in the Cr alloyed NiAl sample. Co alloyed NiAl sample has more NiAl phase and low Ni<sub>3</sub>Al and NiAl<sub>3</sub> phases.

### Acknowledgements

This study was supported by YTU BAP Coordination Unit as project FYL-2018-3354. We would like to thank YTU BAP Coordinator for their support.

### References

- [1] Li, Y., Liu, Y., Geng, H., Nie, D. (2006). Synthesis and cladding of Ni<sub>3</sub>Al intermetallic on steel substrate by laser controlled reactive synthesis, *Journal of Materials Processing Technology* 171 405–410.
- [2] Wang, Y., Chen, W. (2004). Microstructures, properties and high-temperature carburization resistances of HVOF thermal sprayed NiAl intermetallic-based alloy coatings, *Surface and Coatings Technology* 183 18–28.
- [3] Brammer, M. (2011). Improving the phase stability and oxidation resistance of  $\beta$ -NiAl, MSc Thesis, Iowa State University, Ames, Iowa.
- [4] Morsi, K. (2001). Review: reaction synthesis processing of Ni–Al intermetallic materials. *Materials Science and Engineering A299* 1–15.
- [5] Dey G. K. (2003). Physical metallurgy of nickel aluminides. *Sadhana* 28(1 & 2), 247–262
- [6] La, P., Bai, M., Xue, Q., Liu, W. (1999). A study of Ni<sub>3</sub>Al coating on carbon steel surface via the SHS castin groute, *Surface and Coatings Technology* 113 44–51.
- [7] Kaya M., Buğutekin A., Orhan N. (2010) The effect of porosity on thermal conductivity of the porous NiTi SMA fabricated by SHS. *Journal Of Optoelectronics And Advanced Materials*. 12(8), 1250 – 1255.
- [8] Kovalev A.I., Barskaya R.A., Wainstein D.L. (2003). Effect of alloying on electronic structure, strength and ductility characteristics of nickel aluminide. *Surface Science*, 532, 35–40
- [9] Bochenek K., Basista M. (2015). Advances in processing of NiAl intermetallic alloys and composites for high temperature aerospace applications. 79, 136-146

- [10] Kılıç, M. (2015). Kendi ilerleyen yüksek sıcaklık sentezi ile fonksiyonel derecelendirilmiş intermetalik malzemelerin üretimi ve mikroyapılarının incelenmesi, Batman Üniversitesi Yaşam Bilimleri Dergisi; 5(2) 87-98.
- [11] Ulu, R. 2013. Alaşım elementlerinin nial alaşımlarının mikroyapı ve mekanik özelliklerine etkisi. Yüksek Lisans Tezi, Karabük Üniversitesi Fen Bilimleri Enstitüsü, Karabük.
- [12] Kılıç, M. (2014). NiTi ve Ni3Al fonksiyonel derecelendirilmiş malzemesinin reaksiyon sentezlemesi yöntemiyle üretilmesinin araştırılması. Doktora Tezi. Fırat Üniversitesi Fen Bilimleri Enstitüsü, Elazığ
- [13] Kılıç, M., Bekten, M., Özdemir, N. (2019). SHS işlemi sonrası sinterleme işleminin intermetalik kaplamaya etkisinin incelenmesi, Fırat Üniversitesi Müh. Bil. Dergisi 31(1), 167-176.
- [14] Tosun G., Özler L., Kaya M., Orhan N. (2008). SHS yöntemi ile üretilen niti alaşımlarının gözenek oranının incelenmesi. 5th IPMC. Ankara
- [15] Chen, L., Han, Y., (2002) . The microstructure and compressive properties in NiAl(Co) alloys by HPXD technique”, Materials Science and Engineering A329–331. 725–728.
- [16] Kiyotakai, M., Khan T. İ., Ohmi T., Kudoh, M. (2001), Reactive casting of B2 Ni-Al-Co ternary intermetallic alloys, Materials Transactions. 42(2), 263 – 268.
- [17] Cotton J.D. 1991. The influence of chromium on structure and mechanical properties of b2 nickel aluminide alloys. PhD Thesis ,University of Florida.
- [18] Cao, Y., Zhu, P., Zhu, J., Liu, Y. (2016).First-principles study of NiAl alloyed with Co, Computational Materials Science. 111 34–40
- [19] Ozdemir O., Zeytin S., Bindal C. (2010). Characterization of NiAl with cobalt produced by combustion synthesis. Journal of Alloys and Compounds. 508, 216-221.

## EVENT DATA VISUALIZATION THROUGH PROCESS MINING: A CASE FOR EMERGENCY MEDICAL SERVICE SYSTEM IN ADANA

Nuşin UNCU<sup>1</sup>

*Increasing amount of data enables researchers the opportunity of applying new scientific methods to manage and visualize the systems and processes. Process mining is an emerging tool for discovering real processes using event data of complex systems such as communication, information, health care systems, transportation and etc. Emergency Medical Service (EMS) system is an integral part of health care systems and aims to respond cases on time in order to decrease mortality. Although the EMS system process is assumed to be known, related data may indicate some deviations from the real process. Aim of this study is to discover and visualize EMS system in Adana city, in Turkey. EMS system event logs are filtered and visualized by using plug-ins in ProM platform such as Simple Heuristic Filtering plug-in and Log visualizer, respectively. Other plug-ins such as Fuzzy Miner and Inductive Miner are used for discovering process model. The deviations are obtained in EMS system process model showing irregular or rare events that cannot be representable throughout the process. The results indicate that the process of transportation between hospitals should be investigated in order to improve the process of Adana EMS system.*

*Key words: Process mining, Petri nets, Fuzzy miner, Inductive miner, Event logs*

### 1. Introduction

Emergency Medical Service (EMS) system is an integral part of health care systems. EMS system can be classified as Anglo-American “Scoop and Run” and Franco-German “Stay and Play”. While the first one is a paramedic-based system, the latter is physician based system. The key difference between these two systems is that the health staff and equipment are brought to the case in Franco-German systems, while the case is brought to the health center in Anglo-American systems. A more detailed discussion of these two systems can be found in [1]. In Turkey, EMS system works based on Franco-German discipline. For all the types of EMS system, to respond at least required percentage of cases in a predefined time interval is the key performance criterion in order to decrease the mortality.

The process of EMS system starts with receiving an emergency call to a call center where there is a standard call evaluation process to dispatch the available emergency unit to the location within an acceptable time. The nearest and available ambulance is dispatched to the scene including paramedics who perform the first aid. Then the patient is transported to the nearest appropriate hospital and the

---

<sup>1</sup> Department of Industrial Engineering, Adana Alparslan Türkeş Science and Technology University, Adana, Turkey, (nuncu@atu.edu.tr)  <https://orcid.org/0000-0003-3030-3363>

process ends after the ambulance turns back to its destination station. The entire process of EMS systems is illustrated in Figure 1.

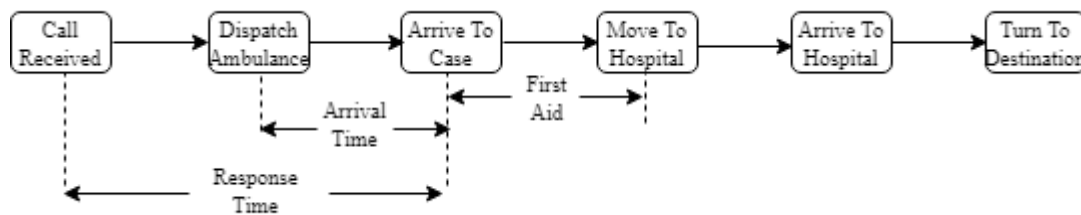


Figure 1. EMS system process chart

Although the EMS system process is assumed to be known, the data may indicate some deviations from the real process. The real process can be discovered from this data by process mining techniques due that the process may be the one that is not what exactly known. Increasing amount of data enables researchers to reach the unknown parts of processes in complex real systems. The idea behind the process mining is to capture real processes and actions from event data. The approach is not just data-centric but also event data-centric. The main steps of process mining are discovering model, conformance checking and enhancement [2]. Discovering model means to explore process model from event logs. However, not all the recorded data are always ready for discovering model phase and data preprocessing in process mining is a time consuming issue. This phase enables to get more accurate data and transfer data in a compatible format while applying process mining techniques.

Main phase in process mining is discovering process model from data. Alpha algorithm is one of the model discovery tools used to explore the causality from a set of event logs [3]. However, alpha algorithm has some limitations while dealing with short loops. In order to tackle with this problem several extensions of alpha algorithm was improved as well other process discovery algorithms such as heuristic miner [4], genetic process mining [5], region based mining [6], inductive miner [7] and interactive process miner [8]. Inductive mining algorithm is one of the Divide-and-Conquer approach aims to split the event log that is difficult to be decomposed by other mining methods. Inductive mining is one of the leading approaches due to its flexibility, formal guarantees and scalability [2].

Process mining tools have been used recently to discover process models from real event data. Process models are useful representations of systems. Transition systems, Petri Nets, WF-Nets (Workflow Nets), BPMN (Business Process Modelling Notation), C-Nets (Causal Nets), EPCs (Event-driven Process Chains), YAWL (Yet Another Workflow Language) and process trees are different ways of generating process models. Among these, Petri Nets are simple and intuitive graphical notation to be executable and applicable to many systems [2]. The early application of Petri Nets in EMS system is found in Xiong et al. [9]. Petri Nets are useful for modelling nondeterministic and complex systems. The main problem handled by researchers is to increase the performance of the system after investigating the actual situation based on the effectiveness and resource utilization.

The applications of process mining tools and methodologies in health care systems are deeply explained in Mans et al. [10]. The survey on case studies can be found in Rojas et al. [11]. A number of related applications of mining techniques are exist in [12-16].

The main idea that emerges in the context of process mining is to investigate a general process model that can represent all possible flows with reasonable level of fitness, precision, generalization and simplicity. An overview of challenges of process mining can be found in [17].

In this study, although the EMS process flow is almost known, deviations from the model and the mostly or rarely occurring traces are aimed to be investigated. The study is constructed in four sections. After an introduction section with a brief literature review, EMS system in Adana is explained in the second section. Filtering, visualizing and mining methods are applied for the case of Adana EMS system in the third section. Finally, the results are concluded in the last section of the paper.

## 2. Materials and Methods

### 2.1. Adana EMS System

Adana is one of the most populated cities in Turkey, located in the south of the country with an area of 14030 km<sup>2</sup>. The population is nearly 2.5 million people in the urban and rural area.

Adana EMS system has 33 stations in the center of the city and 14 stations located in rural areas as well mobilized stations including nearly 40 active ambulances. The call center receives in average 600 emergency calls per day. In 2016, the total number of calls received from all over the region was 187248. The cases are considered under two different types; emergency and transport calls.

The current ambulances and hospitals located in Adana is demonstrated in Figure 2. Due to the large scale of the city map, the locations are approximately chosen according to their destination points representing all the locations over the city.

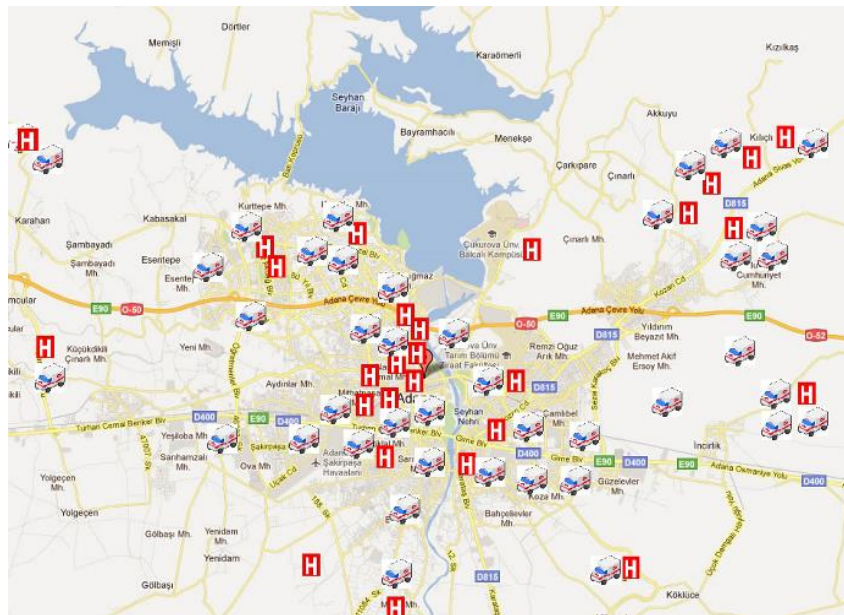


Figure 2. Location of ambulance stations and hospitals over the city of Adana

### 2.2. Visualization of EMS System Data

#### 2.2.1 EMS System Data Preprocessing

EMS system data include 187248 cases. XESame is established by Buijs [18] and enables converting data to .xes file format to be compatible in process mining software, ProM. In order to implement ProM plug-ins, .xls file is edited and necessary arrangements are done before converting it to a .csv file. The .csv file is used in XESame for generating .xes file that is the compatible file format to be used in ProM. Furthermore, EMS system data is revised due to time zone problems. Thus, the date

of the year is changed to 2012. However, we do not expect any lack of accuracy. A sample of event log is shown in Table 1.

**Table 1. A sample of EMS system event logs**

Case ID	Event ID	Properties		
		Activity	Timestamp	Resource
2016-1	201611	CallReceived	01.01.2016 00:02:03	----
	201612	Prepareness	01.01.2016 00:03:00	----
	201613	Move	01.01.2016 00:04:00	7150
	201614	ArriveToScene	01.01.2016 00:06:00	7150
	201615	Getcase	01.01.2016 00:06:00	7150
	201616	DepartfromScene	01.01.2016 00:33:00	7150
2016-2	201621	CallReceived	01.01.2016 00:04:14	
2016-3	201631	CallReceived	01.01.2016 00:12:19	----
	201632	Prepareness	01.01.2016 00:13:00	7190
	201633	Move	01.01.2016 00:14:00	7190
	201634	ArriveToHosp1	01.01.2016 00:20:00	7190
.....	.....	.....	.....	.....

### 2.2.2 Filtering Event Logs

187248 cases are recorded including 1667573 events before filtering. ProM enables the user to filter data from unwanted confusions and discover process model from event logs precisely. Due to the inconsistent and missing data, the EMS system event log is filtered by Simple Heuristic Filter plug-in. The traces are filtered as follows;

*CallReceived* > starting event

*Prepareness & TurnToStation* > ending events

All other events are included in filtering phase. 149875 cases and 1332445 events remained after filtering phase. Almost 20 percent of data is observed unreliable or not recorded precisely. The number of minimum events per case and maximum events per case is given in Table 2. The number representing each activity is demonstrated in Table 3.

**Table 2. EMS system process event logs key data**

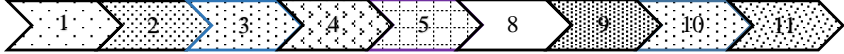
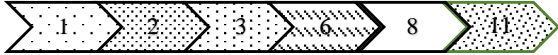
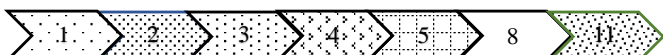
Key Data	Quantity
Process	1
Cases	149875
Events	1332445
Minimum number of events per case	4
Maximum number of events per case	9

**Table 3. Activity names and their representative numbers**

Activity Name	Number	Activity Name	Number
CallReceived	1	ArriveToHosp1	6
Prepareness	2	ArriveToHosp2	7
Move	3	DepartfromScene	8
ArriveToScene	4	FinalHospital	9
Getcase	5	DepartFinalHospital	10
		TurnToStation	11

Seven trace patterns put in order in respect of their percentage of occurrences over all the patterns are demonstrated in Table 4. The first trace representing 89 percent of cases has the pattern of *CallReceived- Preparedness- Move- ArriveToScene- GetCase- DepartfromScene – FinalHosp – DepartFinalHospital – TurnToStation*. This pattern illustrates the emergency cases. The trace with the minimum number of events shows the pattern *CallReceived- Preparedness- Move- TurnToStation* representing the cases that are cancelled after ambulance is allocated to that case. These two patterns may occur if the patient is brought to the hospital by its relatives or the patient do not need any aid anyway or other miscellaneous reasons. The last trace is also similar to this case, however the ambulance arrives the scene and then for some reason turns to station. The trace that is 11 percent of cases stands for transportation of patients to a final hospital while 0.17 percent of cases transportation to patients' home. The fourth trace representing 0.07 percent of cases point out that two of the hospitals does not accepted the patient, so the ambulance visits three hospitals for these cases. Finally, the fifth trace stands for the cases that the patient get well after first aid in the scene.

**Table 4.** EMS system traces after filtering and clearing inaccurate traces

	Trace Patterns	Occurrence	Rate (%)
1		133874	89,32
2		15631	10,4
3		251	0,17
4		98	0,07
5		19	0,01
6		1	0,00
7		1	0,00

### 2.2.3 EMS System Process Model

Inductive Miner plug-in is used to obtain EMS system process model that is given in Figure 3. In the process model, the events flow in the direction of arrows and numbers in the boxes demonstrate the number of occurrence for the corresponding event. In the model, it is seen that while a few number of cases follow the transportation, a great number of cases follow the emergency flow as expected. The arrow above the *ArriveToHosp2* shows the number of cases that are executed from the preceding event but not executed from *ArriveToHosp2*. This model supports the patterns given in Table 4.



In the process model, the paths that have deviations are demonstrated in Figure 4. The numbers on the blue arrows show the cases that are executed from the corresponding event. The red dashed lines show the move-on model that represent the events in the event log but cannot be represented by the process model. A great amount of move-on model occurs for *FinalHospital* and *DepartFinalHospital*. It is obviously seen that EMS system process model in Figure 3 fits all the possible trace patterns in Table 4 while considering the move-on model in Figure 4.

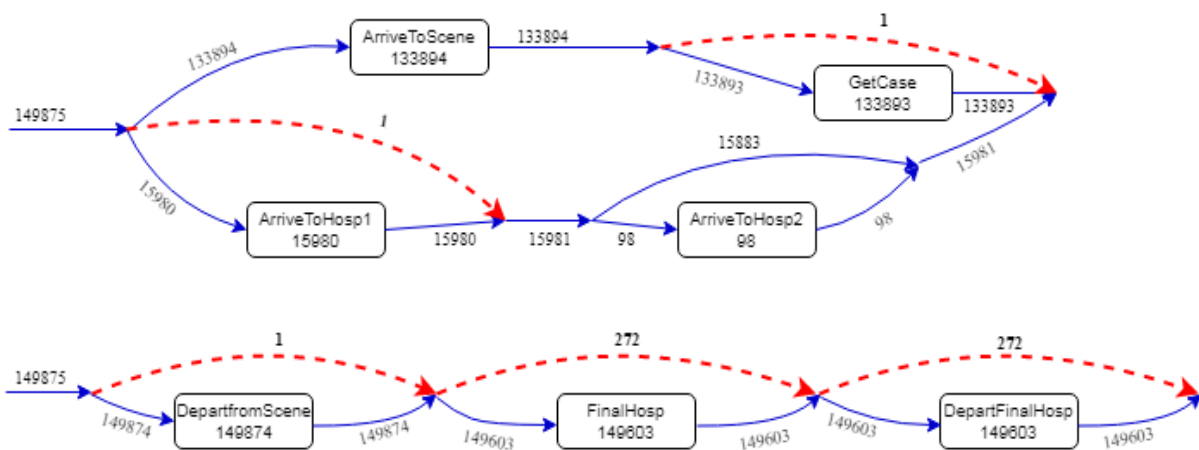


Figure 4. EMS system process model paths and deviations

#### 2.2.4 EMS System Fuzzy Model

Another visualization of EMS system process given in Figure 5 is obtained by using Fuzzy Miner plug-in. In fuzzy model, thickness of the arrows shows the frequency of the corresponding event. The events *ArriveToHosp1* and *ArriveToHosp2* stand for transportation and have less frequency than the emergency cases. The values inside the activity boxes show the occurrence rate of the corresponding event over all the cases. *CallReceived* and *TurnToStation* seem to be main events that exist in almost for all the cases.

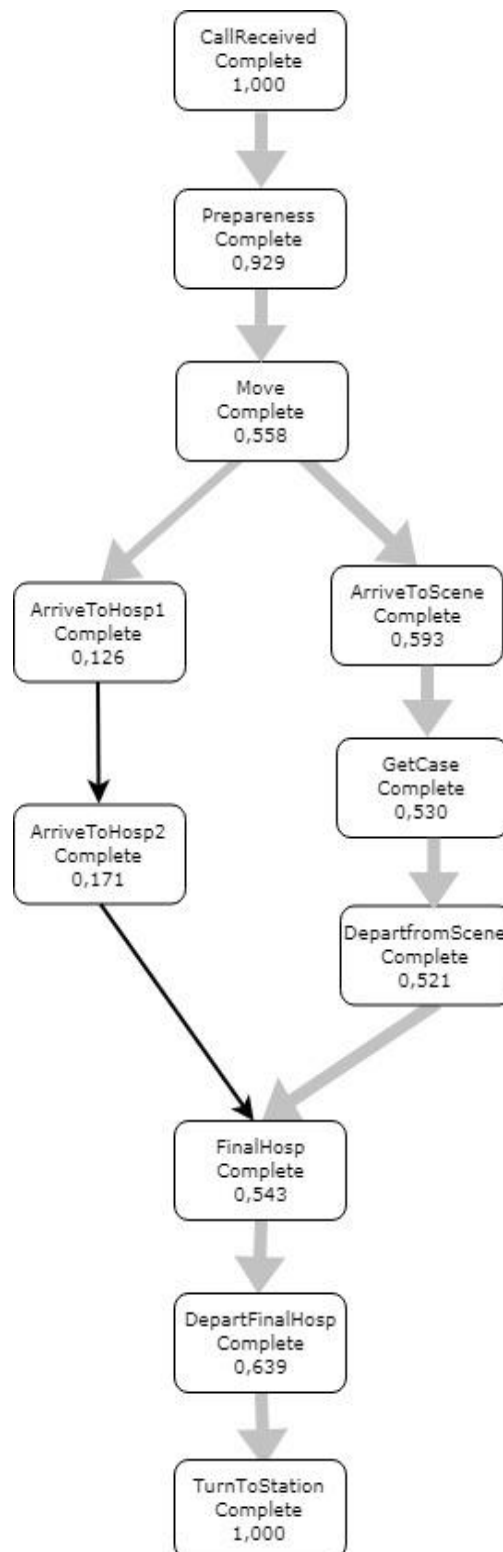


Figure 5. EMS system fuzzy model

### 3. Discussion

EMS system has many unreliable and inaccurate data due to the personnel who are responsible to record the cases and their timestamps. Despite of the fact that preprocessing face enables us to get more reliable and accurate data, it takes too much time to convert data in a compatible file format for process

mining. Thus, the process mining methods are more convenient for the systems such as software, manufacturing in industry 4.0, communication etc. where data are recorded automatically, not manually.

#### 4. Conclusion

Discovering the real process model is necessary task to find the systems bottlenecks in a precise way and enables to enhance the system. Although the general flow of EMS system process is known, a process model that represents many types of different process flows is a good way of understanding the whole system in detail.

In this study, Adana EMS system data is used to demonstrate how to apply process mining techniques and tools while discovering process model and finding the variations in actual EMS system process based on the process model. The ProM Open software and the plug-ins which include process mining algorithms such as inductive miner, fuzzy miner, and heuristics for filtering are used in this application.

The results are useful to see the variations and the mostly or rarely occurring events and patterns. Two main patterns have the highest percentage of occurrences in seven different patterns. The emergency cases and the transportation between hospitals with 89 and 11 percent of total cases, respectively. Moreover, 7 percent of cases are important to be considered by EMS system managers. These cases transport patients from scene to a hospital, but based on the explanations of managers on this subject, the patient for some reason is not accepted by the first hospital and the ambulance must move to another hospital for these type of cases. It should be investigated whether these traces result in mortality because of the delay in transportation between hospitals.

For further studies, the reasons of unexpected trace patterns and deviations can be investigated in detail and the performance of the EMS system on timely basis may be analyzed, so the system performance can be enhanced.

#### Acknowledgment

This study is a part of research granted by The Scientific and Technical Research Council of Turkey (TUBITAK) International Post-Doctoral Research Fellowship Program in the framework of TUBITAK-BIDEB 2219. Thanks to Data Science Centre in Eindhoven University of Technology for their support and hospitality and also Adana Provincial Directorate of Health Center for providing data.

#### References

- [1] Dick, W.F., (2003). Anglo-American vs. Franco-German emergency medical services system. *Prehosp. Disaster Med.*, 18 (1), 29-35.
- [2] Van der Aalst, W.M.P., *Process mining: data science in action*. Springer, Verlag Berlin Heidelberg, 2016.
- [3] Van der Aalst, W.M.P., Weijters ,A.J.M.M., Maruster, L., (2004). Workflow mining: discovering process models from event logs. *IEEE Transactions on Knowledge and Data Engineering*, 16 (9), 1128–1142.
- [4] Weijters, A.J.M.M., Van der Aalst, W.M.P., De Medeiros, A.K.A., (2006).Process mining with the heuristics miner-algorithm. *Technische Universiteit Eindhoven Technical Report WP* , 166, 1-34.

- [5] De Medeiros, A.K.A., Weijters, A.J.M., Van der Aalst, W.P.M., (2005). Genetic process mining: a basic approach and its challenges. *BPM 2005 International Workshops*; Germany: Springer, 203-215.
- [6] Van der Aalst, W.M.P., Rubin ,V., Verbeek, H.M.W., Van Dongen, B.F., Kindler, E., Günther, C.W., (2010). Process mining: a two-step approach to balance between underfitting and overfitting. *Software and Systems Modeling*, 9(1), 87–111.
- [7] Leemans, S.J.J., Fahland, D., Van der Aalst, W.M.P., (2013). Discovering block-structured process models from event logs: A constructive approach. In *Applications and Theory of Petri Nets*, Lecture Notes in Computer Science, Springer, Berlin, 7927, 311-329.
- [8] Yurek, I., Birant, D., Birant, K.U., (2018). Interactive process miner: a new approach for process mining. *Turkish Journal of Electrical Engineering & Computer Sciences*; 26, 1314-1328.
- [9] Mans, R., Schonenberg, H., Leonardi, G., Panzarasa, S., Cavallini, A., Quaglini, S., Van der Aalst, W.M.P.,(2008). Process mining techniques: an application to stroke care. *Studies in Health Technology and Informatics*, 136, 573–578.
- [10] Xiong, H.H., Zhou, M.C., Manikopoulos, C.N., (1994). Modeling and performance analysis of medical services systems using petri nets. In: *IEEE Int. Conf. on Systems, Man and Cybernetic*, 2339-2342.
- [11] Rojas, E., Munoz-Gama, J., Sepulveda, M., Capurro, D., (2016). Process mining in healthcare: a literature review. *Journal of Biomedical Informatics*, 61, 224-236.
- [12] Mans, R.S., Schonenberg, M.H., Song, M., Van der Aalst, W.M.P., Bakker, P.J.M.,(2008) Application of process mining in healthcare – a case study in a Dutch hospital. *International Joint Conference on Biomedical Engineering Systems and Technologies*, 425-438.
- [13] Baker, K., Dunwoodie, E., Jones, R.G., Newsham, A., Johnson, O., Price, C.P., Wolstenholme, J., Leal, J., McGinley, P., Twelves, C., Hall, G., (2019). Process mining routinely collected electronic health records to define real-life clinical pathways during chemotherapy. *International Journal of Medical Informatics*, 103, 32–41.
- [14] Alvarez, C., Rojas, E., Arias, M., Munoz-Gama, J., Sepulveda, M., Herskovic, V., Capurro, D., (2018). Discovering role interaction models in the emergency room using process mining. *Journal of Biomedical Informatics*, 78, 60-77.
- [15] Yooa, S., Cho, M., Kima, E., Kima, S., Simb, Y., Yooc, D., Hwanga, H., Song, M., (2016). Assessment of hospital processes using a process mining technique: Outpatient process analysis at a tertiary hospital. *International Journal of Medical Informatics*, 88, 34-43.
- [16] Yongzhong, C., Zhu, J., Guo, Y., Shi, C., (2018). Process mining-based medical program evolution. *Computers and Electrical Engineering*, 68, 204-214.
- [17] Van der Aalst, W.M.P., (2012). Process mining: overview and opportunities. *ACM Transactions on Management Information Systems*, 3, 1-17.
- [18] Buijs, J.C.A.M, Mapping Data Sources to XES in a Generic Way. Ph D. Thesis , Eindhoven University of Technology, Netherlands, 2010.

## USE OF NANO HEXAGONAL BOR NITRIDE (HBN) ADDED CUTTING FLUID IN MILLING OF HARD TO CUT MATERIALS

*Bilal KURŞUNCU<sup>1</sup>*

*In machining processes, MQL method is substantially preferred in terms of sustainable production because of lower usage of cutting fluid and better cutting performance in comparison with traditional techniques. On the other hand, it is also critical that the cutting fluid used is not hazardous to human and environmental health. In the present study, we aimed to investigate the cutting performance of AISI O2 steel in the presence of the cutting fluid containing various amounts of environmentally friendly Nano hexagonal boron nitride (Nano h-BN) based ethylene glycol (EG) by minimum quantity lubrication (MQL) method. Nano h-BN at 1% and 2% percentage by volume was added to the ethylene glycol and sonication was carried out for one hour for both prepared cutting fluids. Based on the experimental results using prepared cutting fluids, the highest cutting tool life was obtained in tests using 2% h-BN containing cutting fluid with 2.4 m cutting length. The improvement in tool life was approximately 46% using 2% h-BN containing cutting fluid compared to using 1% h-BN containing cutting fluid in milling tests. 2% h-BN containing cutting fluid compared to dry conditions in terms of tool life, the increase was approximately 78%. The improvement in surface roughness value measured on milled surface of workpiece material was approximately 60% using 2% h-BN containing cutting fluid compared to dry conditions. Compared to using 1% h-BN containing cutting fluid the improvement in surface roughness values was approximately 46%. A reduction in the cutting forces measured by the increased h-BN ratio in the prepared ethylene glycol based cutting fluid has occurred. As a result of SEM images and EDS analysis of worn tools, it was observed that the dominant wear mechanism was abrasion in all applied tests.*

*Key words: Minimum quantity lubrication, hardmilling, hBN, 2D structure, AISI O2, tool wear, cutting performance*

### 1. Introduction

The machinability feature of a material is evaluated in terms of tool life, cutting force and surface roughness [1]. In addition, the characteristic of the cutting fluid significantly influences the cutting performance as it removes the heat generated in the cutting zone [2]. Especially at high cutting speeds, the failure of the cutting fluid to penetrate between the workpiece and the tool causes the heat not to be removed effectively

<sup>1</sup> Department of Mechanical Engineering, Bartın University, Bartın, Türkiye, (bilalkursuncu@gmail.com)  <https://orcid.org/0000-0002-2304-2962>

during the process [3]–[7]. Furthermore, the cost of the cutting fluid corresponds to about 5% of the total process cost in some applications and the safe disposal of these fluids is a very important issue [8], [9]. Therefore, in recent years, researchers have been focused on alternative methods such as minimum lubrication technique (MQL) to both reduce the amount of the cutting fluid used and to improve cutting performance [10], [11].

MQL method can be defined as the process of spraying the liquid at a certain pressure and speed into the cutting zone in the literature [12]. MQL method is intensively preferred in cutting processes as it is low cost and sensitive to human and environmental health [13], [14]. Compared to conventional and dry machining, it provides significant contributions to tool life, cutting forces and surface roughness due to reducing heat between tool and workpiece [15]. In the MQL method, it is known that the addition of inorganic additives such as h-BN, MoS<sub>2</sub> and graphite to the cutting fluid improves the cutting performance. Among these additives hexagonal boron nitride (h-BN), has a lamella structure where boron and nitrogen atoms are linked by covalent bonds. In addition, due to the easy separation of the basal plane, h-BN has lubricating properties. h-BN, similar to graphene in terms of physical and chemical properties; it is preferred as an alternative to other solid lubricants due to its inert, environmentally friendly and high temperature endurance [12] [13][18][19][20][21].

In spite of numerous researches on the cutting performance of AISI O2 [22][23][24], the number of studies is limited related to the machinability of AISI O2 using MQL method. Moreover, no literature was existing on used the cutting fluid containing nano h-BN as lubricant by MQL method. On that sense, the study is thought to fill the deficiency of literature due to innovative approach. This research will reveal the cutting performance of AISI O2 steel in terms of tool lifetime, tool wear, cutting force and surface roughness in the presence of the cutting fluid containing different nano h-BN concentration by MQL method.

## 2. Material and Method

### 2.1. Preparation of cutting fluids

Analytical grade nano h-BN as additive was provided from the Bortek company in Eskişehir/Turkey. The ethylene glycol (C<sub>2</sub>H<sub>6</sub>O<sub>2</sub>) used as the base fluid in the experiments was obtained from a commercial company. First, nano h-BN was added to the ethylene glycol solution to prepare solutions of 1% and 2% with a total volume of 800 ml. Then, the obtained suspension was sonicated for 1 h to ensure homogeneity of the solution.

### 2.2. Materials and Methods

AISI O2 cold work tool steel was used in milling tests which has a high dimensional stability in heat treatment, cracking resistance and abrasion resistance [25]. It is widely used in the manufacture of different materials in industry such as dies and molds production. The chemical composition of workpiece material shown in Tab. 1.

**Table 1. Chemical composition of AISI O2 cold work steel (wt. %) [23]**

C	Si	Mn	P	S	Cr	V
0.88	0.29	2.07	0.024	0.09	0.26	0.08

### 2.3. Machine Tool, Cutting Tools, MQL System, Cutting Tests

Sintered carbide cutting tools with R390-11 T3 08M-KM H13A coded from Sandvick were used in milling operations. Sandvick R390-025A25-11L coded with a diameter of 25 mm was selected as tool holder. Although there are two places where the cutting tools can be attached on the tool holder, experiments were performed with a single cutting tool. The devices used in milling tests can be summarized as follows (Fig. 1);

- All milling tests were performed on Falco VMC 855-B CNC 3-axis CNC machining center.
- Werte Micro STN 25 was used as MQL system.
- In order to measure the amount of wear occurring on the flank surface of the cutting tool during milling tests, Vision SX45 stereo zoom microscope was used. A computer software was used to measure the amount of wear on the flank face of cutting tool.
- Mitutoyo SurfTest SJ 310 was used to measure the roughness values on the workpiece machined surface after milling operation.

- Cutting forces were measured by Kistler Multi-Component Dynamometer up to 10 kN Type 9257B.



**Figure 1. Experimental setup**

The work flow chart of the tests can be summarized as follows; AISI O2 cold work tool steel of 150mm\*80mm\*80mm was supplied as workpiece material. On this workpiece, three holes were drilled for fixing on the dynamometer. Then, according to the manufacturer's catalog and previous studies in the literature, cutting parameters were determined. In order to prepare the nano cutting fluid to be used in the MQL system, percentage by volume 1% and %2 h-BN was added to the commercially available ethylene glycol. Then, one-hour sonication was performed to ensure homogenous distribution of the h-BN in the cutting fluid. Then, the milling process started with the specified cutting parameters. After every 150 mm cutting length, the tool holder was removed from the CNC machine and the amount of cutting tool wear was measured on the flank face of cutting tool. In addition, roughness values were measured from seven different locations of the milled surface of the workpiece material and the average of these values was calculated as roughness value. Surface roughness values were measured at each pass up to 0.45 m cutting length. The cutting force values for each pass are transported by DynoWare, a computer program of the dynamometer, with a value of 1000 values per second. After each pass, the amount of wear from the microscope image obtained from the flank surface of the cutting tool was measured. According to ISO 8688-1: 1989 standards, when the amount of wear occurring on the flank face of cutting tool reaches 0.25 mm length, the cutting tool is considered to have completed its tool life. SEM images and EDS analyzes were investigated in order to determine the wear mechanisms occurring in the worn area of cutting tools for both conditions.

**Table 2. Cutting conditions**

Cutting speed, $V_c$	100 m/min
Feed rate, $f_z$	0.05 mm/tooth
Axial depth of cut, $a_p$	0.5 mm
Radial depth of cut, $a_e$	15 mm
Pressure	5 bar
Flow rate	50 ml/h

### 3. Results and Discussion

#### 3.1. Tool lifetime and wear analysis

The tool life of the cutting tools is determined according to the ISO 8688-1 standard. According to this standard, it is determined that the cutting tool is worn when the wear length of the flank face of the cutting tool reaches 0,2 mm. The fig. 2 shows the tool lifetimes obtained after the face milling operations, which are applied in three different conditions. Accordingly, in dry conditions, the tool life is lower than other conditions due to the high temperature that occurs in the cutting zone. Milling with cutting fluid prepared with EG containing 1% h-BN showed an increase in tool life of approximately 22% compared to the dry condition. In the milling operations, the highest tool life was obtained by processing with cutting fluid containing 2% h-BN. In milling using cutting fluid containing 2% h-BN, tool life increased approximately 78% compared to dry condition. Similarly, in terms of tool life of cutting fluid containing 2% h-BN, the increase in tool life was approximately 46% when compared to cutting fluid containing 1% of h-BN. It can be said that, in the milling process applied with cutting fluid containing h-BN, the increase of tool life is provided by reducing the friction coefficient of the h-BN nanoparticles in the cutting zone [2,3].

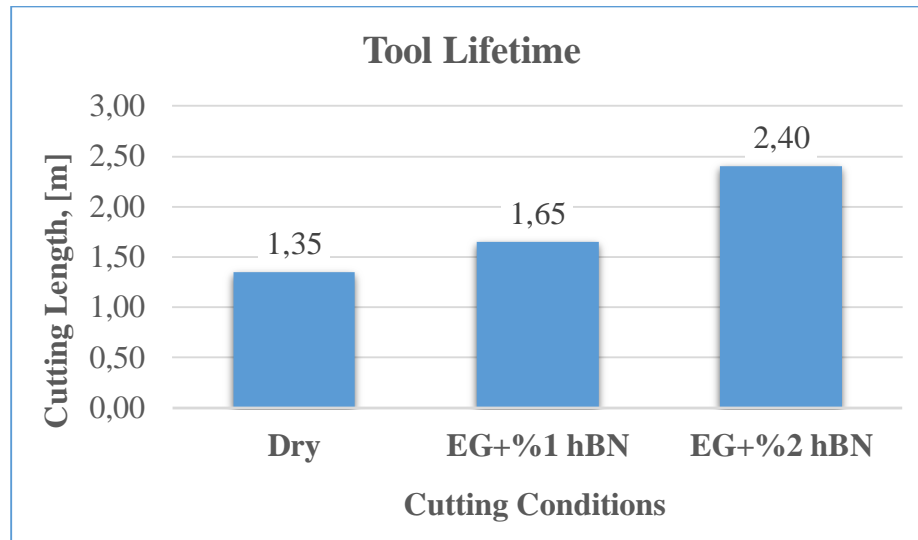


**Figure 2. Comparison of tool life under different cutting conditions.**

### 3.2. Surface Roughness

Ra surface roughness value is often used when determining the surface quality of a part [27]. In the milling process, many parameters affect the surface roughness value, some of them; tool geometry, feed rate, cutting fluid, cutting speed, tool wear [28]. In this study, the influence of the cutting fluid used in the MQL method on the roughness value of Ra was investigated. The surface roughness values, shown in fig. 3 were determined as the average of the measured values from the 7 different parts of the machined workpiece surface, up to a cutting length of 0.45 m, after every cutting length of 0.15 m. Thanks to the lubricating effect of h-BN the surface roughness value was reduced by approximately 20% measured after milling tests with cutting fluid containing 1% h-BN compared with the values measured in dry conditions. The improvement in surface roughness value was approximately 60% using 2% h-BN-containing cutting fluid compared to dry conditions. Smooth workpiece surface obtained with EG solution with 2% h-BN. It can be said that the improvement in surface roughness value is due to the lubricating effect of h-BN in the cutting zone [22] [26].

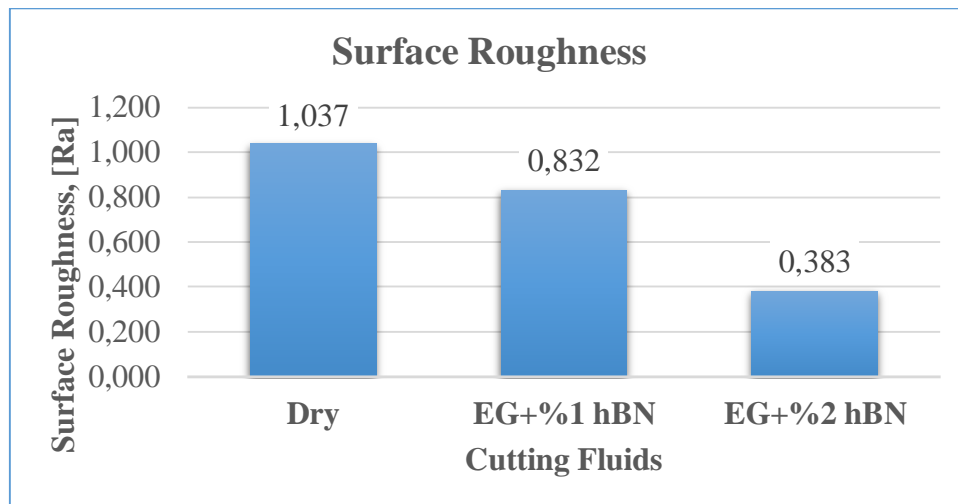


Figure 3. Comparison of surface roughness under different cutting conditions.

### 3.3. Cutting forces

Fig. 4. shows the resultant cutting force  $F_R$  value fluctuations measured at the same cutting length with different cutting conditions. Accordingly, a reduction in cutting forces has occurred with the addition of nano sized h-BN into the cutting fluid. This can be said to be caused by the reduction of the friction in the cutting zone by the lubricating effect of h-BN. In addition, when the cutting tool is outside the workpiece, it is seen that the vibration is less in the milling operations with the h-BN containing liquid.

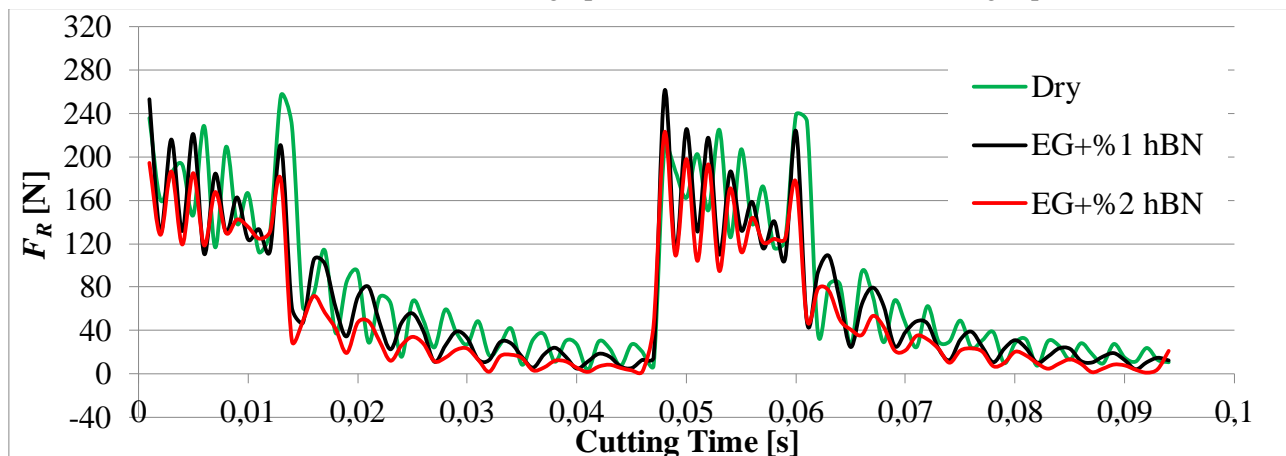
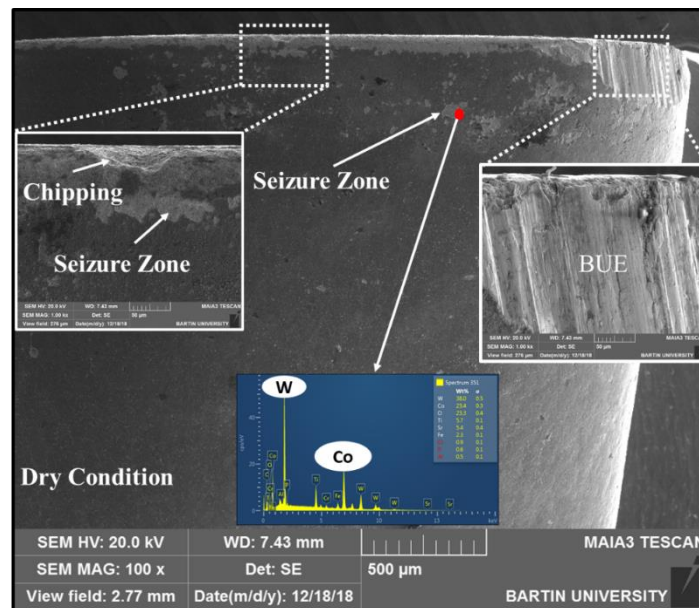


Figure 4.  $F_R$  cutting force fluctuations according to cutting time with using different cutting fluid.

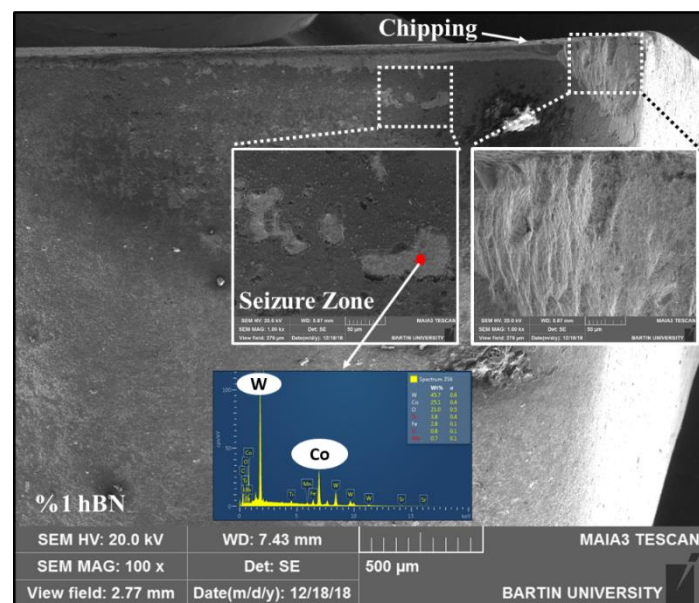
### 3.4. Wear Analysis

Fig. 5. shows the SEM photograph of the worn cutting tool after milling operation in dry condition. According to the photograph taken from the wear zone, due to the high temperature at the cutting zone, the workpiece material adhered to the cutting tool and the BUE was formed. Seizure zones were also formed on the flank surface due to high temperatures. It is seen by EDS analysis that the coating material is deformed in the seizure zone. As a result, the dominant wear mechanisms in the dry milling process were abrasion and adhesion.



**Figure 5. Worn cutting tool SEM image under dry condition**

Figure 6 shows the SEM image of the worn cutting tool after milling in MQL conditions with 1% h-BN containing cutting fluid. After milling with cutting fluid containing 1% h-BN, BUE formation was not observed in the wear zone compared to dry conditions. Chipping was observed in the wear zone due to intermittent cutting. Seizure zone formation has also occurred in the use of 1% h-BN including cutting fluid as in the case of dry milling. The reason for the Seizure zone formation is that the chips at high temperatures adhere to the flank surface of cutting tool and the adhered chips break away with the coating layer in the progressive cutting stages. According to the results obtained from the EDS analysis applied to the worn cutting tool, it was observed that the thin hard film coating was removed.



**Figure 6. SEM image of worn cutting tool using %1 h-BN added cutting fluid**

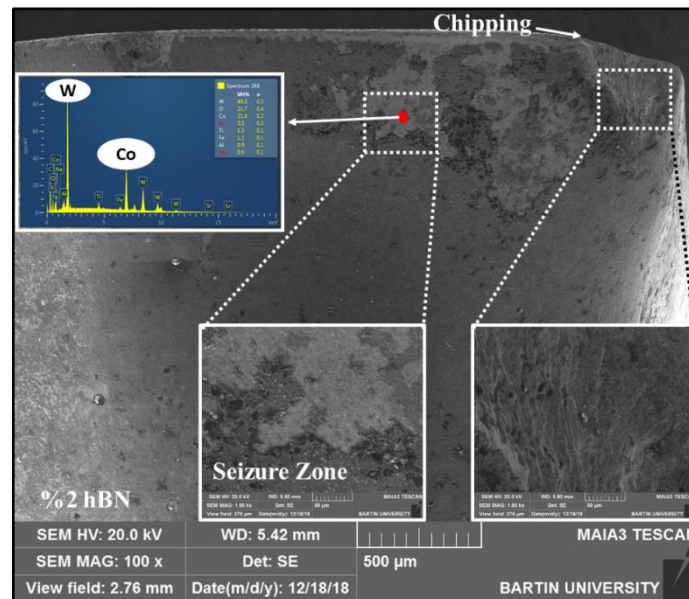


**Figure 7. SEM image of worn cutting tool using %2 h-BN added cutting fluid**

Figure 7 shows the SEM image of the worn cutting tool after milling in MQL conditions with 2% h-BN containing cutting fluid. Similar to the milling process using 1% h-BN added cutting fluid, the BUE in the wear zone was not observed due to the temperature in the cutting zone is reduced with using cutting fluid. Seizure zone formation was also seen this worn tool similar to worn tools that occur under different conditions. According to EDS analysis taken from Seizure zone, it is observed that the coating material is deformed.

#### 4. Conclusions

In this study, the use of an innovative cutting fluid in milling of AISI O2 workpiece as an alternative to cutting fluids which are highly harmful to the environment and human health and used in high amounts in the manufacturing sector have been investigated. Nano-size h-BN was added to ethylene glycol and used as cutting fluid in milling operations of AISI O2 with MQL system. The findings obtained from the study can be summarized as follows;

- The highest cutting tool life was obtained by using 2% h-BN added cutting fluid. The increase in cutting tool life was approximately 78% compared to dry conditions. Similarly increase in cutting tool life was approximately 46% compared to using %1 h-BN added cutting fluid. According to the values obtained after milling for three different condition, cutting tool life increased with the effect of h-BN used in cutting fluid.
- In terms of surface roughness, the best workpiece surface quality was achieved after milling with h-BN containing 2% h-BN. The improvement in surface roughness value was approximately 60% using 2% h-BN-containing cutting fluid compared to dry conditions. The surface roughness value was reduced by approximately 20% in the milling process with h-BN containing 1% h-BN compared with the dry condition. As a result, as the amount of nano h-BN used in the coolant increased, the workpiece surface roughness values were improved.
- In the milling of AISI O2 steel with using MQL system, the cutting forces are reduced by the use of cutting fluid and by the increase in the amount of h-BN in the cutting fluid. The lowest resultant cutting force values were obtained in the milling process using cutting fluid containing 2% h-BN. In addition, the use of h-BN reduced the vibration of the workpiece and in this way, surface roughness values were improved.
- Dominant wear mechanisms have been found to be adhesion and abrasion for both condition. Seizure zones have been observed due to high temperature for both condition on flank face of cutting tools. In dry milling operations, BUE has been observed in the wear zone due to higher temperature than milling operation using cutting fluid.

According to the findings, it was observed that the nano h-BN added cutting fluid, which is harmless to the environment and human health, increased the cutting performance in milling AISI O2 steel. In further

studies, the effect of prepared nano h-BN added cutting fluid on the cutting performance in the machining of hard to cut materials can be examined.

## References

- [1] E. O. Ezugwu, J. Bonney, and Y. Yamane, "An overview of the machinability of aeroengine alloys," *Journal of Materials Processing Technology*, vol. 134, no. 2, pp. 233–253, 2003.
- [2] J. P. Davim, P. S. Sreejith, R. Gomes, and C. Peixoto, "Experimental studies on drilling of aluminium (AA1050) under dry, minimum quantity of lubricant, and flood-lubricated conditions," *Proceedings of the Institution of Mechanical Engineers, Part B: Journal of Engineering Manufacture*, vol. 220, no. 10, pp. 1605–1611, 2006.
- [3] C. Kannan, R. Ramanujam, and A. S. S. Balan, "Machinability studies on Al 7075/BN/Al<sub>2</sub>O<sub>3</sub> squeeze cast hybrid nanocomposite under different machining environments," *Materials and Manufacturing Processes*, vol. 33, no. 5, pp. 587–595, 2018.
- [4] B. Kursuncu, H. Caliskan, S. Y. Guven, and P. Panjan, "Wear behavior of multilayer nanocomposite TiAlSiN/TiSiN/TiAlN coated carbide cutting tool during face milling of inconel 718 superalloy," *Journal of Nano Research*, vol. 47, 2017.
- [5] H. Caliskan, B. Kursuncu, S. Y. Guven, A. C. Karaoglanli, M. Sabri Gok, and A. Alsaran, *Effect of boron nitride coating on wear behavior of carbide cutting tools in milling of inconel 718*, vol. 61, 2016.
- [6] B. Kursuncu, H. Caliskan, S. Y. Guven, and P. Panjan, "Improvement of cutting performance of carbide cutting tools in milling of the Inconel 718 superalloy using multilayer nanocomposite hard coating and cryogenic heat treatment," *International Journal of Advanced Manufacturing Technology*, 2018.
- [7] M. KUNCAN, K. KAPLAN, H. M. ERTUNÇ, and S. KÜÇÜKATEŞ, "5 AXIS CNC PRECISION TIRE SIDE MACHINING," *European Journal of Technique*, vol. 6, no. 2, pp. 117–123, Aug. 2016.
- [8] M. Amrita, R. R. Srikant, and A. V Sitaramaraju, "Performance evaluation of nanographite-based cutting fluid in machining process," *Materials and Manufacturing Processes*, vol. 29, no. 5, pp. 600–605, 2014.
- [9] S. Chinchankar and S. K. Choudhury, "Hard turning using HiPIMS-coated carbide tools: Wear behavior under dry and minimum quantity lubrication (MQL)," *Measurement: Journal of the International Measurement Confederation*, vol. 55, pp. 536–548, Sep. 2014.
- [10] S. Etienne, "Influence of Minimum Quantity Lubrication design parameters on milling finishing process on milling finishing process," *Materials and Manufacturing Processes*, vol. 33, no. JUNE, pp. 69–76, 2014.
- [11] J. S. Dureja, R. Singh, T. Singh, P. Singh, M. Dogra, and M. S. Bhatti, "Performance evaluation of coated carbide tool in machining of stainless steel (AISI 202) under minimum quantity lubrication (MQL)," *International Journal of Precision Engineering and Manufacturing-Green Technology*, vol. 2, no. 2, pp. 123–129, 2015.
- [12] R. W. Maruda, E. Feldshtein, S. Legutko, and G. M. Krolczyk, "Analysis of contact phenomena and heat exchange in the cutting zone under minimum quantity cooling lubrication conditions," *Arabian Journal for Science and Engineering*, vol. 41, no. 2, pp. 661–668, 2016.
- [13] D. Carou, E. M. Rubio, C. H. Lauro, and J. P. Davim, "The effect of minimum quantity lubrication in the intermittent turning of magnesium based on vibration signals," *Measurement*, vol. 94, pp. 338–343, 2016.
- [14] K. Gupta, R. F. Laubscher, J. P. Davim, and N. K. Jain, "Recent developments in sustainable manufacturing of gears: a review," *Journal of Cleaner Production*, vol. 112, pp. 3320–3330, 2016.
- [15] J. Sharma and B. S. Sidhu, "Investigation of effects of dry and near dry machining on AISI D2 steel using vegetable oil," *Journal of Cleaner Production*, vol. 66, pp. 619–623, Mar. 2014.
- [16] O. N. Çelik, N. Ay, and Y. Göncü, "Effect of nano hexagonal boron nitride lubricant additives on

- the friction and wear properties of AISI 4140 steel,” *Particulate Science and Technology*, vol. 31, no. 5, pp. 501–506, 2013.
- [17] A. Yaras, E. Er, H. Çelikkan, A. Disli, and A. Alicilar, “Cellulosic tent fabric coated with boron nitride nanosheets,” *Journal of Industrial Textiles*, vol. 45, no. 6, pp. 1689–1700, Feb. 2015.
- [18] M. Zheng, Y. Gu, Z. Xu, and Y. Liu, “Synthesis and characterization of boron nitride nanoropes,” *Materials Letters*, vol. 61, no. 8–9, pp. 1943–1945, Apr. 2007.
- [19] A. Pakdel, C. Zhi, Y. Bando, T. Nakayama, and D. Golberg, “Boron Nitride Nanosheet Coatings with Controllable Water Repellency,” *ACS Nano*, vol. 5, no. 8, pp. 6507–6515, Aug. 2011.
- [20] T. Sainsbury *et al.*, “Oxygen Radical Functionalization of Boron Nitride Nanosheets,” *Journal of the American Chemical Society*, vol. 134, no. 45, pp. 18758–18771, Nov. 2012.
- [21] J. H. Warner, M. H. Rummeli, A. Bachmatiuk, and B. Büchner, “Atomic resolution imaging and topography of boron nitride sheets produced by chemical exfoliation,” *ACS nano*, vol. 4, no. 3, pp. 1299–1304, 2010.
- [22] B. Kursuncu and A. Yaras, “Assessment of the effect of borax and boric acid additives in cutting fluids on milling of AISI O2 using MQL system,” *The International Journal of Advanced Manufacturing Technology*, vol. 95, no. 5, pp. 2005–2013, 2018.
- [23] H. Caliskan, C. Kurbanoglu, D. Kramar, P. Panjan, and J. Kopac, “Hard Milling Operation Of AISI O2 Cold Work Tool Steel By Carbide Tools,” vol. 15, no. 1, pp. 21–26, 2012.
- [24] B. KURŞUNCU and A. YARAŞ, “AISI O2 Takım Çeliğinin Frezelenmesinde Minimum Miktarda Yağlama (MQL) Sisteminin Kesme Performansına Etkisi,” *Mühendislik ve Teknoloji Bilimleri Dergisi*, vol. 5, no. 2, pp. 125–128, 2018.
- [25] S. Ekinović, S. Dolinšek, and E. Begović, “Machinability of 90MnCrV8 steel during high-speed machining,” *Journal of Materials Processing Technology*, vol. 162–163, no. SPEC. ISS., pp. 603–608, 2005.
- [26] N. Talib, R. M. Nasir, and E. A. Rahim, “Tribological behaviour of modified jatropha oil by mixing hexagonal boron nitride nanoparticles as a bio-based lubricant for machining processes,” *Journal of Cleaner Production*, vol. 147, pp. 360–378, 2017.
- [27] L. Road and G. District, “Chip morphology and surface roughness in high-speed milling of nickel-based superalloy Inconel 718 Fuda Ning , Fuji Wang \*, Zhenyuan Jia and Jianwei Ma,” vol. 15, 2014.
- [28] H. Öktem, T. Erzurumlu, and H. Kurtaran, “Application of response surface methodology in the optimization of cutting conditions for surface roughness,” *Journal of Materials Processing Technology*, vol. 170, no. 1–2, pp. 11–16, 2005.

## THE EXPERIMENTAL INVESTIGATION OF ANNEALING PARAMETERS EFFECTS ON AL2024-T3 MATERIALS' FORMABILITY AND MECHANICAL PROPERTIES

*İbrahim KARAAĞAÇ<sup>1</sup>, M. Okan KABAKÇI<sup>\*</sup>, M. Yasin DEMİREL<sup>2</sup>*

*In this study, the effects of annealing parameters on the formability and mechanical properties of Al2024-T3 sheet material were investigated experimentally. Annealing process were applied at 100 °C, 200 °C, 300 °C, 400 °C annealing temperatures and at 6 minutes, 30 minutes, 60 minutes annealing times. The forming operations were applied in 10 mm / sec deformation velocity and in V bending dies with an angle of 30 °, 60 °, 90 °, 120 °. In the experimental studies, it was determined that there was no significant change in the hardness values of the specimens at temperatures less than 300 ° C annealing temperature and 6 minutes annealing time parameters, but an irregular changes were observed in the mechanical properties of specimens. However, it was observed that there were a significant decrease in the hardness values and mechanical properties of the test specimens after the annealing temperature of 300 ° C and the annealing time of 6 minutes. It has been observed that the samples only has been formed successfully in a 30 ° die angle and at low temperatures (RT - 100 ° C - 200 ° C). It has been observed that a successful forming process has been performed in 30 ° and 60 ° die angles by increasing the annealing parameters values (400 ° C - 30 min or 400 ° C - 60 min). However, forming defects such as cracks and fractures were encountered in forming processes using 90 ° and 120 ° die angled.*

Key words: Al2024-T3, Annealing, Formability, Mechanical Properties

### 1. Introduction

Aluminium 2xxx alloys are widely used in defence industry, aviation industry, and automotive industry due to their high hardness, strength, and lightweight. Al 2024-T3 alloys are most known, have low ductility and formability at room temperature due to its high mechanical properties. Therefore, it may be required to heat during or before the forming process in order to form the geometry and dimensions desired. In literature studies, annealing processes applied to aluminum alloys; it was often seen that solution heat treatment is applied primarily and then natural or artificial aging processes are applied. Also, it has been observed that there are studies in the literature in which all the parts are formed by laser or induction applications or only the forming area is heated. Moreover, it has been intended to

<sup>1\*</sup> Faculty of Technology, Department of Manufacturing Engineering, University of Gazi, Ankara, Turkey, (mokabakci@gazi.edu.tr)

 <https://orcid.org/0000-0003-0086-9294>

<sup>1</sup> Faculty of Technology, Department of Manufacturing Engineering, University of Gazi, Ankara, Turkey, (ibrahimkaraagac@gazi.edu.tr)  <https://orcid.org/0000-0001-6727-3650>

<sup>2</sup> Graduate School of Natural and Applied Sciences, Department of Manufacturing Engineering, University of Gazi, Ankara, Turkey, (yasindemirel@outlook.com)  <https://orcid.org/0000-0002-4244-8562>

further enhancement of the formability by different applications such as heating the female and male portions of the die set [2-9]. Khan et al. [2] investigated the effect of forming process parameters on the formability of Al 2024 alloy by experimental and finite element tests, and they reported that the formability increased by about 10%. Ortiz et al. [3] exposed different aluminum alloys to plastic deformation including Al 2024 which were tempered at various temperatures (T-O, T-8, T-62). After the deformation processes applied, they examined various properties of materials such as tensile strength, ductility, conductivity, hardness, and grain size. They suggested using tempered alloys which give low strength and high ductility values as a result of their study. Moy et al. [4] studied the effects of annealing parameters of the formability and mechanical properties of Al 2024-T3 alloy experimentally. They applied aging process at different times such as 2.5 hours, 2 days, 1 week to the samples which were solution heat-treated at 525 °C. A significant decrease in mechanical properties and an increase, 4 - 6%, in total elongation were observed for two-days-aged samples. In addition, it was observed that the formability of the material was positively affected by the aging process. The effects of annealing process, which consist of a solution heat treatment and aging processes on the mechanical properties of Al 2024-T3 material to have been investigated in many studies. Fujda et al. [5] investigated the changes caused by the solution temperature on the mechanical properties and microstructural properties of Al2024 in annealing processes experimentally. In this study, the test samples were taken into a solution at variable temperatures between 500 - 570 ° C and were kept under vacuum for 2.5 hours. Then, the natural aging process was applied for 300 hours with water quenching. As a result of these studies, it was observed that the mechanical properties and hardness of the alloy decreased but the formability increased while process. Reis et al. [6] investigated the change in mechanical properties of heat-treated Al 2024 aluminum alloy in their experimental study. The samples were solution heat-treated at 495 °C, 505 °C, and 515 °C and then quenched. After, the samples were artificially aged at 190 ° C and 208 ° C and tensile tests were applied to the test samples for determining the mechanical properties. It was observed that the materials which were soluted at 515 °C and artificially aged at 208 °C for 2 hours had the highest yield and tensile strength. Merklein et al. [7] investigated the rearrangement of aluminum alloy properties by regional laser heating. In their work, they applied a short-term heat treatment with the Nd: YANG laser at a temperature of 400 ° C and holding times less than 5 seconds. As a result of the heat treatment, they observed a significant increase in the formability limits of the materials. Mohammadi et al. [8] investigated the bending properties of the locally laser-treated Al 2024-T3 alloy. In this study, the formability with V bending was investigated, and the bending regions of the samples were locally heated with Nd: YANG laser. Therefore, the stresses in the bending regions are reduced by local softening. As a result of the study, it was observed that the amount of spring-back after local heating decreased by 43% in the bending regions where the highest stress occurred. Chen et al. [9] studied the effects of synchronous cooling hot forming process on Al 2024 alloy microstructure and mechanical properties. They have found that the applied synchronous cooling hot forming process highly reduces residual stresses leading to spring-back and increases the dimensional stability of the final product significantly. In spite of all of these studies, heat treatment applications carried to improve the formability of Al2024 alloys can be difficult to apply because of the fact that they are expensive and require numerous consecutive metallurgical processes. In addition, the initial installation costs of such systems are very high and the high energy consumption is experienced during the implementation of some processes.

In this study, it is aimed to investigate the change of mechanical properties and formability of material experimentally by applying annealing process at different holding time and temperature

parameters to Al 2024-T3 alloy. In addition, the data obtained are intended to provide guidance for industrial applications.

## 2. Material and Method

### 2.1. Material

In this study, the test samples which were used to examine the change of mechanical properties and formability were prepared using cutting guillotine shear from 2,5 mm thick Al2024-T3 sheet plate in the rolling direction. Tensile test specimens to be used for the determination of mechanical properties were also prepared by using a wire EDM machine from the Al 2024-T3 sheet plate in accordance with the ASTM-E8M standard in the rolling direction. The image of the prepared tensile test specimen given in Figure 1. Tensile test specimens used for the determination of mechanical properties were annealed together with bending test specimens. In order to analyze the chemical composition of the test materials used in the study, the chemical analysis test was performed with a spectrometer. The results obtained by the chemical analysis tests given in Table 1.



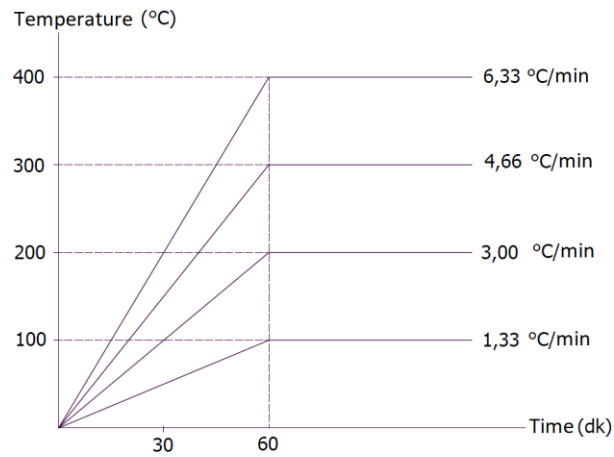
Figure 1. Al 2024-T3 Alloy Tensile Test Specimen.

Table 1. Al 2024-T3 alloy chemical analysis results.

Element (%)	Al	Cu	Mn	Zn	Fe	Ni	Zr	Pb	Other
Al 2024-T3	94,810	4,376	0,427	0,140	0,101	0,009	0,006	0,002	0,129
Nominal	90,7- 94,7	3,8- 4,9	0,3- 0,9	Max. 0,25	Max. 0,5	-	-	-	Max. 0,15

### 2.2. Annealing Process and Parameters

Annealing process was applied at four different annealing temperatures (100 °C, 200 °C, 300 °C, 400 °C) and at three different holding time (6min, 30min, 60min) into test specimens which were prepared with guillotine shears. In the literature research, it was determined that the holding time at annealing temperature was applied as 1 hour for 1 inch (25.4 mm) piece thickness [10]. Since the sheet thickness of the test specimens used in this study was 2.5 mm, the holding time at the annealing temperature was 6min calculated. In addition, 30 and 60 minutes holding times were also included in these study to investigate better the effect of holding time on formability. Figure 2 shows the heating rate parameters used in the annealing process and Figure 3 shows the environment in which the annealing process takes place.



**Figure 2. Heating Rate at Different Temperatures.**



**Figure 3. Annealing Environment (a) PID Unit Furnace; (b) Experimental Specimens.**

### 2.3. Experimental Setup and Experimental Parameters

Figure 4 and Figure 5 shows the computer-controlled test setup in which the forming of annealed test specimens is performed. The specimens were bent at a constant deformation velocity of 10 mm/sec using with a 30° - 60° - 90° - 120° angled V bending dies and a 0 mm punch radius. Figure 6 shows the die-punch sets used in forming operations. The changes of time-dependent force in each bending occurring process were observed simultaneously with the help of data from the load cells on the device. In order to increase the reliability of the data, each experiment performed in this study was repeated 2 times.



**Figure 4. Experimental Environment and Forming Device**

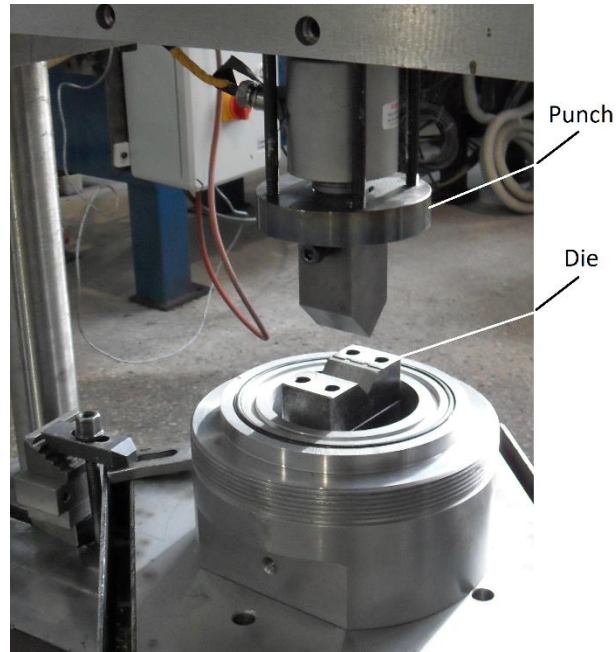


Figure 5. Detail View of Die - Punch Set.

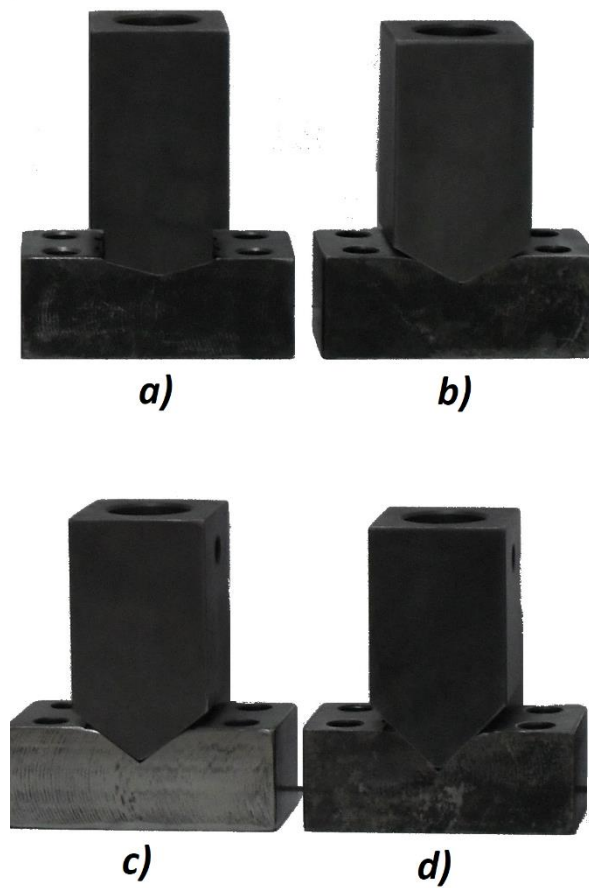


Figure 6. Forming Dies and Punches; a) 30°, b) 60°, c) 90°, d) 120°.

### 3. Experimental Results and Discussion

Al2024-T3 sheet material was subjected to heat treatment at different annealing temperatures at 100 ° C - 200 ° C - 300 ° C - 400 ° C for 6, 30 and 60 minutes by using electronic PID controlled annealing furnace. The changes in the mechanical properties of the annealed Al2024-T3 test specimens and their forming in various angled V bending dies (30°, 60°, 90°, 120°) were investigated experimentally. The changes in mechanical properties after annealing of test specimens were determined by tensile and hardness tests. The distribution of the values determined by the tensile tests according to the annealing parameters given in Table 2. It was observed that the annealing parameters in which applied at 100 ° C and 200 ° C temperature values were caused an irregular change in the mechanical properties of Al2024-T3 sheet metal material and did not cause a significant change in the hardness values. However, in the annealing process at annealing temperatures 300 ° C and higher, it was determined that the annealing temperature and holding time variations caused significant decreases in yield strength and tensile strength of the test specimens. In order to examine the effects of annealing parameters on the formability properties of Al 2024-T3 sheet material, V bending dies which have different bending angles at 30°, 60°, 90°, 120°, punches with zero radii, and constant deformation velocity parameters in 10 mm/s were used. It has been observed that the specimens which were annealed at 400 °C - 30 min and 400 °C - 60 min parameters can be formed in the 30 ° and 60 ° angled V bending dies without any forming defects such as cracking or breaking. Specimens that were annealed at RT - 100 ° C - 200 ° C can be formed without any forming defects in a 30° angled die set. In Table 3, the obtained data shows as a consequence of bending operations. In addition, the results of the hardness test which were performed in three repetitions at 10 mm gaps, shown in Figure 7.

**Table 2. Tensile Test Results for Al 2024-T3 Annealing Parameters.**

Annealing Heat (°C)	Holding Time (min.)	$\sigma_y$ (MPa)	UTS (Mpa)
RT	-	350,112	474,497
100	6	363,259	480,392
	30	355,548	473,828
	60	361,687	479,419
200	6	348,695	463,418
	30	382,157	482,950
	60	381,225	480,102
300	6	348,395	436,760
	30	309,856	403,878
	60	291,348	384,724
400	6	198,621	311,857
	30	130,115	241,611
	60	100,586	237,437

**Table 3. Obtained Data As A Result of Bending Operations.**

Die Angle	Annealing Heat (°C)	Holding Time (min.)	Description	Die Angle	Annealing Heat (°C)	Holding Time (min.)	Description	
30°	RT	-	Success	90°	RT	-	Crack	
		6	Success			6	Crack	
		30	Success			30	Crack	
	100	60	Success		60	Crack		
		200	6		Success	200	6	Crack
			30		Success		30	Crack
	60		Success		60		Crack	
	300	6	Crack		300	6	Broken	
		30	Crack			30	Broken	
		60	Crack			60	Broken	
	400	6	Success		400	6	Crack	
		30	Success			30	Crack	
60		Success	60	Crack				
60°	RT	-	Crack	120°	RT	-	Broken	
		6	Crack			6	Broken	
		30	Crack			30	Broken	
	100	60	Crack		60	Broken		
		200	6		Crack	200	6	Broken
			30		Crack		30	Broken
	60		Crack		60		Broken	
	300	6	Crack		300	6	Broken	
		30	Crack			30	Broken	
		60	Crack			60	Broken	
	400	6	Crack		400	6	Crack	
		30	Success			30	Crack	
60		Success	60	Crack				

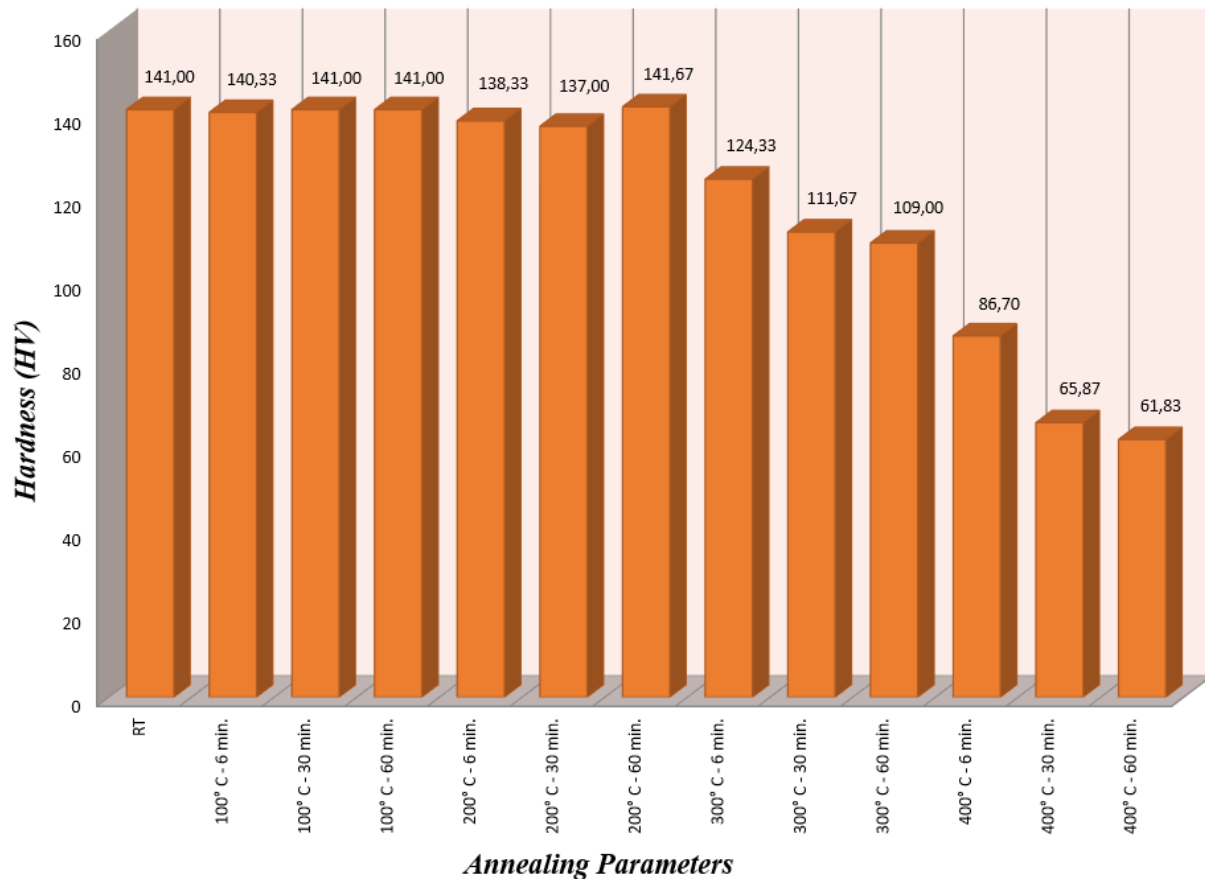


Figure 7. Variation of Hardness Values According to Annealing Parameters.

#### 4. Experimental Results and Discussion

In this study, 2024-T3 aluminum alloy was annealed at variable annealing temperature and holding times. It has been aimed to determine the optimum annealing parameters in which no cracks and breaks occur for the ideal forming. In addition, the effects of annealing on the mechanical properties and hardness values of Al 2024-T3 sheet metal material were investigated. The results obtained from the experiments are given below.

- i. An irregular change in yield strength and tensile strength of the annealed specimens starting from room temperature up to 300 °C annealing temperature was determined. However, a significant decrease in yield strength and tensile strength was observed in 300 °C - 6 min annealing parameters. At 400 °C - 60 min annealing parameters, the heat-treated specimens initially had 350,112 MPa yield strength, decreased by 71.27% to 100,586 MPa. And at the same annealing parameters, a maximum tensile strength in which decreased by 49.96% from 474,497 MPa to 237,437 MPa.
- ii. As a result of the annealing process, it was observed that the hardness values of Al 2024-T3 alloy did not change significantly until the annealing process was carried out at 300 °C. Significant decreases in hardness values were observed annealing parameters in the case of 300 °C - 6 minutes. Also, it was measured that in the 400 °C - 60 min annealing parameters the initial hardness of 141 HV decreased by 56.15% decreased to 61.83 HV value.

- iii. At low temperatures, RT - 100 ° C - 200 ° C, annealed test specimens can be formed only in 30 ° angled bending dies without any cracks or fractures. However, when the annealing parameters were changed to 400 ° C - 30 min or 400 ° C - 60min was observed that it could be formed without any defect in 60 ° angle bending dies.
- iv. It was observed that Al2024 – T3 test specimens which were heat-treated at 400 ° C - 60 min annealing parameters could not be formed in 90 ° and 120 ° angled V bending dies.

### Acknowledgment

This paper was presented at the 1st National Engineering and Technology Congress (UMTK) organized by Karamanoğlu Mehmet Bey University (KMU) on 17-19 October 2019. Declaration number UMTK-145. We thank KMU UMTK for their support.

### References

- [1] L. Wanga, M. Strangwoodb, D. Balinta, J. Lina, T.A. Deanc, “Formability and failure mechanisms of AA2024 under hot forming conditions”, *Materials Science and Engineering A*, 528, pp.2648–2656, 2011.
- [2] Irfan Mahmood Khan M. I., Umair Ismail, D. Noman, M. Zeeshan Siddiqui and M. Shahzad, “Effect of Process Parameters on Formability of Aluminum 2024”, *Journal of Space Technology*, Vol 7, No 1, 2017.
- [3] Ortiz, D., Abdelshehid, M., Dalton, R., Soltero, J., Clark, R., Hahn, M., ... & Stoyanov, P., “Effect of cold work on the tensile properties of 6061, 2024, and 7075 Al alloys”, *Journal of Materials Engineering and Performance*, Volume 16, Issue 5, pp. 515–520, 2007.
- [4] Moy, C. K. S., Weiss, M., Xia, J., Sha, G., Ringer, S. P., “Influence of heat treatment on the microstructure, texture and formability of 2024 aluminium alloy”, *Materials Science and Engineering A* 552, pp.48–60, 2012.
- [5] Fujda, M., Mišičko, R., Rusňáková, L., & Sojko, M. “Effect of solution annealing temperature on structure and mechanical properties of EN AW 2024 aluminium alloy”, *Journal of Metals, Materials and Minerals*, Vol 17 No.1 pp. 35-40, 2017.
- [6] Reis, D. A. P., Couto, A. A., Domingues Jr, N. I., Hirschmann, A. C. O., Zepka, S., Moura neto, C., “Effect of artificial aging on the mechanical properties of an aerospace aluminum alloy 2024”, *Defect and Diffusion Forum Vols. 326*, pp. 193-198, 2012.
- [7] Merklein, M., Böhm, W., & Lechner, M., “Tailoring material properties of aluminum by local laser heat treatment”, *Physics Procedia*, 39, pp. 232-239, 2012.
- [8] Mohammadia, A., Vanhovea, H., Baelb, H. A., and Dufloua, J. R., “Bending properties of locally laser heat treated AA2024-T3 aluminium alloy”, *Physics Procedia*, 39, pp. 257-264, 2012.
- [9] Chen, G., Chen, M., Wang, N., and Sun, J., “Hot forming process with synchronous cooling for AA2024 aluminum alloy and its application”, *The International Journal of Advanced Manufacturing Technology*, 86, pp. 133–139, 2016.
- [10] LeMaster R., Boggs, B., Hubbard, C., Watkins, T., “Grinding induced changes in residual stresses of carburized gears”, *Gear Technology*, March/April, pp.42-49, 2015.